frontiers | Research Topics

Insights in environmental engineering

Edited by
Qingguo Huang, Ricardo Bello-Mendoza, Jeremy Dhainaut and Christian Kennes

Published in
Frontiers in Environmental Engineering

ISSN 1664-8714
ISBN 978-2-8325-6176-8
DOI 10.3389/978-2-8325-6176-8

About Frontiers

Frontiers is more than just an open access publisher of scholarly articles: it is a pioneering approach to the world of academia, radically improving the way scholarly research is managed. The grand vision of Frontiers is a world where all people have an equal opportunity to seek, share and generate knowledge. Frontiers provides immediate and permanent online open access to all its publications, but this alone is not enough to realize our grand goals.

Frontiers journal series

The Frontiers journal series is a multi-tier and interdisciplinary set of open-access, online journals, promising a paradigm shift from the current review, selection and dissemination processes in academic publishing. All Frontiers journals are driven by researchers for researchers; therefore, they constitute a service to the scholarly community. At the same time, the *Frontiers journal series* operates on a revolutionary invention, the tiered publishing system, initially addressing specific communities of scholars, and gradually climbing up to broader public understanding, thus serving the interests of the lay society, too.

Dedication to quality

Each Frontiers article is a landmark of the highest quality, thanks to genuinely collaborative interactions between authors and review editors, who include some of the world's best academicians. Research must be certified by peers before entering a stream of knowledge that may eventually reach the public - and shape society; therefore, Frontiers only applies the most rigorous and unbiased reviews. Frontiers revolutionizes research publishing by freely delivering the most outstanding research, evaluated with no bias from both the academic and social point of view. By applying the most advanced information technologies, Frontiers is catapulting scholarly publishing into a new generation.

What are Frontiers Research Topics?

Frontiers Research Topics are very popular trademarks of the *Frontiers journals series*: they are collections of at least ten articles, all centered on a particular subject. With their unique mix of varied contributions from Original Research to Review Articles, Frontiers Research Topics unify the most influential researchers, the latest key findings and historical advances in a hot research area.

Find out more on how to host your own Frontiers Research Topic or contribute to one as an author by contacting the Frontiers editorial office: frontiersin.org/about/contact

Insights in environmental engineering

Topic editors

Qingguo Huang — University of Georgia, Griffin Campus, United States
Ricardo Bello-Mendoza — University of Canterbury, New Zealand
Jeremy Dhainaut — Centre National de la Recherche Scientifique (CNRS), France
Christian Kennes — University of A Coruña, Spain

Citation

Huang, Q., Bello-Mendoza, R., Dhainaut, J., Kennes, C., eds. (2025). *Insights in environmental engineering*. Lausanne: Frontiers Media SA.
doi: 10.3389/978-2-8325-6176-8

Table of contents

frontiers | Frontiers in Environmental Engineering

TYPE Editorial
PUBLISHED 05 September 2024
DOI 10.3389/fenve.2024.1475091

OPEN ACCESS

EDITED AND REVIEWED BY
Ronei De Almeida,
Rio de Janeiro State University, Brazil

*CORRESPONDENCE
Qingguo Huang,
qhuang@uga.edu

RECEIVED 02 August 2024
ACCEPTED 14 August 2024
PUBLISHED 05 September 2024

CITATION
Dhainaut J, Kennes C, Bello-Mendoza R and Huang Q (2024) Editorial: Insights in environmental engineering.
Front. Environ. Eng. 3:1475091.
doi: 10.3389/fenve.2024.1475091

Editorial: Insights in environmental engineering

Jérémy Dhainaut[1], Christian Kennes[2], Ricardo Bello-Mendoza[3] and Qingguo Huang[4]*

[1]Univ. Lille, CNRS, Centrale Lille, Univ. Artois, , UMR 8181 – UCCS – Unité de Catalyse et Chimie du Solide, Lille, France, [2]University of A Coruña, Faculty of Sciences and Interdisciplinary Centre of Chemistry and Biology – Centro Interdisciplinar de Química y Biología (CICA), BIOENGIN group, Coruña, Spain, [3]Department of Civil and Natural Resources Engineering, University of Canterbury, Christchurch, New Zealand, [4]Department of Crop and Soil Sciences, University of Georgia, Griffin, GA, United States

KEYWORDS

environmental catalysis, wastewaster, solid waste, valorization, resource recovery

Editorial on the Research Topic
Insights in environmental engineering

The Research Topic "*Insights in Environmental Engineering*," cross-listed with the Environmental Catalysis and the Water, Waste, and Wastewater Engineering sections, was initiated on 6 November 2023, and completed on 23 April 2024. Seven papers were published in this Research Topic during its lifespan of less than half a year, including one review, four research, and two perspective articles. A total of 27 authors contributed from nine countries across five continents, including Australia, China, Ethiopia, Germany, India, Spain, Malawi, the United Kingdom, and the United States. This Research Topic, although small, reflects what was intended to solicit in the Research Topic call: forward-looking contributions focused on new insights, novel developments, current challenges, latest discoveries, significant accomplishments, and future perspectives in the field. As of 2 May 2024, it generated 1,018 total downloads and 4,946 total views. Many editors and reviewers have contributed greatly to ensure this Research Topic's timely and quality publications. Their advice and critique have greatly improved the Research Topic's quality through the effective Frontiers interactive review process, which is reflected in the final products.

Two perspective papers in this Research Topic identify the grand challenges and research opportunities in Environmental Catalysis and Water, Waste, and Wastewater Engineering. In "*Grand Challenges Present Great Opportunities in Environmental Catalysis*," Dr. Qingguo (Jack) Huang, Specialty Chief Editor, discusses how more efficient and sustainable catalysis applicable to pollution control, cleaner production, and greener processes provide tools to address the vast challenges that we are facing today, the scarcity of water and the pollution by wastewater, solid wastes, and air/gas emissions (Huang). Furthermore, in his perspective paper titled "*The Grand Challenge of Water, Waste, Wastewater and Emissions Engineering and Valorization*," Specialty Chief Editor Dr. Christian Kennes argues that pollution sources can be considered valuable resources by their reuse, resource recovery, and pollutants valorization. This is a trend in Water, Waste and Wastewater Engineering, in which Environmental Catalysis plays a pivotal role (Kennes).

Through catalytic processes, harmful pollutants can be converted into less toxic substances or even into valuable products, thereby reducing environmental impact and

enhancing resource efficiency. Environmental catalysis is thus essential for addressing pressing environmental concerns and advancing towards a cleaner, more sustainable future. In this context, the study reported in "*Heterogeneous Catalytic Oxidation Regeneration of Desulfurization-Rich Liquor with Fe^{3+} Modified Chitosan*" targets the catalytic remediation of hydrogen sulfide (H_2S) present in industrial streams. The catalyst is based on chitosan, a broadly available biopolymer forming stable hydrogel beads, and coordinated iron (III) cations. Notably, not only does the material efficiently oxidize H_2S, but its activity can be fully recovered in the presence of bubbling oxygen (Liu et al.).

Catalysts may be used as a downstream solution to degrade harmful compounds but also have great potential in shifting towards more sustainable processes, including clean and renewable energy. In line with this, the comprehensive review article "*Biomass-Derived Carbon Nanostructures and Their Applications as Electrocatalysts for Hydrogen Evolution and Oxygen Reduction/Evolution*" explores the potential of biomass-derived carbon nanostructures (CN) and their great potential in electrochemical technologies crucial for energy production, conversion, and storage. Emphasis is given to a better comprehension of the relationships between the physicochemical properties of the CN, and hence their preparation protocol, and their catalytic activity in hydrogen evolution reaction, and the oxygen reduction and evolution reactions (Maliutina et al.).

As reported in the paper "*Major Contributing Factors to the Lower Level of Connection to the Existing Sewer Network in Addis Ababa: the Case of the Kality Catchment*," in some regions of the world, e.g., Addis Ababa, households are still not connected to a sewer network, despite its proximity (Ali and Robele). In this study, an efficient survey allowed the identification of the main factors contributing to this situation, which appeared to be lack of awareness, connection fee, topography, customers' preference for onsite sanitation over sewers, customers' unwillingness to reinstate fences or pavements in their compound, and the unreliability of the water utility service. The lack of regulations for monitoring wastewater management appeared to be another critical Research Topic.

Another paper highlights that the management of sewage sludge is a current key research topic, while its utilization as fertilizer in the European Union is restricted by stringent European environmental regulations. The research "*Acid Leaching of Hydrothermally Carbonized Sewage Sludge: Phosphorus Recovery and Hydrochar Characteristics*" studied different ways to acid leach hydrochar produced by hydrothermal carbonization of sewage sludges, and compared phosphorus recovery and effects on the hydrochar properties (Shettigondahalli Ekanthalu et al.).

The 5-day biochemical oxygen demand (BOD_5) is a commonly used key indicator of water quality in wastewater treatment facilities. However, BOD_5 estimation is a time-consuming and expensive procedure. The research reported on the "*Comparative Study for the Performance of Pure Artificial Intelligence Software Sensor and Selforganizing Map Assisted Software for Predicting 5-Day Biochemical Oxygen Demand for Kauma Sewage Treatment Plant Effluent in Malawi*" outscores the possibility to partly overcome such drawbacks based on the efficient implementation of an Adaptive Fuzzy Inference System, a kind of artificial intelligence algorithm that integrates both neural networks and fuzzy logic principles, to predict BOD_5 (Mng'ombe et al.).

This Research Topic, via a mix of perspective, review and research articles, provides a relatively thorough overview of the environmental engineering field, and some insights into the progress towards more accessible and sustainable waste treatment practices. We look forward to more of this kind forthcoming to serve our communities and our world at large.

Author contributions

JD: Writing–original draft, Writing–review and editing. CK: Writing–original draft, Writing–review and editing. RB-M: Writing–original draft, Writing–review and editing. QH: Writing–original draft, Writing–review and editing.

Funding

The authors declare that no financial support was received for the research, authorship, and/or publication of this article.

Conflict of interest

The authors declare that the research was conducted in the absence of any commercial or financial relationships that could be construed as a potential conflict of interest.

The authors declared that they were an editorial board member of Frontiers, at the time of submission. This had no impact on the peer review process and the final decision.

Publisher's note

frontiers | Frontiers in Environmental Engineering

TYPE Specialty Grand Challenge
PUBLISHED 06 December 2022
DOI 10.3389/fenve.2022.1087494

OPEN ACCESS

EDITED AND REVIEWED BY
Bing-Jie Ni,
University of Technology Sydney,
Australia

*CORRESPONDENCE
Qingguo Huang,
qhuang@uga.edu

SPECIALTY SECTION
This article was submitted to
Environmental Catalysis,
a section of the journal
Frontiers in Environmental Engineering

RECEIVED 02 November 2022
ACCEPTED 10 November 2022
PUBLISHED 06 December 2022

CITATION
Huang Q (2022), Grand challenges
present great opportunities in
environmental catalysis.
Front. Environ. Eng. 1:1087494.
doi: 10.3389/fenve.2022.1087494

Grand challenges present great opportunities in environmental catalysis

Qingguo Huang*

College of Agricultural and Environmental Sciences, University of Georgia, Griffin, GA, United States

KEYWORDS

environmental catalysis, environmental remediation, pollution prevention and control, cleaner production, electrocatalysis, photocatalysis, biocatalysis, low-cost catalysis

Challenges

We are living in a time full of grand challenges that stifle us from achieving Sustainable Development Goals: climate change, resource depletion, water shortage, food crisis, and pandemic diseases, just to name a few. The ever-growing productivity of our society brings wealth and quality of life, but also induces pollution and other environmental issues that have often been major causes of the grand challenges we face today (Lou et al., 2022). These impact people unequally, depending on their wealth and living environments, thus further exacerbating the disparities among populations. Addressing these challenges calls for a holistic approach integrating more efficient pollution control, cleaner production, and greener processes. Environmental catalysis, by developing catalysts having environmental significance, emerges to play a key role in meeting these challenges (Rodríguez-Padrón et al., 2019). Catalytic processes are used to transform contaminants in water, soil, and air for pollution prevention and remediation, produce green energy, reduce CO_2, recycle and reuse waste, and rapidly detect pathogens in the environment. All these can be achieved *via* catalysis, the process that increases the rate of a reaction through the action of a catalyst, with greater efficiency and selectivity at the expense of less material and energy input. Identified below are some examples that may illustrate the opportunities in environmental catalysis and the great potential it holds to help building a sustainable future for all.

Opportunities

Environmental catalysis has long been applied in pollution control by degrading pollutants in different environmental media. Fenton's reagent, developed in the 1890s, is one of the most well-known and probably the longest-used environmental catalysis methods. Hydroxyl radicals produced by H_2O_2 disproportionation with ferrous ions as the catalyst have been used as an advanced oxidation process (AOP) to degrade contaminants in water. Similarly, catalytic activation of persulfate has been devised to produce various reactive oxygen species and sulfate radicals that can be applied in AOPs to degrade a variety of contaminants in water and soil (Lee et al., 2020). Advanced reduction processes (ARPs) have also been proposed for wastewater treatment by producing highly reactive reducing radicals through activation of reducing agents by

ultraviolet (UV) light, electron beam or ultrasound (Vellanki et al., 2013), which exhibit high reactivity with certain pollutants in water.

Catalysis offers specificity and efficiency required to address various contaminants of emerging concern (CEC) that cannot be readily treated by conventional technologies. Some CECs are biologically active, even when they are present in the environment at extremely low concentrations; these include natural hormones and a variety of chemicals mimicking hormonal activities, also known as endocrine disrupting chemicals (EDCs). Efficient treatment of such bioactive micropollutants to no-harm endpoints requires specificity and efficiency that only environmental catalysis can afford. A variety of studies have developed enzyme catalysis procedures to degrade EDCs in water, soil, and biosolids, including natural and synthetic hormones, pharmaceuticals, and personal care products (Zhong et al., 2019). Enzyme catalysis is just one form of biocatalysis that, broadly speaking, also includes the use of whole cells to speed up reactions. In this regard, the microbial processes widely used in municipal wastewater treatment are environmental biocatalysis technologies. Microbes are involved in nitrification and denitrification processes to pull excessive nitrogen out of water. Bioremediation has also been widely practiced, which involves microbes to metabolize pollutants in soil and water, including chlorinated solvents, polychlorinated biphenyls (PCBs), polycyclic aromatic hydrocarbons (PAHs), pesticides, and arsenic (Arora, 2019).

Environmental catalysis has also been tapped to degrade chemicals of persistent nature that cannot be easily degraded otherwise. One prominent example is per- and polyfluoroalkyl substances (PFAS) that have heightened the public concern because of their global distribution, environmental persistence, bioaccumulation, and toxicity. PFAS, often referred to as "forever chemicals", are particularly recalcitrant because of their strong C-F bonds, and thus their degradation for treatment purpose is extraordinarily challenging. Recent studies have indicated the effectiveness of electrochemical oxidation (EO) in degrading PFAS in water. EO is essentially one form of electrocatalysis in which the anode serves as the catalyst that facilitates the transfer of one electron from PFAS to yield radicals that further react with hydroxyl radicals and other reactive species also produced on the anode (Shi et al., 2019). PFAS were also found effectively transformed during enzyme-catalyzed oxidative humification reactions (ECOHRs) (Luo et al., 2018) and UV-based ARPs (Cui et al., 2020). Microbial processes degrading PFAS have also been reported recently (Zhang et al., 2022).

Photocatalysis has long been a major topic of research in environmental catalysis. Numerous studies in the past few decades have focused on water treatment by AOPs enabled by heterogeneous photocatalysis with semiconductor catalysts, such as titanium dioxide (TiO_2) (Lou et al., 2022). The particulate catalyst absorbs photons with energy equal to or greater than its band gap, resulting in the formation of a conduction band electron and valence band hole pair. The electrons or holes thus formed are able to participate in a suite of redox reactions relevant to water treatment and disinfection, with hydroxyl radicals considered the dominant oxidant. Studies in this area have evolved to improve the semiconductor catalyst performance by modifying TiO_2 or using alternative materials for better harness of solar irradiation and higher quantum yield, although their applications appear to trail behind, partly hindered by technology transfer barriers (Loeb et al., 2019).

The use of catalysis for air pollution control has been remarkably successful in consumer market. The heterogeneous catalysts capable of simultaneously converting carbon monoxide, unburned hydrocarbons and nitrogen oxides have been used for nearly 40 years in three-way converters (TWCs) to control automobile emissions (Yentekakis and Dong, 2020). Catalytic conversion technologies have also been developed to control the emissions of other specific air pollutants and greenhouse gases, such as volatile organic compounds (VOCs), SO_x, H_2S, dioxins, and aromatic hydrocarbons from industries and waste incineration, and biogas from landfill and wastewater treatment plants. Catalytic emission control is still under active research for improved performance with reduced cost.

In the face of the grand challenges, environmental catalysis plays a key role not only in pollution control and remediation, but also in recycle and reuse of waste. Heterogeneous catalysis and biocatalysis have been used to convert plastics and other carbonaceous wastes into usable monomers, fuels, synthesis gas, and adsorbents under more sustainable conditions than thermal degradation (Mark et al., 2020). The ongoing studies are focused on the development of catalytic processes to reach higher recovery rates and valorization. More complicated waste like biosolids from wastewater treatment or animal production can also be recycled for its agronomic value in the form of land application, while avoiding the economic and environmental costs associated with disposal by landfill or incineration. Biocatalysis has been used to ameliorate the nutrient value of biosolids and alleviate the risk of contaminant release (Li et al., 2022). Microbial fuel cell involving biocatalysis and electrocatalysis produces electricity while removing nitrogen and carbon from wastewater. A recent study reported a scheme using electrocatalysis to pull nitrate from wastewater and convert it into a concentrated form of ammonium that can be used as fertilizer (Gao et al., 2022).

In addressing the grand challenges, environmental catalysis does not stop at only cleaning and reducing the mess after it has been produced, but also plays a central role in developing cleaner production and greener processes that reduce environmental footprints by utilizing renewable, cheap, and readily available raw materials while generating few to no undesired by-products. Biocatalysis usually acts under mild reaction conditions, and cascade enzymatic processes have been increasingly applied to

produce industrial products, pharmaceuticals, and biofuel from plant-based materials with reduced cost and environmentally friendly processes (Bell et al., 2021). With the discovery of sustainable electrocatalysts having enhanced activity and increased stability, electrocatalysis can now efficiently split water to generate hydrogen as green energy, as well as reduce CO_2 to produce low-carbon fuels (Liu et al., 2022). Photocatalysis is also under active research for production of H_2 or low-carbon fuels from photo-water splitting and CO_2 reduction, although the efficiency of both processes still needs improvement for application (Loeb et al., 2019).

There are many catalysis studies that have environmental ramifications other than pollution control and cleaner production. Catalysis occurring in the natural environment induces redox transformations of both organic and inorganic substances, and thus profoundly impacts their environmental fate and risks. Studies aimed at understanding such natural catalysis processes are of paramount importance for more sensible environmental risk assessment and may inspire design of more efficient catalysis processes. Catalysis has also been used in chemical and biological analyses that have environmental significance. For example, enzyme catalysis is involved in both enzyme-linked immunosorbent assay (ELISA) and polymerase chain reaction (PCR) based methods for detection of SARS-CoV-2 (Covid-19) in human and various environmental samples.

Outlook

Rapid advancements in chemistry, biochemistry, and material science are enabling more efficient and sustainable catalysis and better understanding of the catalytic mechanisms. The immense progress of advanced characterization techniques in combination with rapidly growing computation power and algorithms provide powerful tools for elucidating the mechanisms involved in catalysis. This coupled with the advance in nanotechnology and controllable synthesis enable rational design of multi-component catalysts with nanostructures manipulated towards ultra-active, selective, durable, and cost-effective heterogenous catalysis applicable to innovative photo-, electro-, and thermochemical processes particularly useful in addressing the grand challenges.

The trend in photocatalysis focuses on efficient utilization of solar irradiation with improved catalytic performance towards sunlight-driven pollutant decomposition and a solar based economy. This can be achieved by design and modification of photocatalysts at the nanoclusters and single atom level with newly available synthesis and characterization tools and improved understanding of the catalytic processes. Photocatalytic CO_2 reduction is of a particular interest, because solar energy is infinite, while atmospheric CO_2 is a major cause of climate change. Solar-driven reduction of CO_2 into chemicals and fuels offers the promise of addressing global warming and energy crisis simultaneously. Taking advantage of nano-clusters and single-atom catalysis, more efficient catalysts are also being developed to activate H_2O_2 and persulfate for environmental applications of AOPs (Wu and Kim, 2022), as well as to innovate catalysis for emission control and other applications (Li et al., 2020).

Electrooxidation is an electrocatalysis technology promising for distributed water treatment applications, because it is operable at ambient conditions, applicable to a wide variety of pollutants, and easy to manipulate and automate. The application of electrooxidation in water treatment is however limited by the availability of suitable anode materials that have to meet a few stringent requirements in stability, conductivity and electrocatalytic activity. In particular, a high overpotential for oxygen evolution is desired, so that less energy is spent on water oxidation, contrary to the application of electrocatalysis for water splitting where lower oxygen evolution potential is optimal. Research efforts continue to innovate electrodes and system integration for various electrocatalysis applications (Liu et al., 2022), including contaminant decomposition, waste recycling, solar and wind energy harness, and electrosynthesis.

Biocatalysis research is also rapidly advancing, fueled by progress in protein engineering, genomic database mining and computational methods. Advances in enzyme discovery, *de novo* design, and directed evolution expand the range of accessible biochemical reactions catalyzed by enzymes having high efficiency and selectivity (Bell et al., 2021). Multistep enzyme cascades can now be designed to achieve goals previously unattainable, including the production of chemicals and biofuel from plant-based materials and the decomposition of persistent organic pollutants more efficiently without forming harmful byproducts. There is also a trend of utilizing enzyme-mimicking nanomaterials to overcome the limitations of applying natural enzymes in industrial and environmental applications. In particular, peptides have recently been used in construction of simple biomolecular nanozymes, also known as bionanozymes, for biocatalysis applications (Makam et al., 2022). The peptide sequences are simpler than their natural counterparts but retain sufficient complexity for folding and function. This enables fine tuning the catalytic center and mechanism, and thus paves a way for designing and fabricating highly selective and efficient bionanozymes for specific applications, for example, degradation of micropollutants at very low concentrations.

The advance in catalyst design and synthesis provides more means to develop highly efficient, yet low-cost catalysis applicable to pollution control and remediation. This is particularly meaningful, because low-cost catalysis makes technologies like water disinfection and soil remediation more universally available. Under-developed regions often suffer more from environmental pollution problems, causing environmental

health disparities. Low-cost catalysis technologies can help to address this fundamental disparity, a major factor contributing to social inequalities. Nanozymes, metal-organic frameworks, and doped carbon materials are examples of potential low-cost catalysts. Progresses in these areas will bring more environmental applications of low-cost catalysis.

Environmental catalysis is a multidisciplinary research subject that is rapidly advancing. Taking advantage of the ongoing science and technology advancements in related fields, researchers from various disciplines are developing more efficient and sustainable catalysis applicable to pollution control, cleaner production, and greener processes. These will collectively contribute to a holistic approach to addressing the grand challenges that we are facing today in order to attain a sustainable future for all. This report only identifies a few examples illustrating the opportunities and potential of environmental catalysis, whose scope is still evolving and may only be defined by the many researchers devoting to its study. The critical role of environmental catalysis in the realm of sustainable development represents a remarkable privilege, as well as a significant responsibility, vested in those conducting research in this vibrant, developing field.

Author contributions

All authors listed have made a substantial, direct, and intellectual contribution to the work and approved it for publication.

Conflict of interest

The author declares that the research was conducted in the absence of any commercial or financial relationships that could be construed as a potential conflict of interest.

Publisher's note

References

Arora, P.K. (Editor) (2019). *Microbial metabolism of Xenobiotic compounds* (Singapore: Springer). doi:10.1007/978-981-13-7462-3

Bell, E. L., Finnigan, W., France, S. P., Green, A. P., Hayes, M. A., Hepworth, L. J., et al. (2021). Biocatalysis. *Nat. Rev. Methods Prim.* 1 (1), 46. doi:10.1038/s43586-021-00044-z

Cui, J., Gao, P., and Deng, Y. (2020). Destruction of per- and polyfluoroalkyl substances (PFAS) with advanced reduction processes (ARPs): A critical review. *Environ. Sci. Technol.* 54 (7), 3752–3766. doi:10.1021/acs.est.9b05565

Gao, J., Shi, N., Li, Y., Jiang, B., Marhaba, T., and Zhang, W. (2022). Electrocatalytic Upcycling of nitrate wastewater into an Ammonia fertilizer via an Electrified membrane. *Environ. Sci. Technol.* 56 (16), 11602–11613. doi:10.1021/acs.est.1c08442

Lee, J., von Gunten, U., and Kim, J.-H. (2020). Persulfate-based advanced oxidation: Critical assessment of opportunities and Roadblocks. *Environ. Sci. Technol.* 54 (6), 3064–3081. doi:10.1021/acs.est.9b07082

Li, S., Sun, K., Latif, A., Si, Y., Gao, Y., and Huang, Q. (2022). Insights into the applications of Extracellular laccase-Aided humification in Livestock manure Composting. *Environ. Sci. Technol.* 56 (12), 7412–7425. doi:10.1021/acs.est.1c08042

Li, Z., Ji, S., Liu, Y., Cao, X., Tian, S., Chen, Y., et al. (2020). Well-defined materials for heterogeneous catalysis: From Nanoparticles to Isolated single-atom Sites. *Chem. Rev.* 120 (2), 623–682. doi:10.1021/acs.chemrev.9b00311

Liu, K., Cao, P., Chen, W., Ezeh, C. I., Chen, Z., Luo, Y., et al. (2022). Electrocatalysis enabled transformation of earth-abundant water, nitrogen and carbon dioxide for a sustainable future. *Mater. Adv.* 3 (3), 1359–1400. doi:10.1039/D1MA00814E

Loeb, S. K., Alvarez, P. J. J., Brame, J. A., Cates, E. L., Choi, W., Crittenden, J., et al. (2019). The technology Horizon for Photocatalytic water treatment: Sunrise or Sunset? *Environ. Sci. Technol.* 53 (6), 2937–2947. doi:10.1021/acs.est.8b05041

Lou, S. N., Lim, J., Jeon, T. H., and Choi, W. (2022). Designing Eco-functional redox conversions integrated in environmental photo(electro)catalysis. *ACS ES&T Eng.* 2 (6), 1116–1129. doi:10.1021/acsestengg.2c00009

Luo, Q., Yan, X., Lu, J., and Huang, Q. (2018). Perfluorooctanesulfonate degrades in a laccase-mediator system. *Environ. Sci. Technol.* 52 (18), 10617–10626. doi:10.1021/acs.est.8b00839

Makam, P., Yamijala, S. S. R. K. C., Bhadram, V. S., Shimon, L. J. W., Wong, B. M., and Gazit, E. (2022). Single amino acid bionanozyme for environmental remediation. *Nat. Commun.* 13 (1), 1505. doi:10.1038/s41467-022-28942-0

Mark, L. O., Cendejas, M. C., and Hermans, I. (2020). The Use of heterogeneous catalysis in the chemical Valorization of plastic waste. *ChemSusChem* 13 (22), 5808–5836. doi:10.1002/cssc.202001905

Rodríguez-Padrón, D., Puente-Santiago, A. R., Balu, A. M., Muñoz-Batista, M. J., and Luque, R. (2019). Environmental catalysis: Present and future. *ChemCatChem* 11 (1), 18–38. doi:10.1002/cctc.201801248

Shi, H., Wang, Y., Li, C., Pierce, R., Gao, S., and Huang, Q. (2019). Degradation of perfluorooctanesulfonate by reactive electrochemical membrane composed of magneli phase titanium suboxide. *Environ. Sci. Technol.* 53 (24), 14528–14537. doi:10.1021/acs.est.9b04148

Vellanki, B. P., Batchelor, B., and Abdel-Wahab, A. (2013). Advanced reduction processes: A New Class of treatment processes. *Environ. Eng. Sci.* 30, 264–271. doi:10.1089/ees.2012.0273

Wu, X., and Kim, J.-H. (2022). Outlook on single atom catalysts for persulfate-based advanced oxidation. *ACS ES&T Eng.* 2 (10), 1776–1796. doi:10.1021/acsestengg.2c00187

Yentekakis, I. V., and Dong, F. (2020). Grand challenges for catalytic remediation in environmental and energy applications toward a cleaner and sustainable future. *Front. Environ. Chem.* 1. doi:10.3389/fenvc.2020.00005

Zhang, Z., Sarkar, D., Biswas, J. K., and Datta, R. (2022). Biodegradation of per- and polyfluoroalkyl substances (PFAS): A review. *Bioresour. Technol.* 344, 126223. doi:10.1016/j.biortech.2021.126223

Zhong, C., Zhao, H., Cao, H., and Huang, Q. (2019). Polymerization of micropollutants in natural aquatic environments: A review. *Sci. Total Environ.* 693, 133751. doi:10.1016/j.scitotenv.2019.133751

frontiers | Frontiers in Environmental Engineering

TYPE Specialty Grand Challenge
PUBLISHED 07 February 2023
DOI 10.3389/fenve.2023.1149950

OPEN ACCESS

EDITED AND REVIEWED BY
Bing-Jie Ni,
University of Technology Sydney, Australia

*CORRESPONDENCE
Christian Kennes,
Kennes@udc.es

SPECIALTY SECTION
This article was submitted to Water, Waste, and Wastewater Engineering, a section of the journal Frontiers in Environmental Engineering

RECEIVED 23 January 2023
ACCEPTED 27 January 2023
PUBLISHED 07 February 2023

CITATION
Kennes C (2023), The grand challenge of water, waste, wastewater and emissions engineering and valorization. *Front. Environ. Eng.* 2:1149950. doi: 10.3389/fenve.2023.1149950

The grand challenge of water, waste, wastewater and emissions engineering and valorization

Christian Kennes*

Chemical Engineering Laboratory, Faculty of Sciences and Center for Advanced Scientific Research—Centro de Investigaciones Científicas Avanzadas (CICA), BIOENGIN group, University of La Coruña, A Coruña, Spain

KEYWORDS

biofuels, bioprocess, bioproducts, carbon dioxide, circular economy, greenhouse gases, methane, thermochemical process

Introduction

Water, soil, and air represent the three main environmental ecosystems and natural resources of our planet. They have faced increased environmental concern, mainly over the last century and since the era of industrialization and heavy industrial development, which resulted in significant pollution issues never faced before. On the other hand, wastewater, solid waste, and air/gas emissions are seen as the most important sources of pollution on earth, besides noise, light, and thermal pollution which have more recently been identified to be of environmental concern and affect human health and welfare as well. The current situation of water, waste, wastewater related issues, as well as gas emissions from those sources are briefly addressed hereafter as well as their treatment and valorization alternatives.

Current situation

Water, wastewater

As much as somewhat more than two-third of our planet is covered by water, while only 3% of the earth's water is fresh and hardly about 0.5% is easily accessible for use (e.g., lakes, rivers, and aquifers); the remaining fraction being unavailable for direct use (e.g., glaciers, polluted water). The largest fresh water application is presently for irrigation and agriculture, though many countries suffer from water scarcity. A recent study revealed that by 2050, as much as 87 out of 180 countries will have annual renewable water resources (ARWR) *per capita* below 1700 m^3/year, i.e., they will face water scarcity concerns; while the number of countries with ARWR *per capita* below 500 m^3/year, this is absolute water scarcity, is expected to increase from 25 in 2015 to 45 by 2050 (Baggio et al., 2021).

On the other side, globally, 380 billion m^3 of municipal wastewater are generated yearly and this value is expected to increase further, by about 51% by 2050 (Qadir et al., 2020). A large amount of those wastewaters is still released, untreated, into the environment. Information reported only a few years ago suggested that high-income countries treat about 70% of their wastewaters, while this drops to 38% in upper-middle-income countries, 28% in lower-middle-income countries, and hardly 8% in low-income countries (Sato et al., 2013).

Waste

Besides (waste) water, solid waste is another source of pollutants, mainly generated in the form of municipal waste, industrial waste, and it may also come from agriculture and food,

among others. It is mainly composed of organic compounds as well as non-organic ones such as plastics, glass, metals, or paper. Waste treatment, e.g., in landfills, may additionally result in groundwater contamination from landfill leachates. According to Eurostat data (https://ec.europa.eu/eurostat/, accessed 09-01-2023), 4.8 tonnes of waste were generated per EU citizen in 2020, of which 59.1% was treated in recovery operations, i.e., recycling, backfilling or energy recovery; the remaining fraction being mainly landfilled, or, otherwise, to a lower extent, incinerated without energy recovery or disposed of. The amounts generated per EU member states are highly variable, and range from less than 1.5 tonnes per inhabitant in Portugal to, as much as, 21 tonnes per inhabitant in Finland. In terms of sources and polluting sectors, the industrial sector generates the highest amounts of waste, mainly through activities such as construction and manufacturing. On the other side, municipal waste accounts for about 10% of total wastes produced, which means that around 530 kg waste *per capita* were generated in the EU in 2021. In terms of treatment alternatives, those wastes are mainly landfilled, incinerated, recycled or composted, but, following EU regulations, the main goal of most countries, regarding wastes, is to minimize their accumulation and, as far as possible, maximize recycling, reuse, and valorization.

Air emissions

Next to water pollutants and solid waste, air pollution is one of the most significant health and environmental problems. Air pollution is also related to water pollution and solid waste, as the latter and their treatment plants do often generate emissions of volatile pollutants. These may be greenhouse gases (GHG), such as methane (CH_4), or carbon dioxide (CO_2), but also nitorgen oxides (NO_x), as well as other toxic inorganic and organic volatile compounds (Kennes and Veiga, 2013). According to the World Health Organization (WHO), it is estimated that air pollution kills around seven million people worldwide every year, and almost the entire global population breathes air that exceeds WHO air quality limits (https://www.who.int/news/accessed 09-01-2023). As briefly illustrated hereafter, diverse pollutants are emitted from wastewaters, solid wastes and their treatments plants.

Wastewater treatment processes emit some GHG, i.e., CO_2, CH_4, N_2O, during their biological treatment, while indirect emissions result from off-site power generation mainly and contribute to significant amounts of CO_2. Ammonia can also be released from wastewaters containing nitrogen, though these emissions can be reduced by replacing conventional nitrification-denitrification processes by Anammox processes. N_2O emissions can result from nitrification-denitrification of nitrogen compounds as well. Besides, methane is mainly released during the anaerobic decomposition of organic matter, in the secondary anaerobic treatment process, in the sewer system or in the sludge line. This may also lead to emissions of odorous compounds such as hydrogen sulphide (H_2S). Next to GHG, some volatile organic compounds (VOC) have also been detected at wastewater treatment plants and often result from stripping and volatilization phenomena, e.g., in aerobic activated sludge aeration tanks (Hamoda, 2006). They me be aliphatic or aromatic and their nature and concentrations depend largely on the origin and composition of the wastewater.

In case of solid waste, gas emissions depend on the treatment process applied. In the European Union (27 countries, EU-27), according to 2020-statistics, the energy sector and the combustion of fuels are, by far, still the most significant contributors to greenhouse gas emissions (75%), followed by agriculture (11.5%) and industrial processes and product use (9.5%), and then waste (3.5%) (https://stats.oecd.org/accessed 09-01-2023). Contrary to other types of plants and processes, municipal solid waste landfills are among the major sources of the greenhouse gas methane. Although waste decomposition in landfills is initially aerobic, after several month, conditions become anaerobic and anaerobic methanogens start producing methane and carbon dioxide.

A recent report indicated that landfilling emits nearly 400 kg CO_{2e} per tonne of organic waste, while composting raw organics results in the lowest GHG emissions, at −41 kg CO_{2e} per tonne of waste, and upgrading biogas to renewable natural gas after dry anaerobic digestion results in −36 to −2 kg CO_{2e} per tonne (Nordahl et al., 2020). According to estimates of the European Environmental Agency, greenhouse gas emissions from waste, in the EU-27, have decreased by about 32% between 2000 and 2020 (https://stats.oecd.org/ accessed 09-01-2023). This is due among others to higher levels of waste recycling and composting, concomittant with less waste being disposed in landfills. Odours, ammonia, sulphur oxides (SO_x), as well as some volatile organic compounds (VOC) have also been detected at landiflls and waste treatment sites (Fang et al., 2012). In case of waste landfill sites, a recent study undertaken in China reported the presence of mixtures of VOC at concentrations ranging from 18.1 to 806.3 mg/m^3, while odorous gases and greenhouse gases ranged from 0.4 to 21.2 and 0 to 100.5 mg/m^3, respectively (Wang et al., 2021).

Current treatment and valorization trends

Water, wastewater, and waste tretament technologies have been developed, optimized and applied for many decades, as well as techniques for the treatment of air and gas emissions from such sources, using either biological or non-biological processes, which have been described in scientific literature (Kennes et al., 2009; Metcalf and Eddy et al., 2013; Pichtel, 2013). However, recent trends and approaches are more focussed on the valorization of pollutants, their reuse, and resource recovery from polluting sources. The latter are then considered as valuable resources rather than pollutants to be eliminated and they may even generate benefit instead of resulting in mere treatment and elimination costs. Although a comprehensive overview of all possible and numerous valorization alternatives for (waste) water, waste and their gas emissions is beyond the scope of this brief overview, some basic aspects will be explained herefater.

Water, wastewater

Different methods and different valuable products can be produced or recovered from wastewaters (Puyol et al., 2017). In terms of resource recovery, it is estimated that, on an average, wastewaters contain 16.6 million metric tonnes (Tg) of nitrogen embedded in wastewater produced worldwide annually, while phosphorus stands at 3.0 Tg and potassium at 6.3 Tg. These can be recovered, while simultaneously reducing eutrophication problems

(Qadir et al., 2020). This solves also the problem of possible, near future, progressive shortage of phosphorus, largely obtained from non-renewable mineral resources. Besides, it is considered that energy embedded in municipal wastewater corresponds to the same amount of electricity used in 158 million homes. Energy that can be recovered from municipal wastewater is basically thermal energy (about 80% of energy recovered) and, to a lower extent, chemical energy (20%), and finally, a smaller amount of hydraulic energy. Additionally, the organic compounds present in wastewater can also be converted into methane-rich biogas and although methane is a GHG, if it is recovered, it can be used as a valuable energy source. Wastewater pollutants, mainly the organic fraction, can even be (bio) converted to other biofuels or energy carriers, such as biodiesel or hydrogen (Puyol et al., 2017). It is worth further highlighting that, besides energy sources, wastewater pollutants can be (bio) converted to bioproducts, which can be simple compounds such as short chain and medium chain carboxylic acids (e.g., acetate, propionate, butyrate, valerate, caproate) (Mato et al., 2010), but also higher value commercial compounds such as biopolymers (i.e., bioplastics) (Ben et al., 2016) or single cell proteins (Shoener et al., 2014), to mention only few examples. Finally (waste) water is also an important resource in itself as it can be treated and reused either as potable (i.e., drinking water) or non-potable (e.g., for irrigation, industrial use) water.

Waste

Waste is another potential valuable resource. Part of the non-organic fraction of waste can be recycled, while the organic fraction can decompose and release gases such as methane and carbon dioxide, which can be emitted as GHG involved in climate change. However, in a similar way as with wastewater, that organic fraction can also be valorized and recovered in the form of biogas (methane), used as a biofuel (Eiroa et al., 2012). Composting and vermicomposting are other viable options to valorize organic waste. In vermicomposting, microorganisms and worms convert organic waste into nutrient-rich humus and fertilizers with applications in agriculture (Mupambwa and Mnkeni, 2018). Still more recently, black soldier flies have been shown to grow on organic waste and use their nutrients. They are a potential source of proteins, organic fertlizers and can also generate other bioproducts (Xiao et al., 2018). Again, similarly as for wastewaters, organic waste can be bioconverted to short chain volatile fatty acids (e.g., acetate) or medium chain carboxylic acids (e.g., caproate) (Bermúdez-Penabad et al., 2017). Actually, some of the metabolites obtained from either wastewater or solid waste, such as those fatty acids, can then still further be (bio) converted, in a second stage, into other more or highly valuable end products, e.g., microbial oils or other metabolites accumulated by yeasts (Robles-Iglesias et al., 2023). Studies have also been performed on the direct production of other biofuels, e.g., waste bioconversion to bioethanol (Bibra et al., 2023) or thermochemical waste conversion processes for energy recovery (Kassim et al., 2022). Numerous other non-energy-related bioproducts have been obtained from organic waste as well, e.g., antioxidants (Kaur et al., 2019), lactic acid (Wang et al., 2016), citric acid (Yu et al., 2017), to mention only few.

Air emissions

The valorization of gas emissions from wastewaters and wastes as well as their treatment plants has hardly been studied and research in this field is still rather recent. The most studied gases are methane and carbon dioxide, released, for example, from anaerobic digestion in the water and waste sectors, while aerobic wastewater treatment has also been identified as a main source of CO_2 (Bajón-Fernández et al., 2017). Quite more research has been performed on the valorization of gas emissions, e.g., CO, CO_2, in other industrial sectors such as steel industry emissions, allowing to produce numerous compounds from such gases, such as fatty acids (Ragsdale and Pierce, 2008), bioalcohols (ethanol, butanol, hexanol) (Fernández-Naveira et al., 2017), or numerous other bioproducts (Köpke and Simpson, 2020), which demonstrates the potential of gas valorization in the industrial sector but also many other ones, such as the (waste) water and waste sectors. Besides carbon dioxide, different (thermo) chemical (Ahmad et al., 2022), and biological (Jawaharraj et al., 2020) conversion processes are also available for CH_4 valorization.

There is thus room for much interesting additional research on water, wastewater, and waste engineering and on the valorization of those sources as well as their emissions. Many interesting research data and scientific information are expected to appear in the literature, in the short term, in this fascinating field based on environmentally-friendly and sustainable circular bioeconomy approaches.

Author contributions

The author confirms being the sole contributor of this work and has approved it for publication.

Conflict of interest

The authors declare that the research was conducted in the absence of any commercial or financial relationships that could be construed as a potential conflict of interest.

Publisher's note

References

Ahmad, K., Polychronopoulou, K., and Abi Jaoude, M. (2022). CH_4 valorisation reactions: A comparative thermodynamic analysis and their limitations. *Fuel* 320, 123877. doi:10.1016/j.fuel.2022.123877

Baggio, G., Qadir, M., and Smakhtin, V. (2021). Freshwater availability status across countries for human and ecosystem needs. *Sci. Total Environ.* 792, 148230. doi:10.1016/j.scitotenv.2021.148230

Bajón-Fernández, Y., Soares, A., Koch, K., Vale, P., and Cartmell, E. (2017). Bioconversion of carbon dioxide in anaerobic digesters for on-site carbon capture and biogas enhancement – a review. *Crit. Rev. Environ. Sci. Technol.* 47, 1555–1580. doi:10.1080/10643389.2017.1372001

Ben, M., Kennes, C., and Veiga, M. C. (2016). Optimization of polyhydroxyalkanoate storage using mixed cultures and brewery wastewater. *J. Chem. Technol. Biotechnol.* 91, 2817–2826. doi:10.1002/jctb.4891

Bermúdez-Penabad, N., Kennes, C., and Veiga, M. C. (2017). Anaerobic digestion of tuna waste for the production of volatile fatty acids. *Waste Manag.* 68, 96–102. doi:10.1016/j.wasman.2017.06.010

Bibra, M., Samanta, D., Sharma, N. K., Singh, G., Johnson, G. R., and Sani, R. K. (2022). Food waste to bioethanol: Opportunities and challenges. *Fermentation* 9, 8. doi:10.3390/fermentation9010008

Eiroa, M., Costa, J. C., Alves, M. M., Kennes, C., and Veiga, M. C. (2012). Evaluation of the biomethane potential of solid fish waste. *Waste Manag.* 32, 1347–1352. doi:10.1016/j.wasman.2012.03.020

Fang, J. J., Yang, N., Cen, D. Y., Shao, L. M., and He, P. J. (2012). Odor compounds from different sources of landfill: Characterization and source identification. *Waste Manag.* 32, 1401–1410. doi:10.1016/j.wasman.2012.02.013

Fernández-Naveira, Á., Veiga, M. C., and Kennes, C. (2017). H-B-E (hexanol-butanol-ethanol) fermentation for the production of higher alcohols from syngas/waste gas. *J. Chem. Technol. Biotechnol.* 92, 712–731. doi:10.1002/jctb.5194

Hamoda, M. F. (2006). Air pollutants emissions from waste treatment and disposal facilities. *J. Environ. Sci. Health, Part A* 41, 77–85. doi:10.1080/10934520500298895

Jawaharraj, K., Shrestha, N., Chilkoor, G., Dhiman, S. S., Islam, J., and Gadhamshetty, V. (2020). Valorization of methane from environmental engineering applications: A critical review. *Water Res.* 187, 116400. doi:10.1016/j.watres.2020.116400

Kassim, F. O., Thomas, C. L. P., and Afolabi, O. O. D. (2022). Integrated conversion technologies for sustainable agri-food waste valorization: A critical review. *Biomass Bioenergy* 156, 106314. doi:10.1016/j.biombioe.2021.106314

Kaur, P., Ghoshal, G., and Jain, A. (2019). Bio-utilization of fruits and vegetables waste to produce β-carotene in solid-state fermentation: Characterization and antioxidant activity. *Process Biochem.* 76, 155–164. doi:10.1016/j.procbio.2018.10.007

Kennes, C., Rene, E. R., and Veiga, M. C. (2009). Bioprocesses for air pollution control. *J. Chem. Technol. Biotechnol.* 84, 1419–1436. doi:10.1002/jctb.2216

Kennes, C., and Veiga, M. C. (2013). *Air pollution prevention and control: Bioreactors and bioenergy*. Chichester, UK: J. Wiley & Sons, 549. ISBN 978-1-119-94331-0.

Köpke, M., and Simpson, S. D. (2020). Pollution to products: Recycling of 'above ground' carbon by gas fermentation. *Curr. Opin. Biotechnol.* 65, 180–189. doi:10.1016/j.copbio.2020.02.017

Mato, T., Ben, M., Kennes, C., and Veiga, M. C. (2010). Valuable product production from wood mill effluents. *Water Sci. Technol.* 62, 2294–2300. doi:10.2166/wst.2010.949

Metcalf and Eddy,Tchobanoglous, G., Stensel, H., Tsuchihashi, R., and Burton, F. (2013). *Wastewater engineering: Treatment and reuse*. New York, USA: McGraw-Hill, 2048. ISBN: 978-0073401188.

Mupambwa, H. A., and Mnkeni, P. N. S. (2018). Optimizing the vermicomposting of organic wastes amended with inorganic materials for production of nutrient-rich organic fertilizers: A review. *Environ. Sci. Pollut. Res.* 25, 10577–10595. doi:10.1007/s11356-018-1328-4

Nordahl, S. L., Devkota, J. P., Amirebrahimi, J., Smith, S. J., Breunig, H. M., Preble, C. V., et al. (2020). Life-cycle greenhouse gas emissions and human health trade-offs of organic waste management strategies. *Environ. Sci. Technol.* 54, 9200–9209. doi:10.1021/acs.est.0c00364

Pichtel, J. (2013). *Waste management practices: Municipal, hazardous, and industrial*. Boca Raton, USA: CRC Press, 682. ISBN: 9781466585188.

Puyol, D., Batstone, D. J., Hülsen, T., Astals, S., Peces, M., and Krömer, J. O. (2016). Resource recovery from wastewater by biological technologies: Opportunities, challenges, and prospects. *Front. Microbiol.* 7, 2106. doi:10.3389/fmicb.2016.02106

Qadir, M., Drechsel, P., Jiménez Cisneros, B., Kim, Y., Pramanik, A., Mehta, P., et al. (2020). Global and regional potential of wastewater as a water, nutrient and energy source. *Nat. Resour. Forum* 44, 40–51. doi:10.1111/1477-8947.12187

Ragsdale, S. W., and Pierce, E. (2008). Acetogenesis and the wood–ljungdahl pathway of CO_2 fixation. *Biochimica Biophysica Acta (BBA) - Proteins Proteomics* 1784, 1873–1898. doi:10.1016/j.bbapap.2008.08.012

Robles-Iglesias, R., Naveira-Pazos, C., Fernández-Blanco, C., Veiga, M. C., and Kennes, C. (2023). Factors affecting the optimisation and scale-up of lipid accumulation in oleaginous yeasts for sustainable biofuels production. *Renew. Sustain. Energy Rev.* 171, 113043. doi:10.1016/j.rser.2022.113043

Sato, T., Qadir, M., Yamamoto, S., Endo, T., and Zahoor, A. (2013). Global, regional, and country level need for data on wastewater generation, treatment, and use. *Agric. Water Manag.* 130, 1–13. doi:10.1016/j.agwat.2013.08.007

Shoener, B. D., Bradley, I. M., Cusick, R. D., and Guest, J. S. (2014). Energy positive domestic wastewater treatment: The roles of anaerobic and phototrophic technologies. *Environ. Sci. Process. Impacts* 16, 1204–1222. doi:10.1039/c3em00711a

Wang, J., Chang, Q., Yu, M., Niu, R., Wu, C., and Wang, Q. (2016). SSF production of L-lactic acid from food waste and sophoraflavescens residues. *Procedia Environ. Sci.* 31, 122–126. doi:10.1016/j.proenv.2016.02.017

Wang, Y., Li, L., Qiu, Z., Yang, K., Han, Y., Chai, F., et al. (2021). Trace volatile compounds in the air of domestic waste landfill site: Identification, olfactory effect and cancer risk. *Chemosphere* 272, 129582. doi:10.1016/j.chemosphere.2021.129582

Xiao, X., Mazza, L., Yu, Y., Cai, M., Zheng, L., Tomberlin, J. K., et al. (2018). Efficient co-conversion process of chicken manure into protein feed and organic fertilizer by *Hermetia illucens* L. (Diptera: *Stratiomyidae*) larvae and functional bacteria. *J. Environ. Manag.* 217, 668–676. doi:10.1016/j.jenvman.2018.03.122

Yu, D., Shi, Y., Wang, Q., Zhang, X., and Zhao, Y. (2017). Application of methanol and sweet potato vine hydrolysate as enhancers of citric acid production by *Aspergillus niger*. *Bioresour. Bioprocess.* 4, 35. doi:10.1186/s40643-017-0166-4

frontiers | Frontiers in Environmental Engineering

TYPE Original Research
PUBLISHED 24 March 2023
DOI 10.3389/fenve.2023.1167552

OPEN ACCESS

EDITED BY
Shujuan Zhang,
Nanjing University, China

REVIEWED BY
Seyma Ozkara-Aydinoglu,
Beykent University, Türkiye
Vesna Krstic,
Mining and Metallurgy Institute Bor, Serbia

*CORRESPONDENCE
Kui Qiu,
zhih98liu@163.com

SPECIALTY SECTION
This article was submitted to Environmental Catalysis, a section of the journal Frontiers in Environmental Engineering

RECEIVED 16 February 2023
ACCEPTED 13 March 2023
PUBLISHED 24 March 2023

CITATION
Liu Z, Chen Z, Chen Q, Liu L, Wang Y, Shu P, Zhong Y, Sun Z and Qiu K (2023), Heterogeneous catalytic oxidation regeneration of desulfurization-rich liquor with Fe^{3+} modified chitosan. *Front. Environ. Eng.* 2:1167552. doi: 10.3389/fenve.2023.1167552

Heterogeneous catalytic oxidation regeneration of desulfurization-rich liquor with Fe^{3+} modified chitosan

Zhihao Liu[1], Zhijie Chen[2], Qian Chen[2], Luwei Liu[1], Yingjie Wang[1], Peng Shu[1], Yu Zhong[1], Zeqin Sun[1] and Kui Qiu[1]*

[1]School of Chemistry and Chemical Engineering, Chongqing University of Science and Technology, Chongqing, China, [2]Centre for Technology in Water and Wastewater, School of Civil and Environmental Engineering, University of Technology Sydney, Ultimo, NSW, Australia

To solve the problem of pipeline blockage caused by sulfur deposition in industrial gas wet oxidative desulfurization operations, this study developed an iron-modified chitosan catalyst for the catalytic oxidation regeneration of conventional wet oxidative desulfurization-rich liquids. Detailed characterization results show that Fe^{3+} species are successfully coordinated with the chitosan substrate. The results of desulfurization and regeneration experiments showed that the Fe^{3+}-modified chitosan could effectively regenerate the desulfurization waste stream and remain stable in the acidic desulfurization stream. The powdered iron-based modified chitosan catalyst prepared with a mass ratio of chitosan to $FeCl_3$ of 1:5 and glutaraldehyde of 12.5% by mass has better catalytic performance than the microbead counterpart. The regeneration performance of the catalyst was evaluated by the desulfurization performance of the regenerated desulfurization solution. The iron-based modified chitosan shows a good regeneration performance, and the loss of Fe content is less than 1.5% after five runs. This study provides an efficient way to develop cost-effective catalysts for the regeneration of wet oxidative desulfurization-rich liquids.

KEYWORDS

catalytic oxidation, desulfurization, chitosan, regeneration, Fe^{3+}

1 Introduction

As a toxic and harmful gas, hydrogen sulfide (H_2S) in industrial gas (natural gas, biogas, etc.) poses serious environmental and human hazards in addition to severe corrosion of metal pipelines and production equipment (Liu et al., 2023a). Various desulfurization processes have been developed according to the complex desulfurization scenarios. For small- and medium-scale gas desulfurization, solid adsorption and wet oxidation desulfurization are the widely used. The former is generally applicable to low-sulfur gas purification and the latter one suffers from low sulfur capacity, easy solvent degradation, affluent generation, and poor sulfur quality (Qiu et al., 2022). In addition, the most widely used organic iron-based wet desulfurization solution can easily lead to H_2S oxidation and thereby lead to sulfur blockage in the reactor and pipeline accumulation (Liu et al., 2022). Currently, this phenomenon is widespread in high-pressure and high-sulfur-content scenarios. Therefore, for small to medium-scale industrial gas desulfurization, there are a

few cases where wet oxidation desulfurization is directly utilized at high H_2S concentrations and high pressures (Vogt and Weckhuysen, 2022). The use of multiple process combinations for desulfurization and sulfur recovery complicatesthe process for the many scattered sulfur-bearing single wells around the world.

To address this problem, we propose a stepwise desulfurization-regeneration scheme. More specifically, it is assumed that the desulfurization solution absorbs the H_2S in a non-redox form, and after the rich solution enters the regeneration tower, modified solid catalyst particles containing Fe^{3+} are added, and the air is introduced to oxidize the HS^- in the rich solution of desulfurization to S monomers. This form of non-homogeneous catalytic oxidation can avoid the generation of sulfur particles in the absorption stage and solve the sulfur plugging problem in the wet oxidation desulfurization operation. Its application to small-scale high-pressure industrial gas desulfurization can greatly simplify the well site desulfurization process and effectively achieve green, efficient, and economic sulfur-bearing wellhead gas capacity release (Gu et al., 2008). The antimony-based organic non-aqueous phase desulfurization system developed in our previous work (Liu et al., 2022) is effective in removing H_2S from gas streams through ligand absorption.

Chitosan (CS), known as chitosan-amine or deacetylated chitosan, is a product of the deacetylation of chitinand is the only basic polysaccharide among natural polysaccharides (Dash et al., 2011). Chitosan has a large number of reactive groups such as -OH and -NH_2 in its molecule. The flat-voltage bond structure in the chitosan molecule enables it to interact with a variety of metal ions in coordination, which can provide nucleation sites for the formation of catalysts, with high adsorption efficiency and excellent chelating properties. Microspheres with a high specific surface area are more suitable for efficient adsorbents compared to conventional fibers, membranes, and resins (He et al., 2016). Therefore, chitosan is considered a functional biomaterial with potential applications. In addition, chitosan has the general properties of polymeric compounds in solution, being insoluble in water, alkalis, and organic solvents in general, and chemically stable (Lei et al., 2022).

In view of this, we developed a Fe^{3+}-modified chitosan catalyst for the non-homogeneous catalytic oxidation regeneration of desulfurization solution. XRD and FTIR techniques were used to characterize the structure of the catalyst samples, and the microscopic morphology of the samples was observed by SEM. The regeneration performance of the catalyst for the desulfurization of the desulfurization solution and the change of ORP (oxidation-reduction potential) value of the solution after regeneration were investigated. This work aims to provide a new solution for more desulfurization scenarios (natural gas, biogas, etc.).

2 Experimental

2.1 Materials and reagents

Anhydrous ethanol, ferric chloride, glacial acetic acid, 50% glutaraldehyde, sodium hydroxide (analytically pure), all purchased from Chengdu Jinshan Chemical Reagent Co. Chitosan (CS, deacetylation degree ≥95%) was obtained from Jiangsu Golden Shell Pharmaceutical). Antimony-based desulfurization agent was self-prepared.

H_2S standard gas, 5% H_2S/95% N_2 (Chongqing Lituo Gas Co.), O_2 standard gas, 99.9% O_2 (Chongqing Yongfa Gas Co.).

2.2 Apparatus and instruments

The variations of the functional groups on the fiber surface were observed using a Fourier transform infrared spectrometer (FT-IR, KBr, 4000–500 cm1, BRUKE TENS OR27, Germany). The solution OPR value was determined using a PHS-3E pH meter from Shanghai Yidian Scientific Instrument Co. (China) The crystal structure of the sample was analyzed using a SmartLab-9 type X-ray diffraction (XRD) analyzer (RIKEN, Japan). The surface morphology of the samples was observed using an FSEM-type scanning electron microscope analyzer (FEI, USA), and the elemental content of the sample surface was determined. Determination of Fe element in catalysts by inductively coupled plasma emission spectrometer/mass spectrometer (ICP-OES).

2.3 Preparation of Fe^{3+} modified chitosan

Firstly, all samples were soaked in NMP (N-Methyl-pyrrolidone) solvent for 24 h before the experiments, and it was proved that all samples were insoluble in the desulfurization solution. Taking an appropriate amount of chitosan (CS) and add it to 2% acetic acid solution, stirring until the chitosan was completely dissolved. Then, adding a certain mass of $FeCl_3$ was to the above mixture, stirring well and then left the load for 2 h; then, loading the resting mixed solution into a syringe and slowly dropped it into 2 mol/L sodium hydroxide solution to form iron-based modified chitosan gel microspheres. After that, washing the chitosan gel microspheres with distilled water several times to neutralize them. Then, all of them were placed into a certain concentration of glutaraldehyde solution for cross-linking reaction, and the microspheres were stirred continuously to make full contact with glutaraldehyde for 24 h at room temperature; finally, the cross-linked chitosan microspheres were washed several times with distilled water to neutral, and then dried at 60°C for 24 h. The iron-based modified chitosan microspheres (Fe-CS) were successfully produced.

2.4 Preparation of modified chitosan catalyst

Due to the high density of iron-based modified chitosan microspheres, when the oxygen inflow is slight, many catalyst microspheres will accumulate at the bottom of the U-shaped bubble tube, and only a tiny portion of catalyst microspheres can be suspended in the desulfurization solution. The catalyst cannot fully contact the desulfurization solution, and the regeneration effect is unsatisfactory. For this reason, we prepared iron-based modified chitosan as a powder catalyst. The mixed solution of iron-based chitosan was dropped into 0.5 mol/L sodium hydroxide solution with a syringe, during which the chitosan

FIGURE 1
Fe-CS microspheres (left) and Fe-CS powder (right).

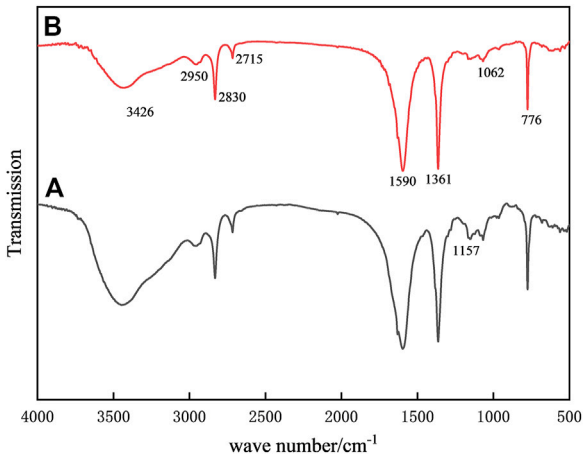

FIGURE 2
FTIR spectra of **(A)** CS and **(B)** Fe-CS.

would gradually disperse in the solution without coalescing into spheres, washed to neutrality and then cross-linked with glutaraldehyde for 24 h. Finally, the dried catalyst was ground into finer iron-based modified chitosan powder through a mortar. As shown in Figure 1, the catalyst after loading Fe^{3+} was obviously reddish compared with the counterpart before the reaction. The powdered catalyst can be better suspended in the desulfurization solution and increase the chance of interaction with S^{2-} (Wang et al., 2022).

2.5 Desulfurization and regeneration experiments

The desulfurization solution used for the experiments was prepared in the laboratory, referring to our previous work (Liu et al., 2022). Its main components were 40 ml of N-methyl pyrrolidone (NMP) and 1 g of antimony chloride ($SbCl_3$). The configured desulfurization solution was stirred well and poured into the bubble reactor, preheated in a water bath at 40°C for 2 min, and the H_2S standard gas was introduced at a volume flow rate of 20 ml/min for the desulfurization experiment, and the experiment was stopped when the mass concentration of tail gas H_2S reached 20 mg/m^3.

2 g of the prepared catalyst was placed in a U-shaped bubble reactor, 40 ml of H_2S-absorbed desulfurization solution was added and regenerated with pure oxygen bubble, the flow rate was set at 200 ml/min, and the ORP of the liquid was measured every 1 h. Separate the desulfurization liquid from the catalyst, and pour the regenerated desulfurization liquid back into the bubble reactor for the second desulfurization experiment. The purification efficiency was plotted with the desulfurization time as the horizontal coordinate and the mass concentration of H_2S in the tail gas as the vertical coordinate. The effect of catalytic oxidation regeneration of the catalyst on the desulfurization-rich liquid was judged according to the desulfurization time of the regenerated desulfurization liquid. The longer the desulfurization time of the solution after regeneration by

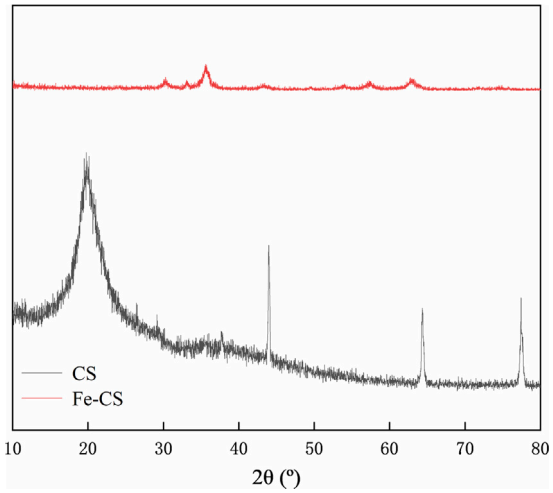

FIGURE 3
XRD analysis of CS and Fe-CS.

catalyst air oxidation, the better the catalytic oxidation regeneration effect of the catalyst on the desulfurization solution.

3 Result and discussion

3.1 Characterization of Fe^{3+} modified chitosan

3.1.1 FTIR analysis

Figure 2 displays the infrared spectra of the samples both before and after alteration. The FTIR spectra of standard chitosan are shown in curve a. Among them, the broad absorption band at 3426 cm^{-1} can be attributed to the stretching vibration of -OH and -NH.while 2950 cm^{-1}, 2830 cm^{-1}, and 2715 cm^{-1} are attributed to the stretching vibration of C-H, 1361 cm^{-1} is the peak of the bending vibration of C-H, respectively (Zheng et al., 2017; Ren et al., 2021); At 1590 cm^{-1}, a clear amide II band appears, which belongs to the bending vibration of N-H, and 1157 cm^{-1} is the peak of the bending vibration of C-H. The amide II band at 1590 cm^{-1} belongs to the bending vibration of N-H, and the peaks at 1157 cm^{-1} and 1062 cm^{-1} belong to the absorption of the C-N stretching vibration (Mohammadi et al., 2019). Compared with the native chitosan, the intensity of the absorption band at 3426 cm^{-1} decreased, indicating that the hydroxyl group of chitosan and the aldehyde group of glutaraldehyde produced acetalization and consumed part of the -OH. In addition, the consumption of the free -NH_2 group by chelation and cross-linking caused the absorption of the C-N stretching vibration at 1157 cm^{-1} and 1062 cm^{-1}. The vibration absorption was significantly weaker, showing that Fe^{3+} was successfully grafted to the sample by coordination with NH_2 (Godelitsas et al., 1999).

3.1.2 XRD analysis

The X-ray diffraction technique can accurately determine the crystal structure of substances and allows for the physical phase analysis of implications. Figure 3 shows the X-ray diffraction patterns of chitosan (CS) and iron-based modified chitosan powder (Fe-CS). It can be seen from the figure that the FeO(OH) standard card JCPDS 13-0518 is matched in the diffraction peak of Fe-CS. Among them can be identified distinct peaks 35.7°, 57.6°, and 62.9°, corresponding to the characteristic diffraction peaks of the (100), (102), and (110) crystal facets of FeO(OH) (Chen et al., 2021; Liu et al., 2023b), which indicates that Fe element was successfully in introduced into the sample.

3.1.3 SEM and EDS analysis

Scanning electron microscopy (SEM) was used to observe the microscopic morphology of the samples and the elemental composition of the surface area of the samples was analyzed through Energy dispersive spectrometry (EDS). The SEM results of chitosan (CS) and iron-based modified chitosan powder (Fe-CS) are shown in Figure 4. As can be seen from Figure 4A, the chitosan surface is relatively smooth and quite compact. After cross-linking with glutaraldehyde and chelating with $FeCl_3$, the morphology of iron-modified chitosan was significantly changed. The surface presents the appearance of folds, which may be caused by the Schiff base structure generated by the reaction between the aldehyde group and the amino group after the modification (Shkvarin et al., 2018). Comparing the microscopic morphology of the samples before and after modification, it can be found that the surface of the sample became rough and the folds increased, which was favorable in loading trivalent iron ions on the surface.

The elemental composition of the Fe-CS sample was analyzed by EDS and the results are shown in Figure 5. The mass fraction of the Fe element reached 24.5%, the highest mass fraction of the C element was 46.95%, and the mass fraction of the O element was 31.43%. Since the chitosan contains only C and O elements and no other impurity elements, a large amount of Fe was detected in the chitosan catalyst after loading with Fe^{3+}, indicating that Fe elements

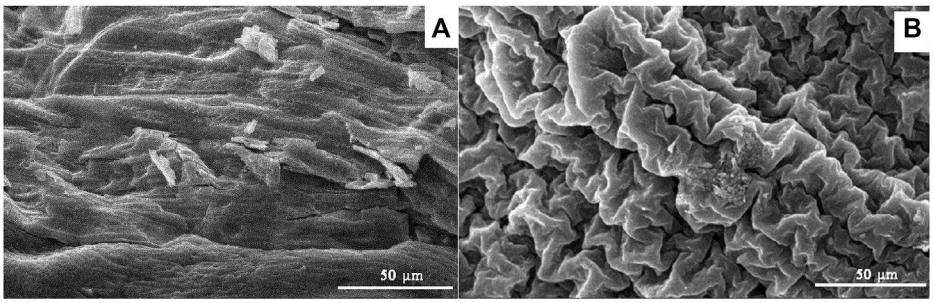

FIGURE 4
SEM photos of **(A)** CS and **(B)** Fe-CS.

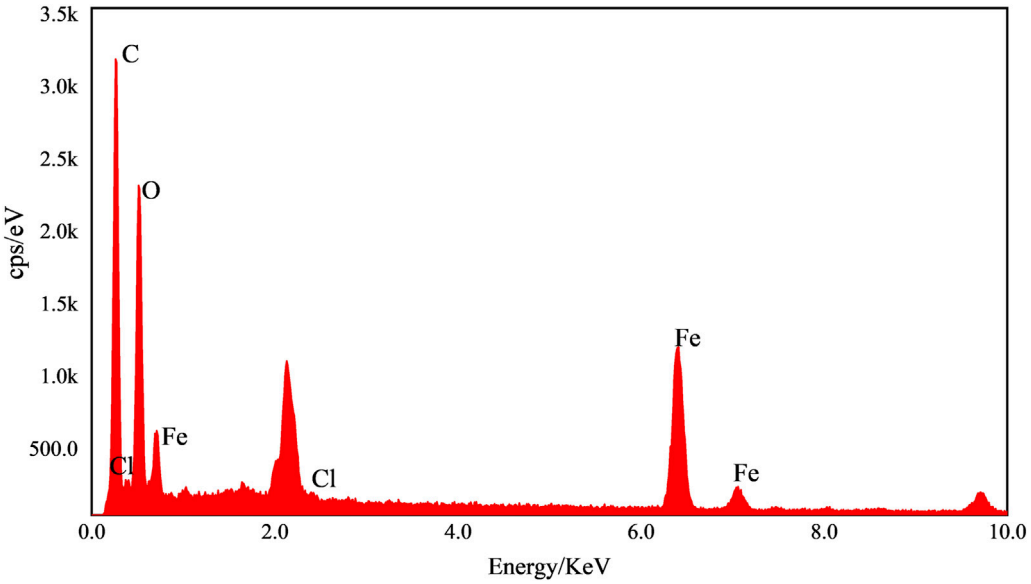

FIGURE 5
EDS analysis diagram of Fe-CS.

did chelate with chitosan and were successfully grafted on the chitosan surface.

3.2 Catalytic performance of Fe^{3+} modified chitosan

3.2.1 Effect of $FeCl_3$ dosage on the performance of modified chitosan catalysts

The amount of $FeCl_3$ dosing is an essential factor in the preparation of iron-based modified chitosan catalysts. Here, the catalytic regeneration reactions were carried out with m (CS)/m ($FeCl_3$) of 1/2, 1/5, and 1/8 to investigate the optimal ratios, respectively. 1 g of the prepared iron-based modified chitosan microspheres with different mass ratios was placed in a homemade U-shaped bubble tube, and oxygen was continuously introduced into the reactor at a gas rate of 300 ml/min. The mass ratio of 1/8 of the iron-based modified chitosan microspheres increased the density of the catalyst microspheres due to the excessive amount of $FeCl_3$, and the amount of oxygen introduced into the microspheres became smaller. The modified chitosan microspheres accumulated in the bottom of the U-shaped bubble tube and could not come in full contact with the desulfurization solution. The regeneration and desulfurization experiments were performed on the modified chitosan microspheres with mass ratios of 1/2 and 1/5 to determine the regeneration capacity of the catalyst. The desulfurization breakthrough curve after regeneration of the desulfurization solution in Figure 6 shows that the length of time to maintain the purification of the desulfurization solution after regeneration of the catalyst with the mass ratio of 1/2 is lower than that of the catalyst with the mass ratio of 1/5 under the same conditions, so the mass ratio of chitosan to $FeCl_3$ is chosen to be 1/5 for the subsequent experiments.

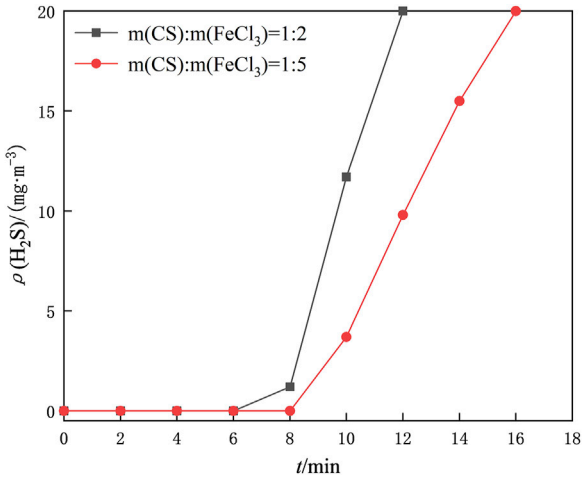

FIGURE 6
Comparison of desulfurization breakthrough time after regeneration of desulfurization fluid by modified chitosan microspheres prepared with different mass ratios of CS/$FeCl_3$.

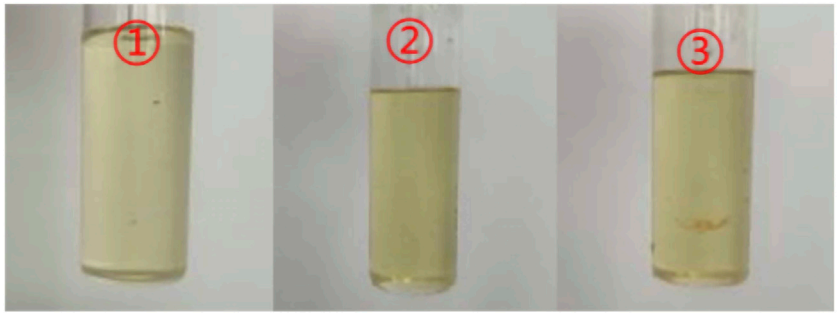

FIGURE 7
Comparison of the stability of modified samples with different mass fractions of glutaraldehyde in desulfurization solution (pictures from left to right are glutaraldehyde mass fractions of 12.5%, 5%, 2.5%).

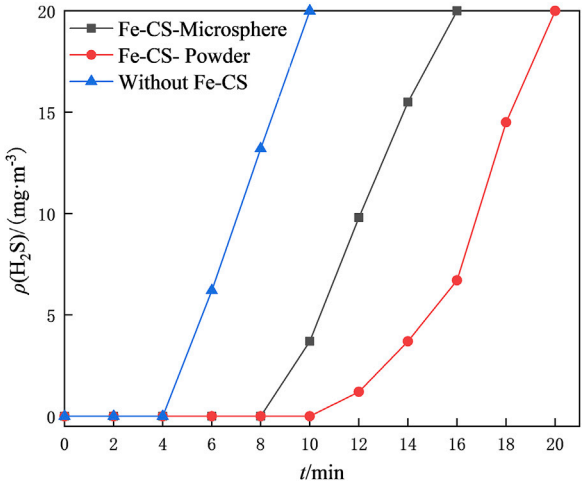

FIGURE 8
Effect of different forms of Fe-CS on the desulfurization capacity of the desulfurization solution after regeneration.

TABLE 1 Variation of ORP value of desulfurization solution after regeneration with different Fe-CS.

Sample	ORP/mV					ΔORP/mV
	0 h	1 h	2 h	3 h	4 h	
Fe-CS-Microsphere	88	106	130	131	134	46
Fe-CS- Powder	88	202	214	221	230	78
Without Fe-CS	88	91	92	96	96	8

3.2.2 Effect of glutaraldehyde dosage on the performance of modified chitosan catalysts

Glutaraldehyde, a commonly used cross-linking agent in the cross-linking process, was added to regulate the stability of modified chitosan microspheres. Here, 2.5%, 5%, and 12.5% of glutaraldehyde with mass percentages were used to prepare iron-based modified chitosan microspheres. 1 g of the prepared catalysts was added to the desulfurization solution and soaked for 24 h to observe whether the solution would change color due to the shedding of trivalent iron as the mass percent of glutaraldehyde added increased to determine whether the grafted Fe^{3+} was stable. As shown in Figure 7, the glutaraldehyde fraction of 12.5% was significantly stronger, and the solution was still clarified without discoloration. The catalyst with 5% loading was darker, and a small amount of solids were observed. The reason for this decolorization may be that the cross-linking with chitosan is weak when glutaraldehyde is not added in sufficient amounts, resulting in the weak adsorption of trivalent iron ions on the surface of modified chitosan (Xue and Liu, 2012). When the glutaraldehyde dosage was 12.5%, the trivalent iron attachment on the catalyst surface was more stable. However, a high dosage of glutaraldehyde would excessively consume the surface amino groups causing the reduction of active sites. In addition, a high glutaraldehyde dosage can lead to agglomeration of the synthesized catalysts and affect the dispersion and homogeneity of the catalysts (He et al., 2016), and thus a glutaraldehyde mass percentage of 12.5% is suitable.

3.2.3 Catalyst oxidation regeneration performance evaluation

To investigate the regeneration performance of the catalyst on the desulfurization waste solution, a static desulfurization experiment was conducted using 40 ml of homemade desulfurization solution, and the ORP values of the post-desulfurization system were measured. Two regeneration bulb tubes were taken, and 1 g of prepared iron-based modified chitosan microbeads and powdered catalysts were added. In addition, another bubble was added with desulfurization waste solution but without a catalyst as a blank control group. Oxygen was continuously injected into the three bubble tubes for 4 h at a flow rate was set of 300 ml/min for regeneration of the desulfurization waste solution, and the redox potential (ORP) of the upper clear solution was measured every 1 h. The regeneration performance of the catalyst on the desulfurization waste stream was investigated using the variation of the OPR value of the desulfurization solution and the desulfurization capacity of the regenerated desulfurization solution as the criteria. The mass concentration of H_2S in the exhaust gas was recorded at 2 min intervals, and the results are shown in Figure 8; Table 1. Table 1 shows that the difference in redox potential (ΔORP) of iron-based modified chitosan microspheres is 46 mV and that of modified chitosan powder is 78 mV after 4 h of regeneration, which indicates that the modified chitosan powder can oxidize the regenerated desulfurization waste stream more efficiently. In Figure 8, it can be seen that the H_2S concentration in the exhaust gas of desulfurization liquid regenerated by modified chitosan microspheres reached 20 mg/m^3 at 16 min, while that of modified chitosan powder reached 20 mg/m^3 at 20 min. This indicates that the desulfurization liquid regenerated by modified chitosan powder can absorb more H_2S in the same regeneration time, and the regeneration performance of modified chitosan powder is better compared with that of microspheres. This phenomenon may be due to the fact that the powdered catalyst has a more dispersed state and can be in full contact with the desulfurization solution (Lo et al., 2022). Due to the higher iron content and higher density of the microsphere catalyst, some of it accumulated at the bottom of the bubble tube during the regeneration process and could not fully contact the desulfurization solution. Accordingly, the regeneration effect was lower than that of the powdered catalyst. Compared with the blank control group, both showed higher ORP values, indicating that both have a certain catalytic ability and can effectively regenerate the desulfurization waste liquid.

3.2.4 Catalyst cycling performance

The reusability of catalysts is directly related to the service life and operating cost and is an essential indicator for evaluating the value of catalysts in practical applications (Graś et al., 2021). Here, the reusability and stability of the catalyst were evaluated by the sulfur capacity level of the desulfurization solution and the iron content on the catalyst after regeneration. After the catalyst is added to the desulfurization solution, the following oxidation-reduction reactions will occur in the solution (Liu et al., 2022; Qiu et al., 2022). Fe^{3+} oxidizes the H_2S originally absorbed by the coordination state to sulfur and removes it separately. After finishing, oxygen is passed to reoxidize Fe^{2+} on the catalyst to Fe^{3+}, thus the catalyst is regenerated.

1 Oxidation process

$$2Fe^{3+} + HS^{-}\ (\text{Coordination status}) \rightarrow 2Fe^{2+} + S\downarrow + H^{+} \quad (1)$$

2 Regeneration process (O_2)

$$2Fe^{2+} + 1/2O_2 + 2H^{+} \rightarrow 2Fe^{3+} + H_2O \quad (2)$$

The changes in the sulfur capacity of the desulfurization solution after regeneration are shown in Figure 9. The modified chitosan powder catalyst still maintained good catalytic performance after five times of reuse. The regenerated desulfurization solution always kept a purification time of about 18 min at higher H_2S concentrations. ICP examined the Fe content of the catalyst, and the difference in Fe content of the catalyst after five uses compared to the fresh catalyst did not exceed 1.5%, indicating that there was no excessive loss of active centers after five cycles. This can be attributed to the interaction between the carrier and Fe^{3+}, which enhances the stability of the catalyst. Overall, the iron-based catalysts prepared in this work have the advantages of stable composition and good reusability.

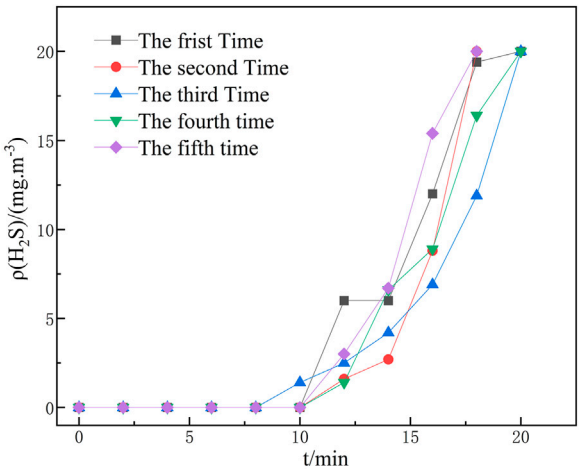

FIGURE 9
Desulfurization regeneration repeatability test results.

4 Conclusion

In this study, chitosan was used as the carrier, and glutaraldehyde was used as the cross-linking agent. The ferric ions were successfully grafted on the carrier through the coordination between the heteroatomic functional groups of chitosan and Fe^{3+} and used for the catalytic oxidative regeneration of desulfurized rich liquid. The catalyst morphology and structure were initially characterized using FTIR, XRD, SEM, EDS, and other characterization methods. The effects of varying the preparation conditions on the iron-based modified chitosan catalyst and the performance on the oxidative regeneration of the desulfurization solution were discussed. The effects of different morphologies of chitosan, $FeCl_3$ dosing, and glutaraldehyde dosing on the catalyst performance were investigated, respectively. The characterization results confirmed the successful loading of Fe^{3+} on chitosan. The desulfurization and regeneration experiments showed that the powdered iron-based modified chitosan catalyst had better catalytic performance than the microbead catalyst at a mass ratio of 1: 5 of chitosan to $FeCl_3$ and 12.5% mass fraction of glutaraldehyde. Overall, the strategy proposed in this work of selective catalytic oxidation of absorbed HS^- to monomeric sulfur by non-homogeneous oxidation enhancement effectively improves the sulfur blockage problem caused by the oxidation of sulfur monomers during the absorption process.

Data availability statement

The original contributions presented in the study are included in the article/supplementary material, further inquiries can be directed to the corresponding author.

Author contributions

ZL: Conceptualization, Methodology, Writing-Original draft, Validation, Resources, Review and editing. ZC: Review and editing. QC: Review and editing. LL: Data curation, Investigation. YW: Editing. PS: Data curation. YZ: Data curation. ZS: Data curation. KQ: Supervision.

Funding

The research was funded by China National Science and Technology Major Project (2016ZX05017) and the Sinopec Group Corporation 2020 Science and Technology Project "Organic Sulfur Catalytic Hydrolysis Technology Improves Quality Research" (No.120049-1).

Conflict of interest

The authors declare that the research was conducted in the absence of any commercial or financial relationships that could be construed as a potential conflict of interest.

Publisher's note

All claims expressed in this article are solely those of the authors and do not necessarily represent those of their affiliated organizations, or those of the publisher, the editors and the reviewers. Any product that may be evaluated in this article, or claim that may be made by its manufacturer, is not guaranteed or endorsed by the publisher.

References

Chen, Z., Zheng, R., Graś, M., Wei, W., Lota, G., Chen, H., et al. (2021). Tuning electronic property and surface reconstruction of amorphous iron borides via W-P co-doping for highly efficient oxygen evolution. *Appl. Catal. B Environ.* 288, 120037. doi:10.1016/j.apcatb.2021.120037

Godelitsas, A., Charistos, D., Dwyer, J., Tsipis, C., Filippidis, A., Hatzidimitriou, A., et al. (1999). Copper(II)-loaded HEU-type zeolite crystals: Characterization and evidence of surface complexation with N,N-diethyldithiocarbamate anions. *Microporous Mesoporous Mater.* 33, 77–87. doi:10.1016/S1387-1811(99)00124-9

Graś, M., Kolanowski, Ł., Chen, Z., Lota, K., Jurak, K., Ryl, J., et al. (2021). Partial inhibition of borohydride hydrolysis using porous activated carbon as an effective method to improve the electrocatalytic activity of the DBFC anode. *Sustain. Energy Fuels* 5, 4401–4413. doi:10.1039/D1SE00999K

Gu, Z., Xiang, X., Fan, G., and Li, F. (2008). Facile synthesis and characterization of cobalt ferrite nanocrystals via a simple Reduction–Oxidation route. *J. Phys. Chem. C* 112, 18459–18466. doi:10.1021/jp806682q

He, X., Li, K., Xing, R., Liu, S., Hu, L., and Li, P. (2016). The production of fully deacetylated chitosan by compression method. *Egypt. J. Aquatic Res.* 42, 75–81. doi:10.1016/j.ejar.2015.09.003

Liu, Z., Qiu, K., Dong, Y., Jin, Z., Liu, L., and Wu, J. (2022). Sb-Fe bimetallic non-aqueous phase desulfurizer for efficient absorption of hydrogen sulfide: A combined experimental and dft study. *Korean J. Chem. Eng.* 39, 3305–3314. doi:10.1007/s11814-022-1253-6

Liu, Z., Qiu, K., Sun, G., Ma, Y., Wang, Y., Peng, J., et al. (2023). Aminated polyacrylonitrile fibers for the removal of hydrogen sulfide from natural gas at room temperature. *Res. Chem. Intermed.* 49, 701–716. doi:10.1007/s11164-022-04897-1

Liu, Z., Sun, G., Chen, Z., Ma, Y., Qiu, K., Li, M., et al. (2023). Anchoring Cu-N active sites on functionalized polyacrylonitrile fibers for highly selective H_2S/CO_2 separation. *J. Hazard. Mater.* 450, 131084. doi:10.1016/j.jhazmat.2023.131084

Lo, R., Manna, D., Lamanec, M., Dračínský, M., Bouř, P., Wu, T., et al. (2022). The stability of covalent dative bond significantly increases with increasing solvent polarity. *Nat. Commun.* 13, 2107. doi:10.1038/s41467-022-29806-3

Mohammadi, A., Saadati, Z., and Joohari, S. (2019). Comparison of the adsorption of H_2S by ZnO–TiO_2 and Ni–ZnO–TiO_2 nanoparticles: An adsorption isotherm and thermodynamic study. *Environ. Prog. Sustain. Energy* 38. e13258. doi:10.1002/ep.13258

Qiu, K., Liu, Z., Dong, Y., Liu, L., Li, W., Niu, S., et al. (2022). [Bmim]$FeCl_4$ efficient catalytic oxidative removal of H_2S by Cu^{2+} synergistic reinforcement. *Chem Eng Technol* 45, 1867–1875. doi:10.1002/ceat.202200235

Ren, Z., Shen, Y., Gao, H., Chen, H., Liu, C., and Chen, Z. (2021). Comparison of sodium oleate and sodium petroleum sulfonate for low-temperature flotation of fluorite and the collecting mechanisms. *Min. Metallurgy Explor.* 38, 2527–2536. doi:10.1007/s42461-021-00494-9

Shkvarin, A. S., Merentsov, A. I., Titov, A. A., Yarmoshenko, Yu.M., Shkvarina, E. G., Píš, I., et al. (2018). Quasimolecular complexes in the $Cu_xTiSe_{2-y}S_y$ intercalation compound. *J. Mat. Chem. C* 6, 12592–12600. doi:10.1039/C8TC04115F

Vogt, C., and Weckhuysen, B. M. (2022). The concept of active site in heterogeneous catalysis. *Nat. Rev. Chem.* 6, 89–111. doi:10.1038/s41570-021-00340-y

Wang, Y., Yang, C., Zhang, C., Duan, M., Wang, H., Fan, H., et al. (2022). Effect of hierarchical porous MOF-199 regulated by PVP on their ambient desulfurization performance. *Fuel* 319, 123845. doi:10.1016/j.fuel.2022.123845

Xue, Q., and Liu, Y. (2012). Removal of minor concentration of H_2S on MDEA-modified SBA-15 for gas purification. *J. Industrial Eng. Chem.* 18, 169–173. doi:10.1016/j.jiec.2011.11.005

Zheng, R., Gao, H., Ren, Z., Cen, D., and Chen, Z. (2017). Preparation of activated bentonite and its adsorption behavior on oil-soluble green pigment. *Physicochem. Problems Mineral Process.* 53 (2), 829–845. doi:10.5277/ppmp170213

frontiers | Frontiers in Environmental Engineering

TYPE Original Research
PUBLISHED 07 June 2023
DOI 10.3389/fenve.2023.1158656

OPEN ACCESS

EDITED BY
Wendong Tao,
SUNY College of Environmental Science and Forestry, United States

REVIEWED BY
Mohammad Abu Hashnat Badsha,
California Polytechnic State University, United States
Alsayed Mostafa,
Inha University, Republic of Korea

*CORRESPONDENCE
Mohammed Ali,
hebamohd4@gmail.com

RECEIVED 04 February 2023
ACCEPTED 09 May 2023
PUBLISHED 07 June 2023

CITATION
Ali M and Robele S (2023), Major contributing factors to the lower level of connection to the existing sewer network in Addis Ababa: the case of the Kality catchment.
Front. Environ. Eng. 2:1158656.
doi: 10.3389/fenve.2023.1158656

Major contributing factors to the lower level of connection to the existing sewer network in Addis Ababa: the case of the Kality catchment

Mohammed Ali* and Sirak Robele

Ethiopian Institute of Water Resources, Addis Ababa University, Addis Ababa, Ethiopia

Many households in Addis Ababa have not been connected to a sewer network, even when it passes by their homes. This study was designed to investigate major factors that have contributed to the lower level of connection to the existing sewer network in the Kality catchment of Addis Ababa. A household survey was conducted via questionnaire to identify the reasons hindering customers from connecting to sewers. The main factors identified were lack of awareness, connection fee, topography, customers' preference for onsite sanitation over sewers, customers' unwillingness to reinstate fences or pavements in their compound, and the unreliability of the water utility service. The survey results were analyzed with a binary logistic regression model using SPSS software. Except for topography (p-value 0.792) and connection fee (p-value 0.446), the other four independent variables had significant p values of less than 0.05, which implied a good model. Customers' preference for onsite sanitations over sewers, followed by the unreliability of the water utility service and customers' unwillingness to reinstate fences or pavements in their compounds were found to be the factors that most contribute to the lower level of user interest in sewer connection. However, a lack of awareness and information was also crucial in determining the rate of connection to sewers in the Kality catchment of Addis Ababa. The study also revealed that there was a gap in legislation and its enforcement: there was neither a regulator nor regulations for monitoring wastewater management, including mandatory sewer connection in the city.

KEYWORDS

connection to sewer, sewer network, sewerage system, Kality catchment, Addis Ababa

1 Introduction

The level of sewerage coverage varies across many of the world's cities. In northern Europe and North America, for example, it is not unusual for every household to have in-house flush toilets connected to a sewer network. However, in global terms, these are a minority (Christop, 2011). A typical example of the opposite is Freetown, Sierra Leone, where a total of 4 km of sewerage partially serves the business district in the center of a city of more than 1 million inhabitants (Christop, 2011). A number of centralized wastewater systems have been built in urban Indonesia, but they do not work at full capacity - only 47% of the designed capacities are in use (WorldBank, 2013a). The main reason for the under-utilization of treatment plant is that sewer networks including in-house connections are not

well developed (WorldBank, 2013a). The focus in the past has mainly been on developing infrastructure: the sewerage network and treatment plants (WorldBank, 2013b). One of the many urban challenges in low- and middle-income countries is how to increase the number of households that connect to sewerage networks (WorldBank, 2020).

Systems for collecting and transporting toilet waste are strongly influenced by the type of toilet in-use because these determine the volume and characteristics of wastewater. For instance, water closets use a lot of water for flushing and require a sewerage connection (Jonathan P., 2014). However, the most common forms of toilets only use a small amount of water for flushing, or no water at all. In these situations, a sewerage system is likely to be inappropriate, and other sludge collection systems needs to be explored (Jonathan P., 2014). The conventional approach to sanitation planning creates an artificial barrier between technical decision making and institutional analysis in its broadest sense. This results in technically 'appropriate' systems which do not work or which do not achieve the desired objectives (Andrew Cotton et al., 2006).

Urban Ethiopia currently has an insufficient water supply to support a comprehensive sewerage service and too few in-house water connections in most areas to make sewerage system necessary or feasible (Chris Heymans, 2017). In fact, no city in Ethiopia other than Addis Ababa has a sewer network: sewage is transported to treatment plants using vacuum trucks. According to a study by MCE (2016), only 12.36% of the population of Addis Ababa was connected to the sewer network, while 40% of customers had an in-house water connection. The Kality wastewater treatment plant (WWTP), commissioned in 2018, operates at 57% of its design capacity (100,000 m^3/d). The main reason for this low level of operation is that users have not connected to the sewer network in the desired numbers (MCE, 2016). In the Kality catchment of Addis Ababa, where a sewerage network does exist, many households have not connected even when it passes in front of their homes (MCE, 2016).

Therefore, the current study aims to assess the major factors contributing to the low level of sewer connection and establish the degree of their effects on the level of sewer connection based on model output parameters.

2 Materials and methods

2.1 Description of the study area

2.1.1 Location

Addis Ababa, the capital of Ethiopia and its largest city, lies high in the foothills of Mount Entoto in central Ethiopia. It is geographically located at 9°N and 38°E between 2000 and 2,500 m above sea level. Addis Ababa is the country's commercial, manufacturing, and cultural center (Figure 1).

2.1.2 Climate

The climate of Addis Ababa is warm and temperate. Over the course of the year, the temperature typically varies from 8.9 to 23.9°C, - rarely reaching below 5.6 C or above 26.7°C. The average annual temperature is 16.3°C and the mean annual precipitation is 1,143 mm (Climate-date, 2021). Average daily sunshine is as high as 9.5 h in November/December and falls to 3 h in July/August (Engida Z., 2001).

2.1.3 Demography

The total population of the city of Addis Ababa in 2020 was 3.689 Million (CSA, 2013). Immigration to Addis Ababa from all corners of Ethiopia in search of employment and services is very high, posing critical challenges that include a high rate of

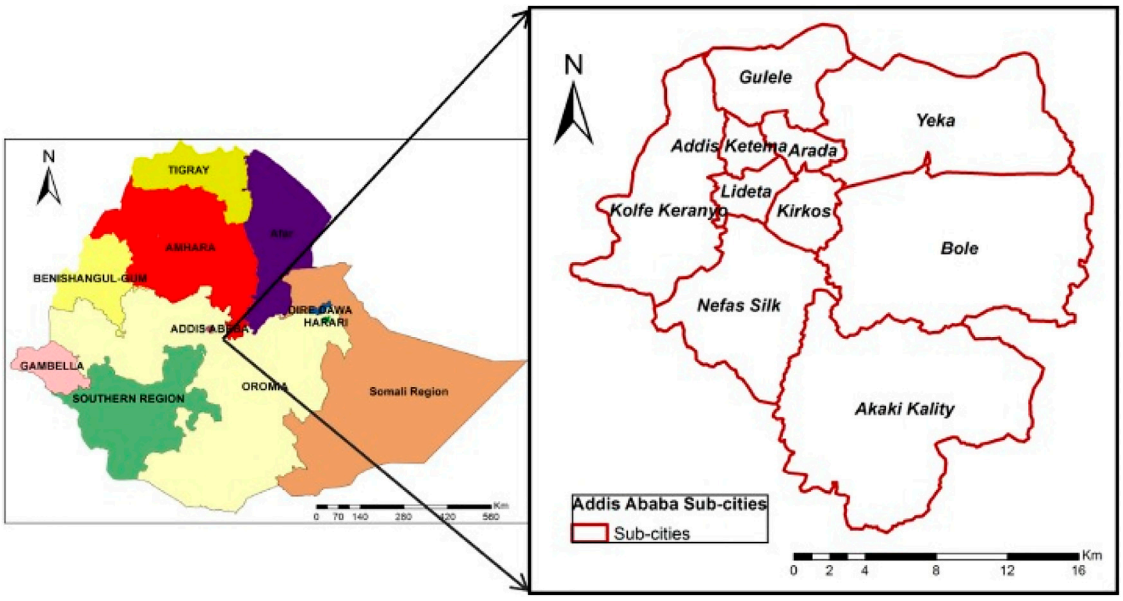

FIGURE 1
Location map of Addis Ababa city (Google, 2020).

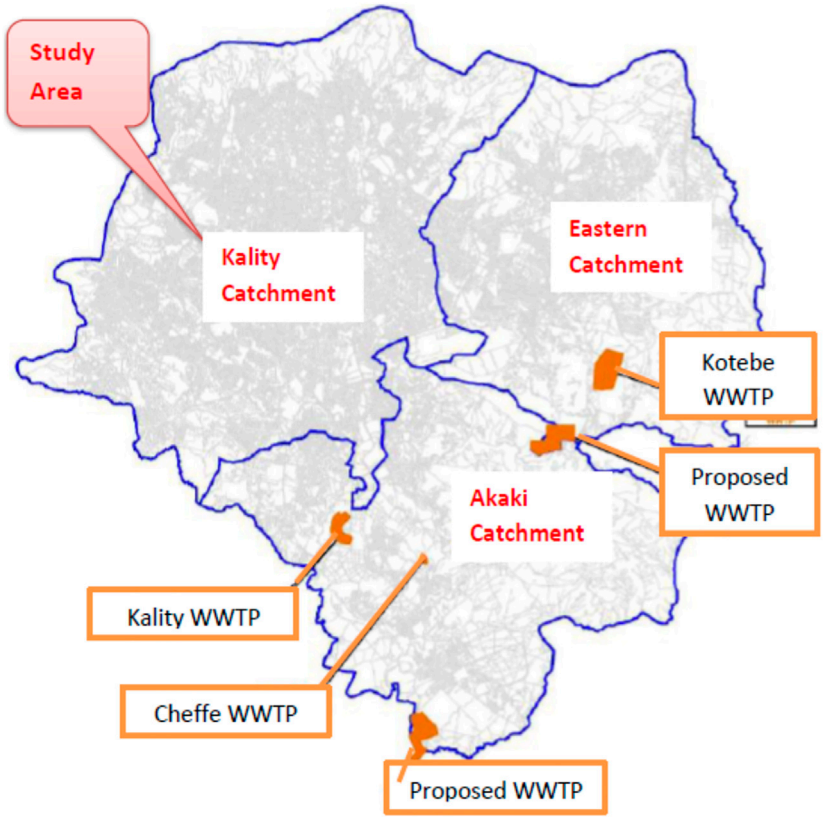

FIGURE 2
Location of study area—Kality Catchment (SWS, 2013).

unemployment, limited housing, and environmental degradation (UN-Habitat, 2008). According to the Central Statistics Authority, the city's population growth could double from 2007 to 2037. As per the 2007 census, the city's population was 2.739 Million and it is set to grow to 5.132 Million by 2037.

2.1.4 Wastewater flow catchment

Addis Ababa is divided into three wastewater flow catchments: Kality, Eastern, and Akaki (Figure 2). This study focuses on the Kality catchment. As shown in Figure 1, Addis Ababa is divided into 10 administrative sub-cities; the Kality wastewater catchment covers the central and northwest of the city, comprising seven sub-cities (Gulele, Kolfe-Keraniyo, Nifas-Silk-Lafto, Arada, Addis Ketema, Lideta, and Kirkos). The sub-city Yeka and Bole lie in the Eastern catchment, and the sub-city Akaki is in the Akaki catchment. According to SWS (2013), the Kality sewerage catchment discharges approximately 80% of the city's wastewater.

2.1.5 Existing sewerage system

The Kality catchment has only one centralized WWTP with an installed capacity of 100,000 m3/d. Commissioned in 2018, the Kality treatment plant is fitted with state-of-the-art technology, including an up flow anaerobic sludge blanket (UASB) and trickling filter units. This plant has been operating at only 57% capacity due to the lower rate of connection to the sewer network. In addition, there were 14 decentralized treatment plants (seven Anaerobic Baffled Reactors, five Membrane Bioreactors and two Waste Stabilization Ponds) constructed at different condominium housing sites with a total installed capacity of 60,240 m3/d. A total of 1207 km of sewer line (trunk main, secondary line and tertiary line) has been constructed in the Kality catchment. Of the 1207 km sewer line, the trunk main (diameter 350–1500 mm) covers 85 km, the secondary sewer line (diameter 160–300 mm) covers 927 km, and the tertiary sewer network (diameter less than 160 mm) covers 195 km. More than 65% of sewer lines are installed in selected sub-cities such as Bole, Kolfe-Keraniyo and Nifas-Silk-Lafto. There is great variation between the quantity of wastewater produced and daily waste treatment capacity in the Kality catchment.

2.2 Research and sampling design

2.2.1 Research method

A quantitative research method with an inductive approach was adopted for the study, and a structured questionnaire was used to capture customer's interest to sewer connection.

2.2.2 Sample size and sampling technique

Structured questionnaires were developed in the English language and translated into the local Amharic language. Four trained data collectors—two male and two women—participated

TABLE 1 Independent variables affecting customer interest in sewer connection.

Variables	Variable types	Variable description and unit of measurement
Dependent variable		
Interest	Dummy	"1" if customer has interest, otherwise "0"
Independent variable		
Awareness	Nominal	"1" if customer is aware, otherwise "0"
Reliability	Nominal	"1" if customer rely on service, otherwise "0"
Onsite sanitation	Nominal	"1" if customer chooses onsite sanitation, "0" prefers sewer
Willingness	Nominal	"1" if customer becomes willing to reinstate pavement/fence, "0" otherwise
Connection fee	Nominal	"1" if customer is able to pay connection fee, "0" if not
Topography	Nominal	"1" if topography is suitable for gravity sewer, "0" if not

in the household survey. The sample size was computed using the following formula by Daniel WW (2013):

$$n = \frac{\mathrm{N} * \mathrm{p} * \mathrm{q} * Z^2}{(\mathrm{N}-1) * e^2 + \mathrm{p} * \mathrm{q} * Z^2}$$

Where n is the desired sample size; N is the population or household size; p is the estimated target population proportion; q is 1-p; Z stands for standard score at 95% confidence level, which is 1.96; and e is the margin of error (in this case 0.05). Since the proportion of the population connected to the sewer network was unknown, we used 50% as the value of p and q.

Our frame from which samples were drawn was households living inside the tertiary pipe network that had access to sewer connection. The water utility branch offices collaborated in quantifying the number of households with access to tertiary sewers. Thus, the size of the population or households (N) from which samples were drawn was 25,228.

The sample size calculated using the aforementioned formula was 387 households. This was compared with the result obtained from an online sample size calculation tool (www.select-statistics.co.uk); both methods gave a similar result.

Pre-test sample sizes are estimated to be from 5 to 15 households (Thomas V. Perneger et al., 2015); however, we carried out the pre-test on 15 households in order to validate the questionnaire. A simple random sample was used to select observations from a population until the desired sample size was achieved.

2.2.3 Data source and collection instrument

Both primary and secondary data sources were used for the research. Data collection using the questionnaire was carried out with the full consent of the respondent. Household heads - either men or women - were interviewed for the survey. In order to meet them, the data were collected on Sundays. Additional information was also collected from key informants (experts working with stakeholders), focus group discussions, and observations. Observations were also employed to assess the suitability of the topography for gravity sewer connection. This study was conducted from 2019 to 2021. Regarding policy issues and regulation enforcement, focus group discussions were conducted with experts from the water utility, environment protection authority, ministry of water, and city administration. Moreover, a range of literature was reviewed, but our study found that very little research had been done in areas similar to our research topic.

2.3 Data analysis

Binary logistic regression is used to predict the effects of independent variables on the dependent variable (Gujarati D., 2004). Predictor or independent variables include lack of awareness, connection fee, topography, reliability of sewerage service, and customers' preference for onsite sanitation (septic tank, pit latrine). In our study, the dependent variable was whether a household was interested in connecting to a sewer network. As the dependent variable had a binary or dichotomous outcome (yes or no), a binary logistic regression model was the most appropriate tool for analysis. SPSS software was therefore used for analysis.

The predictor variables were selected based on previous empirical studies and discussions with the water utility sewerage technicians. Variables such as availability of water and in-house sanitary facilities were also considered. However, water availability was found to correlate with reliability of the service provided by the water utility. Moreover, availability of water and in-house sanitary facilities were highly correlated. Taking these points into consideration, availability of water and in-house sanitary facilities were dropped from the model.

2.3.1 Method specification

The dependent variable (customer interest in connecting to the sewer network) is binary or dichotomous with two outcomes: 1 if a customer was interested in sewer connection and 0 otherwise. Based on Gujarati (2004), the model is specified as follows;

$$\boldsymbol{Pi} = \boldsymbol{E}\left(\boldsymbol{Y} = \frac{\mathbf{1}}{\boldsymbol{Xi}}\right) = \frac{\mathbf{1}}{\mathbf{1} + \boldsymbol{e}^{-(\beta 0 + \beta 1 Xi)}}. \quad (1)$$

In the logistic distribution equation, Pi is the probability of a customer's interest in connecting to the sewer network, Xi is a set of

explanatory/independent variables of the *i*th user; and βo and β_1 are parameters to be estimated.

When $\beta_o+\beta_1 X_i$ in Eq. 1 is replaced by Z_i, Eq. 2 (the probability of a customer's interest in the sewer network) is obtained:

$$Pi = \frac{1}{1+e^{-zi}} = \frac{e^{z}i}{1+e^{z}i}. \quad (2)$$

The possibility of a customer's lack of interest in sewer connection (*1-P*) can be presented in Eq. (3) as follows:

$$1 - Pi = \frac{1}{1+e^{z}i}. \quad (3)$$

From the aforementioned two equations, the odds ratio in favor of a customer being interested in sewer connection is:

$$\frac{Pi}{1-Pi} = e^{zi}. \quad (4)$$

The logit model uses logarithmic transformation to assume the linearity of the outcome variable on the explanatory variable. The logit model can, thus, be expressed as:

$$Li = \ln\left(\frac{Pi}{1-Pi}\right) = Zi = \beta o + \beta 1 Xi. \quad (5)$$

If the disturbance term u_i is considered in the general logit model with a set of variables, the equation becomes:

$$Z_i = \beta_o + \beta_1 X_1 + \beta_2 X_2 +, , , +\beta_n X_n + u_i, \quad (6)$$

Where X_1, X_2, . . . , X_n are independent (explanatory) variables affecting customer interest in the sewer network. The explanatory variables are listed in Table 1.

3 Results and discussion

3.1 Major factors for the lower rate of connection to the existing sewer network

3.1.1 General

Of the survey respondents, 32% were women and 68% were men. Among the surveyed households, 93% owned the house in which they lived, whereas only 7% of houses were rented. Some 78% of the households relied on a septic tank to contain their liquid waste. More than 74% employed private de-sludging services to empty sludge and 26% used the water utility's de-sludging service. More than 50% of respondents replied that it took more than 5 years for their septic tank to fill.

3.1.2 Customers' interest in sewer connection

The household survey result revealed that only 23% of customers were interested in connecting to the sewer network, while 77% showed no interest Taking the level of customer interest in sewer connection as a dependent variable, various major factors (independent variables) that could contribute to the lower level of customer motivation for sewer connection were assessed. Accordingly, lack of awareness, customers' preference to use onsite sanitation facilities, customers' unwillingness to reinstate pavement or fence, and the unreliability of the sewerage service of the water utility were some of the major factors. In the study area, however, the connection fee and topography were found not to be major factors determining customer interest in sewer connection. The existing sewer network was constructed in areas where relatively high-income customers were concentrated, so the connection fee was not considered a major factor.

TABLE 2 Omnibus tests of model coefficients.

		Chi-square	df	Sig
Step 1	Step	226.076	6	0.000
	Block	226.076	6	0.000
	Model	226.076	6	0.000

3.1.3 Lack of awareness

The household survey showed that 78% of customers were not aware of the availability of the sewer network in the area where they lived. Only 22% of customers were aware that the tertiary sewer network passed in front of their homes. With such a low level of customer awareness, it is difficult to expect a high number of customers to have sewer connections. Customers' knowledge about the importance of using a sewer connection over onsite sanitation (septic tank/pit latrine) was evaluated, and only 7% gave correct answers. The importance of a sewer connection over onsite sanitation includes the reduction of frequent de-sludging of the septic tank or pit latrine, avoiding bad smells during de-sludging, saving cost/time/labour, pollution prevention within compounds due to sludge leftovers while dismantling the suction pipes, etc. Therefore, 93% of customers did not give correct responses. These findings coincide with World Bank (2015) and CDSWC (2020) findings a lack of awareness and information are one of the many factors that could hinder customers from connecting to sewers.

3.1.4 Customer preference for onsite sanitation

We found that 81% of customers preferred onsite sanitation facilities (septic tank and pit latrine) over sewer connections. When asked about the main reasons for choosing onsite sanitation facilities (mainly septic tanks), 78% replied that they were comfortable using an existing septic tank and 22% gave different reasons (unreliable service provided by the water utility, septic tank lasts longer and de-sludging septic tank by vacuum truck not costly). This finding agrees with a World Bank study (2013b), which found that home owners do not connect to sewer networks because septic tanks are cheaper. However, the sewer connection fee in Addis Ababa was found to be much cheaper than the cost of constructing a septic tank, so there must be other reasons (enforcement of regulation and legislative issues) for customer preference for onsite sanitation. It is not always true that connecting to sewers is the only viable improved sanitation option (Rebecca Root, 2020). As further discussed in this report, planners must understand factors such as density, topography, cultural preferences, and initial investment finances before choosing citywide sanitation options. Water utilities must heavily invest in the construction of a WWTP and the expansion of the sewer network. Therefore, connecting to the sewer network should be unavoidable option if the topography is suitable for a gravity sewer and there is a sewer network in the area.

TABLE 3 Model summary.

Step	−2 log likelihood	Cox and snell R square	Nagelkerke R square
1	191.300[a]	0.442	0.670

[a]Estimation terminated at iteration number 6 because parameter estimates changed by less than .001.

TABLE 4 Hosmer and lemeshow test.

Step	Chi-square	df	Sig.
1	1.127	3	0.770

3.1.5 Customers' willingness to reinstate pavements or fences

Of the surveyed households, 80% were not willing to reinstate pavements or fences for the purpose of sewer connection; only 20% were willing to do so. This finding coincides with a CDSWC (2020) study, which also found customers unwilling to reinstate pavements or fences for sewer connections. Many cities worldwide require customers to have a sewer connection if there is one in their vicinity.

3.1.6 Reliability of service

Some 75% of customers did not trust the reliability of the water utility's sewer service since the city's water supply provided by the water utility was intermittent. This finding is in line with a study by Victoria A. Beard (2021), which found that intermittent water supply contributes to sewer blockages, resulting in the whole sewer system not functioning as intended. There is, thus, a strong linkage between reliable water supply and sewerage service. According to Chris Heymans (2017), a sufficient supply of water and in-house sanitary connections are vital for a feasible sewerage system. According to MCE (2016), water borne sewerage system can only be provided where the water supply is at least 50 L per person per day: flushed human excreta travels further to reach a sewer manhole than a septic tank as the former is outside of customer's compound. In order to flush a certain mass of human excreta into a sewer manhole, a greater volume of water is required than for a septic tank. Connection to a sewer is more water intensive than onsite sanitation. Therefore, customer suspicion of the reliability of the sewerage service in Addis Ababa has a tangible basis, as the problem of water supplies had become more severe in many parts of the city.

3.1.7 Connection fee

The connection fee for a sewer line is calculated based on its length to a connection manhole, the depth of the trench, and the type of soil. On average, the minimum connection fee was 3,018 Birr (equivalent to USD 63.35). The survey revealed that 89% of the households had the ability to cover the connection fee, with only 11% unable to cover the fee in one installment. This figure does not reflect the situation in the whole Kality catchment as the existing sewer network was constructed in areas where high-income customer lived. In order to understand the effect of a connection fee on sewer connection in other parts of the city, a separate socio-economic survey is needed prior to constructing a sewer network. Therefore, the connection fee would have little effect on reduced customer interest in sewer connection in the survey area.

3.1.8 Topography

Regarding the suitability of topography for sewer connection, 82% of surveyed households' homes were found to be suitable for the gravitational flow of sewage into the sewer network. Topography is important for a gravity sewer connection and its effect is site-specific. For undulating topography like Addis Ababa, its effect on gravity sewer flow is significantly high. However, topography had a minor effect in the surveyed area on hindering customers from sewer connection because the existing sewer networks in the survey area were constructed at sites considered to have suitable topography for gravity connection.

3.2 Model output and its interpretation

The number of cases included in the analysis was 387 (sample size) and there were no missing cases. The Chi-square as illustrated in Table 2 was 226.076 for degree of freedom 6, and the significance level or probability was 0.000. Here, a probability value less than 0.05 implied a good model.

As shown in Table 3, Cox and Snell's R^2 was 0.442, whereas Negelkerke's R^2 was 0.670—between 44.2% and 67.0% of the variance in the dependent variable was explained by our model, which implied that it was very good.

The Hosmer and Lemeshow's Test (Table 4) supported our model; p-value was 0.770, which was greater than 0.05 and insignificant (implied a very good model). In this test, we wanted an insignificant value supporting our model.

In Table 5, the value at the lower right-hand side of table (93.0) is the percentage accuracy classification (PAC). A PAC value of 93% shows that if we ask a customer the six independent variables (awareness, topography, onsite sanitation, connection fee, and reliability of service), we can predict whether a customer is interested in sewer connection by the "Yes" or "No" category using our model with 93% accuracy. This shows that our model has very good predictive capabilities.

In Table 6 under the Significance (Sig.) column, values less than 0.05 are significant. Four out of six independent variables had p values less than 0.05, implying a good model. Only two variables, topography and connection fee, had values out of the required range. This implies that, in terms of predictive capabilities or relationship between dependent variable and independent variables, certain categories provide better information for our model prediction. Therefore, topography and connection fee had lesser predictive capabilities for customer interest in sewer connection than the other four variables.

In Table 6 odds ratio column (ExpB), for reliability of service given by the water utility, the odds ratio of 7.254 tells us that the odds of no interest in connecting to a sewer if the customer did not thrust the reliability of the water utility's service were 7.254 times higher than if customers did trust its service. Thus, the odds of no interest to

TABLE 5 Percentage accuracy classification (PAC) table[a].

Observed			Predicted		
			User's interest to connect to sewer		Percentage correct
			No	Yes	
Step 1	User's interest to connect to sewer	No	290	8	97.3
		Yes	19	70	78.7
	Overall Percentage				93.0

[a]The cut value is 500.

TABLE 6 Equation variables.

		Wald	df	Sig.	Exp(B)	95% C.I.for EXP(B)		Rank
						Lower	Upper	
Step 1[a]	User's awareness about availability of sewer nearby (1)	3.898	1	0.048	0.279	0.079	0.991	6
	Willingness & ability to cover connection fee	0.532	1	0.466	1.634	0.437	6.112	4
	User's willingness to re-instate existing pavement or fence	6.657	1	0.010	5.182	1.485	18.080	3
	User's preference between septic tank/latrine and sewer	22.634	1	0.000	22.911	6.306	83.243	1
	Suitability of topography for sewer connection by gravity	0.069	1	0.792	1.170	0.363	3.777	5
	Reliability of service given by the water utility	9.713	1	0.002	7.254	2.086	25.222	2
	Constant	12.298	1	0.000	0.030			

[a]Variable(s) entered on step 1: User's awareness about availability of sewer nearby, Willingness & ability to cover connection fee, User's willingness to re-instate existing pavement or fense, User's preference b/n septic tank/latrine and sewer, Suitability of topography for sewer connection by gravity, Reliability of service given by the water utility.

connection were 625.4% higher if customers did not thrust the reliability of the water utility service than if the customers trusted it.

The odds ratio results show where the focus of intervention should be in order to increase the number of connections to sewers. As shown in Table 6, more emphasis should be placed on the enforcement of regulations and thereby addressing customers' unwillingness to reinstate fences or pavements as well as their preference for onsite sanitation over sewers. Therefore, planners should focus on high-ranked parameters and follow the ranked order when implementing improvement measures.

3.3 Policy issue and enforcement of regulation

As stated in the urban wastewater management strategy by MoWIE (2017), the issue of wastewater management in Ethiopia was left to individual cities and towns. Regarding municipal wastewater management and control, no regulatory bodies were established, and no regulations have so far been issued by city municipality. In the absence of these, the water utility could not implement enforcement measures throughout sanitation service chains, including mandatory sewer connection. There was also an overlap of responsibilities among regulators as well as between regulators and implementers.

4 Conclusion

Lack of awareness and information as well as knowledge gaps among customers played a crucial role in reducing the rate of connection to the existing sewer network. Many customers were unaware of the availability of sewers in their vicinity and did not understand the importance of sewer connection over onsite sanitation facilities.

There were significant gaps in regulation and its enforcement. The majority of customers did not want to reinstate existing fences or pavements with in their compounds for the purpose of sewer connection. Many of the customers preferred onsite sanitation facilities (septic tank and pit latrine) even though a sewer line passed in front of their homes. Here, enforcement of mandating connection to a sewer where there is one nearby could play an important role in enhancing the rate of connection.

Increasing the reliability of the water supply service would significantly boost customer confidence in the water utility's sewerage service because many of the customers surveyed were suspicious about the reliability of its service. Moreover, water supply and sewerage service (connection to a sewer) are highly interconnected.

Suitable topography has a significant effect in planning a gravity sewer system. Although the topography of Addis Ababa is suitable for a gravity sewerage system, some customer homes in

the surveyed area were found to be unsuitable for such connection.

Connection fees and wastewater discharge tariffs play an important role in planning a sewerage system. So far, no tariff had been applied for discharging wastewater into the sewerage system except for a one-time connection fee. Some surveyed customers were unwilling to pay the one-time connection fee. Different payment modalities (monthly or quarterly) need to be designed in order to ease the burden of a connection fee on customers.

Our study revealed a gap in legislation and its enforcement: there was neither a regulatory body nor regulations for monitoring wastewater management, including mandatory sewer connection.

Data availability statement

The original contributions presented in the study are included in the article/Supplementary Material, further inquiries can be directed to the corresponding author.

Author contributions

All authors listed have made a substantial, direct, and intellectual contribution to the work and approved it for publication.

Acknowledgments

I would like to acknowledge the respondents, data collectors, and all who were instrumental in the research process. And i am indebted to my supervisor SR for his continuous support and guidance throughout the study.

Conflict of interest

The author declares that the research was conducted in the absence of any commercial or financial relationships that could be construed as a potential conflict of interest.

The author SRG declared that they were an editorial board member of Frontiers, at the time of submission. This had no impact on the peer review process and the final decision.

Publisher's note

References

Beard, Victoria A. (2021). Out of sight, out of mind: Understanding the sanitation crisis in global south cities. *J. Environ. Manag.* 306 (2021), 7&11. doi:10.1016/j.jenvman.2021.114285

Cdswc (2020). *Inception Report: Consultancy service for the study, detail design, construction supervision for Kality catchment sewer line project Phase 11*. Addis Ababa, Ethiopia: CDSWC.

Chris Heymans, G. B. (2017). *Improving urban and small towns sanitation services delivery in Ethiopia: Message and lessons from cities, towns and the national policy dialogue*. Washington DC, USA: World Bank.

Christop, A. T. (2011). Sustainable sanitation in cities: A framework for action. *Sustainable sanitation alliance*. The Netherlands: Papiroz Puplishing House.

Climate-date (2021). climate-date. Retrieved January 15, 2021, from en.climate-date.org: http://www.en.climate-data.org.

Cotton, Andrew (2006). *Sanitation 21: Simple approach to complex sanitation*. London, United Kingdom: IWA.

Csa (2013). *Population projection for Ethiopia: 2007-2037*. Addis Ababa, Ethiopia: CSA.

Daniel, W. (2013). *Biostatistics: A foundation for analysis in the health science*. Hoboken, NJ, USA: WILEY.

Engida, Z. (2001). *Ground water study of Addis Ababa*. Addis Ababa, Ethiopia: Addis Ababa.

Google (2020). map-of-addis-ababa-city. Retrieved December 15, 2020, from Maps app: http://www.google.com.

Gujarati, D. (2004). "15. Qualitative model regression model," in *G. D. Basic econometrics*. 4th ed. (New York, NY, USA: McGraw-Hill), 595.

Jonathan, P., C. L. (2014). *Sanitation 21: A planning framework for improving citywide sanitation services*. London, United Kingdom: IWA.

Mce (2016). *Utility water distribution and sewerage coverage percentage for the city of Addis Ababa*. Addis Ababa, Ethiopia: MCE.

MoWIE (2017). Addis Ababa, Ethiopia: MoWIE.Urban wastewater management strategy.

Perneger, Thomas V., Courvoisier, D. S., Hudelson, P. M., and Gayet-Ageron, A. (2015). Sample size for pre-test of questionnaires. *Qual. life Res.* 24, 147–151. doi:10.1007/s11136-014-0752-2

Root, Rebecca (2020). *When are sewers the best option for improved sanitation*. Washington, D.C., USA: devex.

Scott, R. (2019). Integrating basic urban services for better sanitation outcomes. *Sustainability* 11 (6706), 2. doi:10.3390/su11236706

Sws (2013). Addis Ababa, Ethiopia: SWS.Design report: Design of sewer lines for the selected for the selected areas of Kality catchment.

Un-Habitat (2008). *Ethiopia: Addis Ababa urban profile*. Nairobi, Ethiopia: UN-Habitat.

WorldBank (2013b). *Urban sanitation review: A call for action. East asia and the pacific region*. Washington DC: the world bank.

WorldBank (2020). *Connecting the unconnected*. Washington DC, USA: WorldBank.

WorldBank (2015). *Improving on-site sanitation & connections to sewers in south east Asia: Insights from Inddonesia & Vietnam*. Washingon DC, USA: WorldBank.

WorldBank (2013a). *Urban sanitation review: South east asia and the pacific region - Indonesia, vietnam & Philippines*. WashingtonDc: TheWorld Bank.

frontiers | Frontiers in Environmental Engineering

TYPE Original Research
PUBLISHED 23 August 2023
DOI 10.3389/fenve.2023.1223247

OPEN ACCESS

EDITED BY
Christian Kennes,
University of A Coruña, Spain

REVIEWED BY
Przemysław Seruga,
Wroclaw University of Economics, Poland
Yuanzhi Tang,
Georgia Institute of Technology,
United States

*CORRESPONDENCE
Vicky Shettigondahalli Ekanthalu,
vicky.ekanthalu@uni-rostock.de

†PRESENT ADDRESS
Edward Antwi,
Independent Researcher, Schmarl,
Germany

RECEIVED 15 May 2023
ACCEPTED 01 August 2023
PUBLISHED 23 August 2023

CITATION
Shettigondahalli Ekanthalu V, Ender T, Narra S, Antwi E, Bej S and Nelles M (2023), Acid leaching of hydrothermally carbonized sewage sludge: phosphorus recovery and hydrochar characteristics. *Front. Environ. Eng.* 2:1223247. doi: 10.3389/fenve.2023.1223247

Acid leaching of hydrothermally carbonized sewage sludge: phosphorus recovery and hydrochar characteristics

Vicky Shettigondahalli Ekanthalu[1]*, Tommy Ender[1], Satyanarayana Narra[1,2], Edward Antwi[1†], Saptarshi Bej[3] and Michael Nelles[1,2]

[1]Department of Waste and Resource Management, Faculty of Agricultural and Environmental Sciences, University of Rostock, Rostock, Germany, [2]Deutsches Biomasseforschungszentrum (DBFZ), Leipzig, Germany, [3]School of Data Science, Indian Institute of Science Education and Research, Thiruvananthapuram, India

The options for managing sewage sludge and its utilization as fertilizer are becoming progressively limited as a result of stringent environmental regulations imposed by the European Union over the past 10 years. The limitation of moisture present in sewage sludge that affects conventional treatment options like incineration can be obviated by using the hydrothermal carbonization (HTC) process. This research investigates the acid leaching of hydrochar produced by hydrothermally carbonizing sewage sludge. The objective is to investigate and compare the effects of formic acid (HCOOH), sulfuric acid (H_2SO_4), and acetic acid (CH_3COOH) at varying pH levels on total phosphorus (TP) mobilization and hydrochar properties. The impact of independent parameters such as carbonization temperature of hydrochar, acid type, acid concentration, and acid leaching retention time on the TP mobilization, chemical oxygen demand (COD) of the leachate, and the fuel characteristic of the hydrochar was explored. A quadratic and cubic model was proposed to correlate the effects of independent parameters on TP and ortho-P mobilization, acid need, COD of leachate, and fuel characteristics of hydrochar using Design of Experiments and Response Surface Modeling. This approach was chosen in order to maximize the amount of data from a constrained number of experimental trials. The outcome of the study indicated a fractional amount of H_2SO_4 was enough to reach and maintain the lower pH in hydrochar slurry compared to HCOOH and CH_3COOH. TP mobilization from solid to liquid is highly favorable in the presence of H_2SO_4 at lower pH compared to HCOOH and CH_3COOH under similar reaction conditions. In addition, it was discovered that lowering the pH using HCOOH and H_2SO_4 to acid-leach the hydrochar boosted the caloric value of the hydrochar. However, CH_3COOH has a contradictory effect.

KEYWORDS

hydrothermal carbonization, response surface model, design of experiments, regression model, sewage sludge treatment, phosphorus recovery, pKa, organic and inorganic acids

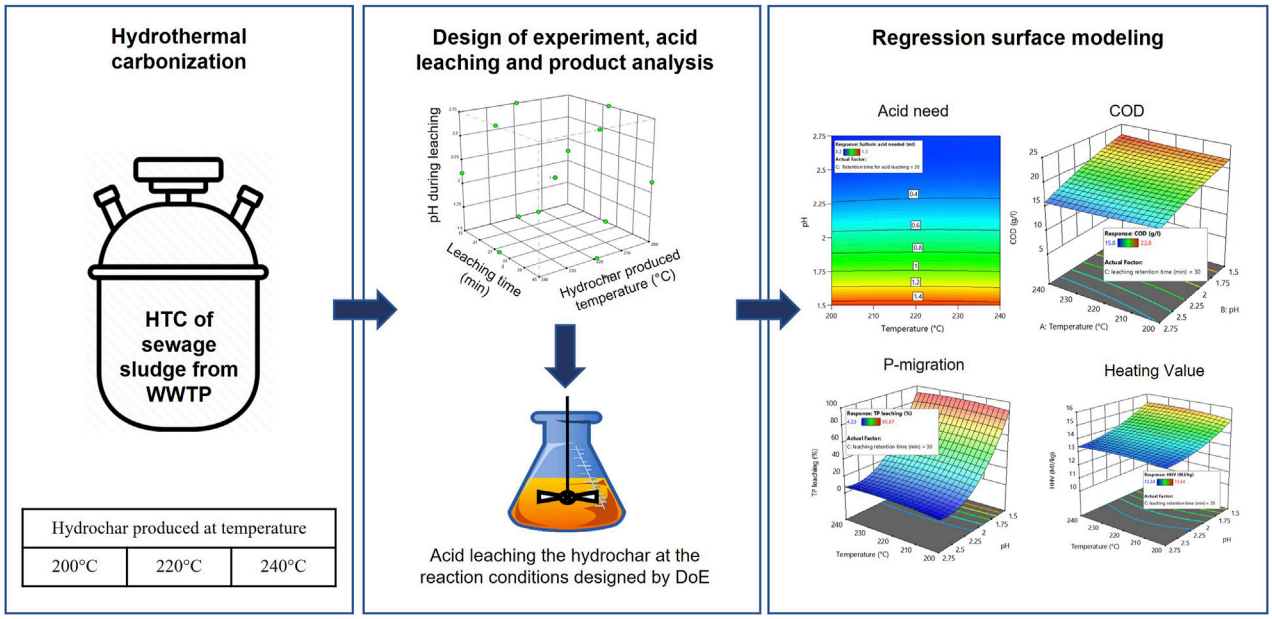

GRAPHICAL ABSTRACT

1 Introduction

Phosphorus (P) is a critical element whose availability is vital for meeting agricultural and industrial demands across the world. In recent years, global phosphate demand has steadily increased due to the accelerated growth of the economy (Cieślik and Piotr Konieczka, 2017). However, the global phosphate mineral resource is non-renewable, limited to a few countries, and projected to be exhausted in 50–100 years (Poirier et al., 2022). As a result, there is an urgent need for the efficient management and recycling of phosphorus-rich by-products in order to meet future global demands. Recovering P from sewage sludge produced in a wastewater treatment plant (WWTP) is one such potential approach. Municipal WWTPs often convert phosphate from wastewater into sludge, making sewage sludge the most popular by-product with a substantial source of P. Recent estimates indicate that the quantity of industrial and domestic wastewater generated annually on a global scale is in the order of billions of tons and is anticipated to increase due to population growth and rising standards of living (Bora et al., 2019). The production of sewage sludge in Europe (EU27) is estimated to be approximately 10 million tonnes of dry matter (DM) annually (Domini et al., 2022). Germany alone has produced 1.72 million tonnes of sewage sludge DM in 2022, which demonstrates the potential of sewage sludge as an alternative source of P (Statistisches Bundesamt Destatis, 2022). Most WWTPs treat phosphorus-containing wastewater with enhanced biological phosphorus removal or chemical precipitation, which transfers >90% of the phosphorus from the unprocessed wastewater to the sewage sludge (Liang et al., 2019). The primary utilization pathway for sewage sludge includes thermal disposal in mono- and co-incineration facilities, recycling in agriculture, recycling in landscaping, and recycling of other materials through humification and composting. The management of sewage sludge varies significantly among EU Member States. In Spain, Ireland, Finland, Hungary, and Cyprus, land-based utilization or composting is the most popular method, whereas the Netherlands, Belgium, Germany, and Austria mostly employ incineration (Domini et al., 2022). The availability of agricultural areas and local regulations are the key factors affecting the decision to recover or dispose of sludge. The direct use of sewage sludge for agricultural purposes is, however, restricted in many countries due to the presence of harmful substances such as heavy metals, organic residues, microplastics, and various pathogens. The sustainable management of sewage sludge is a global concern due to its potential for negative environmental effects. Nevertheless, the organic matter and nutrients present in sewage sludge have the potential to be used to produce renewable energy and are essential for the production of fertilizers.

The German Sewage Sludge Ordinance (AbfKlärV) is a particular regulation under German waste law that specifies the application and utilization of sewage sludge (AbfKlärV, 2017). The new rule set by the German sewage sludge ordinance restricts the direct use of sewage sludge in agriculture and also mandates the recovery of phosphorus from sewage sludge in Germany (AbfKlärV, 2017). Following the 1999 ban on landfilling in the European Union (EU), incineration has become the preferred waste disposal method in the EU-15 (Raheem et al., 2018). In 2022, 1.3 million tonnes DM (approximately 77% of the total generated sewage sludge) have been thermally recycled (mono-incineration, co-incineration, and other thermal disposals), and the trend of sewage sludge being managed by land-based utilization/landscaping is decreasing (Statistisches Bundesamt Destatis, 2022). Although thermal treatment of sewage sludge is generally accepted, the most significant drawback of incineration is the high energy requirements of thermal dewatering (Werther and Ogada, 1991). In this regard, hydrothermal carbonization (HTC) has received increased attention

as an environmentally acceptable and viable approach for treating sewage sludge without dewatering it. The HTC process uses the excess moisture in sewage sludge as a catalyst and converts the sewage sludge into a carbonaceous product at reaction temperatures ranging from 180°C to 260°C at 0.5–24 h retention time and at elevated autogenous pressures (Jellali et al., 2022).

In recent years, there has been considerable interest in the investigation of HTC as a potential treatment option for sewage sludge, as well as studies examining the P transformation during and after HTC. Several studies reported the distribution and transformation of P during HTC of sewage sludge (Wang et al., 2017; Ovsyannikova et al., 2019; Shi et al., 2019), acid leaching of sewage sludge and hydrochar using 2.5 M acid solutions of H_2SO_4 and HCl (Pérez, Boily, and Jansson, et al., 2021), the influence of organic acid (citrate and oxalate) leaching on the P transformation from sewage sludge hydrochar (Pérez, Boily, and Skoglund, et al., 2022), migration and transformation of phosphorus during hydrothermal carbonization of sewage sludge (Zheng et al., 2020b), and phosphorus recovery from sewage sludge incineration ash (Liang et al., 2019). Numerous previous studies have demonstrated that a significant amount of P from sewage sludge is retained in the hydrochar after HTC (Heilmann and Valentas, 2014; Wang et al., 2017; Wang et al., 2019). The previously published results indicate that 97.7%–98.7% of total P (TP) is retained in the resulting hydrochar after HTC treatment of sewage sludge (Shettigondahalli Ekanthalu et al., 2021). Variation in pH has a major effect on the transformation of P from the solid to the liquid phase, and the alteration of pH after HTC was found to be highly efficient (Shettigondahalli Ekanthalu et al., 2022). Prior research has examined the independent effects of organic and inorganic acids on the acid leaching of sewage sludge hydrochar. The effect of acid leaching of sewage sludge hydrochar utilizing organic and inorganic acids under varying conditions of acid strength and time has not been investigated yet, to the authors' knowledge.

This study focuses on acid leaching the sewage sludge hydrochar with formic acid (HCOOH), sulfuric acid (H_2SO_4), and acetic acid (CH_3COOH) at varying pH to determine the effects on P mobilization, hydrochar characteristics, and leachate characteristics. In addition to comprehending the impact of pH on P leaching, the purpose of this study is to investigate what other acid properties influence P leaching from solids to liquids. A Design of Experiments (DoE)/Response Surface Model (RSM) method facilitates the investigation of the selected reaction conditions within a defined reaction space. The DoE/RSM has been widely used in HTC (Mäkelä et al., 2015; Mäkelä et al., 2016; Román et al., 2018), for sewage sludge dewatering (Danso-Boateng et al., 2015; Lühmann and Wirth, 2020), optimization of hydrochar production (Zheng et al., 2020a; Guo et al., 2021; Akbari et al., 2022), and the influence of pH on P release and transformation in hydrothermally carbonized sewage sludge (Lühmann and Wirth, 2020). To date, acid-leaching hydrochar process parameters such as acid usage and the role of pH in P transformation, as well as hydrochar characteristics, have only been studied separately with particular acid utilization. The DoE/RSM methodology employed in this study seeks to comprehend the impacts of various acids and their interactions with hydrochar on the characteristics of hydrochar and leachate, with a specific emphasis on P mobilization. The results of this study offer an in-depth overview of the impact of pH and acid characteristics on the leaching of phosphorus from the solid to liquid phase as well as the properties of hydrochar.

2 Materials and methods

2.1 Materials

The digested and mechanically dewatered sewage sludge used in this investigation was directly obtained from Nordwasser GmbH in Rostock, Germany. The primary wastewater treatment facility in Rostock can handle the wastewater from 320,000 inhabitants and treats both industrial (1/3) and municipal (2/3) wastewater (UBC Sustainable Cities Commission, 2017). This WWTP produced 4,482 tonnes of dry sewage sludge per year on average between the years of 2014 and 2018, and all of the generated sewage sludge is currently incinerated (Tränckner, 2023). Sewage sludge was only sampled once during the treatment plant's steady operation state to ensure consistency of results throughout the investigation. The sewage sludge sample was collected in a sealed sample container and immediately transferred to the laboratory, where it was refrigerated at 4°C until it was used for HTC. The dry matter content of the sewage sludge was 22.0% dry matter content (DM), and the ash content was 7.4% (at 815°C in % original substance). The refrigerated sewage sludge samples were allowed to warm to room temperature before HTC.

A LECO Thermogravimetric Analyzer (TGA) unit TGA701 was used to evaluate the moisture content, volatile organic compound, fixed carbon (FC), and ash content of sewage sludge. The final analysis was carried out using an organic element analyzer in accordance with EN ISO 16948, 2015 (EN ISO 16948 2015). The caloric value of the sample material was evaluated using a Parr 6400 calorimeter (Parr Instruments Inc., United States) in accordance with EN 14918, 2010 (EN 14918 2010). The total phosphate content of the sewage sludge was determined in an external laboratory using EN ISO 11885, 2009 (EN ISO 11885 2009).

Acid-leaching of hydrochar is facilitated using either formic acid 98% pure, sulfuric acid 72%, or acetic acid 100% (all the acid reagents were obtained from AppliChem GmbH, Darmstadt). The amount of acid required to attain the targeted pH was determined by following the methodology of DIN EN 15933:2012 (Deutsches Institut für Normung, 2012).

2.2 Experimental method

An overview of the experimental methodology is provided in Figure 1. The experimental methodology was planned in four stages: stage 1: HTC of sewage sludge, stage 2: DoE using Stat-Ease Design-Expert Software (Version 22.0.0), stage 3: acid leaching of hydrochar, and Stage 4: product recovery, experimental analysis, and regression surface modeling.

2.2.1 Hydrothermal carbonization of sewage sludge

A Parr 4523 reactor (Parr Instrument GmbH, Zeilweg 15, 60439 Frankfurt, Germany) was used to hydrothermally

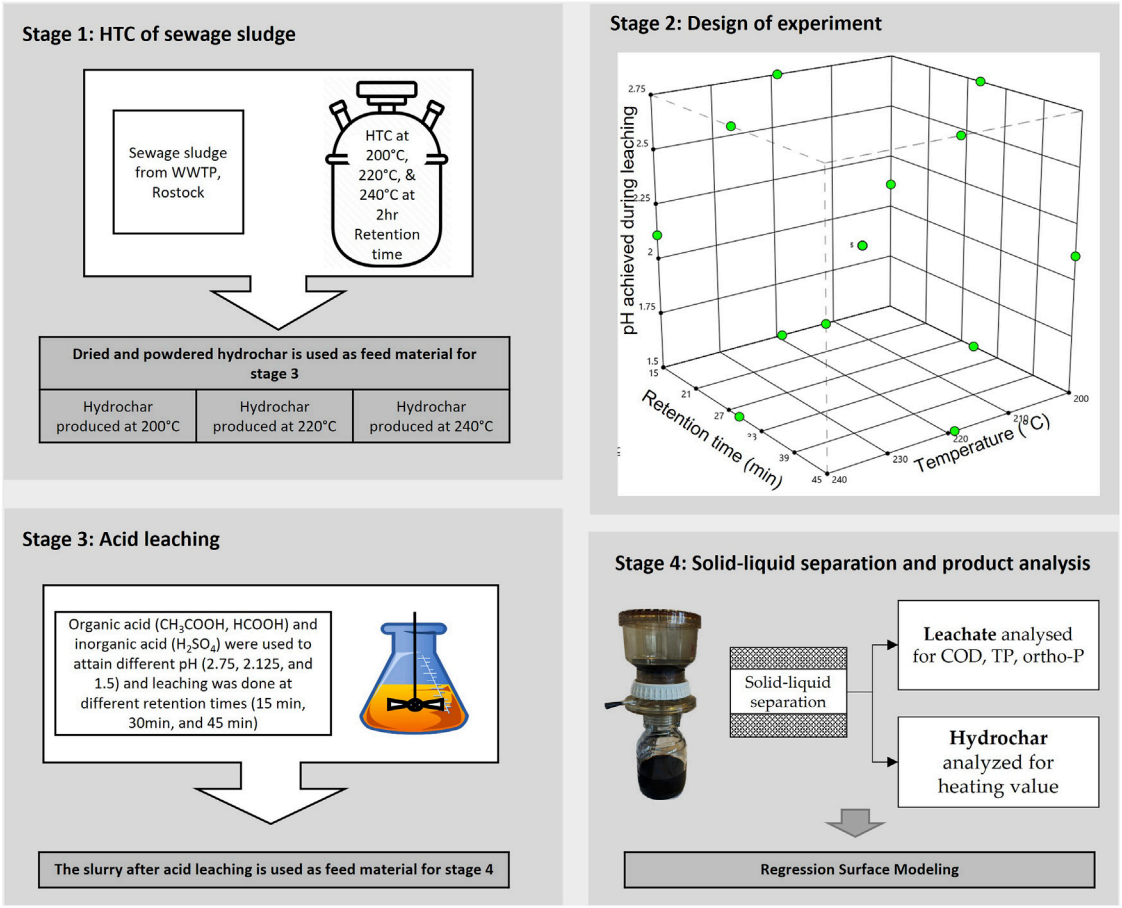

FIGURE 1
Overview of the experimental methodology.

carbonize sewage sludge. The reactor operates at autogenic pressure and is equipped with a 1-L reaction vessel that can tolerate a maximum pressure of 138 bar. The heat for the reactor is provided by a 2 kW heating coil, and the stirring is facilitated by a stirring unit with a connected drive. The pressure and temperature sensors of the reactor are controlled and monitored using a Parr 4848 PID controller unit.

To understand the influence of HTC temperature on the acid leaching of consequently produced hydrochar, HTC was carried out at temperatures of 200°C, 220°C, and 240°C and a retention time of 2 h while continuously stirring the substrate at 150 rpm. Before beginning HTC, certain volumes of sewage sludge and distilled water were combined within the reactor and mixed to generate a homogenous slurry of 10% DM, and the initial pH was noted using a pH meter (WTW pH 3310, Xylem Analytics Germany Sales GmbH). The HTC of sewage sludge slurry was carried out at an autogenic pressure with a continuous heating rate of 4 K/min. Following HTC, the reactor vessel was left to cool to room temperature, and the final pH was recorded. Following the top-feeding method, solids and liquids were separated from the HTC slurry in a Büchner funnel. The hydrochar produced at three different temperatures was oven-dried at 105°C for 24 h. The dried hydrochar was collected separately (according to the temperature at which it was produced), crushed to produce fine powder, and stored in an airtight container at room temperature until used.

2.2.2 Design of experiments

The Design-Expert program from Stat-Ease, Inc., was used to design the experiments, perform regression analysis, and model the response surface. The experiments were designed to reveal the interactions of three independent variables with the targeted responses. The three independent variables selected include the following process conditions: 1) the carbonization temperature at which the hydrochar was produced: 200°C, 220°C, and 240°C, 2) pH during the acid leaching process: 1.5, 2.125, and 2.75, and 3) acid leaching time: 15 min, 30 min, and 45 min. Using Box–Behnken design, three replications at the central points and one point in the middle of each edge of the cubical surface were employed, resulting in 15 experimental runs for every acid used. The product of each experimental run was recovered and experimentally analyzed to generate six different targeted responses. The following responses were considered in this study: TP in leachate, ortho-P in leachate, COD of leachate, acid needed, %TP leached, and higher heating value (HHV) of hydrochar. Figure 1 (stage 2) is a graphical representation of the

experimental design space, and Supplementary Material S1 includes the randomized experimental design.

2.2.3 Acid leaching process

In the experimental design described in Figure 1, three different acids were used to achieve the targeted pH, and the effects of different acids (HCOOH, H_2SO_4, and CH_3COOH) on the TP-transformation, ortho-P transformation, COD, acid need, and HHV of hydrochar were experimentally analyzed. The experimentally analyzed results of the defined responses were fitted into the RSM model to generate respective 3D-surface models. During the acid-leaching process, the amount of acid required to attain the targeted pH was determined following the methodology of DIN EN 15933:2012 (Deutsches Institut für Normung, 2012). The standard DIN EN 1593:2012 specifies a method for determining the pH in suspension of sludge within the pH range of 2–12. However, to maintain uniformity in the experimental procedure, the same standards were used to determine and achieve a pH of 1.5.

A measure of 5 g of hydrochar (produced at 200°C, 220°C, and 240°C) was mixed with 45 mL of deionized water, and a homogeneous slurry was prepared by mixing the content for 15 min on a magnetic stirrer at 250 rpm. After preparing the homogeneous slurry, concentrated acids (one each of HCOOH, H_2SO_4, or CH_3COOH) were slowly titrated against the slurry whilst constantly stirring the content until the desired pH was attained and held constant for 15 min. Later, the pH was held constant for 15 min, 30 min, and 45 min to facilitate the acid leaching of the hydrochar.

2.2.4 Product recovery experimental analysis and regression modeling

2.2.4.1 Product recovery experimental analysis

The hydrochar slurry produced after the acid leaching was sent directly to the polysulfone bottletop vacuum filter for the separation of solids and liquids. The following process conditions were maintained during the solid–liquid separation of the hydrochar slurry: 1) the entire content of the hydrochar slurry after acid-leaching was poured into the polysulfone bottletop vacuum filter and 2) the vacuum pump was turned on to create sufficient vacuum pressure for separating solids and liquids. After the filtering, the liquid was collected in a volumetric flask and kept at 4°C until it was tested for TP, ortho-P, and COD. Similarly, the resulting solids (hydrochar) were oven-dried at 105°C for 24 h before being kept in sealed containers for further examination.

Following the procedure outlined in EN 15170, 2010, the caloric value of the hydrochar was analyzed using a Parr 6400 calorimeter in a manner identical to that of sewage sludge. Liquid (leachate) was analyzed spectrophotometrically for TP and ortho-P using the NANOCOLOR ortho- and total-Phosphate tube test kits in accordance with DIN EN ISO 6878-D11. Lastly, following the standards specified in DIN ISO 15705, the COD of the leachate was analyzed using a NANOCOLOR COD 1500 tube test kit. All the spectrophotometric testing kits were obtained from MACHEREY-NAGEL GmbH & Co. KG, Germany. The studied findings were obtained in triplicate, and the mean value is presented.

2.2.4.2 Regression modeling

The DoE/RSM approach was chosen to understand the interaction between selected independent variables and their resulting responses. A DoE/RSM strategy was used in order to maximize the amount of data from a constrained number of experimental trials (Lühmann and Wirth, 2020). The DoE was designed with a Box–Behnken design of RSM methodology using Design-Expert software. Box–Behnken design is an approach that uses the minimum square technique to fit the model and defines the interactions of parameters and their influence on responses (Akbari et al., 2022).

The regression modeling was performed as described by Montgomery (2013), and the interactions between the selected variables and the resulting responses were modeled using quadratic Eq. 1 and cubic Eq. 2.

$$y = \beta_0 + \sum_{i=1}^{n} \beta_i x_i + \sum_{1 \le i \le j \le n}^{n} \beta_{ij} x_i x_j + e \quad (1)$$

$$y = \beta_0 + \sum_{i=1}^{n} \beta_i x_i + \sum_{1 \le i \le j \le n}^{n} \beta_{ij} x_i x_j + \sum_{1 \le i \le j \le k \le n}^{n} \beta_{ijk} x_i x_j x_k + e \quad (2)$$

where y denotes the predicted response, β_0 represents the constant coefficient, β_i $(1 \le i \le n)$ is the coefficient of the linear term, β_{ij} $(1 \le i \le j \le n)$ represent the coefficients of the quadratic terms (Eq. 1), and β_{ijk} $(1 \le i \le j \le k \le n)$ represents the coefficients of the cubic terms (Eq. 2). x_i, x_j, and x_k are the coded values of the independent variables in the regression function, and e is the vector for random error.

A specific model was chosen for every particular response to reduce the lack of fit value in relation to the pure error. For the quadratic and cubic models, the respective lack of fit values were analyzed with respect to the pure error. A non-significant lack of fit value (p-value greater than 0.05) indicates good predictive generalizability of the regression model. In some cases, reduced versions of the original quadratic and cubic models were used to ensure that the lack of fit value was non-significant. This ensures that the potential for overfitting of simpler or reduced versions of the original models decreases by improving their overall predictive reliability on an unseen data space. Table 1 and Supplementary Material S2 illustrate the specifications of the quadratic and cubic regression models that were obtained in the current study.

3 Results and discussion

3.1 Characteristics of sewage sludge and consequently produced hydrochar

The results of the initial and final analysis of sewage sludge are shown in Table 2. The sewage sludge used in this study had a moisture content of 78.00% and a total solid content of 22.00%. The initial analysis depicted that the sewage sludge had an ash content of 33.64% DM at 815°C and volatile solids (VS) of 65.00% DM, which was consistent with the previous investigation ranges (Peng et al., 2016; Wang et al., 2017; Shettigondahalli Ekanthalu et al., 2020). The final analysis results had a typical value for C-H-N-S-O content for

TABLE 1 Process order of every analyzed response.

Response	HCOOH	H_2SO_4	CH_3COOH
TP in leachate	Reduced quadratic	Quadratic	Reduced cubic
Ortho-P in leachate	Quadratic	Quadratic	Reduced cubic
Acid needed	Reduced quadratic	Quadratic	Quadratic
%TP in leachate	Reduced cubic	Quadratic	Reduced cubic
COD of leachate	Quadratic	Reduced cubic	Reduced cubic
Higher heating value	Quadratic	Reduced cubic	Quadratic

sewage sludge in Germany (Roskosch and Heidecke, 2018), with C: 34.70%; H: 4.90%; N: 4.80%; S: 1.60%; and O: 17.60% on a dry basis. The dry sewage sludge is known to contain a high concentration of phosphorus and moderate heating value. The TP content in the feedstock was determined to be 34.4 g/kg, accounting for 3.4% of total dry sludge, and the heating value was observed to be relatively higher, at 14.72 MJ/kg (HHV), than was observed in previous studies (Peng et al., 2016; Wang et al., 2017; Roskosch and Heidecke, 2018). The overall characteristics of the feedstock have the typical composition of sewage sludge in Germany.

3.2 RSM process optimization

Table 3 shows the analysis of variance (ANOVA) and fit statistics for the regression model. These quantities signify the reliability of the regression model based on the experimental data used to model the response surface. Fischer (F) test results and probability (p-value) can be used to gauge the regression model's effectiveness. An F-value is the ratio of two group variations used to determine the statistical significance between the means of the groups. A p-value is a statistical measurement used to validate a hypothesis against the observed data. A regression model with larger F-values and smaller p-values is more reliable. As depicted in Table 3, all the analyzed responses have p-values <0.05 and a larger F-value, indicating a greater statistical significance of the designed models.

The ANOVA of the residual data depicts unexplained variations in the response. Lack of fit refers to the situation where a statistical model fails to adequately fit the underlying data. In other words, it occurs when a regression model does not capture the relationship between the independent variables and the dependent variables. A strong lack of fit (p-value greater than 0.05) is an undesirable property because it indicates that the model does not fit the data well. It is desirable to have an insignificant lack of fit (p-value smaller than 0.05). As shown in Table 3, the lack-of-fit p-values for all the obtained responses were not significant relative to the pure error, meaning the model fits well, and the parameters have a significant effect on the output response.

The fit statistics shown in Table 3 are intended to provide the reader with an understanding of the quality of the regression model. Fit statistics include the data on R^2, predictive R^2 ($Pred.R^2$), adjusted R^2 ($Adj.R^2$), and adequate precision. R^2 measures the amount of variation around the mean explained by the model. If the model captures all variations around the mean, R^2 equals one, and if the model cannot account for any variation, R^2 equals zero. R^2 is closest to 1 when all terms are included in the model; it is possible to not include terms in the model that do not have a statistically

TABLE 2 Initial and final analysis of sewage sludge and hydrochar.

Parameter	Unit	Sewage sludge	Hydrochar produced at 200°C	Hydrochar produced at 220°C	Hydrochar produced at 240°C
Moisture content	% original sample	79.37	—	—	—
Total solids	% original sample	20.63	100	100	100
Volatile solids	% dry basis	65.00	45.63	44.53	42.32
Ash	% dry basis	33.64	47.25	48.35	50.23
Fixed carbon	% dry basis	1.36	7.124	7.124	7.45
HHV	MJ/kg, dry basis	14.72	13.43 (±0.11)	13.72 (±0.04)	13.95 (±0.35)
Nitrogen	% dry basis	4.71	3.05	2.89	2.66
Carbon	% dry basis	31.8	30.30	30.40	30.60
Sulfur	% dry basis	1.66	1.68	1.80	1.95
Hydrogen	% dry basis	4.81	3.94	3.91	3.84
Total phosphorus	mg/kg dry basis	34,200.0	50,300.00	50,800.00	53,900.00
Total phosphorus	% dry basis	3.42	5.03	5.08	5.39

HHV, higher heating value.

TABLE 3 Analysis of variance (ANOVA) fit statistics of modeled responses.

Response	ANOVA			Fit statistics			
	Model		Residual				
	F-value	*p*-value	Lack-of-fit *p*-value	R^2	R^2adj	R^2pred	Adeq precision
HCOOH							
TP in leachate	232.10	<0.0001	0.06	0.9968	0.9925	0.9678	43.11
Ortho-P in leachate	269.69	<0.0001	0.63	0.9979	0.9942	0.9807	46.94
Acid needed	191.45	<0.0001	0.05	0.9961	0.9909	0.9615	37.02
%TP in leachate	1398.19	<0.0001	0.07	0.9992	0.9991	0.9701	68.07
COD of leachate	22.64	0.0016	0.34	0.9760	0.9329	0.7110	14.48
HHV of hydrochar	50.31	0.0002	0.74	0.9891	0.9694	0.9140	22.07
H_2SO_4							
TP in leachate	486.85	<0.0001	0.87	0.9989	0.9968	0.9936	55.12
Ortho-P in leachate	352.53	<0.0001	0.08	0.9984	0.9956	0.9760	50.48
Acid needed	42.82	0.0003	0.23	0.9872	0.9641	0.8229	16.15
%TP in leachate	515.76	<0.0001	0.91	0.9989	0.9970	0.9946	54.64
COD of leachate	66.08	0.0027	0.07	0.9959	0.9808	-	27.69
HHV of hydrochar	212.86	0.0005	0.92	0.9987	0.9940	-	41.37
CH_3COOH							
TP in leachate	146.86	<0.0001	0.11	0.9962	0.9894	0.9288	39.77
Ortho-P in leachate	63.33	0.0001	0.08	0.9913	0.9757	0.8331	22.51
Acid needed	3491.70	<0.0001	0.31	0.9998	0.9996	0.9979	157.09
%TP in leachate	40.75	0.0001	0.06	0.9866	0.9623	0.7427	22.24
COD of leachate	4.10	0.0353	0.54	0.7545	0.5704	0.3200	6.18
HHV of hydrochar	25.38	0.0012	0.48	0.9786	0.9400	0.7621	15.25

significant effect (Lühmann and Wirth, 2020). $Adj.R^2$ is the measure of the amount of variation around the mean explained by the model. The $Adj.R^2$ decreases as the number of terms in the model increases if those additional terms do not add value to the model. $Pred.R^2$ measures the number of variations in new data explained by the model. The $Adj.R^2$ and $Pred.R^2$ should be within approximately 0.20 of each other to be in "reasonable agreement." If they are not, there may be a problem with either the data or the model (Stat-Ease, Inc., 2022). In this study, $Pred.R^2$ was in reasonable agreement with the $Adj.R^2$ value in majority of cases; this, in turn, depicts the reliability of the model (see Table 3).

Adequate precision is a measure of the range in predicted response relative to its associated error; in other words, it is a signal-to-noise ratio. A ratio greater than four is desirable (Stat-Ease, 2022). All the obtained adequate precision values in this study were >4, confirming an adequate signal and the possibility of using the model to navigate the design space with greater reliability.

3.3 Acid requirement in achieving the targeted pH

Figure 2 displays the response surface plot of the amount of acid required to achieve and maintain the desired pH in the hydrochar slurry for 30 min of acid leaching. The demand for acid was unaffected by a 15-min change in leaching time either way (See Supplementary Figure S3). In comparison to organic acids, using inorganic acid required less acid to achieve and maintain the desired pH. Among the organic acids, acetic acid required ~seven-fold more acid than formic acid to achieve a similar pH. For instance, ~1.5 mL of H_2SO_4 (72% sulfuric acid) is required to achieve and maintain the pH of 1.5 in a 50 g hydrochar slurry of 10% dry matter with an initial pH of ~5.73 (+/− 0.2); ~15 mL of formic acid (98% formic acid) is required to achieve the same conditions, and the acid requirement for acetic acid (100% acetic acid) increases significantly to ~100 mL. Several parameters influence the target of achieving and maintaining a lower pH during acid leaching of hydrochar. The primary influencing parameter is the type of acid; acid strength and other

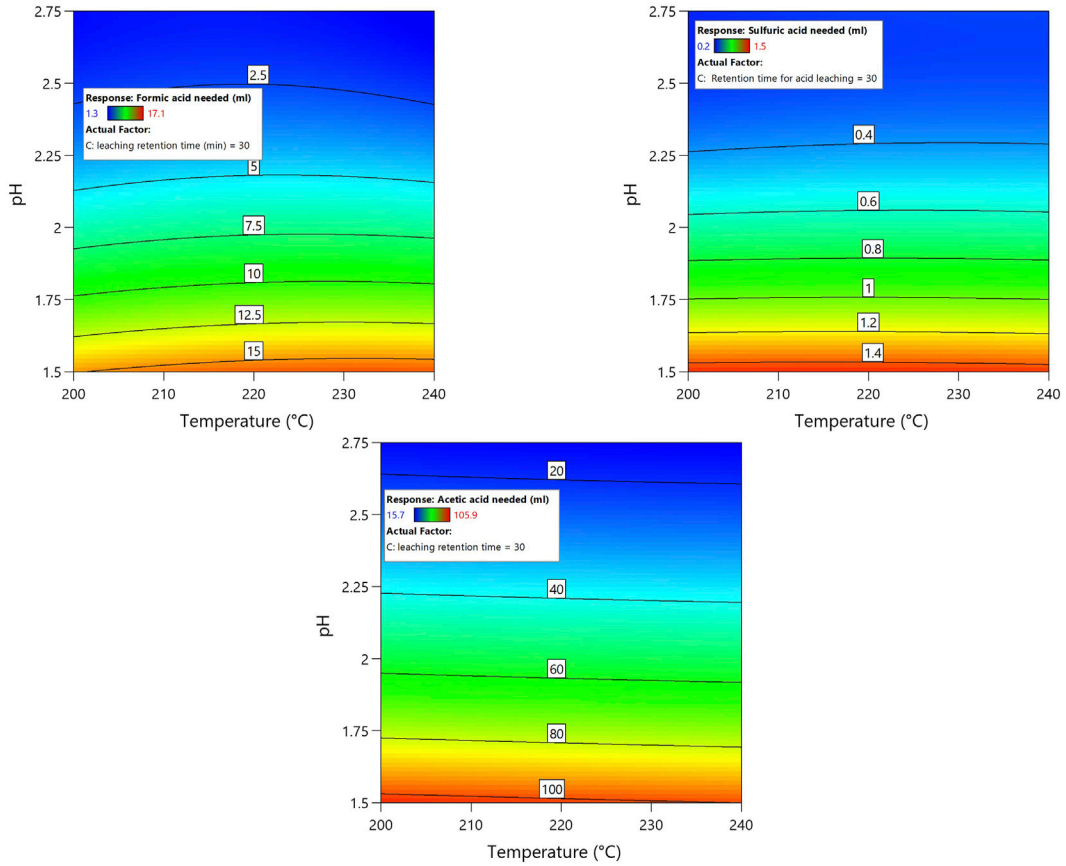

FIGURE 2
Regression model contour plot depicting the influence of acids on reaching the targeted pH.

parameters include the HTC process and diverse chemical reaction that occurs within the process.

It was seen in the experimental analysis that H_2SO_4 needed a fractional amount of acid compared to CH_3COOH and HCOOH to reach and maintain the lower pH. Similarly, HCOOH also needed less acid than CH_3COOH. This phenomenon can be explained using the strength of the acid. One approach for describing the strength of any acid is its pKa value. The negative log of the Ka value, also known as the acid dissociation constant, is the pKa value (Helmenstine, 2020). A stronger acid is indicated by a lower pKa value, and the lower pKa value indicates that the acid can be fully dissociated in water (Helmenstine, 2020). Of the different acids used in this investigation, H_2SO_4 is the strongest acid with a pKa value of −3.0, indicating the presence of highly acidic components that can readily donate protons in water (Stumm and Morgan, 1981). Formic acid, a simple carboxylic acid with a pKa value of 3.75, is a weaker acid than H_2SO_4. However, formic acid is relatively stronger than acetic acid, which has a higher pKa value of 4.7 (Stumm and Morgan, 1981). Hence, H_2SO_4, with its lower pKa value, needs only a fraction of the amount of acid required to achieve and maintain lower pH in hydrochar slurry compared to the amount needed for CH_3COOH and HCOOH with their higher pKa values.

When half of the acid has dissociated, pKa and pH are equal. When the pKa and pH values are close, the buffering capacity of a species, or its ability to maintain the pH of a solution, is greatest. Therefore, the optimal choice for a buffer is one with a pKa value close to the desired pH of the chemical solution (Helmenstine, 2020). In the hydrolysis phase of the HTC process, volatile fatty acids (VFAs) are created, which results in the production of organic acid molecules and contributes to acidification (Danso-Boateng et al., 2015; Woriescheck, 2019). The presence of increased VFAs after the HTC of sewage sludge could also be one parameter influencing the larger amount of an organic acid (CH_3COOH and HCOOH) required to achieve a lower pH compared to the amount of inorganic acids (H_2SO_4) required.

3.4 Effect of different acid utilization and acid leaching retention time on COD of leachate

The HTC process water is organically and inorganically contaminated, and COD is characterized as one of several organic contaminants. The organic contaminants in the process water produced by HTC usually have high levels of COD that depend upon the HTC process conditions and input materials (Woriescheck, 2019). During the HTC of sewage sludge, the decomposition of the organic acidic compounds and their

displacement from the solid to the liquid phase contributes to the acidification of the liquid phase and simultaneous increase in COD (Jellali et al., 2022). In general, the HTC process decreases the pH and increases the soluble COD content, particularly for the digested and dewatered sludge (Merzari et al., 2020). Several organic compounds, especially the VFAs, create a major organic load in the process water after HTC, in turn increasing the COD of the process water. VFAs are formed during the hydrolysis stage of the HTC process and produce acids such as acetic acid, propionic acid, butyric acid, valeric acid, and levulinic acid (Danso-Boateng et al., 2015). The presence of these acids in the liquid phase increases the concentration of protons or hydroxide ions, further catalyzing decarboxylation and dehydration reactions (Reza et al., 2015; Guo et al., 2021). Among VFAs, acetic acid is the main organic acid produced during HTC through the hydrolysis and dehydration of straight-chain polymers, such as cellulose and hemicellulose, or simple monomers in the presence of subcritical water (Liu et al., 2020).

Figure 3 depicts the response surface plot of the COD of the leachate obtained after acid leaching the hydrochars using different acids at different pH levels with a 30 min retention time. The influence of acid leaching retention time on COD was insignificant with varying acid leaching retention time (+/−15 min) (see Supplementary Figure S4). In general, during the acid leaching process, using organic acids (HCOOH and CH_3COOH) to achieve the targeted pH results in higher COD in the leachate compared to the use of an inorganic acid (H_2SO_4). COD was found to increase with increasing pH when H_2SO_4 and HCOOH were used for acid leaching. However, the use of CH_3COOH for acid leaching did not have a greater influence on the COD, irrespective of varying pH. Compared to the use of organic acids, the use of inorganic acids might have leached a larger amount of organic material, furfural, and 5-HMF, together with nutrients. This could explain the significantly increased COD with H_2SO_4 compared to organic acid utilization. Additionally, an increased COD can be seen with formic acid utilization as well as an increase in the acid concentration. However, there is no increase in COD with the use of acetic acid despite the increase in the pH. One reason for such phenomena could be that acetic acid is the main organic acid produced during the HTC process, and further addition of acetic acid during acid leaching processes decreases the pH but does not increase the organic load or influence the COD concentration.

3.5 Effect of different acids on P-transformation from solid to the liquid phase

Figure 4 displays the response surface plot showing the effects of the different acid types and their concentration (pH) on the transformation of TP from solid to liquid phase during an acid-leaching process. TP in the leachate was analyzed spectrophotometrically after acid hydrolysis and oxidation of the sample, and the results were used to plot the RSM plot. Figure 4 depicts the results from an acid leaching retention time of 30 min. Altering the acid leaching retention time by +/−15 min did not have a great influence on TP transformation (See Supplementary Figure S5, S6). In brief, the results show that acid leaching the hydrochar slurry using H_2SO_4 at pH 1.5 transformed approximately 90% (+/−1%) of TP from the solid to the liquid phase, whereas HCOOH and CH_3COOH transformed only approximately 36% (+/−6%) and 2.5% (+/−1%), respectively, under similar reaction conditions. The ortho-P transformation from solid to liquid also had a similar trend to that of TP and is depicted in the response surface plot of Figure 5.

Following the acid leaching of hydrochar, the highest TP transformation from solid to liquid (5,268 mg/L or 90.87%) was observed by using H_2SO_4 and acid leaching at pH 1.5. The maximum TP transformation from solid to liquid following acid leaching at pH 1.5 using HCOOH and CH_3COOH was 1,721 mg/L (42.08%) and 59.5 mg/L (3.36%), respectively. The results suggested that compared to inorganic acid (H_2SO_4), organic acids (HCOOH and CH_3COOH) with similar pH have a limited impact on transforming TP from solid to liquid, which agrees with the previous studies (Ekpo et al., 2016; Wang et al., 2017; Shettigondahalli Ekanthalu et al., 2021). In addition to the acid used and the pH, the reaction temperature at which the hydrochar was produced also had a slight influence on the TP transformation. The hydrochar generated at 240°C had an 8.7% greater TP transition from solid to liquid than the hydrochar produced by acid-leaching (H_2SO_4, pH 1.5) at 200°C. The TP transformation of HCOOH was 11.5% higher under identical reaction circumstances, while the impacts of CH_3COOH were too small to support any conclusion.

During HTC of sewage sludge, the presence of a higher concentration of multivalent metal ions, such as Al^{3+}, Ca^{2+}, Fe^{3+}, and Mg^{2+}, is responsible for forming phosphate with low solubility and, in turn, enabling the phosphate to be retained in subsequently produced hydrochar (Huang et al., 2018). The solubility of these multivalent metal ions has a significant impact on the TP mobility from a solid to a liquid during the acid-leaching procedure. Factors influencing the TP transformation from solid to liquid include the strength of the acid (Dai et al., 2017), the pH of the leaching medium (Petzet et al., 2012), and the ability of the acid to mobilize the phosphorus-holding compounds (ferric phosphate, ferrous phosphate, aluminum phosphate, calcium phosphate, and magnesium phosphate). The primary chemical reactions for the TP transformation from solid to liquid are included in the following equation.

$$AlPO_4 + 3H^+ \rightarrow Al^{3+} + H_3PO_4 \quad (3)$$

$$Fe_3(PO_4)_2 + 6H^+ \rightarrow 3Fe^{2+} + 2H_3PO_4 \quad (4)$$

$$FePO_4 + 3H^+ \rightarrow Fe^{3+} + H_3PO_4 \quad (5)$$

$$Ca_9(Al)(PO_4)_7 + 21H^+ \rightarrow 9Ca^{2+} + Al^{3+} + 7H_3PO_4 \quad (6)$$

The reactions in Eqs 3–6 are highly favorable under strongly acidic conditions and, particularly, the presence of strong acids like H_2SO_4. To facilitate the primary reactions for TP transformation, there is a requirement for greater acid concentration to overcome the buffering resistance provided by the hydrochar slurry (Shettigondahalli Ekanthalu et al., 2022). Figure 6 displays the concentration of Al^{3+} and Fe^{3+} ions in the leachate produced by acid-leaching hydrochar with HCOOH, H_2SO_4, and CH_3COOH at pH values of 1.5, 2.125, and 2.75. The use of stronger acids or acids with lower pKa values has

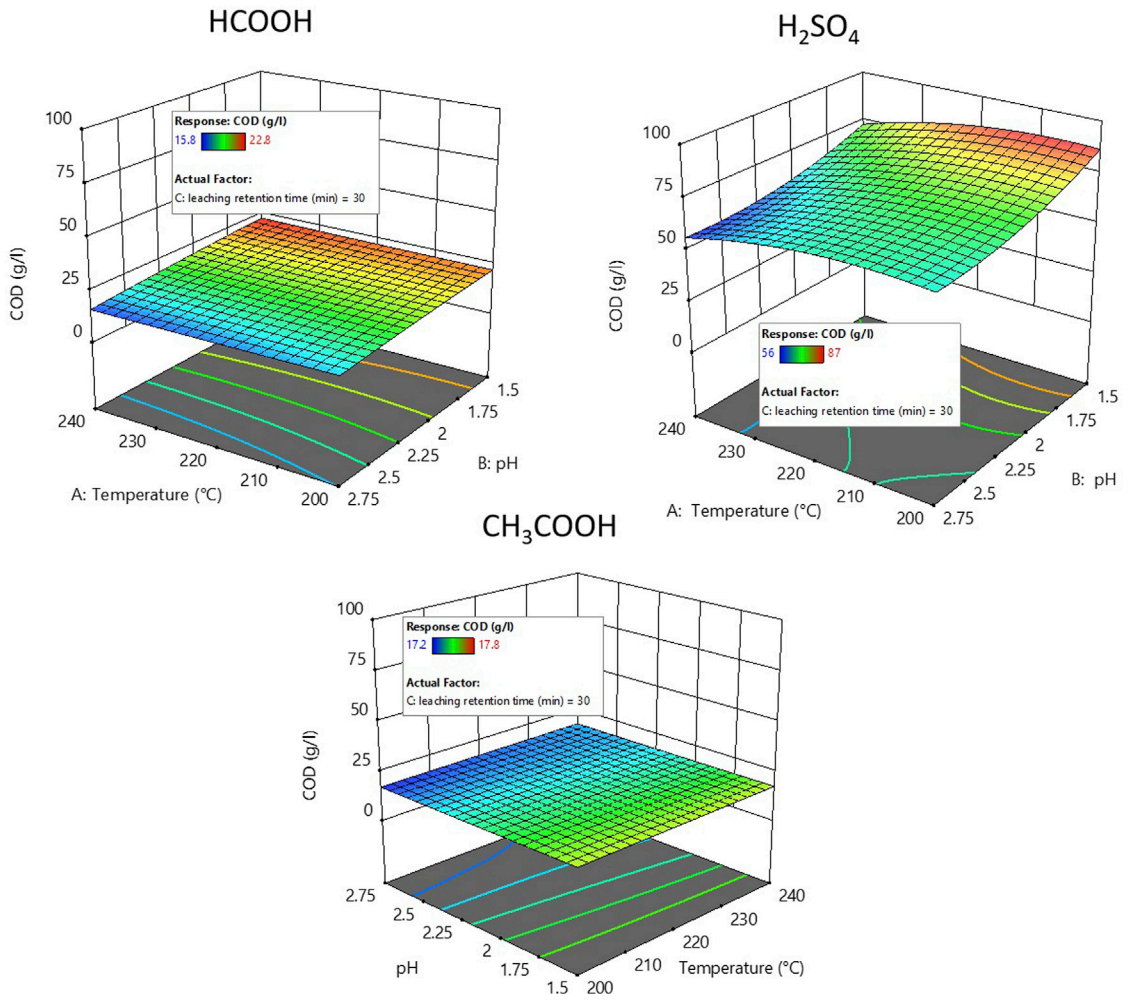

FIGURE 3
Response surface plot showing COD of the leachate produced after acid leaching using H_2SO_4, HCOOH, and CH_3COOH.

a substantially greater effect on the dissolution of Al^{3+} and Fe^{3+} ions and their corresponding P, as demonstrated by the experimental findings. Using H_2SO_4, which has a pKa value of −3.0, resulted in the greatest Al^{3+} and Fe^{3+} ion discharge, followed by HCOOH and CH_3COOH, which have pKa values of 3.75 and 4.70, respectively. The use of CH_3COOH for acid leaching has shown visibly poor dewaterability compared to H_2SO_4 and HCOOH. The hydrophilic nature of hydrochar slurry produced by the addition of CH_3COOH can also hinder the migration of phosphorus-containing compounds from solid to liquid.

With the utilization of H_2SO_4, a slight decrease in the pH of the acid-leaching medium significantly increased the TP mobilization from solids to liquid. This is because at lower acid concentrations, most of the acid present in the reaction medium is utilized to offset the buffer resistance provided by acid-consuming compounds present in the reaction medium with relatively higher neutral points; see Eqs 5, 6.

$$CaCO_3 + 2H^+ \rightarrow Ca^{2+} + H_2O + CO_2 \quad (7)$$

$$Primary\ rock\ mineral + 2H^+ + H_2O \rightarrow cations + H_4SiO_4 + Secondary\ minerals \quad (8)$$

3.6 Effects of different acid utilization on the caloric value of hydrochar produced after acid leaching

The caloric value of the hydrochar produced after acid leaching using different acids at different pH levels is illustrated in Figure 7. The illustrated Figure 7 particularly shows the caloric value of hydrochar produced at an acid leaching retention time of 30 min. Increasing or decreasing the leaching time by 15 min did not have any greater influence on the caloric value of the hydrochar produced (See Supplementary Figure S7). Treating the hydrochar with different acid-leaching conditions influenced its caloric value. Prior to acid leaching, hydrochar had a caloric value ranging between 13.43 MJ/kg and 13.95 MJ/kg, and after acid leaching, the caloric value of hydrochar ranged between

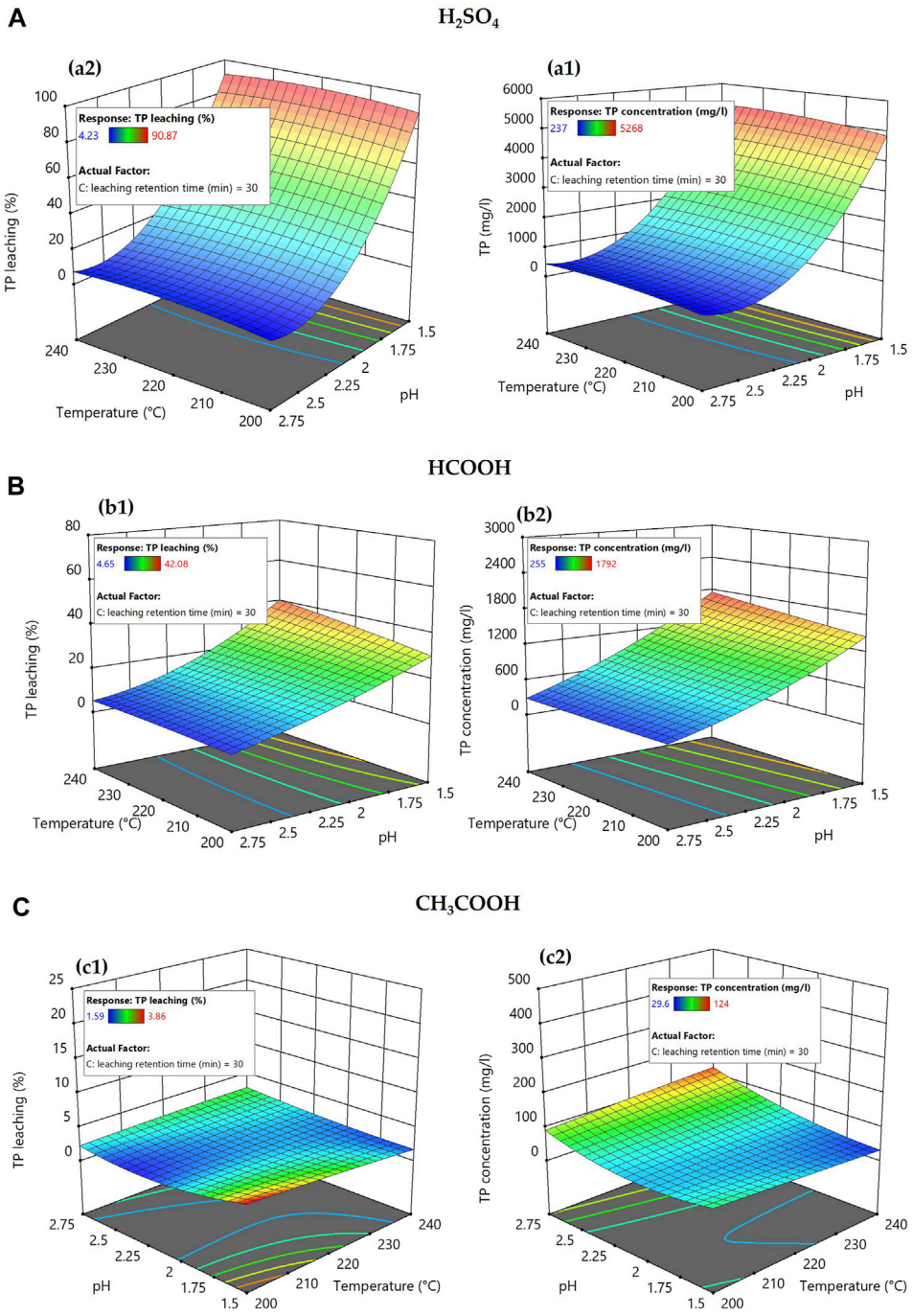

FIGURE 4
Response surface plot showing the effect of carbonization temperature of hydrochar and acid leaching pH on the transformation of TP from solid to liquid phase.

10.97 MJ/kg and 15.64 MJ/kg. The caloric value for the hydrochar after acid leaching using HCOOH and H_2SO_4 ranged between 15.64 MJ/kg and 13.43 MJ/kg and between 14.16 MJ/kg and 12.19 MJ/kg, respectively, which is comparable to the findings of other research examining the caloric value of hydrochar produced by hydrothermally carbonizing digested sewage sludge (He et al., 2013; Shettigondahalli Ekanthalu et al., 2021; Shettigondahalli Ekanthalu et al., 2022). However, the caloric value for the hydrochar after treatment with CH_3COOH was in the range of 13.49–10.97 MJ/kg, which is less than that of

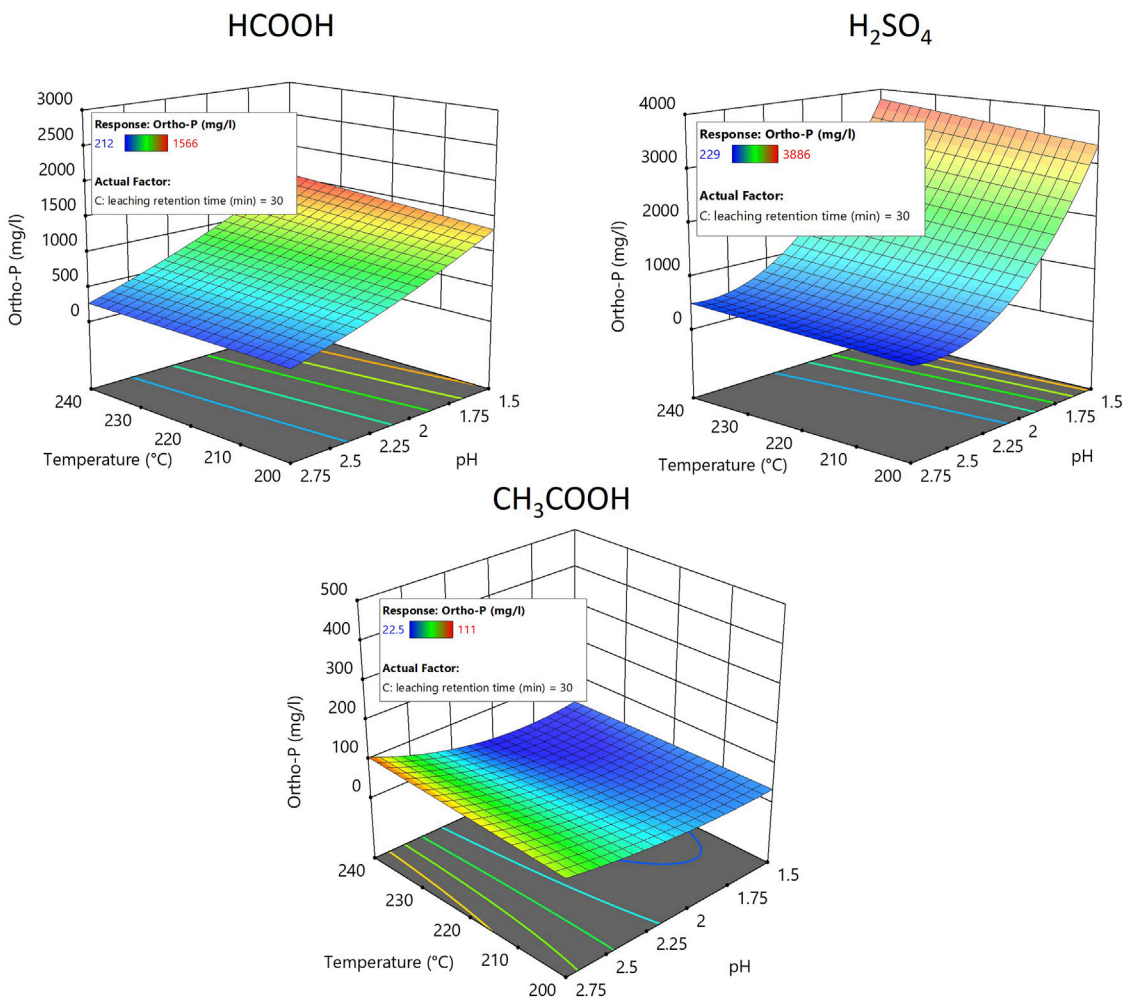

FIGURE 5
Response surface plot showing the effect of the carbonization temperature of hydrochar and acid leaching pH on the transformation of ortho-P from solid to liquid phase.

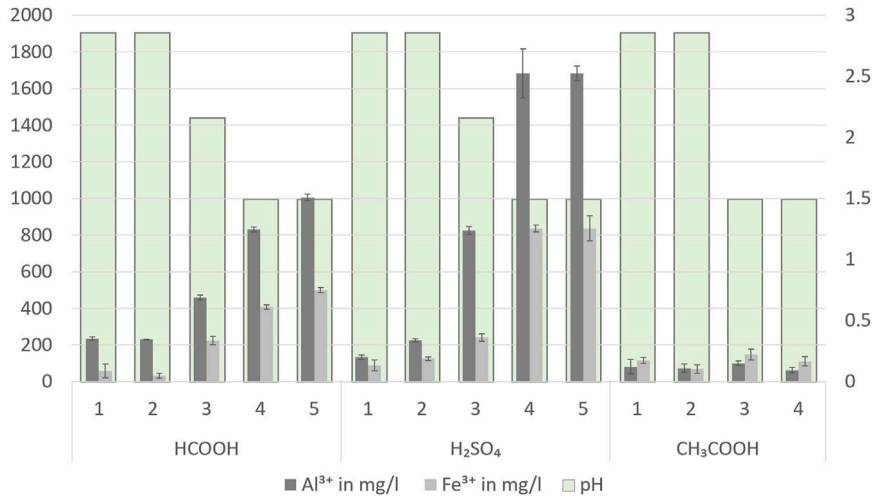

FIGURE 6
Al^{3+} and Fe^{3+} concentrations in the leachate produced after acid leaching the hydrochar.

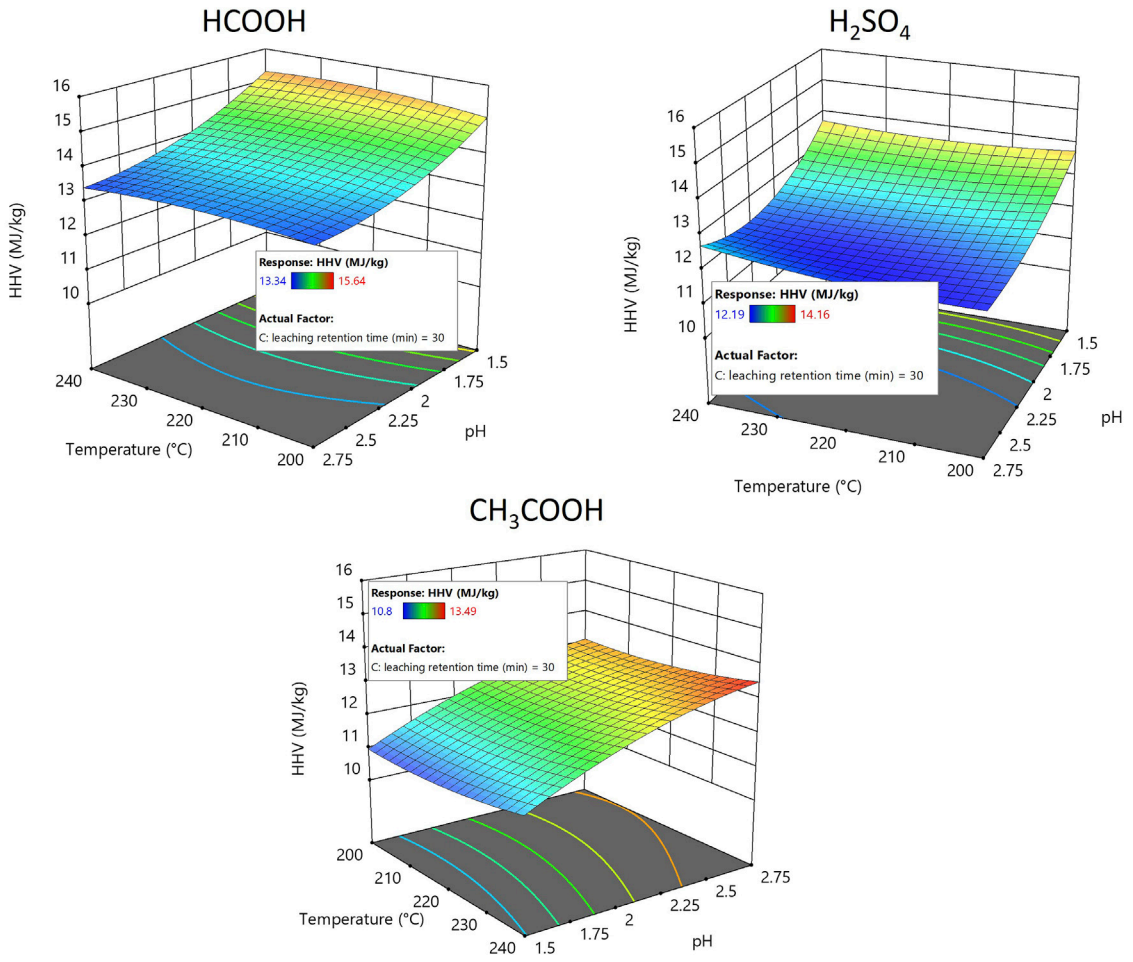

FIGURE 7
Response surface plot showing the influence of acid leaching using H_2SO_4, HCOOH, and CH_3COOH on the caloric value of hydrochar.

hydrochar treated using different acids in this study. Furthermore, it was also noticed that decreasing the pH during acid leaching using HCOOH and H_2SO_4 increased the caloric value of hydrochar. In contrast, the use of CH_3COOH for acid leaching adversely affected the caloric value of hydrochar with decreasing pH.

Several previous studies showed a strong correlation between the increase in HTC reaction temperature and the caloric value (Danso-Boateng et al., 2015); similar results were found during this research. An increase in reaction temperature increased the caloric value of the produced hydrochar (see Table 1). The heating value of the sewage sludge tends to increase after HTC due to aromatization, polymerization, and condensation reactions that occur during the HTC process (Mazumder et al., 2020).

Numerous studies have demonstrated a significant correlation between FC content and caloric value. FC is the remaining combustible material that is present after the volatile solids in the hydrochar are burnt. The caloric value of hydrochar increases with the increasing FC concentration of hydrochar (Putra et al., 2018; Anshariah and Irvan, 2020; Shettigondahalli Ekanthalu et al., 2021). Before HTC, sewage sludge typically has high VS and low FC content, but a series of reactions that occurs during HTC considerably increases both FC and the caloric value of hydrochar (Putra et al., 2018). The initial analysis and caloric value of selected hydrochar samples obtained after 30 min acid leaching time are shown in Table 4.

When H_2SO_4 was used for acid leaching, the FC value of the hydrochar was found to increase with decreasing pH. Acid leaching the hydrochar using H_2SO_4 and decreasing the pH from 2.75 to 1.5 increased the FC content of the hydrochar from 7.25% to 9.15%. A similar effect was observed when HCOOH was used for acid leaching: decreasing the pH from 2.75 to 1.5 increased the FC content of the hydrochar from 6.76% to 8.93%. In contrast, when CH_3COOH was used, decreasing pH from 2.75 to 1.5 adversely affected the FC content of hydrochar by decreasing it from 6.23% to 5.33% and decreasing the caloric value from 12.93 MJ/kg to 10.97 MJ/kg.

TABLE 4 Proximate analysis and caloric value of hydrochar samples obtained after 30 min acid leaching time.

Sample description			Proximate analysis of solids after acid leaching			HHV
Acid used	Acid leaching pH	Temperature	Volatile solids	Fixed carbon	Ash	MJ/kg
HCOOH	2.75	200	47.26	6.76	45.98	13.49 (±0.04)
	2.75	240	43.41	7.25	49.34	13.34 (±0.02)
	2.125	220	49.16	7.2	43.63	13.93 (±0.05)
	1.5	200	51.99	8.31	39.7	15.16 (±0.02)
	1.5	240	51.31	8.8	39.8	15.28 (±0.02)
H_2SO_4	2.75	200	45.49	7.25	47.26	12.2 (±0.11)
	2.75	240	41.73	8.77	49.5	12.71 (±0.2)
	2.125	220	46.69	8.24	45.07	12.36 (±0.13)
	1.5	200	51.97	9.15	38.88	13.78 (±0.02)
	1.5	240	50.69	8.93	40.38	13.74 (±0.14)
CH_3COOH	2.75	200	45.9	6.23	47.87	12.93 (±0.02)
	2.75	240	42.46	6.56	50.98	13.49 (±0.2)
	2.125	220	44.92	5.76	49.32	12.59 (±0.08)
	1.5	200	42.88	6.18	50.94	10.97 (±0.1)
	1.5	240	44.13	5.33	50.54	11.51 (±0.23)

4 Conclusion

The acid leaching of hydrothermally carbonized sewage sludge was studied to understand and compare the effects of independent parameters like carbonization temperature of hydrochar, acid type (H_2SO_4, HCOOH, and CH_3COOH), acid concentration (pH), and acid leaching retention time on the P mobilization, hydrochar properties, acid need, and COD of the leachate. The results of the study indicated that the use of acids with lower pKa values has a significantly greater impact on the solubility and mobility of phosphorus-containing compounds from solids to liquids. TP mobilization from solid to liquid is highly favorable in the presence of H_2SO_4 (~90%) at lower pH (1.5) in comparison with HCOOH (~36%) and CH_3COOH (~2.5%) at similar acid-leaching reaction conditions. It was also observed that a smaller amount of acid (H_2SO_4) with a lower pKa value is enough to achieve and maintain a lower pH in hydrochar slurry when compared to acids with a higher pKa value (CH_3COOH and HCOOH). Regarding the COD of the leachate, the use of organic acid, specifically CH_3COOH, tends to induce additional organic acidic compounds, which simultaneously contributes to an increase in COD. Concerning the energy characteristic of hydrochar, the utilization of CH_3COOH negatively impacted the FC content of hydrochar while concurrently decreasing its caloric value. In contrast, the use of H_2SO_4 and HCOOH had positive effects on the FC content and the caloric value of hydrochar. Future research should evaluate and compare the economic effectiveness of using sulfuric acid to leach sewage sludge hydrochar with sewage sludge ash in order to provide an economic viewpoint of P recovery.

Data availability statement

The original contributions presented in the study are included in the article/Supplementary Material; further inquiries can be directed to the corresponding author.

Author contributions

VS: conceptualization, methodology, writing—original draft, formal analysis, validation, visualization, and writing—review and editing. TE: writing—review and editing. SN: supervision. EA: writing—review and editing. SB: writing—review and editing. MN: supervision. All authors contributed to the article and approved the submitted version.

Funding

This publication was funded by the German Research Foundation (DFG) and the Open Access Publication Fund of the University of Rostock.

Acknowledgments

The authors would like to thank Ruth Gebauer, Jan Sprafke, Kersten Eckermann, and Annabell Reiner for their kind assistance during the preparation of this article.

Conflict of interest

The authors declare that the research was conducted in the absence of any commercial or financial relationships that could be construed as a potential conflict of interest.

Publisher's note

All claims expressed in this article are solely those of the authors and do not necessarily represent those of their affiliated organizations, or those of the publisher, the editors, and the reviewers. Any product that may be evaluated in this article, or claim that may be made by its manufacturer, is not guaranteed or endorsed by the publisher.

Supplementary material

The Supplementary Material for this article can be found online at: https://www.frontiersin.org/articles/10.3389/fenve.2023.1223247/full#supplementary-material

References

AbfKlärV (2017). Verordnung über die Verwertung von Klärschlamm, Klärschlammgemisch und Klärschlammkompost. *Rep. Ger. Sew. sludge Ord.*

Akbari, Hamed, Akbari, Hamed, Fanaei, Farzaneh, and Adibzadeh, Amir (2022). Optimization of parameters affecting the hydrothermal carbonization of wastewater treatment plant sewage sludge. *Biomass Convers. Biorefinery*. doi:10.1007/s13399-022-03427-8

Anshariah, A. M. Imran, Imran, A., Widodo, S., and Irvan, U. R. (2020). Correlation of fixed carbon content and calorific value of South Sulawesi Coal, Indonesia. *IOP Conf. Ser. Earth Environ. Sci.* 473, 012106. doi:10.1088/1755-1315/473/1/012106

Bora, Akash Pratim, Gupta, Dipanshu Prakash, and Durbha, K. S. (2020). Sewage sludge to bio-fuel: a review on the sustainable approach of transforming sewage waste to alternative fuel. *Fuel* 259 (73352), 116262. doi:10.1016/j.fuel.2019.116262

Cieślik, Bartłomiej, and Konieczka, Piotr (2017). A review of phosphorus recovery methods at various steps of wastewater treatment and sewage sludge management. The concept of "no solid waste generation" and analytical methods. *J. Clean. Prod.* 142 (4), 1728–1740. doi:10.1016/j.jclepro.2016.11.116

Dai, Lichun, Yang, Bo, Li, H., Tan, Furong, Zhu, Nengmin, Zhu, Qili, et al. (2017). A synergistic combination of nutrient reclamation from manure and resultant hydrochar upgradation by acid-supported hydrothermal carbonization. *Bioresour. Technol.* 243, 860–866. doi:10.1016/j.biortech.2017.07.016

Danso-Boateng, E., Shama, G., Wheatley, A., Martin, S., and Holdich, R. G. (2015). Hydrothermal carbonisation of sewage sludge: effect of process conditions on product characteristics and methane production. *Bioresour. Technol.* 177, 318–327. doi:10.1016/j.biortech.2014.11.096

Deutsches Institut für Normung (2012). *Sludge, treated biowaste and soil—determination of pH (EN 15933:2012)*. Berlin: Deutsches Institut für Normung.

Domini, M., Bertanza, G., Vahidzadeh, R., and Pedrazzani., R. (2022). Sewage sludge quality and management for circular economy opportunities in lombardy. *Appl. Sci.* 12, 10391. doi:10.3390/app122010391

Ekpo, U., Ross, A. B., Camargo-Valero, M. A., and Fletcher, L. A. (2016). Influence of pH on hydrothermal treatment of swine manure: impact on extraction of nitrogen and phosphorus in process water. *Bioresour. Technol.* 214, 637–644. doi:10.1016/j.biortech.2016.05.012

En 14918 (2010). *Solid biofuels - determination of calorific value*. Geneva, Switzerland: International Organization for Standardization.

En Iso 11885 (2009). *Determination of selected elements by inductively coupled plasma optical emission spectrometry (ICP-OES)*. Geneva, Switzerland: International Organization for Standardization.

En Iso 16948 (2015). *Solid biofuels — determination of total content of carbon, hydrogen and nitrogen*. Geneva, Switzerland: International Organization for Standardization.

Guo, Shuai, Xu, DanDan, Guo, Xin, Li, Xingcan, and Zhao, Chenchen (2021). Hydrothermal carbonization of sewage sludge: multi-response optimization of hydrochar production and CO2-assisted gasication performance. *Res. Square*. doi:10.21203/rs.3.rs-954940/v1

He, Chao, Giannis, Apostolos, and Wang, Jing-Yuan (2013). Conversion of sewage sludge to clean solid fuel using hydrothermal carbonization: hydrochar fuel characteristics and combustion behavior. *Appl. Energy* 111, 257–266. doi:10.1016/j.apenergy.2013.04.084

Heilmann, Steven M., Molde, J. S., Timler, J. G., Wood, B. M., Mikula, A. L., Vozhdayev, G. V., et al. (2014). Phosphorus reclamation through hydrothermal carbonization of animal manures. *Environ. Sci. Technol.* 48 (17), 10323–10329. doi:10.1021/es501872k

Helmenstine, Anne Marie (2020). pKa definition in chemistry. https://www.thoughtco.com/what-is-pka-in-chemistry-605521 (Accessed April 17, 2023).

Huang, Rixiang, Fang, Ci, Zhang, Bei, and Tang, Yuanzhi (2018). Transformations of phosphorus speciation during (Hydro)thermal treatments of animal manures. *Environ. Sci. Technol.* 52 (5), 3016–3026. doi:10.1021/acs.est.7b05203

Jellali, S., Zorpas, A. A., Alhashmi, S., and Jeguirim, M. (2022). Recent advances in hydrothermal carbonization of sewage sludge. *Energies* 15 (18), 6714. doi:10.3390/en15186714

Liang, Sha, Chen, Haoming, Zeng, Xiaohui, Li, Zhibin, Yu, Wenbo, Xiao, Keke, et al. (2019). A comparison between sulfuric acid and oxalic acid leaching with subsequent purification and precipitation for phosphorus recovery from sewage sludge incineration ash. *Water Res.* 159, 242–251. doi:10.1016/j.watres.2019.05.022

Liu, Xiangmin, Zhai, Yunbo, Li, Shanhong, Wang, Bei, Wang, Tengfei, Liu, Yali, et al. (2020). Hydrothermal carbonization of sewage sludge: effect of feed-water ph on hydrochar's physicochemical properties, organic component and thermal behavior. *J. Hazard. Mater.* 388, 122084. doi:10.1016/j.jhazmat.2020.122084

Lühmann, Taina, and Wirth, Benjamin (2020). Sewage sludge valorization via hydrothermal carbonization: optimizing dewaterability and phosphorus release. *Energies* 13 (17), 4417. doi:10.3390/en13174417

Mäkelä, M., Benavente, V., and Fullana, A. (2015). Hydrothermal carbonization of lignocellulosic biomass: effect of process conditions on hydrochar properties. *Appl. Energy* 155, 576–584. doi:10.1016/j.apenergy.2015.06.022

Mäkelä, Mikko, Benavente, Verónica, and Fullana, Andrés (2016). Hydrothermal carbonization of industrial mixed sludge from a pulp and paper mill. *Bioresour. Technol.* 200, 444–450. doi:10.1016/j.biortech.2015.10.062

Mazumder, Shanta, Saha, Pretom, and Toufiq Reza, M. (2020). Co-Hydrothermal carbonization of coal waste and food waste: fuel characteristics. *Biomass Conversion and Biorefinery*. Springer, Berlin, Germany, doi:10.1007/s13399-020-00771-5

Merzari, F., Goldfarb, J., Andreottola, G., Mimmo, T., Volpe, M., and Fiori, L. (2020). Hydrothermal carbonization as a strategy for sewage sludge management: influence of process withdrawal point on hydrochar properties. *Energies* 13 (11), 2890. doi:10.3390/en13112890

Montgomery, Douglas C. (2013). *Design and analysis of experiments*. Singapore: John Wiley & Sons Inc.

Ovsyannikova, Ekaterina, Arauzo, Pablo J., Becker, Gero C., and Kruse, Andrea (2019). Experimental and thermodynamic studies of phosphate behavior during the hydrothermal carbonization of sewage sludge. *Sci. Total Environ.* 692, 147–156. doi:10.1016/j.scitotenv.2019.07.217

Pérez, Carla, Boily, Jean-François, Skoglund, Nils, Jansson, Stina, and Fick, Jerker (2022). Phosphorus release from hydrothermally carbonized digested sewage sludge using organic acids. *Waste Manag.* 151, 60–69. doi:10.1016/j.wasman.2022.07.023

Peng, Chuan, Zhai, Yunbo, Zhu, Y. U. N., Xu, Bibo, Wang, Tengfei, Li, Caiting, et al. (2016). Production of char from sewage sludge employing hydrothermal carbonization: char properties, combustion behavior and thermal characteristics. *Fuel* 176, 110–118. doi:10.1016/j.fuel.2016.02.068

Pérez, Carla, Boily, Jean-François, Jansson, Stina, Gustafsson, Tomas, and Fick, Jerker (2021). Acid-induced phosphorus release from hydrothermally carbonized sewage sludge. *Waste Biomass Valorization* 12, 6555–6568. doi:10.1007/s12649-021-01463-5

Petzet, Sebastian, Peplinski, Burkhard, and Cornel, Peter (2012). On wet chemical phosphorus recovery from sewage sludge ash by acidic or alkaline leaching and an optimized combination of both. *Water Res.* 46 (12), 3769–3780. doi:10.1016/j.watres.2012.03.068

Poirier, Yves, Jaskolowski, A., and Clúa, Joaquín (2022). Phosphate acquisition and metabolism in plants. *Curr. Biol.* 32, 623–629. doi:10.1016/j.cub.2022.03.073

Putra, Herlian Eriska, Damanhuri, Enri, and Dewi, KaniaAri Darmawan Pasek (April 2018). Hydrothermal carbonization of biomass waste under low temperature condition. Proceedings of the 2nd International Conference on Engineering and Technology for Sustainable Development. Samara, Russia, doi:10.1051/matecconf/201815401025

Raheem, A., Sikarwar, V. S., He, J., Dastyar, W., Dionysiou, D. D., Wang, W., et al. (2018). Opportunities and challenges in sustainable treatment and resource reuse of sewage sludge: a review. *Chem. Eng. J.* 337, 616–641. doi:10.1016/j.cej.2017.12.149

Reza, M. Toufiq, Rottler, Erwin, Herklotz, Laureen, and Wirth, Benjamin (2015). Hydrothermal carbonization (HTC) of wheat straw: influence of feedwater pH prepared by acetic acid and potassium hydroxide. *Bioresour. Technol.* 182, 336–344. doi:10.1016/j.biortech.2015.02.024

Román, S., Libra, J., Berge, N., Sabio, E., Ro, K., Li, L., et al. (2018). Hydrothermal carbonization: modeling, final properties design and applications: a review. *Energies* 11, 216. doi:10.3390/en11010216

Roskosch, Andrea, and Heidecke, Patric (2018). *Sewage sludge disposal in the Federal Republic of Germany*. Dessau-Roßlau, Germany: German Environment Agency.

Shettigondahalli Ekanthalu, V., Morscheck, Gert, Narra, S., and Nelles, Michael (2020). Hydrothermal carbonization—a sustainable approach to deal with the challenges in sewage sludge management. *Urban Min. Sustain. Waste Manag.* 293, 293–302. doi:10.1007/978-981-15-0532-4_29

Shettigondahalli Ekanthalu, V., Narra, S., Ender, Tommy, Antwi, E., and Nelles, M. (2022). Influence of post- and pre-acid treatment during hydrothermal carbonization of sewage sludge on P-transformation and the characteristics of hydrochar. *Processes* 10 (151), 151. doi:10.3390/pr10010151

Shettigondahalli Ekanthalu, V., Narra, S., Sprafke, J., and Nelles, M. (2021). Influence of acids and alkali as additives on hydrothermally treating sewage sludge: effect on phosphorus recovery, yield, and energy value of hydrochar. *Processes* 9 (4), 618. doi:10.3390/pr9040618

Shi, Yan, Luo, Gang, Rao, Y., Chen, Huihui, and Zhang, Shicheng (2019). Hydrothermal conversion of dewatered sewage sludge: focusing on the transformation mechanism and recovery of phosphorus. *Chemosphere* 228, 619–628. doi:10.1016/j.chemosphere.2019.04.109

Stat-Ease (2022). *Adequate precision - tutorial.* Minneapolis, Minnesota , United States: Stat-Ease, Inc.

Stat-Ease, Inc (2022). Design-expert V22.0, tutorials. https://www.statease.com/docs/latest/tutorials/(Accessed June 03, 2023).

Statistisches Bundesamt Destatis (2022). Abwasserbehandlung – klärschlamm. https://www-genesis.destatis.de/genesis/online?operation=ergebnistabelleUmfang&levelindex=2&levelid=1682687234807&downloadname=32214-0001-DLAND#abreadcrumb (Accessed April 28, 2023).

Stumm, Werner, and Morgan, James J. (1981). *Aquatic chemistry - an introduction emphasizing chemical equilibria in natural water*. Hoboken, New Jersey, United States: Wiley.

Tränckner, Simone (2023). *KS Anfall und Verbleib ZKA Rostock. interview by Tommy Ender.*

UBC Sustainable Cities Commission (2017). Enhanced nutrient removal with bio-filter at Rostock WWTP. https://www.balticwaterhub.net/solutions/bio-filter-wwtp-rostock.

Wang, Liping, Chang, Yuzhi, and Li, Aimin (2019). Hydrothermal carbonization for energy-efficient processing of sewage sludge: a review. *Renew. Sustain. Energy Rev.* 108, 423–440. doi:10.1016/j.rser.2019.04.011

Wang, Tao, Zhai, Yunbo, Zhu, Yun, Peng, C., Wang, Tengfei, Xu, Bibo, et al. (2017). Feedwater pH affects phosphorus transformation during hydrothermal carbonization of sewage sludge. *Bioresour. Technol.* 245, 182–187. doi:10.1016/j.biortech.2017.08.114

Werther, J., and Ogada, T. (1999). Sewage sludge combustion. *Prog. Energy Combust. Sci.* 25 (1), 55–116. doi:10.1016/S0360-1285(98)00020-3

Woriescheck, Tim (2019). *PhD thesis*. Oldenburg, Germany: Institut für Chemie, Carl von Ossietzky Universität Oldenburg.Charakterisierung, Aufreinigung und Wertstoffgewinnung von Prozesswasser der Hydrothermalen Carbonisierung

Zheng, Xiaoyuan, Jiang, Zhengwei, Ying, Zhi, Song, Jiaxing, Chen, Wei, and Wang, Bo (2020a). Role of feedstock properties and hydrothermal carbonization conditions on fuel properties of sewage sludge-derived hydrochar using multiple linear regression technique. *Fuel* 271, 117609. doi:10.1016/j.fuel.2020.117609

Zheng, Xiaoyuan, Jiang, Zhengwei, Ying, Zhi, Ye, Yutong, Chen, Wei, Wang, Bo, et al. (2020b). Migration and transformation of phosphorus during hydrothermal carbonization of sewage sludge: focusing on the role of pH and calcium additive and the transformation mechanism. *ACS Sustain. Chem. Eng.* 8 (21), 7806–7814. doi:10.1021/acssuschemeng.0c00031

frontiers | Frontiers in Environmental Engineering

TYPE Review
PUBLISHED 01 November 2023
DOI 10.3389/fenve.2023.1228992

OPEN ACCESS

EDITED BY
Zacharias Frontistis,
University of Western Macedonia, Greece

REVIEWED BY
Maria Laura Tummino,
National Research Council of Italy (CNR), Italy
Bampos Georgios,
University of Patras, Greece

*CORRESPONDENCE
Liangdong Fan,
fanld@szu.edu.cn
Kristina Mikhailovna Maliutina,
maliutinak@cardiff.ac.uk
Andrea Folli,
follia@cardiff.ac.uk

RECEIVED 25 May 2023
ACCEPTED 04 September 2023
PUBLISHED 01 November 2023

CITATION
Maliutina KM, Omoriyekomwan JE, He C, Fan L and Folli A (2023), Biomass-derived carbon nanostructures and their applications as electrocatalysts for hydrogen evolution and oxygen reduction/evolution.
Front. Environ. Eng. 2:1228992.
doi: 10.3389/fenve.2023.1228992

Biomass-derived carbon nanostructures and their applications as electrocatalysts for hydrogen evolution and oxygen reduction/evolution

Kristina Mikhailovna Maliutina [1,2,3]*, Joy Esohe Omoriyekomwan [4], Chuanxin He [1,2], Liangdong Fan [1,2]* and Andrea Folli [5]*

[1]Department of New Energy Science & Technology, College of Chemistry and Environmental Engineering, Shenzhen University, Shenzhen, Guangdong, China, [2]College of Physics and Optoelectronic Engineering, Key Lab of Optoelectronic Devices and Systems of Ministry of Education/Guangdong Province, Shenzhen University, Shenzhen, Guangdong, China, [3]School of Chemistry, Cardiff University, Cardiff, United Kingdom, [4]Key Laboratory of Advanced Coal and Coking Technology of Liaoning Province, School of Chemical Engineering, University of Science and Technology Liaoning, Anshan, China , [5]School of Chemistry, Net Zero Innovation Institute, Cardiff Catalysis Institute, Cardiff University, Cardiff, United Kingdom

Biomass derived electrocatalysts with rationally designed activity, selectivity, and stability present a major sustainable approach for the electrochemical production of fuels and value-added chemicals. This review presents recent advances in the field of biomass-derived electrocatalytic nanostructures for the hydrogen evolution reaction (HER) and the oxygen reduction and evolution reactions (oxygen reduction reaction and oxygen evolution reaction), that are subject of major research efforts, as well as public and private investment, as they will play a crucial role in the energy transition and in achieving net zero carbon emissions. The review summarises experimental and theoretical investigations aiming at tuning electrocatalytic performances of sustainable C-based nanostructured materials, and present opportunities for future commercialization of innovative energy materials and applications. In reviewing relevant literature in the field, we focus on the correlation between electrocatalytic activity/selectivity and synthesis methods, composition, physical chemical characteristics, in the attempt to uncover a clear structure-activity relationship. Furthermore, this study provides a critical comparison of the different electrocatalysts in light of their catalytic mechanisms, limiting phenomena, and practical applications for sustainable future technologies.

KEYWORDS

carbon nanomaterials, electrochemistry, biomass-derived electrocatalyst, heteroatom doping, active sites engineering

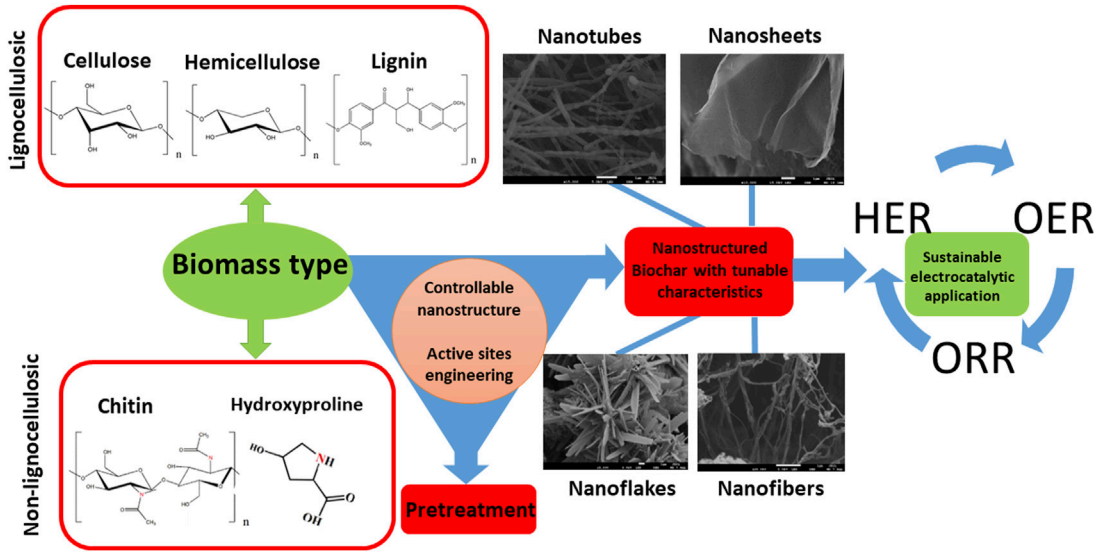

GRAPHICAL ABSTRACT

Highlights

- Carbon nanomaterials from biomass for electrocatalytic application were summarized
- Determination of structure-to-activity relationship from biomass and their precursors
- Pretreatment is a crucial step towards nano-microstructural engineering
- Actual active sites through non-metal and metal doping based on electrochemical figures of merit
- Integration of computational and experimental studies is highly desired

1 Introduction

Continuous disruptive impact on nature, climate change, environmental crisis, and energy shortage has shifted the research community attention towards pursuing non-hazardous, sustainable and renewable energy conversion and storage. Since the second half of the 20th Century, electrochemical transformations of small, molecules such as H_2O, O_2, N_2, as well as greenhouse gases such as CO_2, CH_4, and N_2O, into fuels and value-added chemicals have increasingly dominated the field of electrochemistry. Electrochemical water splitting and electrochemical hydrogen evolution reaction (HER) for hydrogen production had already been demonstrated in the 19th Century by Nicholson and Carliste (Kreuter and Hofmann, 1998). A second major milestone was achieved in the 1960s with the report on the electrochemical CO_2 reduction reaction (CO_2RR) by Jordan and Smith (Jordan and Smith, 1960; Meshitsuka et al., 1974), followed 30 years later, by the work of Hori and co-workers on the possibility of producing chemicals and fuels using this process (Hori et al., 1985; Hori et al., 1986; Hori et al., 1989). As of today, more than 30,000 research articles have been published on electrochemical transformations such as HER and CO2RR. Despite major recent developments, and deployment of industrial scale electrolysers for water splitting and H_2 production, these electrochemical processes are confronted with the shortcoming of electrocatalysts based on rare and expensive noble metals as the bottleneck toward practical implementation.

A promising alternative for conventional fossil fuels and combustion engines is next-generation energy production/conversion/storage technologies, such as fuel cells (FCs), electrolytic cells, water splitting systems, capacitors and batteries that generate clean, eco-friendly electricity by electrochemically reducing O_2 and oxidizing a fuel, i.e., H_2, into water. FCs are small in size, silent energy conversion devices that directly convert the chemical energy of different fuels into electrical energy at a much promising efficiency, both theoretically and practically, as compared to conventional power generation sources (Fan et al., 2018; Sayed et al., 2019; Abdelkareem et al., 2021). Recent FC technologies includes alkaline membrane fuel cells (AMFCs), solid (or solid-state) alkaline fuel cells (SAFCs), hydroxide exchange membrane fuel cells (HEMFCs), alkaline polymer electrolyte fuel cells (APEFCs) and polymer electrolyte alkaline fuel cells (PEAFCs) (Dekel, 2018). For instance, a proton exchange membrane fuel cell (PEMFC) fuelled by hydrogen generates water as a byproduct, with a small release of waste heat. This is very promising compared to the huge gaseous emissions, waste heat, and cooling demand in conventional power generation systems. Microbial FCs are another class of devices that utilize microbes, hence, more environmental-friendly and eco-sound with a wide range of applications, ranging from power generation to desalination.

Once again, bottlenecks hindering global applicability and scale up are large amounts of noble metal electrocatalysts, durability, as well as overpotentials required for the HER (Tang et al., 2018a; Tang et al., 2018b; Tang et al., 2019), oxygen reduction reaction (ORR)

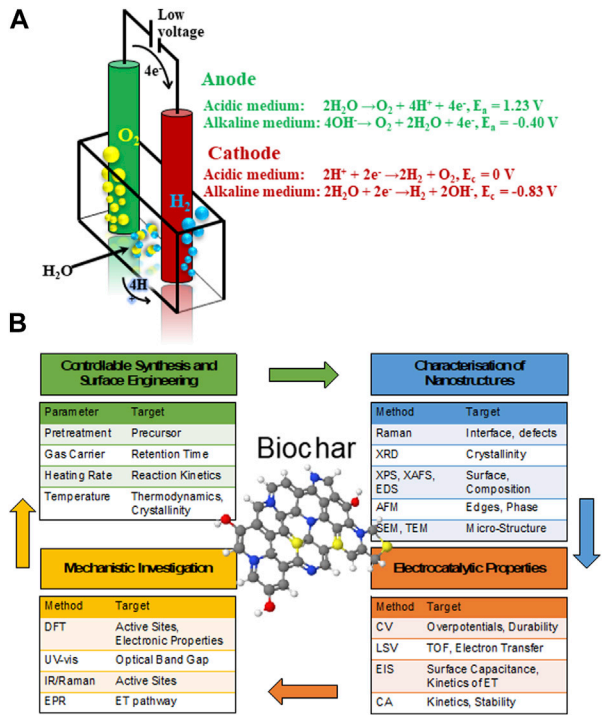

FIGURE 1
Schematic diagram of **(A)** representation of a water splitting electrolytic cell and **(B)** multistep approach for rational synthesis and characterization of biomass-derived carbon nanocarbons for electrochemical application.

(Shao et al., 2016; Fan et al., 2018; Li F. et al., 2020; Maliutina et al., 2021a; Li et al., 2023) and oxygen evolution reaction (OER) (Li et al., 2021; Huang et al., 2022).

J. R. Deiman and Adriaan Paets van Troostwijk demonstrated a water electrolysis in 1789, while a typical electrolytic cell for water splitting is illustrated in Figure 1A (Wang J. et al., 2020). The water splitting process involves two half-cell reactions: anodic oxidation or oxygen evolution reaction (OER) and cathodic reduction or HER, respectively. The recent insights on electrochemical mechanisms in both alkaline and acidic environments are highlighted in details in the Supporting Material (SI). However, efficient catalysts are desired to overcome the sluggish kinetics and large overpotential of these electrochemical reactions. Nevertheless, the scarcity, high cost and poor tolerance of widely employed standart platinum group metals-based electrodes severely hinder a large-scale applications of fuel cells and water splitting devices.

The development of abundant, stable and low-cost electrocatalysts as cathode material is a colossal issue (Nie et al., 2015). Recently, many researchers shifted attention towards Earth abundant alternatives to noble metals, such as carbon-based electrocatalysts (Zhang Y. et al., 2016; Borghei et al., 2017; Zhang et al., 2018). Among various carbonaceous assemblies, carbon nanomaterials (CNs) are recognized amongst as potentially active and versatile electrocatalysts with a good degree of tunability of their physical chemical properties. Heteroatom-doped graphene (Wang S. et al., 2012), thin carbon nanosheets (Jiang et al., 2019a), carbon nanotubes (CNTs) (Gong et al., 2009; Maliutina et al., 2021a) and nanofibers (CNFs) (Wu M. et al., 2018) and recently synthesized graphdyine (Zhao et al., 2018) are amongst the emerging C-based materials being investigated as promising electrocatalysts.

The potential of using biomass to produce such C-based materials for electrocatalysis has recently been investigated (Chen et al., 2014; Ye et al., 2015; Zhang Y. et al., 2016; Huang et al., 2017; Cheng et al., 2021), including challenges associated to their complex and non-regular organic structure (Khiari et al., 2019; Munawar et al., 2021). Several studies have illustrated different pretreatment pathways of biomass, including alkaline, acidic, hypersaline and a variety of extraction methods for fabrication of advanced nanomaterials, such as pyrolysis and carbonization with controllable and reproducible carbon structure (Prakash Menon et al., 2017; Omoriyekomwan et al., 2019; Maliutina et al., 2021b). However, a clear understanding on how to rationally design nanostructured electrocatalysts with desired structure and activity from biomass is lacking, in great part due to the difficulty of standardising synthetic procedures. This is mostly due to the substantial variability of different biomass sources in terms of chemical composition and structure. Systematically reviewing the major achievements in biomass-derived nanomaterials for electrocatalytic applications, in particular HER, ORR, and OER, can help to unravel interesting trends and correlations that would improve the way we engineer improved kinetics and mechanisms of electrocatalytic processes based on biomass derived nanostructured electrocatalysts (Figure 1B). This review presents a comprehensive comparison and discussion on how starting biomass feedstocks influence final electrocatalyst active sites, electronic properties and performances, and evaluates crucial aspects such as biomass pretreatment methods as well as synthetic conditions.

Particular attention is given to the role of biomass sources, composition, and physical chemical properties determining morphologies and electronic structure of the final electrocatalysts. We also examine the impact of heteroatom doping on electrocatalytic activity and mechanisms that over the last few years have emerged as a strategy to further improve electrocatalytic performances (Borghei et al., 2017; Li Y. et al., 2019; Zhou et al., 2020). Finally, we propose outlook and perspectives on future applications of biomass-derived C-based electrocatalysts.

2 The role of biomass variability on the yield and structure of C-based materials

2.1 Biomass as a source for advanced carbon-based nanomaterials

According to the classification proposed by Vassilev et al., biomass is a non-fossil, complex and biogenic heterogeneous mixture of organic and inorganic matter that is primarily generated by photosynthesis, such as natural constituents from lands and water-based vegetation; animal or human food digestion; anthropogenic processing of wood, plants and other organic matter, such as manure or household waste (Vassilev et al., 2010). Biomass is typically utilized for solid, liquid and gaseous products from non-edible residues formed by floras and faunas, such as corn cobs, wheat stalk, cornstalk, and manure (Supplementary Table S1). Biomass is carbon-rich, sustainable,

and renewable. This has made it a sought-after precursor for generating green CNs (solid component) as well as being used for the production of value-added chemicals and biofuels (predominantly liquid and gaseous component) (Bhaskar et al., 2011; Titirici et al., 2015; Anca-Couce, 2016; Kumar et al., 2016).

Biomass can be divided into two major groups with the same characteristics of origin and chemical structure, i.e., lignocellulosic and non-lignocellulosic biomass (Martin, 2010; Kosinkova et al., 2015).

Lignocellulosic biomass is considered one of the most promising renewable sources for producing carbon materials and fuels while remaining environmentally friendly (Cai et al., 2015; Kabir and Hameed, 2017; Li et al., 2017). Lignocellulosic biomass is mainly a waste of wooden and crop industries; primarily rich in hemicellulose (15%–40%), cellulose (25–50 wt%), and lignin (10%–40%) (Chen, 2014; Kumar et al., 2016; Maliutina et al., 2017; Li Y. et al., 2020).

Cellulose is a linear polysaccharide that unsoluble in water and consists of D-glucose monomers bonded together via β-(1–4) glycosidic bonds (Abraham et al., 2011). The inter and intramolecular hydrogen bonds that give cellulose its crystalline form are formed between the three hydroxyl groups on each glucose monomer (Harmsen et al., 2010). Cellulose microfibrils are formed due to the coalescence of the polymer chains to form fibers, which in turn gives cellulose its crystalline structure (Shafizadeh, 1982). Hemicellulose comprises of various monomers such as glucose, mannose, arabinose, and xylose, which vary in quantity according to the type of biomass (Li, 2014). Hemicellulose take place in association with cellulose in the cell wall, but unlike cellulose, hemicelluloses are soluble in dilute alkali. Hence, xylan, which is the most abundant monomeric hemicellulose unit up to about 10% and 30% of the dry weight of the species (Yaman, 2004). Unlike cellulose, hemicellulose does not exhibit a crystalline structure due to the high number of branched chains and acetyl groups linked to a polymer chain. Lignin is an aromatic polymer in nature that consists of p-coumaryl, coniferyl, and sinapyl alcohol monomers and hydroxyl, carbonyl, and methoxy functionalities to form a firm composition (Chen, 2014). During pyrolysis or carbonization processes, hemicellulose decomposition occurs first at 200°C–260°C. Cellulose fragments and lignin structure break up at 240°C–350°C (Wang et al., 2015) and 280°C–500°C (Ramanayaka et al., 2020), respectively. The ratio of every single compound of hemicellulose, cellulose, or lignin is not regular and constant, which is related to the species, age, soil, place of origin (Liu et al., 2019).

Non-lignocellulosic biomass is predominantly comprised of carbohydrates, lipids, proteins and inorganic minerals (Li and Jiang, 2017). Apart from algal biomass, non-lignocellulosic type includes animal hair, feathers, bones, fish and seafood waste, sewage sludge, and manure (Li and Jiang, 2017). Sewage sludge encompasses different constituents like organics, inorganics, and microbes (Yu et al., 2021). Algae is considered a significant component of the Earth's biomass, whose growth rate and CO_2 fixation effectiveness are higher than any earthly plant (Zhao et al., 2015). Algae consist mainly of lipids, proteins, ash, and carbohydrates. The main elements in algae are C and O, which account for 25%–55% and 15%–50%, while H and N are accounts for 5%–10% of algae, respectively (Li et al., 2017).

The conversion of biomass to advanced nanostructures is influenced by source, physical and chemical composition, that is highly variable in terms of origin and growth factors (e.g., environment) which can either enrich or deplete different compounds and elements (Vassilev et al., 2015). On average, the elemental composition of biomass consists of 99.9% of C, Ca, Cl, H, K, Mg, N, Na, O, P, and S, with ≤0.1% of trace elements (Vassilev et al., 2013). In summary, biomass has proven to be the an ideal source for CNs, given a series of advantages, including its relatively low cost and worldwide abundance; the absence of competition with the food industry; the natural viability of N, S, P, and O, allowing for doping and formation of chemical functionalities, without the need of extra chemicals.

2.2 Biochar

Biochar is a carbon-rich material that is produced by heating organic matter, such as wood chips, agricultural waste, or manure, in an oxygen-depleted atmosphere (Li Z. et al., 2019). The chemical nature of biochar is complex and depends on the type of biomass used, the thermal treatment conditions, and the post-treatment processes. Biochar is predominantly composed of carbon, with content ranging from 50% to 95% depending on the production process (Li Y. et al., 2020). The carbon in biochar is present in various forms, including elemental carbon, amorphous carbon, and graphite-like structures. These different forms of carbon are distributed throughout the biochar, creating a porous structure that provides high surface area and high adsorption capacity (Omoriyekomwan et al., 2021a). Apart from C, biochar also contains other elements such as H, O, N, and S, which are present in smaller quantities, and that can be included in C-based structures as dopants (Maliutina et al., 2018). The elemental composition of biochar significantly depends on the type of biomass used and the production conditions (Maliutina et al., 2017).

Biochar also contains a range of functional groups, such as carboxylic acids, phenols, ketones, and aldehydes. These functional groups are in large extent responsible for biochar chemical reactivity. The possibility of rationally designing these types of moieties on biochar surfaces presents a powerful strategy for tuning their potential catalytic properties, as well as influencing the adsorption of ions and molecules in the environment, by adjusting the overall acidity and basicity of the biochar surfaces. The surface area and porosity of biochar are further crucial features influencing chemical and catalytic properties. The porous structure of biochar is ordinarily emerging from the thermal preparation process, when the volatile constituents in the biomass are released, leaving behind a charred residue (Sch et al., 2011). Once again, the possibility of rationally designing high surface area and porosity, would provide a large number of active sites for adsorption and catalysis. Besides its potential applications as a catalyst or catalyst support, biochar is being investigated and employed in advanced sorbents, fertilizers, *etc.* (Huang et al., 2016; Uzun et al., 2016).

The chemical nature of biochar can also be modified through post-treatment processes, such as acid washing or chemical activation. These processes can alter the surface chemistry and functional groups of biochar, resulting in enhanced adsorption capacity and improved performance in environmental applications. Besides more or less complex C-based structures, thermal treatments of biomass for biochar production, often

leaves K–Ca–Mg–Na carbonates, Ca–K–Mn silicates, K–Na–Ca chlorides, Ca–Al–Mn oxides, sulphates, and phosphates (Vassilev et al., 2014; Omoriyekomwan et al., 2021a; Vassilev et al., 2012), which content in the final biochar product can be adjusted via post-treatment processes.

The phenomena of mass transfer on the surface of biochar during heterogeneous catalysis can be divided into the following stages (Lee et al., 2017): a) diffusion of the reagent from bulk gas or liquid film to the external surface of the catalyst; b) diffusion of the reagent to the inner surface of the catalyst through the pores of the catalyst; c) adsorption of the reagent on the surface of the catalyst; d) reactions occurring on the catalytic active centres on the catalyst surface; e) desorption of product from the catalyst surface; f) diffusion of product to the internal surface of the catalyst through catalyst pores; g) diffusion of product from the external catalyst surface to bulk gas or liquid film (Lin and Huber, 2009). Thus, catalytic activity is highly contingent on accessibility to catalytic active sites dispersed throughout internal pores. Although biochar is a porous material, the morphology and porosity of biochar without activation demonstrates poor catalytic properties. Various pretreatments can be applied to modify biochar morphology and porosity, as highlighted in Section 2.3. Surface area, pore size, pore volume, pore type [i.e., micropores, mesopores and macropores (Bikbulatova et al., 2017)] are vital properties, that impact overall catalytic ability.

Despite discussed benefits, the effective conversion of biomass into high-performing nanomaterials on a large scale for electrocatalytic purposes remains challenging (Alston and Arnold, 2011; Sharma et al., 2011). Amongst the major technical barriers presenting significant challenges in terms of materials comparison or standardisation of production processes, we can mention the high water soluble fraction, the (already discussed) huge variability of organic compositions of different biomasses, and to some extent, the large variability of inorganic components too (Alston and Arnold, 2011; Sharma et al., 2011).

2.2.1 Thermochemical biomass-to-biochar conversion processes

As previously described, the solid material obtained from the thermochemical conversion of biomass in an oxygen-limited environment is referred to as biochar (Liu et al., 2015a). Biochar can be produced via *pyrolytic*, *hydrothermal*, *carbonization* and *graphitization* methods. Because biochar can be constituted by multifunctional CNs, the thermochemical conversion of biomass into biochar for catalytic purposes is regarded as a biomass upgrading process (Liu et al., 2015b).

Pyrolysis is one of the most developed process for the conversion of biomass into biochar and it is ordinarily carried out in the 400°C–700°C temperature range and in an inert environment. Compared to other thermochemical conversion methods, pyrolysis is characterised by generally higher heating rates when compared to other thermochemical processes, benefitting the production of gaseous and liquid phases (Shafizadeh, 1982; Liu et al., 2015b). Pyrolytic processes are ordinarily performed via either conventional or microwave heating. From a structure perspective, pyrolytic biochar products are mainly constituted of amorphous carbon phases with low degree of crystallinity, specific surface, and porosity (Jatav et al., 2017).

Hydrothermal carbonisation (HTC) treatments operating at relatively low-temperature ranges, of about 170°C–250°C, and over a period of time ranging from a few hours to a day, offer significant advantages for biochar production, including a much reduced energy requirements for temperature; post thermal treatment drying processes; and enhanced compatibility with high water levels in the biomass feedstocks (Sch et al., 2011). HTC biochar is usually constituted by carbonaceous species with a high level of O-doping and/or a large amount of oxygen-containing functional groups, and generally high oxygen content. Depending on the final application and/or targeted properties/characteristics of the CNs catalyst, further treatments and modifications might be necessary, especially if O-free catalysts are desired.

Carbonization of biomass can generate a carbonaceous framework at a higher (compare to pyrolysis) temperature range, and in general between 700oCand 900°C (Liu et al., 2015b). Volatile components present in the source biomass are removed up to 95% at these temperatures, resulting in the formation of hierarchically porous carbons (HPCs). HPCs exhibit high specific surface areas (<1,000 $m^2 g^{-1}$) and large pore volumes (<1.5 $cm^3 g^{-1}$). HPCs show great application potential as catalyst supports for fuel cells and supercapacitors (Zhang L.-L. et al., 2023).

Graphitization is a thermal treatment of carbonaceous materials at temperatures ordinarily in the range 900oC–1800°C, or higher, in an inert atmosphere. Graphitization is a process that converts low-ordered amorphous-like carbonaceous layers or turbostratic carbon into highly ordered structures (Andrews et al., 2001). Graphitization is usually a further step in the production of highly ordered nanostructured biochar produced via pyrolysis or carbonization, useful for tuning structural as well as electronic properties (Thompson et al., 2015).

2.2.2 Temperature dependent types of biochar and main nanostructured features

The use of hydrocarbon-rich organic waste has made significant progress in the growth of CNs leading to promising paths for their commerzialization (Wang et al., 2018; Omoriyekomwan et al., 2021b). Volatile compounds, such as alcohols, phenols, CO, and hydrocarbons derived from biomass (Shen et al., 2011; Omoriyekomwan et al., 2016) are critical carbon sources for the production of CNs by chemical vapor deposition (CVD) process (Kuznetsov et al., 2001; Maruyama et al., 2002; Zhao et al., 2006). It has been investigated that biomass undergoes a physical-chemical transition process as charring temperature increases from 300oC to 700°C (Keiluweit et al., 2010). Four types of biochars encompass a distinct mixture of physical and chemical phases: 1) Amorphous biochars characaterised by a random mixture between heat-altered molecules and incipient aromatic polycondensates; 2) Transition biochars where the crystalline character of the precursor is preserved; 3) Composite biochars comprising graphene stacks which are poorly ordered and embedded in amorphous phases; 4) Turbostratic biochars characterised by disordered graphitic crystallites (Keiluweit et al., 2010). Concurrently, when metals such a Fe and Mg are involved in the carbonization of biomass, biochar with a high occurrence of aromatic compounds was reported (Zhang et al., 2013).

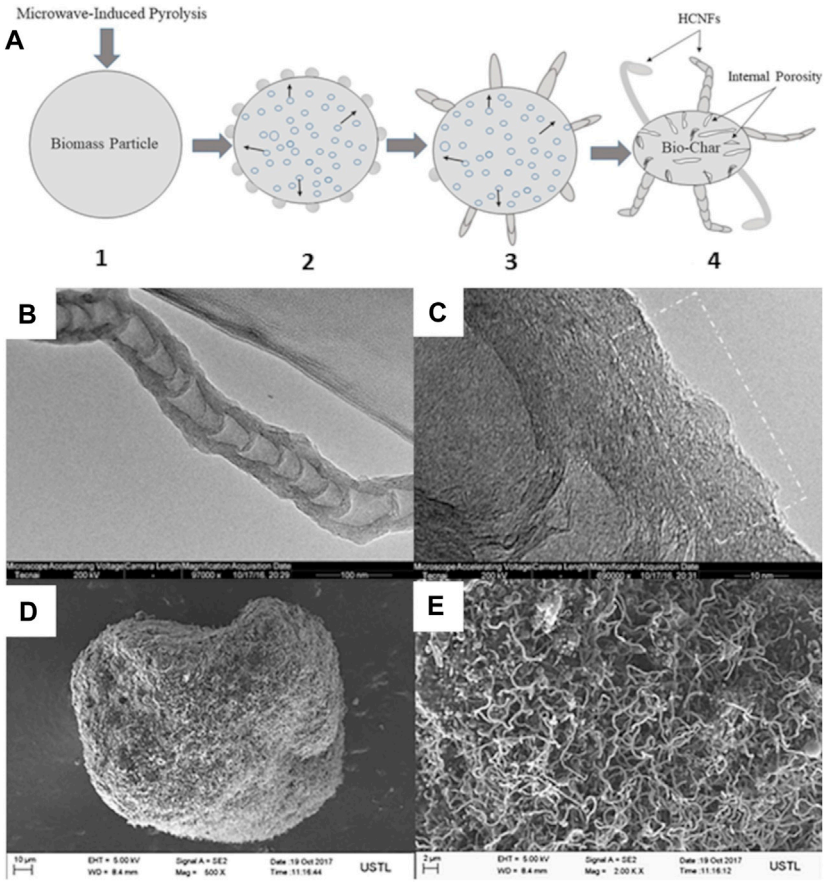

FIGURE 2
(A) Self-extrusion mechanism of the growth steps of HCNFs: (1) microwave-induced pyrolysis of biomass; (2) self-extrusion of volatiles from inside of the biomass particle through pores on biomass surface and resolidification of volatiles on the particle surface, initiating the HCNFs formation; (3) continuous volatiles through nano-sized channels, initiating the growth of the HCNFs; (4) growth of HCNFs on porous bio-char; **(B)** TEM and **(C)** HRTEM images of HCNFs on microwave pyrolytic PKS biochar at 600°C (Omoriyekomwan et al., 2017). **(D, E)** SEM images of bio-chars obtained during microwave pyrolysis of isolated cellulose from PKS components via the alkali-acid method at 600°C (Omoriyekomwan et al., 2019). Reproduced and modified with permission.

There has been extensive research in fabrication of CNs such as CNTs/CNFs, nanoribbons, graphene, fullerenes, via biomass as a low cost and green carbon source (Shi et al., 2014; Omoriyekomwan et al., 2017; Sun et al., 2018; Omoriyekomwan et al., 2019). Generally, all CNs can be divided into: a) zero-dimensional (0D) quantum dots, fullerenes, nanosphere, core@shell, yoke@shell; b) one-dimensional (1D) nanorods, nanowires, CNTs, CNFs; c) two-dimensional (2D) nanosheets, graphene, nanoplates, nanobelts; d) three-dimensional (3D) hierarchical mesoporous nanostructured assembly, metal organic frameworks (MOFs). The properties of 0D/1D/2D/3D CNs can vary in mechanical strength, surface area, hydrophobic adsorption, scarcity, *etc.* The mechanism of biochar network formation divided into the main crucial steps (decomposition, rapid volatilization, polymerization-depolymerization, dehydration, intramolecular rearrangement, intramolecular condensation and aromatization). The biochar network obtained from various biomass can be transformed into more ordered graphitic nanostructures involving dehydration, decarboxylation, rearrangements, aromatization, and intramolecular condensation to form 0D, 1D, 2D nanostructures or it can be converted to the low molecular 3D carbon nanomaterials.

2.3 Biomass pretreatment methods

Chemical pretreatment of biomass is often regarded as a strategy to impart a particular porosity, microstructure and/or morphology to the final CNs. Omoriyekomwan et al. (Omoriyekomwan et al., 2017) compared microwave-assisted and conventional (fixed-bed) of raw palm kernel shell (PKS) pyrolysis approaches. Hollow carbon nanofibers (HCNFs) were successfully produced on the surface of bio-chars during microwave pyrolysis of PKS at 500 °C and 600°C. The observed HCNFs onto the PKS biochar was attributed to the microwave heating condition only and not detected under conventional heating. Authors explained this phenomenon by the difference in heat transfer mechanism in microwave and conventional heating. The yield of observed hollow carbon nanofibers (HCNFs) increased with temperature and reached 9.88 wt% at 600°C (Omoriyekomwan et al., 2017). A self-extrusion mechanism of volatiles from inside of the biomass particle through pores on biomass surface and resolidification of volatiles on particle surface bio-component was attributed for CNTs formation under microwave irradiation at 600°C (Figure 2). Additionally, the presence of Fe, K, and Ca in raw PKS biomass

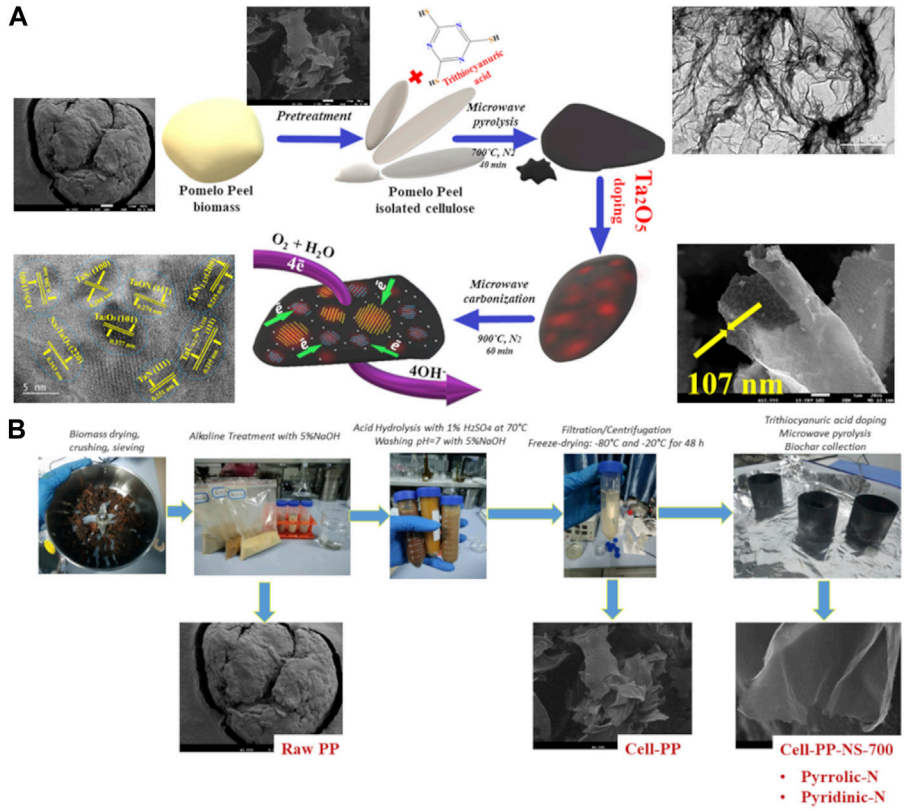

FIGURE 3
(A) Schematic diagram introducing the evolution of carbonaceous nanostructure during the pretreatment of biomass and pyrolysis process and **(B)** the detailed synthesis route of the N, S, Ta-doped carbon nanosheets. Reproduced and modified with permission (Maliutina et al., 2021b).

and in the HCNFs structure was considered to have an important role during their formation and growth (Omoriyekomwan et al., 2017).

In another study of Omoriyekomwan et al. (Omoriyekomwan et al., 2019), microwave pyrolysis for 1 h at 600°C was carried out on the raw PKS (Figures 2B, C) and isolated cellulose without addition of external catalyst (Figures 2D, E). Two different pretreatment methods, i.e., alkali-acid and formic acid/acetic acid were systematically compared. The higher yield of formed CNTs was correlated with the two-step alkali-acid (NaOH for lignin isolation/ H_2SO_4 for cellulose isolation) route of the raw PKS biomass (Omoriyekomwan et al., 2019). The chemical alkali-acid pretreatment displayed effective synthesis of CNTs that greatly enhanced their length (600–1800 nm in this study vs 200–1,600 nm of commercial CNTs) (Figure 2E) (Omoriyekomwan et al., 2019). The observed Raman I_D/I_G ratio for CNTs synthesised in this study was lower (0.86) compared to that of commercial CNTs (0.96) was attributed to lower amount of defects and higher order of the nanostructure, resulting in higher quality (Omoriyekomwan et al., 2019).

Recently, Maliutina et al. (Maliutina et al., 2021b) reported two-step chemical pretreatment and pyrolysis methods that were employed to pomelo peel biomass to obtain mesoporous carbon nanosheets (Maliutina et al., 2021b). The formation of carbon nanosheets with a thickness of about 107 nm (Figure 3A) was obtained from irregularly shaped pomelo peel as a precursor using a chemical pretreatment process, involving alkaline etching with KOH and acid hydrolysis with H_2SO_4 (Figure 3B). The final cell-PP-NS-700-Ta-900 nanosheet sample also exhibited a moderate graphitization degree (ID_1/IG ratio of 1.11) and high specific surface area (SSA) of 336.82 $m^2\ g^{-1}$. This chemical pretreatment method was regarded as a promising route for fast and tunable conversion of the complex pristine biomass microstructure into a nano framework with desirable properties.

Cyclic oxidation pretreatment of biomass for CNs synthesis has been reported in other works (Kang et al., 2005; Goodell et al., 2008). The cyclic oxidation process allows for the conversion of biomass into tubular carbon nanostructure via a repetitive (i.e., cyclic) oxidation process. Goodell et al. (Goodell et al., 2008) used six different feedstock, including wood fibers, avicel cellulose, bamboo, alpha-cellulose, organosolv lignin, and wood fibers. All samples were preheated before cyclic oxidation at 240°C and 400°C, respectively. They reported hard tubular CNTs formation in cellulose samples, organosolv lignin, and filter paper. It was concluded that the original biomass structure played an essential role in the formation of CNs via the cyclic oxidation method.

The Authors proposed a nanoscale channel formed at low-temperature carbonization treatment that acted as the templates for the CNTs' growth (Goodell et al., 2008). The formation of nano-channels at low-temperature carbonization promoted cellulose ablation, which contributed to CNTs synthesis. Nevertheless, when pure biomass components (such as lignin and cellulose) were subjected to cyclic oxidation, tubular CNTs were not formed.

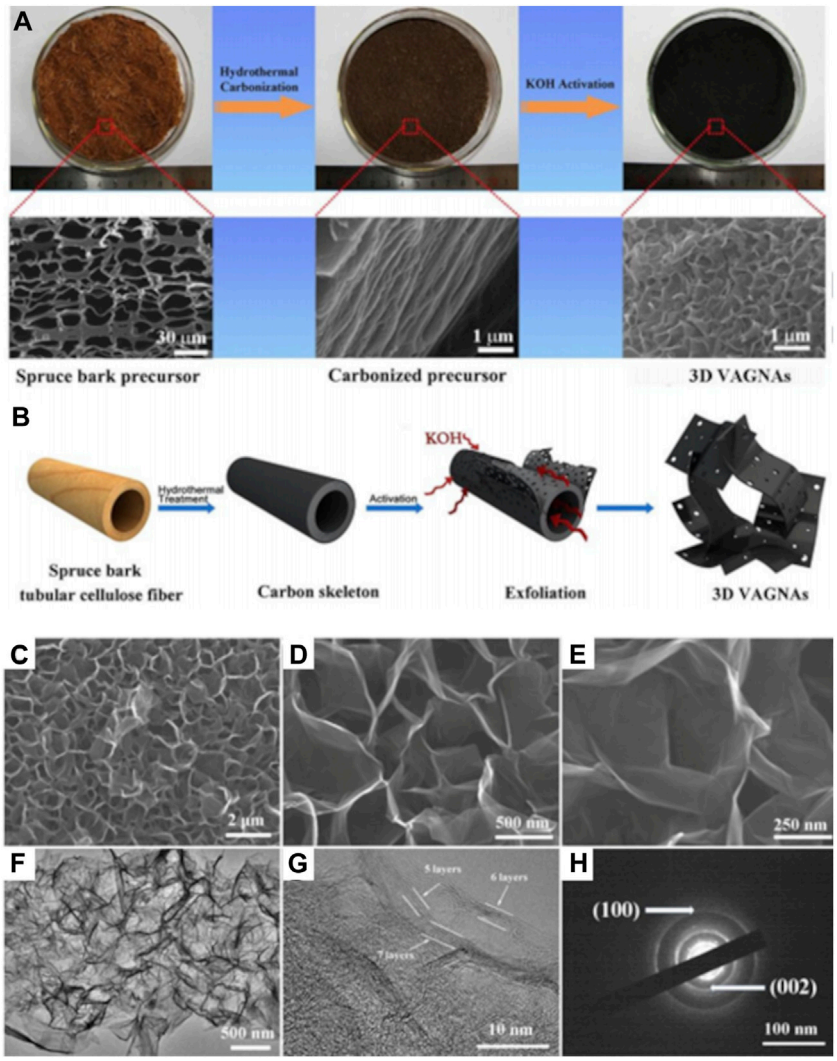

FIGURE 4
Schematic illustrations of carbonization and chemical activation treatment process **(A)** overall formation process and **(B)** the synthetic mechanism of 3D the vertically aligned graphene nanosheets (VAGNAs); **(C)** SEM image of the microstructures of VAGNA-900; **(D, E)** High magnification SEM pictures showing the vertically aligned graphene nanosheets of VAGNA-900; **(F)** TEM image of VAGNA-900; **(G)** HR-TEM image of VAGNA-900 demonstrating its few-layer feature; **(H)** SAED image of VAGNA-900. Reproduced and modified with permission (Sun et al., 2018).

Mechanical activation treatment was proposed by Chen et al. (Chen and Chadderton, 2004) when they reported the synthesis of aligned CNTs from iron phthalocyanine pyrolysis after ball milling treatment. Milling time was observed to be the most important controlling parameter in this process (Chen and Yu, 2005; Onishchenko et al., 2012; Onishchenko et al., 2013a). Onishchenko et al. (Onishchenko et al., 2013b) reported the formation of CNTs from sphagnum moss and agricultural wastes via a mechanical activation process. The CNTs content after mechanical activation was 11.52 wt%, 24.45 wt%, 34.06 wt%, and 42.75 wt% for mechanical pretreatment duration of 7, 10, 16, and 27 h, respectively (Onishchenko et al., 2013b). It was observed that after 10 h of mechanical treatment, most of the materials were enriched with CNTs. In other study of Reva et al. (Reva et al., 2016a), abundant CNTs were presented in all bulk material derived from brown sphagnum moss biomass after 36 h treatment. Electrostatic interaction of the CNs was reported to be responsible for the felt-like aggregates forming with a size of 20–100 μm, consisting of CNTs and amorphous carbon (Reva et al., 2016a; Reva et al., 2016b). It is worth noting that there was no catalyst involved in synthesizing CNs from biomass using mechanical treatment, while amorphous carbons acting as the precursor of CNs before mechanical activation were readily obtained from biomass. Therefore, mechanical pretreatment is a favorable technique for the synthesis of CNs as a result of the low cost of technology and feedstock.

H_3PO_4, and $ZnCl_2$ are also used alongside KOH as pretreatment agents prior to pyrolysis (Chaparro-Garnica et al., 2021). This method has showed to enhance porosity and ensurehigh specific surface area (SSA) of the final CNs (Chen et al., 2016). Li et al. pretreated willow catkin in KOH aqueous solution based on a mass ratio of 1:1 and obtained an interconnected porous carbon nanosheet after pyrolysis (Li et al., 2016). Meanwhile, large SSA of 2,385 m^2g^{-1}, a large pore volume, and easily accessible open

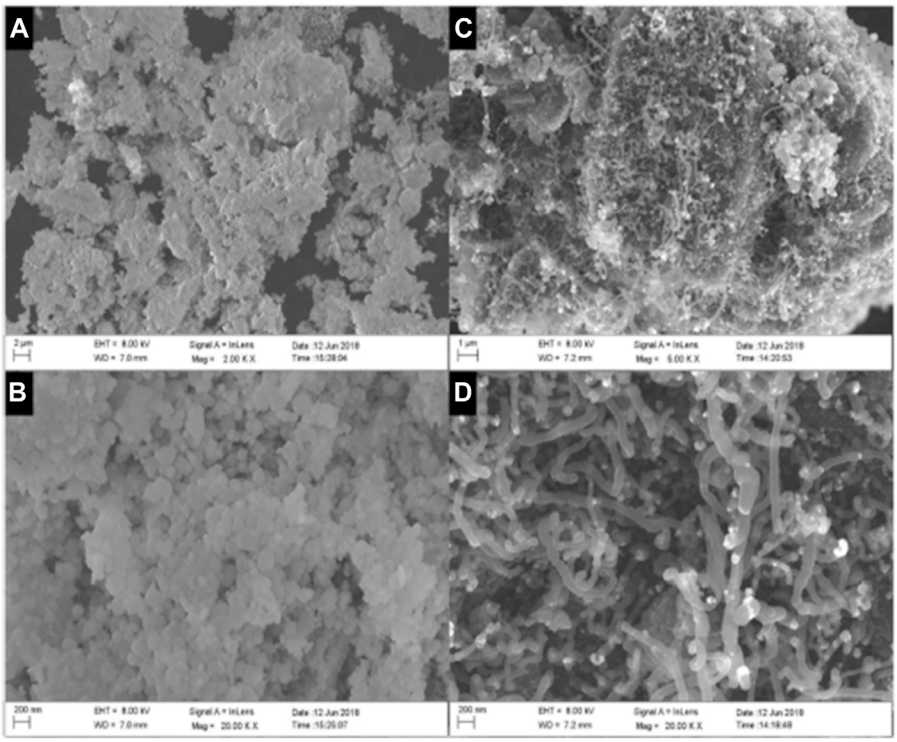

FIGURE 5
SEM images of biochar-NiO and biochar-CNT-NiO: **(A)** and **(B)** different magnifications of biochar-NiO; **(C, D)** different magnifications of biochar-CNT-NiO. Reproduced with permission (Zhang et al., 2021).

surfaces of graphene nanosheets were achieved from spruce bark after HTC at 180°C and KOH pretreatment (Figures 4A–H) (Sun et al., 2018). Chemical pretreatments of biomass were also proven to be beneficial in the case of biochar synthesis from graphitisation processes (Sun et al., 2013; Mahmoudian et al., 2016; Su et al., 2017). Interesting observations were also reported in the case of chemical pretreatment prior pyrolytic biochar synthesis via microwave heating rather than conventional heating. Zhang et al. (Zhang et al., 2021) synthesized biochar-CNTs composite from char from pine nutshell char via microwave heating (Figures 5A–D).

The Authors impregnated the source biomass with Ni catalyst and applied microwave heating in an inert environment of CH_4/N_2 gas (60/40 vol%) for 20 min reaching 600°C. Enhanced CNTs growth was reported and ascribed to the conversion of Ni nanoparticles into highly-crystallized NiO nanoparticles (Zhang et al., 2021). Supplementary Table S2 summarises biomass-based CNs obtained from different pretreatment and fabrication methods that were examined by this review.

It can be seen in Supplementary Table S2, that the preferable temperature range to produce CNTs enriched biochar is 700°C–800°C, while production of carbon nanosheets correlates with the range of 700°C–900°C. It is worth to note, that the microwave pyrolysis method assists to produce CNTs at the lower temperature range of 600°C–700°C. It can be explained by the difference in heat transfer mechanism in microwave and conventional heating. Unlike conventional heating, during microwave irradiation the particle temperature is higher than the surrounding area due to the selective heating under microwave. During microwave pyrolysis, the released volatiles are extruded through pores on biomass particle surface. Upon release, the high molecular weight tar precursors solidify due to lower temperatures at particle surface compared to particle core, initiating CNTs/CNFs formation and growth via CVD mechanism. Graphene nanosheets can be obtained at temperatures above 850°C during the graphitisation process, but requires a catalyst, such as Fe or Zn based.

3 Electrocatalysis of biomass-derived nanostructures

As already mentioned, one of the major drive for the use of biomass-derived nanostructured electrocatalysts remains the replacement of precious and rare metals in electrocatalytic processes. This can open up exciting new opportunities for very large scale deployment of electrocatalytic processes (i.e., electrolytic water splitting for hydrogen generation), that are sustainable, circular in their economy, and significantly cheap than current processes based on platinum group metals. In order to achieve this, major techno-scientific barriers such as the general low efficiencies of biomass-derived electrocatalysts (Seh et al., 2017), when compared to their precious metal-based counterparts, need to be overcome. In this review, we focus our attention on recent advancements reported in the field of biomass-derived electrocatalysts for hydrogen evolution and oxygen reduction/evolution, at the heart of water splitting, fuel cells and metal-air

batteries (Martín and Pérez-Ramírez, 2019) technologies, that urgently require alternatives to currently used platinum group metal-based electrocatalysts. A true rational design of novel C-based, sustainable, electrocatalysts can only be achieved through creating and controlling active sites, in conjunction with an in-depth understanding of electrocatalytic reaction mechanisms and kinetics. With the intent of promoting and encouraging such an approach, this review will try to develop a framework for rationalising activity trends and guiding electrocatalyst design contextualising recent results and observations on the basis of a combination of materials science, computational science, and inorganic chemistry (Hwang et al., 2017).

3.1 Benchmarks for biomass-derived electrocatalyst for ORR/OER/HER and targeted structural attributes

As an alternative to precious metal-based catalysts, various CNs, such as CNTs/CNFs (Wu Z.-Y. et al., 2018), and graphene-based nanosheets (Gong et al., 2019; Tang and Qiao, 2019) have been reported as ORR/OER electrocatalysts. CNs are generally functionalized via doping, allowing to generate functionalised electrocatalysts with a superior electrocatalytic activity (Zhang et al., 2016b). Dopants alter the amount of crystal and surface defects acting as potential catalytic active sites and modify the electronic structure of the CNs (Zheng et al., 2014; Wu et al., 2017), with a direct influence on the thermodynamics and charge carrier distribution in the carbon-based electrocatalysts (Sharifi et al., 2012; Lu et al., 2017; Mamtani et al., 2018; Jiang et al., 2019b). Typical types of doping include mono/dual/multiple heteroatoms doping; defective/vacancy doping; and charge-transfer doping.

Doping of graphene frameworks with non-metal elements such as N or O has been reported as a convenient strategy to tune the electrochemical as well as optical properties of graphene nanostructures (Inagaki et al., 2018). Zhang L. et al. (Zhang and Xia, 2011) investigated the role of nitrogen heteroatom towards ORR based on density functional theory (DFT) calculations applied to a N-doped nanographene model ($C_{45}NH_{20}$) in acidic medium. Nitrogen doping introduces an unpaired electron (the latter causing localized distribution of the molecule orbitals) with the overall result of enhancing the chemical reactivity of the graphene itself. Their simulations demonstrated that ORR on N-doped graphene is a direct four electron pathway, and consistent with experimental observations. Interestingly, the Authors identified the active catalytic sites on single nitrogen doped graphene, having either high positive spin density or high positive atomic charge density. N doping introduces asymmetry spin density and atomic charge density, allowing for N-graphene to exhibit high electroncatalytic activities for the ORR (Zhang and Xia, 2011). The electrocatalytic performance of the heteroatom-doped CNs partially depends on the electronic structure of the heteroatoms in comparison to the positively charged C atoms. In this case, the selectivity of a specific reduced product strongly depends on the affinity of active sites towards the corresponding intermediate motifs. This is quite different from the conventional pristine CNs.

Experimentally, different N functionalities in the carbonaceous skeleton can be easily probed and interrogated via X-Ray photoelectron spectroscopy (XPS) given the distinguishable N 1s binding energy of pyridinic-N (ca. 398 eV), pyrrolic-N (399–400 eV), graphitic-N or quaternary-N (ca. 401 eV), and pyridinic N oxide (402–406 eV) (Maliutina et al., 2018; Jiang et al., 2019a; Maliutina et al., 2021b). Pyridinic-N exists on the edge of the graphene layer and bonds to two carbon atoms, containing a lone electron pair, which can boost the electron-donor capability of the carbon material, resulting in the improvement of the adsorption capacity of O_2 and onset potential for ORR (Lai et al., 2012). Whilst incorporated into the graphene layer and bonded to surrounding three carbon atoms, graphitic-N donates one extra electron to the carbonaceous skeleton that weaken the O-O bonds and decrease the energy barrier for the first electron transfer (rate-determining step). Overall, graphitic-N functionalities facilitate the limiting current density and electron transfer for ORR. Wang and co-workers (Wang D.-W. et al., 2012) postulated that pyridinic-N and pyrrolic-N improve the storage of hydrogen atoms and accelerate protonation. At the same time, the oxidized-N functionalities exhibit a high affinity to electrons, unlike less positively charged pyridinic-N. The edge plane graphitic-N (valley) acts the same as pyridinic-N centers via a four-electron pathway, while graphitic-N (center) acts via a two-electron pathway, as elucidated by Sharifi and co-authors (Sharifi et al., 2012). Xing and co-authors postulated that the pyridinic-N form and the neighboring carbon atom play a crucial role in ORR activity (Xing et al., 2014). The ORR and OER activity was observed to increase with an increase in pyridinic-N site density. Mamtani and co-workers postulated the correlation between higher content of the pyridinic-N active site and electrocatalytic activity towards both ORR and OER (Mamtani et al., 2018). Notwithstanding, the research community still debates what form of nitrogen, pyridinic-N, graphitic-N, or their particular ratio make a more significant contribution to electrochemical performance based on both computational and empiric features (Matter et al., 2006; Guo et al., 2016; Singh et al., 2019).

Incorporation of the elements from the second row of the Periodic Table with a larger radius than carbon leads to significant distortion of planar structures creating defects that act as active centers towards ORR/OER as well as HER. S-doping can effectively alter spin/charge density distribution and distorts the carbon lattice by creating large electroactive sites. Sulfur doping was observed to alter spin density distribution via formation of several different sulfur-containing functionalities, including thiophene (aromatic sulfur), thiol, thioesters, sulfoxide, sulfone, and sulfonic acid (Zhao et al., 2012).

XPS showed that a series of four major peaks (S 2p peaks appear as doublets of 2p3/2 and S 2p1/2 due to spin-orbit splitting) can be expected in the C lattice; i.e., at binding energies of 163.80 eV and 165.20 eV corresponding to the S 2p3/2 and S 2p1/2 peaks of the C–S–C bonds, and at binding energies of 167.7 eV and 169.3 eV corresponding to S 2p3/2 and S 2p1/2 indicative of C–SOx–C species, where x is 2, 3, and 4, respectively. (Wang Z. et al., 2014; Zhang J. et al., 2020; Maliutina et al., 2021b). Furthermore, the doping of carbon framework with phosphorous introduces reduced unstable P–O groups as phosphate, phosphine oxide, phosphonic acid, and substituted C-P-C phosphine, thereby improving the electrochemical properties. The XPS P *2p* spectra of carbonaceous metal-free materials exhibit a predominant P–C

characteristic peak and P–O bond at 131.0 ±0.7 eV and 133.7 ± 0.5 eV (Huang et al., 2018). In particular, it has been reported that the co-doping of CNs with two [such as N/S (Wang X. et al., 2014; Ito et al., 2015), N/P (Borghei et al., 2017; Cheng et al., 2021), or N/F (Akula et al., 2021)] or even multi-doping [such as N, S, P and F (Liu et al., 2016; Huang et al., 2018; Li Y. et al., 2019)] with several heteroatoms is an effective way to boost their electrochemical activity synergistically. Recently, Li et al. reported no synergetic effect between N and S dual-doping towards ORR, while the sequence of doped heteroatoms played a critical role (Li J.-C. et al., 2019). Due to this phenomenon, doping of S followed by doping of N promotes the formation of pyridinic-N functionalities. This is attributed as the most active functional group in N, S dual-doped electrocatalyst towards the ORR, while on the counter doping of N followed by doping of S reduces the content of pyridinic-N species, which leads to a nadir of ORR performance (Li J.-C. et al., 2019).

For oxygen adsorption, only the sample with pyridinic-N functionalities possesses binding energy of −1.4 eV, which is superior to that of pyridinic-N-S (−1.0 eV), graphitic N (−1.1 eV), and graphitic-N-S (−1.0 eV) (Li J.-C. et al., 2019). Additionally, the Gibbs free energy diagrams for different catalyst models in an alkaline environment were presented by authors (Li J.-C. et al., 2019) observed all the reaction intermediates (O_2*, OOH*, O* and OH*) formed during ORR. Pyridinic N (green line) plentifully contributes the ORR *via* the OOH* formation with a small energy barrier (0.3 eV), as well as the fact that only the pyridinic N can chemically adsorb O_2 that overall contribute to the ORR. Pyridinic-N functionality was also mentioned as the major responsible active site in other valuable studies (Rao et al., 2010; Zhang and Xia, 2011; Vikkisk et al., 2014; Xing et al., 2014). Notwithstanding, it is still difficult to distinguish the role of secondary or especially tertiary doped heteroatoms not only by computational DTF simulations but especially for such a complex biomass-derived carbonaceous matrix both experientially and theoretically.

The synergy between various techniques can avoid, to a great extent, the limitations of using one sole technique. For example, the advances in using a combination of *operando* XRD and Raman spectroscopy are desired, which enables the complementary characterisation of nanocatalysts in both surface and bulk levels (Zhang H. et al., 2023). Under *operando* conditions, the adsorbate and intermediate species, as well as the structural parameters of the catalyst can be simultaneously traced for an extensive understanding of the reaction pathways and elucidate the role of active centres. Structural defects, such as vacancies, substitutional or interstitial impurities, are regions of absorptive binding for gases and ions are successfully examined by scanning tunnelling microscopy (STM) (Feng et al., 2018; Xiao et al., 2021). X-ray absorption spectroscopy (XAS) has become a universal and in-depth characterisation technique that has been widely used in many fields due to the rapid development of synchrotron radiation sources. (Gao et al., 2017). Because of the difference in the relative absorption threshold of energy, the XAS can be divided into two parts: XANES (X-ray absorption near-edge structure, approximately 40 eV and below) and EXAFS (extended X-ray absorption fine structure, beyond the XANES region) (Xiao et al., 2017). The XAS analysis provides a myriad of information about the structure CNs and their dopants, such as the structure symmetries, element valence, bond distance and adjacent coordination environment of the atom (Liu et al., 2017). Although tremendous amount of works has described *in-situ* electrocatalytic characterisation, *in-situ* and operando characterization techniques and devices with a high resolution are necessary to elucidate the mechanism of defects due to the complexity of electrochemical reactions and the variety of imperfections. Consequently, the synergetic studies based on models of biomass compounds and comprehensive studies on *in situ* tunable engineering and activity of heteroatom-based active sites are highly desired for carbon-based electrocatalysts and a sustainable future.

3.2 Single doped biomass-derived nanocatalysts

Up to date, there are tons of works that report N-doped electrocatalysts towards ORR and a major part is belongs to alkaline electrolyte catalysis. Predominantly, their catalytic performance is still far from that of the Pt/C benchmark, although the characterization of nanomaterials very often describes similar nitrogenized functionalities and analogous distributions (Supplementary Table S3). Rationally incorporating one specific type of heteroatom for designing catalytic active sites remains one of the major challenges when thermochemically valorising biomass for production of efficient electrocatalysts for water splitting.

Zheng and co-authors derived a nitrogen self-doped carbon hollow cubes (NCHCs) was derived from L-lysine precursor at 1,000°C (Zheng et al., 2017). When used as electrocatalysts for the ORR, this composite exhibited an onset potential of 0.92 V vs RHE. This corresponds to a cathodic shift of only 61 mV of the half-wave potential of NCHCs when compared to that of commercial Pt/C (20 wt%), i.e., a common and widely used benchmark for ORR. Interestingly, the NCHCs composite also showed activity for the OER statistically comparable to another widely used commercially available OER standard, i.e., RuO_2/C (20 wt%). The E_{onset} potential close of that of Pt/C was attributed to the role of pyridinic-N and graphitic-N active structures. Wang and others used chitin biomass to fabricate N-doped 3D graphene-like nanosheets (N-DC/G) by doping with pretreating biomass with urea and proceeding with carbonization at 800°C (Wang et al., 2016).

The HRTEM image of the as-prepared N-DC/G sample displayed thickness of the layer less than 50 nm coupled with uniformly distributed porous structure. The corresponding K-L plots showed first-order kinetics towards ORR at different potentials and electron transfer number (n) of about 4, suggesting a direct four-electron pathway attributed to the presence of pyridinic-N and graphitic-N active sites. In another study, He and co-authors (He et al., 2019) used Taro stem plant biomass, impregnation with melamine, followed by KOH activation and carbonization at 800°C. The obtained biochar (3DNPC-800) displayed meso-/microporous 3D architecture with large SSA of 1,012 $m^2 g^{-1}$ and enriched nitrogen content, measured equal to 4.8 at %. The as-prepared biomass-derived 3DNPC-800 electrocatalyst exhibited ORR long-term stability (96.5% retention of the current density after 5.5 h) and resistance to methanol poisoning, which was attributed to the promoted formation of graphitic-N functionalities and developed 3D porous structure. Zhang and co-workers (Zhang

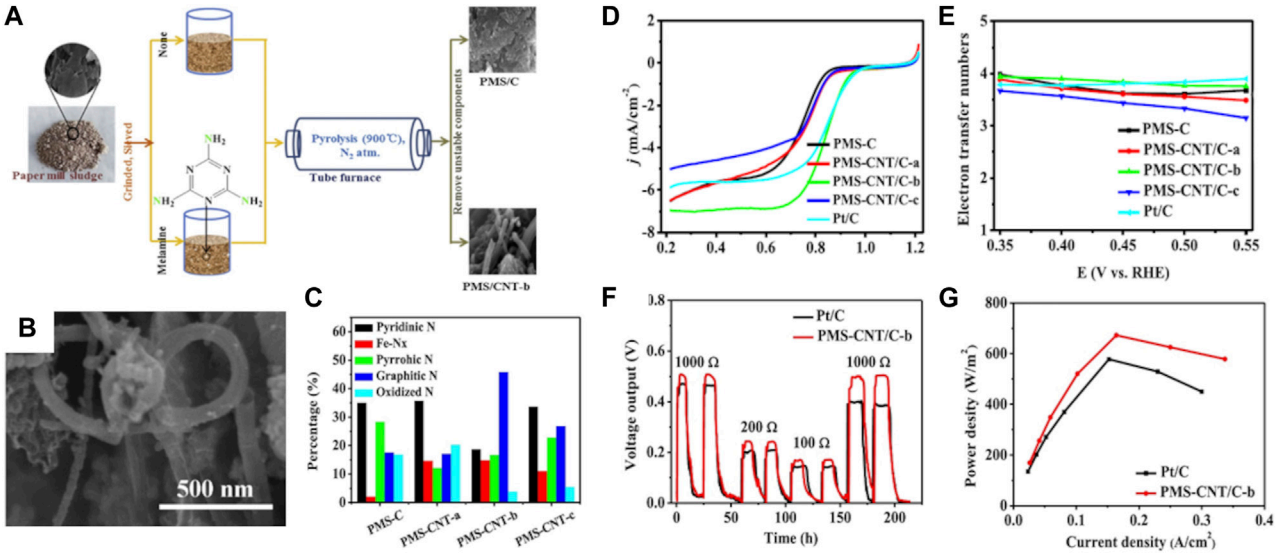

FIGURE 6
Illustration of the preparation process for the paper mill sludge-base catalysts of PMS-CNT/C-b sample **(A)**; SEM image of PMS-CNT/C-b sample **(B)**; nitrogen content as a function of differently prepared samples **(C)**; RDE curves of PMS-CNT/C-b sample at different rotation rates **(D)**; K-L plots at different potentials for PMS-CNT/C-b sample **(E)**; voltage outputs under three different loads **(F)** and polarization curves of Pt/C and PMS-CNT/C-b as the cathodes **(G)**. Reproduced and modified with permission (Zhang et al., 2019).

et al., 2019) synthesised N-doped CNTs from paper mill sludge (PMS) by treatment with melamine (PMS/CNTs-b) and carbonization at 900°C. Results are illustrated in Figures 6A–C.

The as-fabricated biochar displayed enriched formation of CNTs with predominant graphitic-N functionalities. The exceptional ORR activity of PMS/CNTs-b catalyst in contrast to that of Pt/C benchmark results in the most positive E_{onset} potential of 0.99 V vs RHE and current density of −6.96 mA cm^2 shown in Figure 6D. The calculated electron transfer number of the PMS/CNTs-b catalyst is a direct four-electron pathway, as can be seen in Figure 6E. The formation of CNTs was attributed to the addition of melamine, which was at first just considered as a nitrogen source to develop N-doped PMS-based catalysis in this work, during the pyrolysis of PMS. The remarkable ORR performance of PMS-CNT/C-b was correlated with the formed nanotube/nanoporous structure and the synergistic effect of abundant N groups, iron nitrides and thiophene-S. It can be seen in Figures 6F,G that the PMS/CNTs-b catalyst was employed in microbial fuel cells and possessed a power density of 675.72 W/m^2 that is improved when compared to Pt/C cathode (580.46 W/m^2).

A collection of biomass-based nanostructures with single heteroatom doping are reported in Supplementary Table S3 alongside physical chemical properties, and claimed active sites. From a comparison of the data reported in Supplementary Table S3 (as well as for most of the considered bifunctional or trifunctional electrocatalysts), graphitic-N was mentioned as the predominant active site.

3.2.1 Dual-doped biomass-derived nanocatalysts

The additional introduction of secondary heteroatoms, such as S, P, B and/or F into N-doped carbon is a promising strategy for boosting the electrochemical performance of carbon-based electrocatalysts (Xian et al., 2019; Zhang J. et al., 2020), although single S, P, B or F-doped biomass derived materials have shown electrocatalytic efficiency not as good as in the case of single N-doped. The complete picture explaining this enhancement effect promoted by the second dopant has yet to emerge, however, creation of catalytically active defects induced by the secondary heteroatom doping, as well as improvement of electronic properties of active site and surrounding which ultimately favour catalysis have both been proposed (Zhang et al., 2016c). In addition, the simultaneous presence of dopants and vacancies was observed to be more effective than doping alone, for example, in enhancing quantum capacitance as well as surface charge storage of graphene (Zhou et al., 2020).

Amiinu and co-workers synthesized N,S-codoped 3D assembled ultrathin graphene-like nanosheets (NSG) using cysteine as carbon precursor via thermochemical treatment at 900°C in the effort of developing bifunctional electrocatalysts for ORR/OER (Figure 7A) (Amiinu et al., 2016). Their graphene nanosheets exhibited mesoporous structure with BET SSA of 319.93 m^{2}g^{-1} and uniformly distributed heteroatoms (Figures 7B,C) with predominant graphitic-N, pyridinic-N, and thiophene-S species (Figures 7D,E). As shown in Figures 7F,G, the as-prepared graphene layers displayed comparable ORR performance to that of standard Pt/C electrode ($E_{1/2}$= −0.19 V and j_L= −5.34 mA cm^{-2} at −1.0 V) in an alkaline environment. Additionally, the NSG sample possessed promising OER activity and stability of 10 mA cm^{-2} at 0.69 V vs. SCE that is similar to that of IrO_2 (0.64 V vs. SCE) and a slight decrease of the oxidation potential only on 17 mV after the 1000th cycle, as shown in Figures 7H,I.

Han et al. (Han et al., 2020) proposed fructus azedarach biomass-derived N,P-codoped electrocatalyst (NPDC-1.09) as an

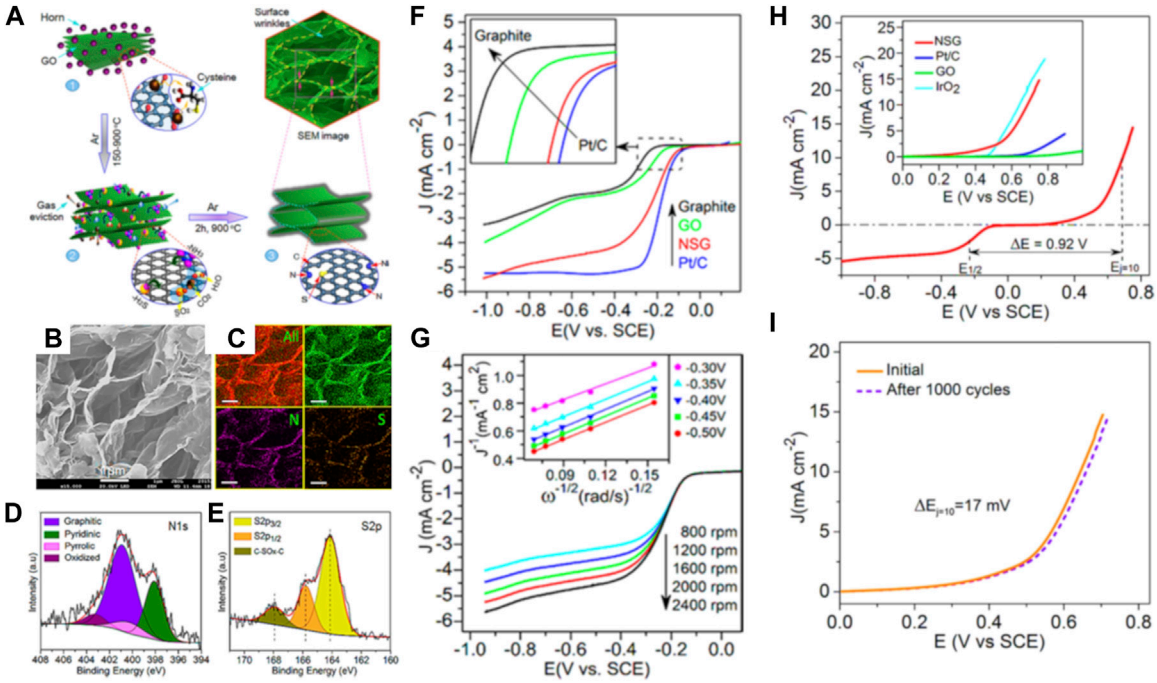

FIGURE 7
(A) Schematic illustration of the formation of NSG sample: (stage 1) Homogeneous mixture of graphene oxide and horn, (stage 2) disintegration/release of cysteine moieties and coverage of GO surface leading to the reaction of functional groups, eviction of gaseous species, and the formation of S and N containing moieties (e.g., H_2S, NH_3, *etc.*), and (stage 3) doping of N and S into the graphene carbon network;**(B)** FE-SEM image; **(C)** Elemental distribution EDX mapping of carbon, nitrogen and sulfur; **(D)** N 1s spectra and **(E)** S 2p spectra of NSG sample; **(F)** ORR LSV curves of graphite, GO, NSG, and Pt/C, and **(G)** ORR LSV at different rotation rates, Inset is the corresponding K-L plots; **(H)** Overall LSV potential curve of NSG sample (Inset is the comparison of OER currents of NSG, Pt/C, GO, and IrO2), **(I)** Stability of OER current before and after accelerated CV for 1,000 cycles. All data were recorded in 0.1 M KOH solution. Reproduced and modified with permission (Amiinu et al., 2016).

electrocatalyst for the ORR. TEM and HRTEM images show that the prepared NPDC-1.09 catalyst displayed a 3D porous nanosheet network with an interlayer spacing of 0.340 nm, indicating an amorphous structure with an I_D/I_G ratio of 1.09, suggesting a formation of numerous amount of defects due to N and P codoping. According to XPS characterization, nitrogen existed in pyridinic-N, pyrrolic-N, and graphitic-N forms, while phosphorous existed in P-O, P-N, and P-C moieties with an N: P ratio of 1.09 am %. Based on in-depth XPS and Raman observations, the theoretical structure of the carbon nanosheet of the NPDC-1.09 sample possible position of heteroatom defects in the carbonaceous backbone.

The electrocatalytic ORR activity was determined by LSV tests, where NPDC-1.09 catalyst exhibited E_{onset} potential of 0.94 V vs RHE and $E_{1/2}$ potential of 0.84 V vs RHE, and the potential gap of $E_{1/2}$ between Pt/C and NPDC-1.09 was 50 mV. The Tafel slopes of NPDC-1.09 and Pt/C reached close values of 119 and 120 mV dec^{-1}, respectively, suggesting promising activity towards ORR with reasonable kinetics for potential fuel cell applications. In other studies of Xiao and co-authors, phytic acid was used as a precursor to obtain N,P-codoped ultrathin nanosheets coated with multi-walled nanotubes at 900°C (CNT@NPC-900) (Xiao et al., 2019). The synthesized CNT@NPC-900 electrocatalyst displayed remarkable HER activities with overpotentials to reach a current density of 10 mA cm^{-2} of 167, 440, and 304 mV in acidic, neutral, and alkaline environments, respectively. Such promising activities were attributed to uniformly distributed N and P heteroatoms and formed pyridinic-N and P-O active sites. Additionally, the CNT@NPC-900 sample exhibited little degradation after 3000 CV cycles and supreme working efficiency for more than 100 h (Xiao et al., 2019).

Wang et al., 2017 employed guanidine carbonate salt as a biomass precursor to obtain B,N-codoped carbon nanosheets (BCN) to be tested for ORR (Figure 8A). Polyvinyl alcohol (PVA), boric acid, and guanidine carbonate molecules were used for cross-linking polymerization, then the gel precursor was pretreated with a symmetric triblock copolymer comprising polyethylene oxide and polypropylene oxide in an alternating linear fashion, PEO-PPO-PEO (Pluronic® P123), for the development of porous and nanosheet structure. After carbonization at 900°C in an N_2 environment, the gel precursor converted into 2D nanosheet layers architecture with uniformly distributed B and N heteroatoms (Figures 8A–C). Potential active sites were interrogated by XPS spectroscopy (Figures 8D–F), and it was found that boron formed B-N-C and B-O junctions whilst nitrogen showed the formation of C-N-B, pyridinic-N, pyrrolic-N, and graphitic-N functionalities. The SSA of 817 $m^2 g^{-1}$ and an enriched porous structure were ascribed to the templating pretreatment with Pluronic® P123. It can be seen in Figure 8G that the BNC nanosheet sample possessed E_{onset} and $E_{1/2}$ values of 0.940 and 0.82 V vs. RHE, both of which are comparable to those of

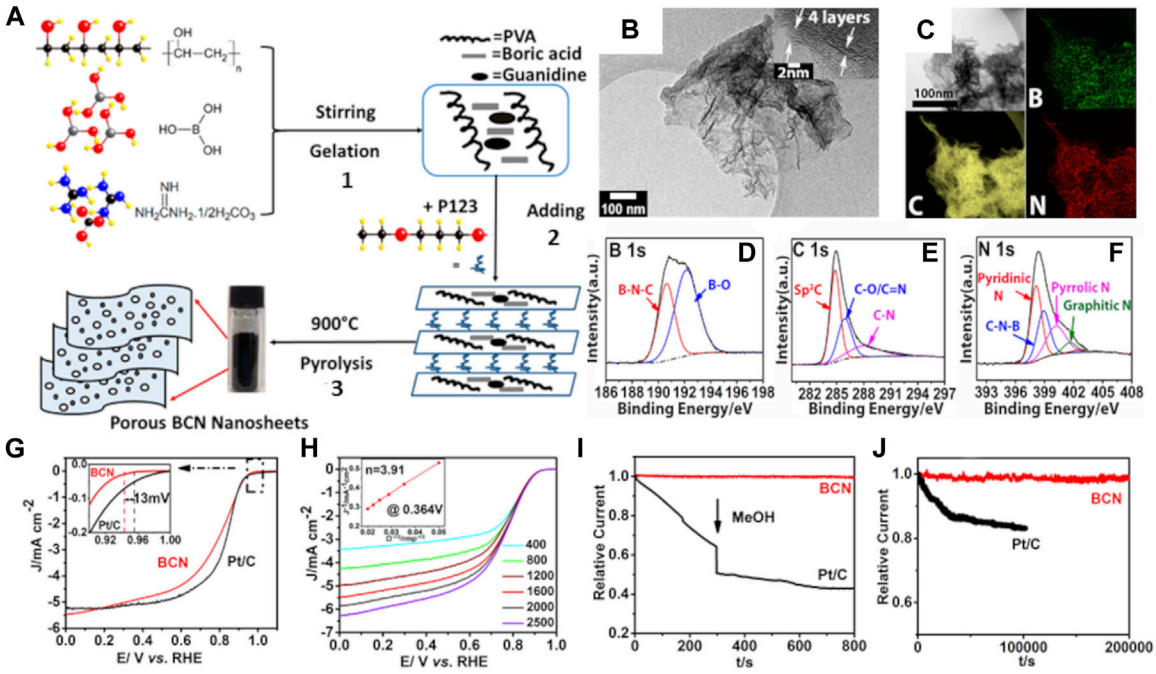

FIGURE 8
(A) The schematic synthesis process of porous BCN nanosheets including (1) Gelation of polymer precursor, (2) Addition of P123, and (3) Pyrolysis at 900°C under N_2; **(B)** TEM image of BCN nanosheet with 3–5 graphene layers; **(C)** TEM image of BCN nanosheets and corresponding EDS mapping of B, C, and N elements; XPS **(D)** B 1s, **(E)** C 1s, and **(F)** N 1s spectra of BCN nanosheets; **(G)** ORR catalytic performance of the porous few-layered BCN in 0.1 M KOH. LSV curves of BCN catalysts and Pt/C at a rotation rate of 1,600 rpm and a scan rate of 5 mV/s. The inset shows the higher magnification of LSV curves between 0.9 and 1.0 V vs. RHE; **(H)** LSV curves of BCN catalysts with various rotation rates from 400 to 2,500 rpm at a scan rate of 5 mV/s. The inset shows the corresponding Koutecky–Levich plot; **(I)** Chronoamperometric measurement for few-layered BCN and Pt/C in an O_2-saturated 0.1 M KOH solution and when 3.0 M methanol is added at around 300 s at an electrode rotation rate of 1,600 rpm; **(J)** Current-time chronoamperometric response of few-layered BCN and Pt/C in an O_2-saturated 0.1 M KOH solution at a rotation rate of 1,600 rpm. Reproduced with permission from (Wang et al., 2017).

Pt/C electrode, i.e., 0.953 and 0.84 V vs. RHE, respectively. The electrons transferred number is estimated to be 3.91 at 0.364 V vs. RHE derived from the Koutecky–Levich (K-L) plot and attributed to a four-electron pathway for ORR, as seen in Figure 8H. Finally, the BNC porous sample showed supreme crossover effect to methanol poisoning and outstanding long-time durability performance in alkaline medium (Figure 8J). Same remarkable that Pt/C ORR characteristics were reported in an acidic environment (Wang et al., 2017). Some of the outstanding codoped biomass-derived nanostructures towards electrocatalytic ORR/OER/HER are summarized in Supplementary Table S4.

3.2.2 Multi-doped biomass-derived nanocatalysts

One of the prospective ways to tune the photo-response property, generate higher electroconductivity, and facilitate the transport of the photoinduced charge carriers to the surfaces of the catalysts is the metal-free multidoping (i.e., three or even four heteroatoms simultaneously) due to diminished recombination of the electron-hole pairs with additional electrons. Non-metal multidoping strategies are yet to be fully understood and a significant amount of empiricism remains around multidoping in biomass-derived electrocatalysts, making any attempt at rational design very difficult (Wu et al., 2015; Zheng et al., 2016; Chang et al., 2020). Controversies also arise as to whether or not heteroatoms exhibit synergistic effects (Li Y. et al., 2019). The mechanism of multidoping and substitution is rather complex and thorough kinetic and mechanistic investigations need to be undertaken.

Huang and co-authors employed guanine as a precursor for the fabrication of N,S,P-multidoped nanosheets (GSP-1000) at 1,000°C (Huang et al., 2018).

The GSP-1000 sample exhibited ultrathin 2D carbon nanosheets and developed porous structure with uniform distribution of N, S, P, and O heteroatoms indicating sufficient development of defects in the carbonaceous matrix. XPS analysis indicated promoted the formation of graphitic-N, pyridinic-N, thiophene-S, and P-C defects. Rotating disk electrode (RDE) derived LSV ORR curve of GSP-1000 exhibited a comparable trend to that of commercial Pt/C activity with onset potentials (0.99 V vs RHE and 1.03 V vs RHE) and half-wave potentials (0.84 V vs RHE and 0.85 V vs RHE), respectively. The average electron transfer numbers derived from the linear Koutecky–Levich (K–L) plots demonstrated a favorable four-electron reduction pathway towards ORR. Good stability with the initial activity decreased only to 90.7% after a 4 h test and superior resistance to the methanol poisoning. In other study, authors also used guanine compounds to obtain similar to previous study 3D mesoporous graphene-like nanosheets (Huang et al., 2019). It was found that high temperature carbonization in the CO_2 environment leads to the controllable generation of mesopores and high SSA due to the etching effect of partial gasification reaction $C + CO_2 \rightarrow 2CO$.

TABLE 1 Summary of the multi-doped metal-free biochar-based electrocatalyst for ORR/HER/OER.

Pristine biomass	Obtained nanostructure	Approach	Synthesis method	Physical properties	Electrochemical properties	Active sites	Refs
Yeast and glucose	Yolk-shell	ORR	Pyrolysis at 800°C in N_2 for 2 h	SSA of 574.7 m^2 g^{-1} for mesopores and 580.6 m^2 g^{-1} for micropores; Structural defects (I_D/I_G = 1.25) due to the doping of N, P, and B	E_{onset}= 0.846 V vs RHE; 4e− pathway (n=3.78–3.90); Tafel slope of 72 mV dec^{-1} in O_2-sat. 0.1 M KOH; Good durability after 15,000 cycles	N/P/B-doping; Formation of N-B-C and B-N-C moieties; Doping of B attributed to boosting of ORR	Zheng et al. (2016)
Softwood kraft pulp	3D interconnected carbon nanofiber	HER	Solvothermal extraction of cellulose nanofibrils in tetrahydrofuran (THF) at 245°C/4.5 h; Pyrolysis with melamine and phytic acid at 400°C/2 h; Carbonization at 900°C/2 h	SSA of 682 m^2 g^{-1}; Structural defects (I_D/I_G = 0.88) due to the doping of N, P, and S	Tafel slope value of 99 mV dec^{-1}; An overpotential η_{10} of 331 mV vs. RHE in 0.5 M H_2SO_4	N/P/S-multidoping; predominant graphitic and pyridinic-N; thiophene-S	Mulyadi et al. (2017)
Guanine	Few-layered carbon nanosheets	ORR	Washing in H_2SO_4 and H_3PO_4 for 24 h; Pyrolysis at 1,000°C in N_2 for 1 h; Soaking in 1 M HCl for 10 h; Pyrolysis at 1,000°C in N_2 for 1 h	SSA of 486 m^2 g^{-1}	4e− pathway (n=3.8) in 0.1 M KOH; $E_{1/2}$ is 0.84 V $E_{1/2}$ is 0.67 V in 0.1 M $HClO_4$; $E_{1/2}$ is 0.70 V vs RHE in 0.1 M PBS	N//S/P-multidoping; pyridinic and graphitic N	Huang et al. (2018)
Spinach leaves	3D interconnected carbon nanosheets	ORR	Chemicsl activation with $ZnCl_2$ and carbonization at 850°C	numerous amount of defects (I_D/I_G = 1.17)	4e− pathway (n=3.81) in 0.1 M KOH; $E_{1/2}$=0.82 V vs commercial 20% Pt/C ($E_{1/2}$=0.86 V vs RHE)	N/S/P self-doping; pyridinic-N, pyrrolic-N, C-P, C-S-C, and C-N/P	Huang et al. (2020)

Lately, authors represented B,N,F-multidoped carbon nanosheets (BNFC-800) by using cigarette butts as biowaste precursors at 800°C (Zhang Q. et al., 2020). The as-prepared nanosheets possessed a mesoporous structure with uniformly distributed B, N and F heteroatoms. The XPS high-resolution spectra of B 1s heteroatom exhibited formation of B_4C, BC_3, BC_2O, B-N and BCO_2 functionalities indicating the sufficient substitution of carbon atoms at the edge by boron atoms and development of defective sites. Parallel, deconvolution of N1s spectra showed the formation of B-N, pyrrolic-N, pyridinic-N, graphitic-N and oxidized-N moieties, suggesting efficient incorporation of N heteroatom. The detected B-N bond (397.7 eV) displayed the interaction between B and N heteroatoms. F 1s spectrum consisted of ionic C-F (684.7 eV), C-F (687.8 eV) and semi-ionic C-F (690.4 eV) moieties. Authors attributed formed pyridinic-N, BC_3 and C-F species as active centers towards ORR and OER.

BNFC-800 sample possessed a Pt-like ORR activity with half-wave potential $E_{1/2}$ = 853 mV vs RHE. Following, OER activity was tested in 1 M KOH electrolyte. BNFC-800 showed a low overpotential of 313 mV to deliver 10 mA cm^{-2}, which was similar to IrO_2 benchmark. Furthermore, the as-prepared BNFC-800 electrocatalyst possessed a high battery performance of 51 mW cm^{-2} that is superior to Pt/C-IrO_2 with the maximum power density of 39 mW cm^{-2} (Zhang Q. et al., 2020).

Unfortunately, up to date, there is a lack of papers on metal-free multi-doped biomass-derived nanostructures towards ORR due to the complexity of controlling the formation of a desired structure from a given biomass or waste precursor (Table 1). Determining and rationally designing catalytic active centres and controlling surface engineering is far tougher than in the case of single-doped or dual-doped structures. To complicate this landscape is the lack of strong evidence on the synergistic effect of having multiple dopants and how (depending on their chemical nature) they interac with eachother and with the carbonaceous backbone.

3.3 Earth abundant metal-doped carbon nanostructures

Doping biomass derived carbonaceous nanostructured with Earth abundant, or not rare, metals can exploit the electrocatalytic properties of transition metals at relatively low costs, compositional flexibility, and provide opportunities for large scale production and deployment eliminating major barriers associated with the economy, origin, abundancy, production and supply chain typical of rare and precious metals (Han et al., 2019). Rationally designing earth-abundant hybrid electrocatalysts for ORR/HER/OER approaches as rare and precious metal substitutes is of extraordinarily importance in the quest to reach net zero carbon emissions. In order to enhance the electrocatalytic activity of carbonaceous catalysts and further extend their feasibility for electrochemical energy generation and storage devices, introducing certain TMs (Fe, Mn, Co, Ni, Cu, Mo, Ti, Ta, *etc.*) and their derivatives in form of oxides/suboxide, sulfides, selenides, nitrides/oxynitrides, carbonitrides is a sought after strategy. Previous studies indicate that adding iron (Wang K. et al., 2020) or cobalt

TABLE 2 Summary of the metal-doped biochar-based nanomaterials as electrocatalyst for ORR/HER/OER.

Pristine biomass	Obtained nanostructure	Approach	Synthesis method	Physical properties	Electrochemical properties	Active sites	Refs
Wine mash	Ultrathin nanoribbons	ORR	Pre-pyrolysis at 200°C in N_2 for 0.5 h; Washing in 3 M HCl; Carbonization at 850°C in N_2 for 1 h	SSA of 1,066.6 m^2 g^{-1}; Large structural defects, amorphous structure (I_D/I_G = 3.06) due to the doping of N and insufficient graphitization	4e− pathway (n=3.7) in 0.1 M KOH; $E_{1/2}$ is 0.84 V (vs RHE); Stability for 30,000 s maintains 90% of initial current	Metal-N (Fe-N); pyridinic-N	Wang et al. (2019)
Cellulose microfibrils	3D interconnected graphene nanosheets	ORR	Activation with KOH for 12 h and carbonization at 650°C 700°C for	Structural defects (I_D/I_G = 1.12) due to the doping of N	E_{onset}= 0.0 V vs Ag/AgCl; $E_{1/2}$= −0.15 V vs Ag/AgCl; 4e− pathway (n=3.91)	Single atom (Fe); Fe-N; Pyridinic-N	Li et al. (2019d)
Spirulina microalgae	3D honeycomb-like nanosheet network with rough edges	ORR	Carbonization of spirulina at 800°C in N_2 for 2 h; Doping with g-C_3N_4 and urea; Carbonization of the mixture at 900°C in N_2	Ultralarge SSA of 1927.41 m^2 g^{-1}; Large structural defects, amorphous (I_D/I_G = 2.3) due to the doping of N and unsufficiemt graphitization	E_{onset}= 0.99 V vs RHE; $E_{1/2}$= 0.86 V vs RHE; 4e− pathway (n=3.87); Zn-Air Battery: OCV 1.44 V; P_{max} 179 mW cm^{-2}; the specifc capacity of 641.9 mA h g^{-1}; the energy density of 837.4 W h kg^{-1}	N content of 4.30 at%; S consists in pristine biomass; Single-atom (Fe) integrated with Fe_2O_3 clusters; Metal-N (Fe-N_x); C-S-C thiophene	Lei et al. (2020)
Vitamine B12	3D porous nanosheets	ORR/HER	Doping with g-C_3N_4; Pyrolysis at 500°C in N_2 for 2 h; Carbonization at 800°C in N_2 for 4 h; Washing in H_2SO_4 for 18 h	SSA of 634.9 m^2 g^{-1}; Structural defects (I_D/I_G = 0.94) due to the partial graphitization	ORR: $E_{1/2}$= 0.87 V vs RHE. HER: low overpotential (η_{10} = 319 mV). Zn-air battery: a peak power density of 101.3 mW cm^{-2} at a potential of 0.71 V	Co., N, P-doping; CoN_x-active sites	Niu et al. (2020)
Pomelo peel	Mesoporous carbon nanosheets	ORR	Pretreatment-KOH etching and H_2SO_4 hydrolysis; Isolation of cellulose nanofibers; Doping with trithiocyanuric acid and microwave pyrolysis at 700°C for 40 min; Microemulsion addition of Ta_2O_5 Carbonization in N_2 for 40 min	SSA of 336.82 m^2 g^{-1}; Structural defects (I_D/I_G = 1.11) due to the co-doping of N and S and low graphitization	E_{onset}= 0.931 V; $E_{1/2}$= 0.82 V; j_L= −5.24 mA cm^{-2}; 4e− pathway (n=3.87); Tafel slope of 76 mV dec^{-1}	N,S-dual doping; Metal-N (Ta-N_x/Ta-OCN); Suboxide TaO_x species; Pyridinic and graphitic-N	Maliutina et al. (2021b)

In O_2-sat. 0.1 M KOH, otherwise specifically noted.

(Zhang et al., 2018) salts into a porous carbon catalyst can significantly improve the ORR catalytic performance of the resulting samples. Furthermore, nickel-based (Ding et al., 2019) carbon materials have been extensively considered as a highly efficient HER/OER electrocatalyst. In synthesis of bifunctional/trifunctional electrocatalysts, doping of metal or metal oxides onto a biomass-derived CNs may be an alternative manner. This section represents recent progress towards the next-generation of multifunctional hybrid metal-loaded green catalysts, as summarized in Table 2 and Supplementary Table S5. It can be seen in Table 2 and Supplementary Table S5, that the most of widespread metal-based interractions are presented by Fe-N_x (or Fe-N-C) and Co-N_x NPs (or Co-N-C) heterojunctions, i.e., a central TM cation coordinated to pyridinic nitrogen on edges of the graphitic surface. Despite that, pyridinic-N can be found as the most common active sive for ORR/OER of biomass-derived carbonaceous nanosupport.

Recently, Zhang et al. (2018) employed chitosan biomass for *in situ* synthesis of Co,N-codoped CNTs, amongst other N and Co doped nanosheets. It can be seen that the synthesized CNT electrocatalysts possess tubular morphology with uniform distribution of N and Co atoms. A sample of Co(16%) and N codoped CNT (Co16%-NCNT-T800) synthesized at 800°C has been found to display the highest ORR current density (6.92 mA cm^{-2}) among other carbon based catalysts and Pt (40 wt%)/C (5.06 mA cm^{-2}) and a half-wave potential closest to Pt (40 wt %)/C. In line with recent research showing that M–N–C active sites formed via coordination of the metal with pyridinic nitrogen plays a crucial role in enhancing ORR activities, Zhang et al. (2018) showed that key for high ORR activity is an effective formation of the Co–N–C active sites (via pyridinic nitrogen). The Authors also found that the Co16%-NCNT-T800 sample exhibited the highest specific capacitance of all electrocatalysts. The higher the specific capacitance (the latter resulting directly from electrochemical specific surface area), the higher the amount of active sites for current density enhancement. Furthemore, the as-prepared Co16%-NCNT-T800 electrocatalyst showed exceptional resistance to the

methanol poisoning with no obvious drop in current (in contrast to that of Pt/C benchmark) and long-time stability.

In a recent study, of Lv and others (Lv et al., 2019) fabricated a hierarchical porous Co,N-codoped bio-carbon bifunctional electrocatalyst (CoTBrPP@bio-C) for an all-pH ORR and HER by using a simple one-pot co-pyrolysis over a commercially available mushroom template with adsorbed Br-substituted porphyrinato cobalt (CoTBrPP). The as-prepared nanosheets displayed a porous stratified volcanic rock-like structure with Co-N_x functionalities. XPS was executed to determine the impact of Br on the formation and distribution of nitrogenized functionalities. Autors claimed that the addition of Br can promote the formation of Co-N_x and graphitic-N species, attributed to active centers for ORR and HER. Further, ORR and HER electrocatalytic activity were evaluated in 0.1 M KOH and 1 M KOH environments, respectively. The obtained biomass-derived CoTBrPP@bio-C hybrid electrocatalyst possessed outstanding activity towards ORR (E_{onset}=0.93 V vs. RHE and $E_{1/2}$=0.85 V vs. RHE) as well as HER activity. The excellent Zn-air battery performance of the CoTBrPP@bio-C hybrid with the open-circuit voltage remained at 1.51 V, while the discharging polarization and the corresponding power density of 100 mW cm^{-2} at 155 mA cm^{-2}, were superior to that of Pt/C (78 mW cm^{-2} at 119 mA cm^{-2}).

4 Nanostructured biochar: economic evaluation and circular economy approach

The physical-chemical characteristics of biochar, influenced by biomass type, thermal conversion, and preparation circumstances, contribute to its electrocatalytic activities. Altering these features through physical and chemical activation techniques can enhance biochar's surface functional groups, surface area, and porous structure. Biochar-based catalysts show potential as renewable alternatives to expensive benchmark noble-based materials. Using CNs from biochar offers economic and environmental benefits. However, addressing limitations and knowledge gaps is crucial, such as scaling up production and utilization of machine learning models.

In general, cost analysis of biochars production consist of the following crucial steps and factors: (a) feedstock purchase cost, (b) transportation costs, (c) synthetic/fabrication costs, (d) operating labor/employed personnel costs, (e) storage costs, (f) maintenance, insurance, and other costs. It was reported that a charcoal production stage (carbonization) cost 113 \$ ton^{-1} charcoal (Norgate and Langberg, 2009). Production stage cost for three different biochars production plants were studied (Shackley et al., 2011). Production stage cost including capital, storage, utility, labor and other plant cost ranged from 98 US\$ ton^{-1} to 353 US\$ ton^{-1} charcoal (Suopajärvi and Fabritius, 2013). A life cycle analysis for overall biochar production via the pyrolysis process found the great importance of biochar in the soil is the carbon sink effect which accounts for 50% of the total negative emissions (or contribution of −368 $kgCO_2$/ton of dried feedstock based on the carbon footprint calculation) (Costa et al., 2023). However, the lack of comprehensive studies on synergistic assessment of nanostructured biochar and the circular economy is remaining. Therefore, these areas need more attention and further investigation.

Furthermore, there is a gap in understanding the long-term performance and scalability of CNs derived from biomass. It is crucial to assess the durability and regeneration potential of nanostructured biochar, as well as its impact on the surrounding environment. Economic feasibility studies are also needed to evaluate the cost-effectiveness of implementing large-scale biochar treatment systems. Moreover, there is a need for comprehensive life cycle assessments to understand the overall environmental impacts of utilizing biomass-derived biochar in electrocatalytic systems. This includes assessing the carbon footprint, energy requirements, and potential by-products or emissions associated with its production and use. Addressing these innovation and research gaps will contribute to the development of efficient, sustainable, and economically viable biochar-based solutions for sustainable energy generation/storage within the circular economy framework.

Although, depending on the final target, biochars should be modified to improve certain functions. Thus, some of the future perspectives of nanostructured biochars to be used as cost-efficient electrocatalysts may include:

(0) Comparing the cost and overall electrochemical properties of biomass-derived NCs with other benchmark catalysts, such as Pt/C, doped CNTs, CNFs, graphene, *etc.*,;
(1) Study on the optimisation of price factor for maximum yield of nanomaterials at an optimum pyrolysis temperature/pressure/heating rate/reaction time/atmosphere *etc.*
(2) Conduct commercial scale cost analysis of nanostructured biochars production plant.
(3) *In situ* or post-treatment modification of biochar surfaces utilizing different modifying agents to achieve selectivity and optimum performance.

5 Conclusion and future horizons

In this review, we have discussed the recent advances in biomass-derived CNs as non-noble electrocatalysts with the sustainable goal of establishing an environmentally sensible circulation of energy and materials. The role of biomass originality and pretreatment methods were elucidated with a focus on the formation of CNs. The performance of recently reported biomass-derived CNs is discussed, reflecting on mechanistic understanding of principles for biomass conversion based on their origin. Specifically, the current status of the most superior biomass-derived electrocatalysts for the ORR/HER/OER based on a common set of figures of merit, namely, overpotential, half-wave potential, current density, stability, and durability, as well as methanol tolerance tests in case of ORR and OER were explored in detail. Various design strategies to construct a heteroatom-supported 2D or 3D nanocatalyst architecture promote a large number of active sites including doping/defect introduction, chemical functionalization/activation well as the synthesis method and conditions, were discussed. Furthermore, the need to elucidate the kinetics and reaction barriers at the electrolyte-electrode interface and the modalities of electron/proton transfers cannot be exaggerated. In this regard, one of the main conclusions is to establish an integrated scheme to

strengthen both experimental and theoretical insightful tools towards the design, synthesis, characterization, and testing of feasibility for practical catalyst systems. Despite significant progress made as discussed above, there are still many challenges ahead in the development of electrocatalysts for ORR/HER/OER, and further efforts are also required to elucidate other factors that can expedite the advancements. Prospective research studies in this regard can focus on the following:

(1) An in-depth understanding of the related mechanism for each reaction, especially over specific facile biomass-derived nanostructures, will provide a knowledge-driven scheme for the design and development of efficient catalysts by optimizing computational studies towards reaction mechanisms. Specifically, the investigation into the mechanism can guide structural modification, electronic reconfiguration, and prevention of catalyst active site degradation during cycling. Most reported computational studies are based on simplified synthetic precursor-derived models and lack accurate prediction of the actual kinetics and reaction mechanisms at given operating conditions.

(2) Morphology-engineered metal-free biomass-derived nanostructures have demonstrated high-performance efficacy and stability in the considered electrocatalytic processes. On this account, the catalyst with abundant active sites can be fabricated into specific configurations (such as nanosheets, CNTs/CNFs) to improve the catalysts' physiochemical properties. By so doing, the porosity and number of accessible active sites are increased; hence, facilitating species adsorption, activation, and electron diffusion. Therefore, the construct of these nanocatalysts must be optimized.

(3) Generally, the extensive integration of computational and experimental studies in the construct of catalyst systems is lacking, particularly in the fabrication methods for the engineered catalysts. Most reported studies in this regard are theory-based, with little or no detailing of experimental schemes to effectuate the newly developed catalyst active sites. Ideally, integrating all mechanistic information demands a rigorous standardization of experimental setups and procedures, in-depth understanding beyond surficial catalyst interactions, and multi-scale modeling entailing all these aspects.

(4) Thorough knowledge based on the above outlooks is essential to developing novel or improved electrocatalysts. Thereupon, the controlled development of functional nanostructured composites with better catalytic activity and stability from biomass is not far-fetched. For instance, various heteroatom-doped functional carbon-based nanomaterials or metal-added hybrids have displayed exceptional potential towards overall water splitting due to their tuneable structure, available active sites, and durability in alkaline/acidic electrolytes. In summary, the optimization of these advanced functional materials is vital to the practical application of these processes.

(5) In addition to the optimization of composite catalysts, measures can be adopted to expedite this process via accelerating catalyst discovery. Due to advancements in machine learning and material genome databases, accelerating catalyst discovery by high-throughput assessment and non-supervised analytical techniques such as AI algorithms, aided with identifying key synthetic parameters, is realistic. *In situ* and *an operando* studies are highly required for online evaluation of reaction kinetics, such as *in situ* Raman spectroscopy, *in situ* electron paramagnetic resonance (EPR) *in situ* differential electrochemical mass spectrometry (DEMS). Moreover, the state-of-the-art computer-aided robotic and automated facilities enable autonomous and controlled nanocatalyst synthesis from biomass precursors, characterization, and performance evaluation, which could significantly boost discovery of the advanced catalysts for electrochemical conversion of water and other molecules such as ammonia and carbon dioxide.

(7) According to recent life-cycle assessment (LCA) studies, nanostructured biochars are promising and economic feasible materials that are believed to provide multiple-advantages for both environmental and agricultural activities and the future practical implementation of electrochemical systems. Moreover, no literature has mentioned the deployment of circular economy in the combination of biomass/waste derived CNs and electrochemical systems/devices toward the benefits of alternative energy generation and storage. Therefore, to facilitate the progression of the carbon-negative circular economy, the future directions of applying biomass/waste-derived CNs can be suggested, i.e., (1) establishing regional circular centres utilizing various biomasses and wastes, (2) advancing the electrochemical systems and storage devices towards large-scale demonstration, and (3) evaluating the environmental benefits, potential harms, and CO2 reduction potentials.

(8) Based on observed literature scope we summarise the following factors towards efficient generation of CNs from biomass for electrochemical approaches: (a) the optimal temperature range for maximized yield of CNs in biochar is between 450°C and 800 °C. Different feedstocks require specific pyrolyzing temperatures due to their particular structures and chemical compositions: lignocellulosic-based generally require higher temperatures for decomposition/biochar formation compare to that non-lignocellulosic biomass; (b) generally, the maximized CNs yield in biochar was reported for pyrolysis in oxygen-limited or nitrogen atmosphere for reaction time between 1 and 2 h; (c) microwave-assisted pyrolysis can significantly decrease the pyrolysis time and facilitate the formation and grow of CNTs/CNFs features due to proposed CVD mechanisms.

(9) For large-scale and cost-effective implementation in the cutting-edge fuel cells, water splitting systems, supercapacitors, and rechargeable batteries, it is necessary to maintain the efficiency of biomass conversion and the quality of CNs without additional processing step. During the functionalization of biochar (i.e., surface oxidation, amination, sulfonation, *etc.*), complex operations and toxic chemicals should be avoided in order to preserve an environmentally friendly solution. Regardless of the pre/post-treatments, residual impurities can always remain in the biochar, which can negatively affect the operation of the

devices. Develop strategies to reduce the content of impurities to an acceptable minimum is necessary.

(10) In view of the technological advancement in this field, researchers underscore the importance of developing more resolute legal and techno-economic frameworks that can successfully promote sustainable solutions by internalizing environmental costs and hinder drawbacks. Overall, a level of parallelism between the technological, economic and legal aspects of these technologies both at the initial stage of development and coordinated efforts based on a long-term view should be established. However, the processes are still a long way away from global practical application and feasibility tests on a pilot scale for the highly efficient biomass-derived nanomaterials are paramount on the way for a sustainable future.

Author contributions

KM: Investigation, Validation, Data curation, Formal analysis, Visualization, Writing—original draft, Writing—review and editing. JO: Software, Data curation, Writing—review and editing. CH: Software, Formal analysis, Writing—review and editing. LF: Formal analysis, Writing—review and editing, Supervision, Project administration, Funding acquisition. AF: Conceptualization, Methodology, Resources, Writing—review and editing, Project administration, Funding acquisition.

Funding

This work was supported by the Natural Science Foundation of Guangdong Province (2021A1515012356), the Scientific Foundation of Guangdong Provincial Education Department (2019KTSCX151), Shenzhen Government's Plan of Science and Technology (JCYJ20180305125247308), and the National Natural Science Foundation of China (51402093). The Net Zero Innovation Institute of Cardiff University is kindly acknowledged for supporting AF via a University Research Fellowship in Electrocatalysis.

Conflict of interest

The authors declare that the research was conducted in the absence of any commercial or financial relationships that could be construed as a potential conflict of interest.

The author(s) AF declared that they were an editorial board member of Frontiers, at the time of submission. This had no impact on the peer review process and the final decision.

Publisher's note

Supplementary material

The Supplementary Material for this article can be found online at: https://www.frontiersin.org/articles/10.3389/fenve.2023.1228992/full#supplementary-material

References

Abdelkareem, M. A., Elsaid, K., Wilberforce, T., Kamil, M., Sayed, E. T., and Olabi, A. (2021). Environmental aspects of fuel cells: a review. *Sci. Total Environ.* 752, 141803. doi:10.1016/j.scitotenv.2020.141803

Abraham, E., Deepa, B., Pothan, L., Jacob, M., Thomas, S., Cvelbar, U., et al. (2011). Extraction of nanocellulose fibrils from lignocellulosic fibres: a novel approach. *Carbohydr. Polym.* 86, 1468–1475. doi:10.1016/j.carbpol.2011.06.034

Akula, S., Varathan, P., Menon, R. S., and Sahu, A. K. (2021). Rationally constructing nitrogen–fluorine heteroatoms on porous carbon derived from pomegranate fruit peel waste towards an efficient oxygen reduction catalyst for polymer electrolyte membrane fuel cells. *Sustain. Energy & Fuels* 5, 886–899. doi:10.1039/d0se01214a

Alston, S. M., and Arnold, J. C. (2011). Environmental impact of pyrolysis of mixed WEEE plastics Part 2: life cycle assessment. *Environ. Sci. Technol.* 45, 9386–9392. doi:10.1021/es2016654

Amiinu, I. S., Zhang, J., Kou, Z., Liu, X., Asare, O. K., Zhou, H., et al. (2016). Self-organized 3D porous graphene dual-doped with biomass-sponsored nitrogen and sulfur for oxygen reduction and evolution. *ACS Appl. Mat. Interfaces* 8, 29408–29418. doi:10.1021/acsami.6b08719

Anca-Couce, A. (2016). Reaction mechanisms and multi-scale modelling of lignocellulosic biomass pyrolysis. *Prog. Energy Combust. Sci.* 53, 41–79. doi:10.1016/j.pecs.2015.10.002

Andrews, R., Jacques, D., Qian, D., and Dickey, E. C. (2001). Purification and structural annealing of multiwalled carbon nanotubes at graphitization temperatures. *Carbon* 39, 1681–1687. doi:10.1016/s0008-6223(00)00301-8

Bhaskar, T., Bhavya, B., Singh, R., Naik, D. V., Kumar, A., and Goyal, H. B. (2011). "Chapter 3 - thermochemical conversion of biomass to biofuels," in *Biofuels*. Editors A. Pandey, C. Larroche, S. C. Ricke, C.-G. Dussap, and E. Gnansounou (Amsterdam: Academic Press), 51–77.

Bikbulatova, S., Tahmasebi, A., Zhang, Z., and Yu, J. (2017). Characterization and behavior of water in lignocellulosic and microalgal biomass for thermochemical conversion, Fuel Process. *Fuel Process. Technol.* 160, 121–129. doi:10.1016/j.fuproc.2017.02.025

Borghei, M., Laocharoen, N., Kibena-Põldsepp, E., Johansson, L.-S., Campbell, J., Kauppinen, E., et al. (2017). Porous N,P-doped carbon from coconut shells with high electrocatalytic activity for oxygen reduction: alternative to Pt-C for alkaline fuel cells. *Appl. Catal. B Environ.* 204, 394–402. doi:10.1016/j.apcatb.2016.11.029

Cai, C. L., Liu, Q. Y., and Wang, T. J. (2015). Progress on reaction pathway and catalysts for preparation of long chain alkanes from lignocellulosic biomass. *Chem. Ind. For. Prod.* 35, 153–162. doi:10.3969/j.issn.0253-2417.2015.06.025

Chang, Y., Shi, H., Yan, X., Zhang, G., and Chen, L. (2020). A ternary B, N, P-Doped carbon material with suppressed water splitting activity for high-energy aqueous supercapacitors. *Carbon* 170, 127–136. doi:10.1016/j.carbon.2020.08.013

Chaparro-Garnica, J., Salinas-Torres, D., Mostazo-López, M. J., Morallón, E., and Cazorla-Amorós, D. (2021). Biomass waste conversion into low-cost carbon-based materials for supercapacitors: a sustainable approach for the energy scenario. *J. Electroanal. Chem.* 880, 114899. doi:10.1016/j.jelechem.2020.114899

Chen, C., Yu, D., Zhao, G., Du, B., Tang, W., Sun, L., et al. (2016). Three-dimensional scaffolding framework of porous carbon nanosheets derived from plant wastes for high-performance supercapacitors. *Nano Energy* 27, 377–389. doi:10.1016/j.nanoen.2016.07.020

Chen, H. (2014). *Chemical composition and structure of natural lignocellulose, biotechnol, lignocell.* Dordrecht: Springer, 25–71.

Chen, P., Wang, L.-K., Wang, G., Gao, M.-R., Ge, J., Yuan, W.-J., et al. (2014). Nitrogen-doped nanoporous carbon nanosheets derived from plant biomass: an efficient catalyst for oxygen reduction reaction. *Energy Environ. Sci.* 7, 4095–4103. doi:10.1039/c4ee02531h

Chen, Y., and Chadderton, L. T. (2004). Improved growth of aligned carbon nanotubes by mechanical activation. *J. Mater. Res.* 19, 2791–2794. doi:10.1557/jmr.2004.0398

Chen, Y., and Yu, J. (2005). Growth direction control of aligned carbon nanotubes. *Carbon* 43, 3183–3186. doi:10.1016/j.carbon.2005.07.015

Cheng, C., Li, Y., Maouche, C., Li, B., Zhou, Y., Wang, S., et al. (2021). Green synthesis of N, P-co doped porous reduced graphene oxide as an active metal-free electrocatalyst toward oxygen reduction reaction. *J. Electroanal. Chem.* 883, 115058. doi:10.1016/j.jelechem.2021.115058

Costa, J. A. V., Zaparoli, M., Cassuriaga, A. P. A., Cardias, B. B., Vaz, B. d. S., Morais, M. G. d., et al. (2023). Biochar production from microalgae: a new sustainable approach to wastewater treatment based on a circular economy. *Enzyme Microb. Technol.* 169, 110281. doi:10.1016/j.enzmictec.2023.110281

Dekel, D. R. (2018). Review of cell performance in anion exchange membrane fuel cells. *J. Power Sources* 375, 158–169. doi:10.1016/j.jpowsour.2017.07.117

Ding, J., Ji, S., Wang, H., Gai, H., Liu, F., Linkov, V., et al. (2019). Mesoporous nickel-sulfide/nickel/N-doped carbon as HER and OER bifunctional electrocatalyst for water electrolysis. *Int. J. Hydrogen Energy* 44, 2832–2840. doi:10.1016/j.ijhydene.2018.12.031

Fan, L., Zhu, B., Su, P.-C., and He, C. (2018). Nanomaterials and technologies for low temperature solid oxide fuel cells: recent advances, challenges and opportunities. *Nano Energy* 45, 148–176. doi:10.1016/j.nanoen.2017.12.044

Feng, H., Xu, Z., Ren, L., Liu, C., Zhuang, J., Hu, Z., et al. (2018). Activating titania for efficient electrocatalysis by vacancy engineering. *ACS Catal.* 8, 4288–4293. doi:10.1021/acscatal.8b00719

Gao, S., Sun, Z., Liu, W., Jiao, X., Zu, X., Hu, Q., et al. (2017). Atomic layer confined vacancies for atomic-level insights into carbon dioxide electroreduction. *Nat. Commun.* 8, 14503. doi:10.1038/ncomms14503

Gong, K., Du, F., Xia, Z., Durstock, M., and Dai, L. J. s. (2009). Nitrogen-doped carbon nanotube arrays with high electrocatalytic activity for oxygen reduction. *Science* 323, 760–764. doi:10.1126/science.1168049

Gong, Y., Yang, Z., Lin, Y., Zhou, T., Li, J., Jiao, F., et al. (2019). Correction: controlled synthesis of bifunctional particle-like Mo/Mn-NixSy/NF electrocatalyst for highly efficient overall water splitting. *Dalton Trans.* 48, 7025. doi:10.1039/c9dt90089f

Goodell, B., Xie, X., Qian, Y., Daniel, G., Peterson, M., and Jellison, J. (2008). Carbon nanotubes produced from natural cellulosic materials. *J. Nanosci. Nanotechnol.* 8, 2472–2474. doi:10.1166/jnn.2008.235

Guo, D., Shibuya, R., Akiba, C., Saji, S., Kondo, T., and Nakamura, J. (2016). Active sites of nitrogen-doped carbon materials for oxygen reduction reaction clarified using model catalysts. *Science* 351, 361–365. doi:10.1126/science.aad0832

Han, L., Cui, X., Liu, Y., Han, G., Wu, X., Xu, C., et al. (2020). Nitrogen and phosphorus modification to enhance the catalytic activity of biomass-derived carbon toward the oxygen reduction reaction. *Sustain. Energy & Fuels* 4, 2707–2717. doi:10.1039/c9se00985j

Han, M., Shi, M., Wang, J., Zhang, M., Yan, C., Jiang, J., et al. (2019). Efficient bifunctional Co/N dual-doped carbon electrocatalysts for oxygen reduction and evolution reaction. *Carbon* 153, 575–584. doi:10.1016/j.carbon.2019.07.075

Harmsen, P. F. H., Huijgen, W., Bermudez, L., and Bakker, R. (2010). *Literature review of physical and chemical pretreatment processes for lignocellulosic biomass*. Wageningen, Netherlands: Food Biobased Research, 1–49.

He, D., Zhao, W., Li, P., Liu, Z., Wu, H., Liu, L., et al. (2019). Bifunctional biomass-derived 3D nitrogen-doped porous carbon for oxygen reduction reaction and solid-state supercapacitor. *Appl. Surf. Sci.* 465, 303–312. doi:10.1016/j.apsusc.2018.09.185

Hori, Y., Kikuchi, K., Murata, A., and Suzuki, S. (1986). Production of methane and ethylene in electrochemical reduction of carbon dioxide at copper electrode in aqueous hydrogencarbonate solution. *Chem. Lett.* 15, 897–898. doi:10.1246/cl.1986.897

Hori, Y., Kikuchi, K., and Suzuki, S. (1985). Production of CO and CH_4 in electrochemical reduction of CO_2 at metal electrodes in aqueous hydrogencarbonate solution. *Chem. Lett.* 14, 1695–1698. doi:10.1246/cl.1985.1695

Hori, Y., Murata, A., and Takahashi, R. (1989). Formation of hydrocarbons in the electrochemical reduction of carbon dioxide at a copper electrode in aqueous solution. *J. Chem. Soc.* 85, 2309–2326. doi:10.1039/f19898502309

Huang, B., Liu, Y., Huang, X., and Xie, Z. (2018). Multiple heteroatom-doped few-layer carbons for the electrochemical oxygen reduction reaction. *J. Mat. Chem. A* 6, 22277–22286. doi:10.1039/c8ta06743k

Huang, B., Liu, Y., Wei, Q., and Xie, Z. (2019). Three-dimensional mesoporous graphene-like carbons derived from a biomolecule exhibiting high-performance oxygen reduction activity. *Sustain. Energy & Fuels* 3, 2809–2818. doi:10.1039/c9se00365g

Huang, B., Liu, Y., and Xie, Z. (2017). Biomass derived 2D carbons via a hydrothermal carbonization method as efficient bifunctional ORR/HER electrocatalysts. *J. Mat. Chem. A* 5, 23481–23488. doi:10.1039/c7ta08052b

Huang, J., Su, T., Zhao, H., Li, F., Chiu, T.-W., Singh, M., et al. (2022). Nano and phase engineering of Fe-Cu alloy exsolved perovskite oxide-based hetero-catalysts for efficient oxygen evolution reaction. *Fuel* 356, 129479. doi:10.1016/j.fuel.2023.129479

Huang, N.-b., Zhang, J.-j., Sun, Y., Sun, X.-n., Qiu, Z.-y., and Ge, X.-w. (2020). A non-traditional biomass-derived N, P, and S ternary self-doped 3D multichannel carbon ORR electrocatalyst. *New J. Chem.* 44, 14604–14614. doi:10.1039/d0nj03283b

Huang, Y.-F., Chiueh, P.-T., and Lo, S.-L. (2016). A review on microwave pyrolysis of lignocellulosic biomass. *Sustain. Environ. Res.* 26, 103–109. doi:10.1016/j.serj.2016.04.012

Hwang, J., Rao, R. R., Giordano, L., Katayama, Y., Yu, Y., and Shao-Horn, Y. (2017). Perovskites in catalysis and electrocatalysis. *Science* 358, 751–756. doi:10.1126/science.aam7092

Inagaki, M., Toyoda, M., Soneda, Y., and Morishita, T. (2018). Nitrogen-doped carbon materials. *Carbon* 132, 104–140. doi:10.1016/j.carbon.2018.02.024

Ito, Y., Cong, W., Fujita, T., Tang, Z., and Chen, M. J. A. C. (2015). High catalytic activity of nitrogen and sulfur co-doped nanoporous graphene in the hydrogen evolution reaction. *Angew. Chem.* 127, 2159–2164. doi:10.1002/ange.201410050

Jatav, H., Goyam, S., Kumar, V., Jayant, H., Chattopadhyay, A., Dhawal, S., et al. (2017). Role of biochar: in agriculture sector its implication and perspective. *Int. J. Chem. Stud.* 14, 14–18.

Jiang, H., Gu, J. X., Zheng, X. S., Liu, M., Qiu, X. Q., Wang, L. B., et al. (2019a). Defect-rich and ultrathin N doped carbon nanosheets as advanced trifunctional metal-free electrocatalysts for the ORR, OER and HER. *Energy Environ. Sci.* 12, 322–333. doi:10.1039/c8ee03276a

Jiang, H., Gu, J., Zheng, X., Liu, M., Qiu, X., Wang, L., et al. (2019b). Defect-rich and ultrathin N doped carbon nanosheets as advanced trifunctional metal-free electrocatalysts for the ORR, OER and HER. *Energy Environ. Sci.* 12, 322–333. doi:10.1039/c8ee03276a

Jordan, J., and Smith, P. T. (1960). Free-radical intermediate in the electroreduction of carbon dioxide. *Proceed. Chem. Soc.* 1960, 246–247.

Kabir, G., and Hameed, B. H. (2017). Recent progress on catalytic pyrolysis of lignocellulosic biomass to high-grade bio-oil and bio-chemicals. *Renew. Sustain. Energy Rev.* 70, 945–967. doi:10.1016/j.rser.2016.12.001

Kang, Z., Wang, E., Mao, B., Su, Z., Chen, L., and Xu, L. (2005). Obtaining carbon nanotubes from grass. *Nanotechnology* 16, 1192–1195. doi:10.1088/0957-4484/16/8/036

Keiluweit, M., Nico, P. S., Johnson, M. G., and Kleber, M. (2010). Dynamic molecular structure of plant biomass-derived black carbon (biochar). *Environ. Sci. Technol.* 44, 1247–1253. doi:10.1021/es9031419

Khiari, B., Jeguirim, M., Limousy, L., and Bennici, S. (2019). Biomass derived chars for energy applications. *Renew. Sustain. Energy Rev.* 108, 253–273. doi:10.1016/j.rser.2019.03.057

Kosinkova, J., Doshi, A., Maire, J., Ristovski, Z., Brown, R., and Rainey, T. J. (2015). Measuring the regional availability of biomass for biofuels and the potential for microalgae. *Renew. Sustain. Energy Rev.* 49, 1271–1285. doi:10.1016/j.rser.2015.04.084

Kreuter, W., and Hofmann, H. (1998). Electrolysis: the important energy transformer in a world of sustainable energy. *Int. J. Hydrogen Energy* 23, 661–666. doi:10.1016/s0360-3199(97)00109-2

Kumar, R., Singh, R. K., and Singh, D. (2016). Natural and waste hydrocarbon precursors for the synthesis of carbon based nanomaterials: graphene and CNTs. *Renew. Sustain. Energy Rev.* 58, 976–1006. doi:10.1016/j.rser.2015.12.120

Kuznetsov, V. L., Usoltseva, A. N., Chuvilin, A. L., Obraztsova, E. D., and Bonard, J.-M. (2001). Thermodynamic analysis of nucleation of carbon deposits on metal particles and its implications for the growth of carbon nanotubes. *Phys. Rev. B* 64, 235401. doi:10.1103/physrevb.64.235401

Lai, L., Potts, J. R., Zhan, D., Wang, L., Poh, C. K., Tang, C., et al. (2012). Exploration of the active center structure of nitrogen-doped graphene-based catalysts for oxygen reduction reaction. *Energy Environ. Sci.* 5, 7936–7942. doi:10.1039/c2ee21802j

Lee, J., Kim, K.-H., and Kwon, E. E. (2017). Biochar as a catalyst. *Renew. Sustain. Energy Rev.* 77, 70–79. doi:10.1016/j.rser.2017.04.002

Lei, Y., Yang, F., Xie, H., Lei, Y., Liu, X., Si, Y., et al. (2020). Biomass *in situ* conversion to Fe single atomic sites coupled with Fe2O3 clusters embedded in porous carbons for the oxygen reduction reaction. *J. Mat. Chem. A* 8, 20629–20636. doi:10.1039/d0ta06022d

Li, D. C., and Jiang, H. (2017). The thermochemical conversion of non-lignocellulosic biomass to form biochar: a review on characterizations and mechanism elucidation. *Bioresour. Technol.* 246, 57–68. doi:10.1016/j.biortech.2017.07.029

Li, F., Mushtaq, N., Su, T., Cui, Y., Huang, J., Sun, M., et al. (2023). NCNT grafted perovskite oxide as an active bifunctional electrocatalyst for rechargeable zinc-air battery. *Mater. Today Nano* 21, 100287. doi:10.1016/j.mtnano.2022.100287

Li, F., Yin, Y., Zhang, C., Li, W., Maliutina, K., Zhang, Q., et al. (2020a). Enhancing oxygen reduction performance of oxide-CNT through *in-situ* generated nanoalloy bridging. *Appl. Catal. B Environ.* 263, 118297. doi:10.1016/j.apcatb.2019.118297

Li, J.-C., Qin, X., Hou, P.-X., Cheng, M., Shi, C., Liu, C., et al. (2019c). Identification of active sites in nitrogen and sulfur co-doped carbon-based oxygen reduction catalysts. *Carbon* 147, 303–311. doi:10.1016/j.carbon.2019.01.018

Li, W., Yin, Y., Xu, K., Li, F., Maliutina, K., Wu, Q., et al. (2021). Enhancement of oxygen evolution activity of perovskite $(La_{0.8}Sr_{0.2})_{0.95}MnO_{3-\delta}$ electrode by Co phase surface modification. *Catal. Today* 364, 148–156. doi:10.1016/j.cattod.2020.02.015

Li, X., Zhang, Y., Zhang, J., and Wang, C. (2019d). Isolated Fe atoms dispersed on cellulose-derived nanocarbons as an efficient electrocatalyst for the oxygen reduction reaction. *Nanoscale* 11, 23110–23115. doi:10.1039/c9nr07914a

Li, Y. (2014). *Studies on cellulose hydrolysis and hemicellulose monosaccharide degradation in concentrated hydrochloric acid*. Ottawa: University of Ottawa. Master of Applied Science.

Li, Y., Wang, G., Wei, T., Fan, Z., and Yan, P. (2016). Nitrogen and sulfur co-doped porous carbon nanosheets derived from willow catkin for supercapacitors. *Nano Energy* 19, 165–175. doi:10.1016/j.nanoen.2015.10.038

Li, Y., Wen, H., Yang, J., Zhou, Y., and Cheng, X. (2019a). Boosting oxygen reduction catalysis with N, F, and S tri-doped porous graphene: tertiary N-precursors regulates the constitution of catalytic active sites. *Carbon* 142, 1–12. doi:10.1016/j.carbon.2018.09.079

Li, Y., Xing, B., Ding, Y., Han, X., and Wang, S. (2020b). A critical review of the production and advanced utilization of biochar via selective pyrolysis of lignocellulosic biomass. *Bioresour. Technol.* 312, 123614. doi:10.1016/j.biortech.2020.123614

Li, Y., Zhou, L. W., and Wang, R. Z. (2017). Urban biomass and methods of estimating municipal biomass resources. *Renew. Sustain. Energy Rev.* 80, 1017–1030. doi:10.1016/j.rser.2017.05.214

Li, Z., Wang, L., Li, Y., Feng, Y., and Feng, W. (2019b). Carbon-based functional nanomaterials: preparation, properties and applications. *Compos. Sci. Technol.* 179, 10–40. doi:10.1016/j.compscitech.2019.04.028

Lin, Y.-C., and Huber, G. W. (2009). The critical role of heterogeneous catalysis in lignocellulosic biomass conversion. *Energy Environ. Sci.* 2, 68–80. doi:10.1039/b814955k

Liu, R., Wang, Y., Liu, D., Zou, Y., and Wang, S. (2017). Water-plasma-enabled exfoliation of ultrathin layered double hydroxide nanosheets with multivacancies for water oxidation. *Adv. Mater.* 29, 1701546. doi:10.1002/adma.201701546

Liu, W.-J., Jiang, H., and Yu, H.-Q. (2015a). Development of biochar-based functional materials: toward a sustainable platform carbon material. *Mater.* ***Chem. Rev.*** 115, 12251–12285. doi:10.1021/acs.chemrev.5b00195

Liu, W.-J., Jiang, H., and Yu, H.-Q. (2019). Emerging applications of biochar-based materials for energy storage and conversion. *Energy Environ. Sci.* 12, 1751–1779. doi:10.1039/c9ee00206e

Liu, W.-J., Jiang, H., and Yu, H.-Q. (2015b). Thermochemical conversion of lignin to functional materials: a review and future directions. *Green Chem.* 17, 4888–4907. doi:10.1039/c5gc01054c

Liu, Z., Wang, F., Li, M., and Ni, Z.-H. (2016). N, S and P-ternary doped carbon nanopore/tube composites derived from natural chemicals in waste sweet osmanthus fruit with superior activity for oxygen reduction in acidic and alkaline media. *RSC Adv.* 6, 37500–37505. doi:10.1039/c6ra08371d

Lu, Z., Wang, J., Huang, S., Hou, Y., Li, Y., Zhao, Y., et al. (2017). N,B-codoped defect-rich graphitic carbon nanocages as high performance multifunctional electrocatalysts. *Nano Energy* 42, 334–340. doi:10.1016/j.nanoen.2017.11.004

Lv, X., Chen, Y., Wu, Y., Wang, H., Wang, X., Wei, C., et al. (2019). A Br-regulated transition metal active-site anchoring and exposure strategy in biomass-derived carbon nanosheets for obtaining robust ORR/HER electrocatalysts at all pH values. *J. Mat. Chem. A* 7, 27089–27098. doi:10.1039/c9ta10880g

Mahmoudian, L., Rashidi, A., Dehghani, H., and Rahighi, R. (2016). Single-step scalable synthesis of three-dimensional highly porous graphene with favorable methane adsorption. *Chem. Eng. J.* 304, 784–792. doi:10.1016/j.cej.2016.07.015

Maliutina, K., He, C. J., Huang, J. J., Yu, J. L., Li, F. J., He, C. X., et al. (2021b). Structural and electronic engineering of biomass-derived carbon nanosheet composite for electrochemical oxygen reduction. *Sustain. Energy & Fuels* 5, 2114–2126. doi:10.1039/d0se01631d

Maliutina, K., Huang, J., Su, T., Yu, J., and Fan, L. (2021a). Biomass-derived Ta,N,S co-doped CNTs enriched carbon catalyst for efficient electrochemical oxygen reduction. *J. Alloys Compd.* 888, 161479. doi:10.1016/j.jallcom.2021.161479

Maliutina, K., Tahmasebi, A., Yu, J., and Saltykov, S. N. (2017). Comparative study on flash pyrolysis characteristics of microalgal and lignocellulosic biomass in entrained-flow reactor. *Energy Convers. Manag.* 151, 426–438. doi:10.1016/j.enconman.2017.09.013

Maliutina, K., Tahmasebi, A., and Yu, J. (2018). The transformation of nitrogen during pressurized entrained-flow pyrolysis of Chlorella vulgaris. *Bioresour. Technol.* 262, 90–97. doi:10.1016/j.biortech.2018.04.073

Mamtani, K., Jain, D., Dogu, D., Gustin, V., Gunduz, S., Co, A. C., et al. (2018). Insights into oxygen reduction reaction (ORR) and oxygen evolution reaction (OER) active sites for nitrogen-doped carbon nanostructures (CNx) in acidic media. *Appl. Catal. B Environ.* 220, 88–97. doi:10.1016/j.apcatb.2017.07.086

Martín, A. J., and Pérez-Ramírez, J. (2019). Heading to distributed electrocatalytic conversion of small abundant molecules into fuels, chemicals, and fertilizers. *Joule* 3, 2602–2621. doi:10.1016/j.joule.2019.09.007

Martin, M. A. (2010). First generation biofuels compete. *New Biotechnol.* 27, 596–608. doi:10.1016/j.nbt.2010.06.010

Maruyama, S., Kojima, R., Miyauchi, Y., Chiashi, S., and Kohno, M. (2002). Low-temperature synthesis of high-purity single-walled carbon nanotubes from alcohol. *Chem. Phys. Lett.* 360, 229–234. doi:10.1016/s0009-2614(02)00838-2

Matter, P. H., Zhang, L., and Ozkan, U. S. (2006). The role of nanostructure in nitrogen-containing carbon catalysts for the oxygen reduction reaction. *J. Catal.* 239, 83–96. doi:10.1016/j.jcat.2006.01.022

Meshitsuka, S., Ichikawa, M., and Tamaru, K. (1974). Electrocatalysis by metal phthalocyanines in the reduction of carbon dioxide. *J. Chem. Soc. Chem. Commun.* 1974, 158–159. doi:10.1039/c39740000158

Mulyadi, A., Zhang, Z., Dutzer, M., Liu, W., and Deng, Y. (2017). Facile approach for synthesis of doped carbon electrocatalyst from cellulose nanofibrils toward high-performance metal-free oxygen reduction and hydrogen evolution. *Nano Energy* 32, 336–346. doi:10.1016/j.nanoen.2016.12.057

Munawar, M. A., Khoja, A. H., Naqvi, S. R., Mehran, M. T., Hassan, M., Liaquat, R., et al. (2021). Challenges and opportunities in biomass ash management and its utilization in novel applications. *Renew. Sustain. Energy Rev.* 150, 111451. doi:10.1016/j.rser.2021.111451

Nie, Y., Li, L., and Wei, Z. (2015). Recent advancements in Pt and Pt-free catalysts for oxygen reduction reaction. *Chem. Soc. Rev.* 44, 2168–2201. doi:10.1039/c4cs00484a

Niu, H.-J., Wang, A.-J., Zhang, L., and Feng, J.-J. (2020). Bioinspired one-step pyrolysis fabrication of 3D porous Co, N, P-doped carbon nanosheets with enriched $CoN_{<i>x</i>}$ active sites as high-performance bifunctional oxygen electrocatalyst for rechargeable Zn–air battery. *ACS Appl. Energy Mat.* 3, 2781–2790. doi:10.1021/acsaem.9b02450

Norgate, T., and Langberg, D. (2009). Environmental and economic aspects of charcoal use in steelmaking. *ISIJ Int.* 49, 587–595. doi:10.2355/isijinternational.49.587

Omoriyekomwan, J. E., Tahmasebi, A., Dou, J., Tian, L., and Yu, J. (2021a). Mechanistic study on the formation of silicon carbide nanowhiskers from biomass cellulose char under microwave. *Mater. Chem. Phys.* 262, 124288. doi:10.1016/j.matchemphys.2021.124288

Omoriyekomwan, J. E., Tahmasebi, A., Dou, J., Wang, R., and Yu, J. (2021b). A review on the recent advances in the production of carbon nanotubes and carbon nanofibers via microwave-assisted pyrolysis of biomass. *Fuel Process. Technol.* 214, 106686. doi:10.1016/j.fuproc.2020.106686

Omoriyekomwan, J. E., Tahmasebi, A., and Yu, J. (2016). Production of phenol-rich bio-oil during catalytic fixed-bed and microwave pyrolysis of palm kernel shell. *Bioresour. Technol.* 207, 188–196. doi:10.1016/j.biortech.2016.02.002

Omoriyekomwan, J. E., Tahmasebi, A., Zhang, J., and Yu, J. (2017). Formation of hollow carbon nanofibers on bio-char during microwave pyrolysis of palm kernel shell. *Energy Convers. Manag.* 148, 583–592. doi:10.1016/j.enconman.2017.06.022

Omoriyekomwan, J. E., Tahmasebi, A., Zhang, J., and Yu, J. L. (2019). Mechanistic study on direct synthesis of carbon nanotubes from cellulose by means of microwave pyrolysis. *Energy Convers. Manag.* 192, 88–99. doi:10.1016/j.enconman.2019.04.042

Onishchenko, D. V., Reva, V. P., Chakov, V. V., Kuryavyi, V. G., and Petrov, V. V. (2013a). Promising nanocomposite materials based on renewable plant resources. *Metallurgist* 56, 679–683. doi:10.1007/s11015-013-9635-y

Onishchenko, D. V., Reva, V. P., and Kuryavyi, V. G. (2012). Vacuum annealing of carbon nanotubes produced from amorphous carbon. *Coke Chem.* 55, 467–469. doi:10.3103/s1068364x12120034

Onishchenko, D. V., Reva, V. P., and Voronov, B. A. (2013b). Farm crop waste as a promising resource for forming carbon nanotubes. *Russ. Agric. Sci.* 39, 540–543. doi:10.3103/s1068367413050121

Prakash Menon, M., Selvakumar, R., Suresh kumar, P., and Ramakrishna, S. (2017). Extraction and modification of cellulose nanofibers derived from biomass for environmental application. *RSC Adv.* 7, 42750–42773. doi:10.1039/c7ra06713e

Ramanayaka, S., Vithanage, M., Alessi, D. S., Liu, W.-J., Jayasundera, A. C. A., and Ok, Y. S. (2020). Nanobiochar: production, properties, and multifunctional applications. *Environ. Sci. Nano* 7, 3279–3302. doi:10.1039/d0en00486c

Rao, C. V., Cabrera, C. R., and Ishikawa, Y. (2010). In search of the active site in nitrogen-doped carbon nanotube electrodes for the oxygen reduction reaction. *J. Phys. Chem. Lett.* 1, 2622–2627. doi:10.1021/jz100971v

Reva, V. P., Filatenkov, A. É., Mansurov, Y. N., and Kuryavyi, V. G. (2016a). Stages in multilayer carbon nanotube formation with mechanical activation of amorphous carbon. *Refract. Industrial Ceram.* 57, 141–145. doi:10.1007/s11148-016-9943-4

Reva, V. P., Filatenkov, A. E., Yagofarov, V. U., Gulevskii, D. A., Kuryavyi, V. G., and Mansurov, Y. N. (2016b). Analysis of the formation of multi-layer carbon nanotubes in the process of mechanical activation of the pyrolysis products of vegetable raw materials. *IOP Conf. Ser. Mat. Sci. Eng.* 127, 012008. doi:10.1088/1757-899X/127/1/012008

Sayed, E. T., Eisa, T., Mohamed, H. O., Abdelkareem, M. A., Allagui, A., Alawadhi, H., et al. (2019). Direct urea fuel cells: challenges and opportunities. *J. Power Sources* 417, 159–175. doi:10.1016/j.jpowsour.2018.12.024

Schneider, D., Escala, M., Supawittayayothin, K., and Tippayawong, N. J. I. (2011). Characterization of biochar from hydrothermal carbonization of bamboo. *Int. J. Energy Environ.* 2, 647–652.

Seh, Z. W., Kibsgaard, J., Dickens, C. F., Chorkendorff, I., Nørskov, J. K., and Jaramillo, T. F. (2017). Combining theory and experiment in electrocatalysis: insights into materials design. *Science* 355, eaad4998. doi:10.1126/science.aad4998

Shackley, S., Hammond, J., Gaunt, J., and Ibarrola, R. (2011). The feasibility and costs of biochar deployment in the UK. *Carbon Manag.* 2, 335–356. doi:10.4155/cmt.11.22

Shafizadeh, F. (1982). Introduction to pyrolysis of biomass. *J. Anal. Appl. Pyrolysis* 3, 283–305. doi:10.1016/0165-2370(82)80017-x

Shao, M., Chang, Q., Dodelet, J. P., and Chenitz, R. (2016). Recent advances in electrocatalysts for oxygen reduction reaction. *Chem. Rev.* 116, 3594–3657. doi:10.1021/acs.chemrev.5b00462

Sharifi, T., Hu, G., Jia, X., and Wågberg, T. (2012). Formation of active sites for oxygen reduction reactions by transformation of nitrogen functionalities in nitrogen-doped carbon nanotubes. *ACS Nano* 6, 8904–8912. doi:10.1021/nn302906r

Sharma, Y. C., Singh, B., and Korstad, J. (2011). A critical review on recent methods used for economically viable and eco-friendly development of microalgae as a potential feedstock for synthesis of biodiesel. *Green Chem.* 13, 2993–3006. doi:10.1039/c1gc15535k

Shen, D., Xiao, R., Gu, S., and Luo, K. (2011). The pyrolytic behavior of cellulose in lignocellulosic biomass: a review. *RSC Adv.* 1, 1641–1660. doi:10.1039/c1ra00534k

Shi, K., Yan, J., Lester, E., and Wu, T. (2014). Catalyst-free synthesis of multiwalled carbon nanotubes via microwave-induced processing of biomass. *Industrial Eng. Chem. Res.* 53, 15012–15019. doi:10.1021/ie503076n

Singh, S. K., Takeyasu, K., and Nakamura, J. (2019). Active sites and mechanism of oxygen reduction reaction electrocatalysis on nitrogen-doped carbon materials. *Adv. Mat.* 31, 1804297. doi:10.1002/adma.201804297

Su, X.-L., Cheng, M.-Y., Fu, L., Yang, J.-H., Zheng, X.-C., and Guan, X.-X. (2017). Superior supercapacitive performance of hollow activated carbon nanomesh with hierarchical structure derived from poplar catkins. *J. Power Sources* 362, 27–38. doi:10.1016/j.jpowsour.2017.07.021

Sun, L., Tian, C., Li, M., Meng, X., Wang, L., Wang, R., et al. (2013). From coconut shell to porous graphene-like nanosheets for high-power supercapacitors. *J. Mat. Chem. A* 1, 6462–6470. doi:10.1039/c3ta10897j

Sun, Z., Zheng, M., Hu, H., Dong, H., Liang, Y., Xiao, Y., et al. (2018). From biomass wastes to vertically aligned graphene nanosheet arrays: a catalyst-free synthetic strategy towards high-quality graphene for electrochemical energy storage. *Chem. Eng. J.* 336, 550–561. doi:10.1016/j.cej.2017.12.019

Suopajärvi, H., and Fabritius, T. (2013). Towards more sustainable ironmaking—an analysis of energy wood availability in Finland and the economics of charcoal production. *Sustainability* 5, 1188–1207. doi:10.3390/su5031188

Tang, C., Hu, Q., Li, F., He, C., Chai, X., Zhu, C., et al. (2018b). Coupled molybdenum carbide and nitride on carbon nanosheets: an efficient and durable hydrogen evolution electrocatalyst in both acid and alkaline media. *Electrochimica Acta* 280, 323–331. doi:10.1016/j.electacta.2018.05.129

Tang, C., and Qiao, S.-Z. (2019). 2D atomically thin electrocatalysts: from graphene to metallene. *Matter* 1, 1454–1455. doi:10.1016/j.matt.2019.10.023

Tang, C., Zhang, H., Xu, K., Hu, Q., Li, F., He, C., et al. (2018a). Scalable synthesis of heterostructure molybdenum and nickel sulfides nanosheets for efficient hydrogen generation in alkaline electrolyte, Catal. *Catal. Today* 316, 171–176. doi:10.1016/j.cattod.2018.03.010

Tang, C., Zhang, H., Xu, K., Zhang, Q., Liu, J., He, C., et al. (2019). Unconventional molybdenum carbide phases with high electrocatalytic activity for hydrogen evolution reaction. *J. Mat. Chem. A* 7, 18030–18038. doi:10.1039/c9ta04374h

Thompson, E., Danks, A. E., Bourgeois, L., and Schnepp, Z. (2015). Iron-catalyzed graphitization of biomass. *Green Chem.* 17, 551–556. doi:10.1039/c4gc01673d

Titirici, M.-M., White, R. J., Brun, N., Budarin, V. L., Su, D. S., del Monte, F., et al. (2015). Sustainable carbon materials. *Chem. Soc. Rev.* 44, 250–290. doi:10.1039/c4cs00232f

Uzun, B. B., Apaydın Varol, E., and Pütün, E. (2016). "Pyrolysis: sustain, way from biomass biofuels biochar," in *Biochar region. Suppl. Chain app*. Editors B. B. Uzun, E. Apaydın Varol, J. Liu, and V. J. Bruckman (Cambridge: Cambridge University Press), 239–265.

Vassilev, S. V., Baxter, D., Andersen, L. K., Vassileva, C. G., and Morgan, T. J. (2012). An overview of the organic and inorganic phase composition of biomass. *Fuel* 94, 1–33. doi:10.1016/j.fuel.2011.09.030

Vassilev, S. V., Baxter, D., Andersen, L. K., and Vassileva, C. G. (2010). An overview of the chemical composition of biomass. *Fuel* 89, 913–933. doi:10.1016/j.fuel.2009.10.022

Vassilev, S. V., Baxter, D., Andersen, L. K., and Vassileva, C. G. (2013). An overview of the composition and application of biomass ash. Part 1. Phase–mineral and chemical composition and classification. *Fuel* 105, 40–76. doi:10.1016/j.fuel.2012.09.041

Vassilev, S. V., Vassileva, C. G., and Baxter, D. (2014). Trace element concentrations and associations in some biomass ashes. *Fuel* 129, 292–313. doi:10.1016/j.fuel.2014.04.001

Vassilev, S. V., Vassileva, C. G., and Vassilev, V. S. (2015). Advantages and disadvantages of composition and properties of biomass in comparison with coal: an overview. *Fuel* 158, 330–350. doi:10.1016/j.fuel.2015.05.050

Vikkisk, M., Kruusenberg, I., Joost, U., Shulga, E., Kink, I., and Tammeveski, K. (2014). Electrocatalytic oxygen reduction on nitrogen-doped graphene in alkaline media. *Appl. Catal. B Environ.* 147, 369–376. doi:10.1016/j.apcatb.2013.09.011

Wang, B., Li, S., Wu, X., Liu, J., and Chen, J. (2016). Biomass chitin-derived honeycomb-like nitrogen-doped carbon/graphene nanosheet networks for applications in efficient oxygen reduction and robust lithium storage. *J. Mat. Chem. A* 4, 11789–11799. doi:10.1039/c6ta02858f

Wang, D.-W., Li, F., Yin, L.-C., Lu, X., Chen, Z.-G., Gentle, I. R., et al. (2012b). Nitrogen-doped carbon monolith for alkaline supercapacitors and understanding nitrogen-induced redox transitions. *Chem. Eur. J.* 18, 5345–5351. doi:10.1002/chem.201102806

Wang, J., Hao, J., Liu, D., Qin, S., Portehault, D., Li, Y., et al. (2017). Porous boron carbon nitride nanosheets as efficient metal-free catalysts for the oxygen reduction reaction in both alkaline and acidic solutions. *ACS Energy Lett.* 2, 306–312. doi:10.1021/acsenergylett.6b00602

Wang, J., Yue, X., Yang, Y., Sirisomboonchai, S., Wang, P., Ma, X., et al. (2020a). Earth-abundant transition-metal-based bifunctional catalysts for overall electrochemical water splitting: a review. *J. Alloys Compd.* 819, 153346. doi:10.1016/j.jallcom.2019.153346

Wang, K., Chen, H., Zhang, X., Tong, Y., Song, S., Tsiakaras, P., et al. (2020b). Iron oxide@graphitic carbon core-shell nanoparticles embedded in ordered mesoporous N-doped carbon matrix as an efficient cathode catalyst for PEMFC. *Appl. Catal. B Environ.* 264, 118468. doi:10.1016/j.apcatb.2019.118468

Wang, N., Tahmasebi, A., Yu, J., Xu, J., Huang, F., and Mamaeva, A. (2015). A Comparative study of microwave-induced pyrolysis of lignocellulosic and algal biomass. *Bioresour. Technol.* 190, 89–96. doi:10.1016/j.biortech.2015.04.038

Wang, S., Zhang, L., Xia, Z., Roy, A., Chang, D. W., Baek, J.-B., et al. (2012a). BCN graphene as efficient metal-free electrocatalyst for the oxygen reduction reaction. *Angew. Chem. Int. Ed.* 51, 4209–4212. doi:10.1002/anie.201109257

Wang, X., Wang, J., Wang, D., Dou, S., Ma, Z., Wu, J., et al. (2014b). One-pot synthesis of nitrogen and sulfur co-doped graphene as efficient metal-free electrocatalysts for the oxygen reduction reaction. *Chem. Commun.* 50, 4839–4842. doi:10.1039/c4cc00440j

Wang, Y., Duan, D., Ma, J., Gao, W., Peng, H., Huang, P., et al. (2019). Waste wine mash-derived doped carbon materials as an efficient electrocatalyst for oxygen reduction reaction. *Int. J. Hydrogen Energy* 44, 31949–31959. doi:10.1016/j.ijhydene.2019.10.100

Wang, Z., Li, P., Chen, Y., He, J., Zhang, W., Schmidt, O. G., et al. (2014a). Pure thiophene–sulfur doped reduced graphene oxide: synthesis, structure, and electrical properties. *Nanoscale* 6, 7281–7287. doi:10.1039/c3nr05061k

Wang, Z., Shen, D., Wu, C., and Gu, S. (2018). State-of-the-art on the production and application of carbon nanomaterials from biomass. *Green Chem.* 20, 5031–5057. doi:10.1039/c8gc01748d

Wu, J., Zheng, X., Jin, C., Tian, J., and Yang, R. (2015). Ternary doping of phosphorus, nitrogen, and sulfur into porous carbon for enhancing electrocatalytic oxygen reduction. *Carbon* 92, 327–338. doi:10.1016/j.carbon.2015.05.013

Wu, M., Wang, Y., Wei, Z., Wang, L., Zhuo, M., Zhang, J., et al. (2018a). Ternary doped porous carbon nanofibers with excellent ORR and OER performance for zinc–air batteries. *J. Mat. Chem. A* 6, 10918–10925. doi:10.1039/c8ta02416b

Wu, X., Li, S., Wang, B., Liu, J., and Yu, M. (2017). From biomass chitin to mesoporous nanosheets assembled loofa sponge-like N-doped carbon/g-C3N4 3D network architectures as ultralow-cost bifunctional oxygen catalysts. *Microporous Mesoporous Mater.* 240, 216–226. doi:10.1016/j.micromeso.2016.11.022

Wu, Z.-Y., Ji, W.-B., Hu, B.-C., Liang, H.-W., Xu, X.-X., Yu, Z.-L., et al. (2018b). Partially oxidized Ni nanoparticles supported on Ni-N co-doped carbon nanofibers as bifunctional electrocatalysts for overall water splitting. *Nano Energy* 51, 286–293. doi:10.1016/j.nanoen.2018.06.071

Xian, F., Gao, L., Zhang, Z., Zhang, H., Dong, S., and Cui, G. (2019). N, P dual-doped multi-wrinkled nanosheets prepared from the egg crude lecithin as the efficient metal-free electrocatalyst for oxygen reduction reaction. *Appl. Surf. Sci.* 476, 76–83. doi:10.1016/j.apsusc.2018.12.293

Xiao, F., Chen, Z., Wu, H., Wang, Y., Cao, E., Lu, X., et al. (2019). Phytic acid-guided ultra-thin N,P co-doped carbon coated carbon nanotubes for efficient all-pH electrocatalytic hydrogen evolution. *Nanoscale* 11, 23027–23034. doi:10.1039/c9nr07362k

Xiao, Z., Wang, Y., Huang, Y.-C., Wei, Z., Dong, C.-L., Ma, J., et al. (2017). Filling the oxygen vacancies in Co3O4 with phosphorus: an ultra-efficient electrocatalyst for overall water splitting. *Energy Environ. Sci.* 10, 2563–2569. doi:10.1039/c7ee01917c

Xiao, Z., Xie, C., Wang, Y., Chen, R., and Wang, S. (2021). Recent advances in defect electrocatalysts: preparation and characterization. *J. Energy Chem.* 53, 208–225. doi:10.1016/j.jechem.2020.04.063

Xing, T., Zheng, Y., Li, L. H., Cowie, B. C. C., Gunzelmann, D., Qiao, S. Z., et al. (2014). Observation of active sites for oxygen reduction reaction on nitrogen-doped multilayer graphene. *ACS Nano* 8, 6856–6862. doi:10.1021/nn501506p

Yaman, S. (2004). Pyrolysis of biomass to produce fuels and chemical feedstocks. *ChemInform* 35, 651–671. doi:10.1002/chin.200431298

Ye, D., Wang, L., Zhang, R., Liu, B., Wang, Y., and Kong, J. (2015). Facile preparation of N-doped mesocellular graphene foam from sludge flocs for highly efficient oxygen reduction reaction. *J. Mat. Chem. A* 3, 15171–15176. doi:10.1039/c5ta03060a

Yu, L., Huang, J., Li, Y., Jing, Y., Maliutina, K., Ma, R., et al. (2021). Electrochemical performance of low-temperature solid oxide fuel cells running on syngas from pyrolytic urban sludge. *Ceram. Int.* 47, 16956–16963. doi:10.1016/j.ceramint.2021.02.268

Zhang, B., Chen, R., Yang, Z., Chen, Y., Zhou, L., and Yuan, Y. (2019). Melamine-assisted synthesis of paper mill sludge-based carbon nanotube/nanoporous carbon nanocomposite for enhanced electrocatalytic oxygen reduction activity. *Int. J. Hydrogen Energy* 44, 31094–31103. doi:10.1016/j.ijhydene.2019.10.045

Zhang, H., Zhou, Z., Lei, Q., and Lo, T. W. B. (2023b). Recent advances in the operando structural and interface characterisation of electrocatalysts. *Curr. Opin. Electrochem.* 38, 101215. doi:10.1016/j.coelec.2023.101215

Zhang, J., He, J., Zheng, H., Li, R., and Gou, X. (2020a). N,S dual-doped carbon nanosheet networks with hierarchical porosity derived from biomass of Allium cepa as efficient catalysts for oxygen reduction and Zn–air batteries. *J. Mat. Sci.* 55, 7464–7476. doi:10.1007/s10853-020-04535-4

Zhang, J., Qu, L., Shi, G., Liu, J., Chen, J., and Dai, L. (2016c). N,P-Codoped carbon networks as efficient metal-free bifunctional catalysts for oxygen reduction and hydrogen evolution reactions. *Angew. Chem. Int. Ed.* 55, 2230–2234. doi:10.1002/anie.201510495

Zhang, J., Tahmasebi, A., Omoriyekomwan, J. E., and Yu, J. (2021). Microwave-assisted synthesis of biochar-carbon-nanotube-NiO composite as high-performance anode materials for lithium-ion batteries. *Fuel Process. Technol.* 213, 106714. doi:10.1016/j.fuproc.2020.106714

Zhang, J., Zhou, H., Liu, X., Zhang, J., Peng, T., Yang, J., et al. (2016b). Keratin-derived S/N co-doped graphene-like nanobubble and nanosheet hybrids for highly efficient oxygen reduction. *J. Mat. Chem. A* 4, 15870–15879. doi:10.1039/c6ta06212a

Zhang, L.-L., Tong, L., Ding, Y., Zhang, W., and Liang, H.-W. (2023a). Synthesis of hierarchically porous carbon materials by zinc salts-assisted carbonization of biomass and organic solid wastes. *Particuology* 84, 45–52. doi:10.1016/j.partic.2023.03.002

Zhang, L., and Xia, Z. (2011). Mechanisms of oxygen reduction reaction on nitrogen-doped graphene for fuel cells. *J. Phys. Chem. C* 115, 11170–11176. doi:10.1021/jp201991j

Zhang, M., Gao, B., Varnoosfaderani, S., Hebard, A., Yao, Y., and Inyang, M. (2013). Preparation and characterization of a novel magnetic biochar for arsenic removal. *Bioresour. Technol.* 130, 457–462. doi:10.1016/j.biortech.2012.11.132

Zhang, Q., Luo, F., Ling, Y., Xiao, S., Li, M., Qu, K., et al. (2020b). Identification of functionality of heteroatoms in boron, nitrogen and fluorine ternary-doped carbon as a robust electrocatalyst for nitrogen reduction reaction powered by rechargeable zinc–air batteries. *J. Mat. Chem. A* 8, 8430–8439. doi:10.1039/d0ta01572e

Zhang, Y., Lu, L., Zhang, S., Lv, Z., Yang, D., Liu, J., et al. (2018). Biomass chitosan derived cobalt/nitrogen doped carbon nanotubes for the electrocatalytic oxygen reduction reaction. *J. Mat. Chem. A* 6, 5740–5745. doi:10.1039/c7ta11258k

Zhang, Y., Zuo, L., Zhang, L., Huang, Y., Lu, H., Fan, W., et al. (2016a). Cotton wool derived carbon fiber aerogel supported few-layered MoSe2 nanosheets as efficient electrocatalysts for hydrogen evolution. *ACS Appl. Mat. Interfaces* 8, 7077–7085. doi:10.1021/acsami.5b12772

Zhao, B., Wang, X., and Yang, X. (2015). Co-Pyrolysis characteristics of microalgae isochrysis and chlorella: kinetics, biocrude yield and interaction. *Bioresour. Technol.* 198, 332–339. doi:10.1016/j.biortech.2015.09.021

Zhao, N. Q., He, C. N., Du, X.-W., Shi, C., Li, J. J., and Cui, L. (2006). Amorphous carbon nanotubes fabricated by low-temperature chemical vapor deposition. *Carbon* 44, 1859–1862. doi:10.1016/j.carbon.2006.03.010

Zhao, X., Zhang, Q., Chen, C.-M., Zhang, B., Reiche, S., Wang, A., et al. (2012). Aromatic sulfide, sulfoxide, and sulfone mediated mesoporous carbon monolith for use in supercapacitor. *Nano Energy* 1, 624–630. doi:10.1016/j.nanoen.2012.04.003

Zhao, Y., Wan, J., Yao, H., Zhang, L., Lin, K., Wang, L., et al. (2018). Few-layer graphdiyne doped with sp-hybridized nitrogen atoms at acetylenic sites for oxygen reduction electrocatalysis. *Nat. Chem.* 10, 924–931. doi:10.1038/s41557-018-0100-1

Zheng, X., Cao, X., Li, X., Tian, J., Jin, C., and Yang, R. (2017). Biomass lysine-derived nitrogen-doped carbon hollow cubes via a NaCl crystal template: an efficient bifunctional electrocatalyst for oxygen reduction and evolution reactions. *Nanoscale* 9, 1059–1067. doi:10.1039/c6nr07380h

Zheng, X., Cao, X., Wu, J., Tian, J., Jin, C., and Yang, R. (2016). Yolk-shell N/P/B ternary-doped biocarbon derived from yeast cells for enhanced oxygen reduction reaction. *Carbon* 107, 907–916. doi:10.1016/j.carbon.2016.06.102

Zheng, Y., Jiao, Y., Zhu, Y., Li, L. H., Han, Y., Chen, Y., et al. (2014). Hydrogen evolution by a metal-free electrocatalyst. *Nat. Commun.* 5, 3783. doi:10.1038/ncomms4783

Zhou, Q., Ju, W., Yong, Y., Zhang, Q., Liu, Y., and Li, J. (2020). Effect of the N/P/S and transition-metal co-doping on the quantum capacitance of supercapacitor electrodes based on mono- and multilayer graphene. *Carbon* 170, 368–379. doi:10.1016/j.carbon.2020.08.045

Glossary

AFM	Atomic force microscopy
AI	Artificial intelligence
CNs	Carbon nanomaterials
CNTs	Carbon nanotubes
CNFs	Carbon nanofibres
CO2RR	Carbon dioxide reduction reaction
CV	Cyclic voltammetry
CVD	Chemichal vapour deposition
DFT	Density functional theory
EDS	Energy-dispersive X-ray spectroscopy
EIS	Electrochemical impedance spectroscopy
ENPs	Engineered nanoparticles
EPR	Electron paramagnetic resonance
FC	Fuel cell
HER	Hydrogen evolution reaction
HOR	Hydrogen oxidation reaction
HPCs	Hierarchically porous carbons
HTC	Hydrothermal carbonization
IR/FT-IR	Infrared/Fourier-transform infrared spectroscopy
LCA	Life-cycle assessment
LSV	Linear sweep voltammetry
MOF	Metal organic framework
NPs	Nanoparticles
SSA	Specific surface area
TMs	Transition metals
QD	Quantum dot
OER	Oxygen evolution reaction
ORR	Oxygen reduction reaction
SEM/ FE-SEM	Scanning electron microscopy/field-emission scanning electron microscopy
TEM/ HR-TEM	Transmission electron microscopy/high-resolution transmission electron microscopy
XAFS	X-ray absorption fine structure
XPS	X-ray photoelectron spectroscopy
XRD	X-ray power diffraction
UV-vis	Ultraviolet–visible spectroscopy

frontiers | Frontiers in Environmental Engineering

TYPE Original Research
PUBLISHED 16 May 2024
DOI 10.3389/fenve.2024.1373881

OPEN ACCESS

EDITED BY
Qingguo Huang,
University of Georgia, Griffin Campus, United States

REVIEWED BY
Ke Li,
University of Georgia, United States
Norhaliza Abdul Wahab,
Universiti Teknologi Malaysia, Malaysia

*CORRESPONDENCE
E. W. Mtonga,
eddiemtonga@gmail.com

RECEIVED 20 January 2024
ACCEPTED 02 April 2024
PUBLISHED 16 May 2024

CITATION
Mng'ombe MH, Mtonga EW, Chunga BA, Chidya RCG and Malota M (2024), Comparative study for the performance of pure artificial intelligence software sensor and self-organizing map assisted software sensor in predicting 5-day biochemical oxygen demand for Kauma Sewage Treatment Plant effluent in Malawi.
Front. Environ. Eng. 3:1373881.
doi: 10.3389/fenve.2024.1373881

Comparative study for the performance of pure artificial intelligence software sensor and self-organizing map assisted software sensor in predicting 5-day biochemical oxygen demand for Kauma Sewage Treatment Plant effluent in Malawi

M. H. Mng'ombe[1,2], E. W. Mtonga[1]*, B. A. Chunga[1], R. C. G. Chidya[1] and M. Malota[1]

[1]Department of Water and Sanitation, Faculty of Environmental Sciences, Mzuzu University, Mzuzu, Malawi, [2]Hydro-Informatics Engineering Centre, Lilongwe, Malawi

Introduction: Modeling plays a crucial role in understanding wastewater treatment processes, yet conventional deterministic models face challenges due to complexity and uncertainty. Artificial intelligence offers an alternative, requiring no prior system knowledge. This study tested the reliability of the Adaptive Fuzzy Inference System (ANFIS), an artificial intelligence algorithm that integrates both neural networks and fuzzy logic principles, to predict effluent Biochemical Oxygen Demand. An important indicator of organic pollution in wastewater.

Materials and Methods: The ANFIS models were developed and validated with historical wastewater quality data for the Kauma Sewage Treatment Plant located in Lilongwe City, Malawi. A Self Organizing Map (SOM) was applied to extract features of the raw data to enhance the performance of ANFIS. Cost-effective, quicker, and easier-to-measure variables were selected as possible predictors while using their respective correlations with effluent. Influents' temperature, pH, dissolved oxygen, and effluent chemical oxygen demand were among the model predictors.

Results and Discussions: The comparative results demonstrated that for the same model structure, the ANFIS model achieved correlation coefficients (R) of 0.92, 0.90, and 0.81 during training, testing, and validation respectively, whereas the SOM-assisted ANFIS Model achieved R Values of 0.99, 0.87 and 0.94. Overall, despite the slight decrease in R-value during the testing stage, the SOM- assisted ANFIS model outperformed the traditional ANFIS model in terms of predictive capability. A graphic user interface was developed to improve user interaction and friendliness of the developed model. Integration of the developed model with

supervisory control and data acquisition system is recommended. The study also recommends widening the application of the developed model, by retraining it with data from other wastewater treatment facilities and rivers in Malawi.

KEYWORDS

adaptive neuro-fuzzy inference system, self-organizing map, biochemical oxygen demand, sewage treatment plant, wastewater, artificial intelligence

Introduction

Monitoring of effluent from wastewater treatment plants is crucial in identifying possible pollutants that may be released into receiving water bodies. Surface water quality is often evaluated using indices such as the 5-day biochemical oxygen demand (BOD_5), a commonly used method for measuring organic load in water resource systems (Arlyapov et al., 2022). However, the traditional method for determining BOD_5 using hard sensors has significant setbacks. As Hassen and Asmare, (2018) point out, this approach is difficult, time-consuming, requiring a 5-day incubation period, making it unsuitable for real-time process control (Arlyapov et al., 2022), which can feed into an integrated resource planning framework. Besides, it requires a certified laboratory equipped with expensive instruments and chemicals to administer. Furthermore, the BOD_5 test is complicated by factors such as the oxygen demand caused by algal respiration within the sample and the probable oxidation of ammonia (Noori et al., 2013a). The conditions under which BOD_5 is measured in laboratories frequently differ from those observed in natural aquatic systems, resulting in significant differences in the interpretation of results and their implications (Noori et al., 2013b).

Biosensors have been developed as a result of efforts to address these challenges (Karube et al., 1977; Arlyapov et al., 2022). However, these endeavors have been unsuccessful for many reasons. Biosensors, while promising, face challenges such as the high cost of purchasing and maintenance, the need for significant calibration, toxicity, and inhibitor interference (Rustum, 2009; Pitman et al., 2015; Liu et al., 2020). Practitioners are pressed with the need to balance between treatment operations and testing costs, which includes instrumentation on one hand and allowing for continuous monitoring with the ability to make instant decisions for remedial works for process control to achieve the treatment plant's desired performance objectives (O'Brien et al., 2011). To resolve such complex processes, researchers are developing an interest in machine learning (MA), a branch of artificial intelligence (AI) to model complex problems and apply deep learning from available data (El Alaoui El Fels et al., 2023).

AI algorithms can be broadly categorized into supervised learning or unsupervised learning paradigms (El Alaoui El Fels et al., 2023). Supervised learning involves training algorithms on labeled data, wherein every input-output pair is explicitly supplied during the training process (Pourzangbar et al., 2023). As a result, the algorithm can learn a mapping from inputs to outputs and use that knowledge to make judgments or predictions on new, unobserved data. Conversely, unsupervised learning involves training algorithms on unlabeled data, where the algorithm's task is to figure out the data's underlying structure or patterns without direct supervision (El Alaoui El Fels et al., 2023; Pourzangbar et al., 2023). This frequently entails using dimensionality reduction techniques or grouping comparable data elements. AI algorithms like Artificial Neural Networks (ANN) (Hassen and Asmare, 2018; Bekkari and Zeddouri, 2019; Alsulaili and Refaie, 2021; Lin et al., 2022), Random Forests (RF) (Ward et al., 2021), and Support Vector Machines (SVM) (Zhu et al., 2022) have widely been used in wastewater treatment research where most of them are based on supervised learning. However, there remains a significant research gap regarding the application of unsupervised algorithms like Self-Organizing Maps (SOM). Moreover, studies on optimization techniques demonstrate the extensive application of genetic algorithms (GA) in model calibration (El Alaoui El Fels et al., 2023).

This research was an attempt to improve the performance of AI model capacity in predicting BOD_5 with certainty through the integration of various AI algorithms. Integration of ANN with fuzzy inference system (FIS) was performed. ANN and FIS Models have limitations, particularly in manual parameter tuning and interpretation. To address this, researchers have explored innovative approaches, including the integration of the FIS with ANN, leading to the development of the adaptive network-based fuzzy inference system (ANFIS) (Abunama et al., 2019). SOM assisted ANFIS outperforms individual ANN or FIS models by combining neural network learning capabilities with the interpretability and human knowledge representation of FIS. Unlike conventional FIS models, which require manual parameters and fuzzy rule tuning, ANFIS automates this procedure with neural network learning techniques (Karami et al., 2022; Mohanty et al., 2022). Furthermore, it tackles neural networks' black box characteristics by giving clear fuzzy rules (Rustum and Adeloye, 2011a). This integration produces a more accurate and interpretable modeling method while avoiding the limitations of individual systems. ANFIS combines the benefits of neural networks and fuzzy logic systems, resulting in higher modeling accuracy and simpler implementation, making it a better alternative for a variety of applications (Cheng et al., 2018).

Recent studies have investigated the use of the Adaptive Neuro-Fuzzy Inference System (ANFIS) in wastewater treatment plant (WWTP) processes, with an emphasis on predicting effluent removal quality and influent characteristics. Qiao et al. (2023) studied ANFIS's efficacy in forecasting major pollutant elimination and found satisfactory findings with the coefficient of determination (R^2) values greater than 0.950. However, disparities between anticipated and actual results demonstrated that the model's performance certainty needed improvement. Similarly,

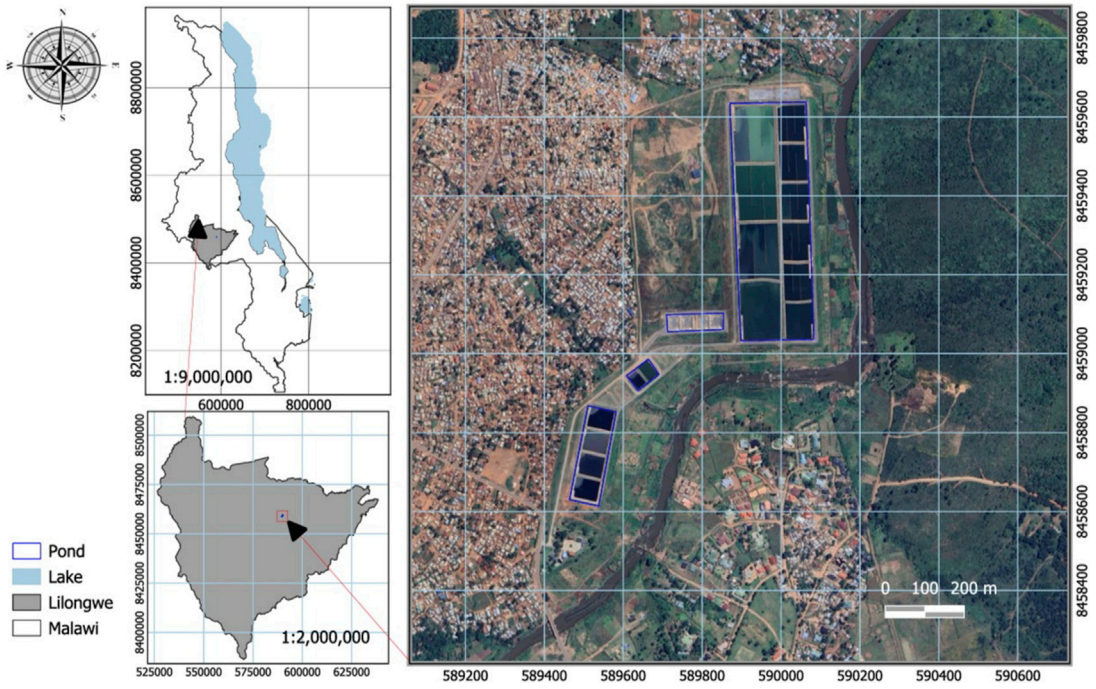

FIGURE 1
Map of Malawi showing the study area.

Cheng et al. (2018) introduced a multi-scale ANFIS methodology that outperformed previous methods for predicting influent characteristics. Okeke et al. (2022) compared ANFIS to Multi-Linear Regression (MLR) for WWTP performance prediction, with MLR demonstrating higher accuracy.

Self-organizing map (SOM) is a nonlinear computational platform introduced by Kasslin et al. (1992) and later by Kohonen et al. (1996). It is an unsupervised learning algorithm with the capacity to establish relationships among process variables. It consists of an array of units arranged in a grid which makes it suitable as a dimensionality reduction technique.

The development of advanced monitoring applications on the SOM platform has been rare and more so in wastewater treatment (Linkkonen et al., 2013). However, integrating ANFIS with SOM or other unsupervised algorithms may address existing accuracy and certainty limitations, demanding further research in this area. This study bridges this gap by investigating the integration of advanced optimization approaches, such as SOM and ANFIS. While these techniques have the potential to improve modeling accuracy, their use is limited, particularly in low-cost wastewater treatment technologies like waste stabilization ponds that are common in developing countries like Malawi (El Alaoui El Fels et al., 2023). Therefore, it was critical to examine this approach in Malawi to establish contextualized monitoring strategies for treatment processes, effectively address local challenges, optimize resource allocation, and promote long-term development in sanitation infrastructure.

The present study employed a modified methodology that uses a SOM algorithm to improve ANFIS precision. SOM-ANFIS models were thoroughly validated with historical wastewater quality data from the Kauma Sewage Treatment Plant (KSTP) in Lilongwe, Malawi. This study aimed to contribute to the field of wastewater management by improving the synergy between new computational approaches and established modeling frameworks ultimately enhancing predictive accuracy.

Materials and methods

Description of the study area

This research was carried out at the KSTP in Lilongwe, Malawi (Figure 1). The facility receives wastewater from the following sewered areas of the city; 3, 6, 12, 13, 16, 18, 19, 20, 30, 47, and 48. The treatment plant comprises septage lagoons (Figure 2) designed to accommodate fecal sludge transported from various non-sewered areas of the city. Vacuum trucks operated by several private entities also convey and discharge fecal sludge to the treatment facility.

Sampling and data collection procedures

The study utilized both secondary and primary data, with a sole focus on domestic sewage. A comprehensive review of documents related to the KSTP produced secondary data. On the other hand, primary data was collected for 30 days from 11 February 2022, to 17 March 2022, twice per day (morning and evening). Wastewater samples were collected systematically from influent raw wastewater, and composite samples were carefully analyzed using standard

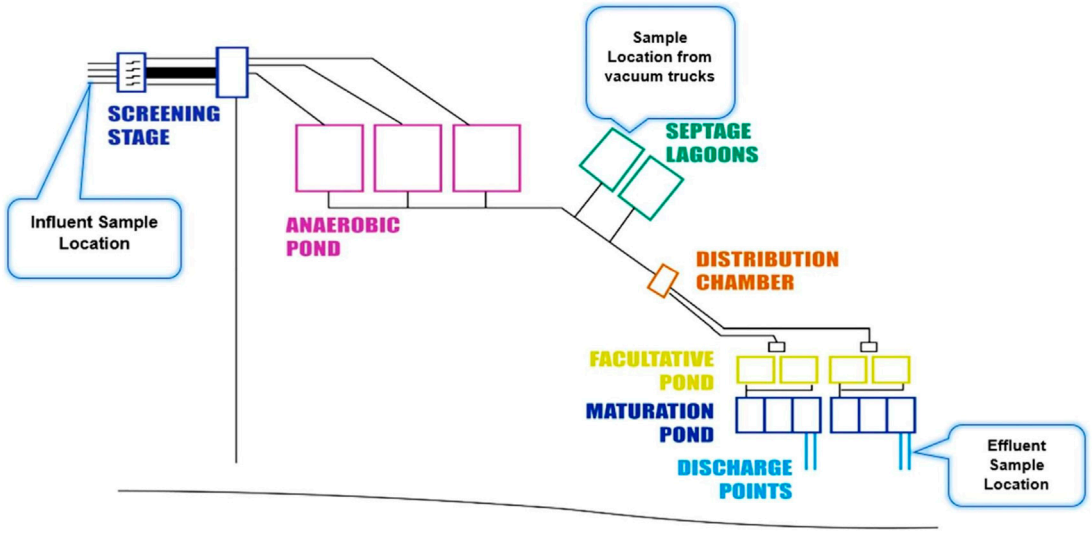

FIGURE 2
A schematic diagram of the Kauma sewage treatment plant. Not drawn to scale (Adapted with permission from Mtethiwa et al., 2008; Ravina et al., 2021).

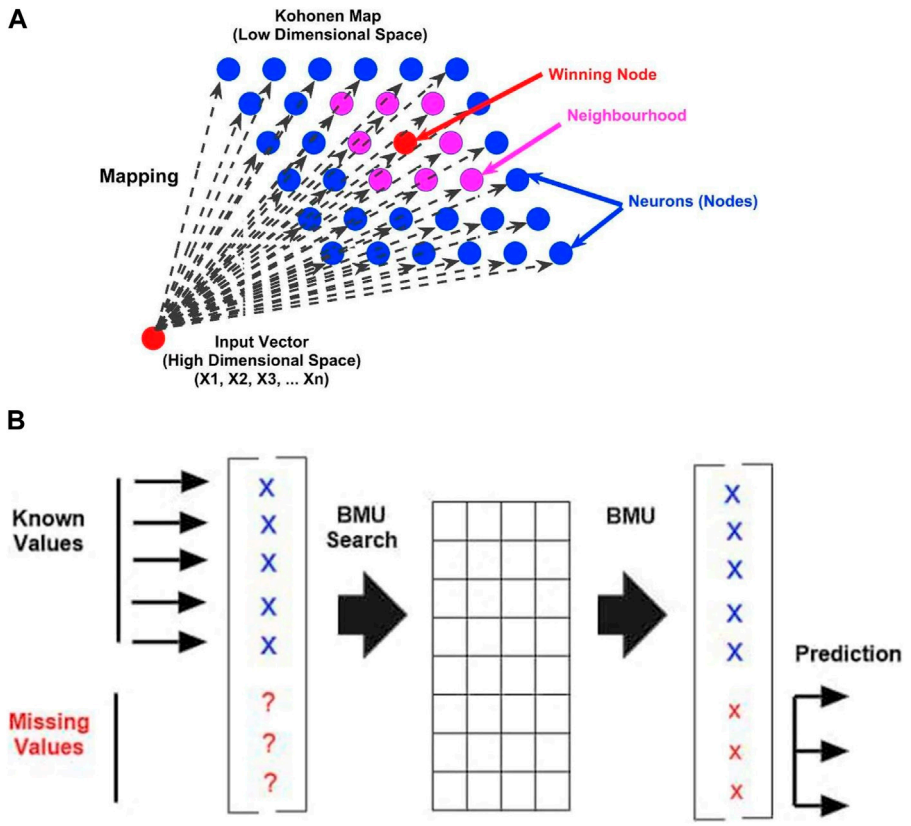

FIGURE 3
(A) Representation of Winning Node and its neighborhood in Kohonen Self Organizing Map (source: Rustum, 2009). **(B)** Figure 4: Prediction of missing components of the input vector using the Self-Organizing Map (BMU, Best Matching Unit) (Source: Rustum and Adeloye, 2011b).

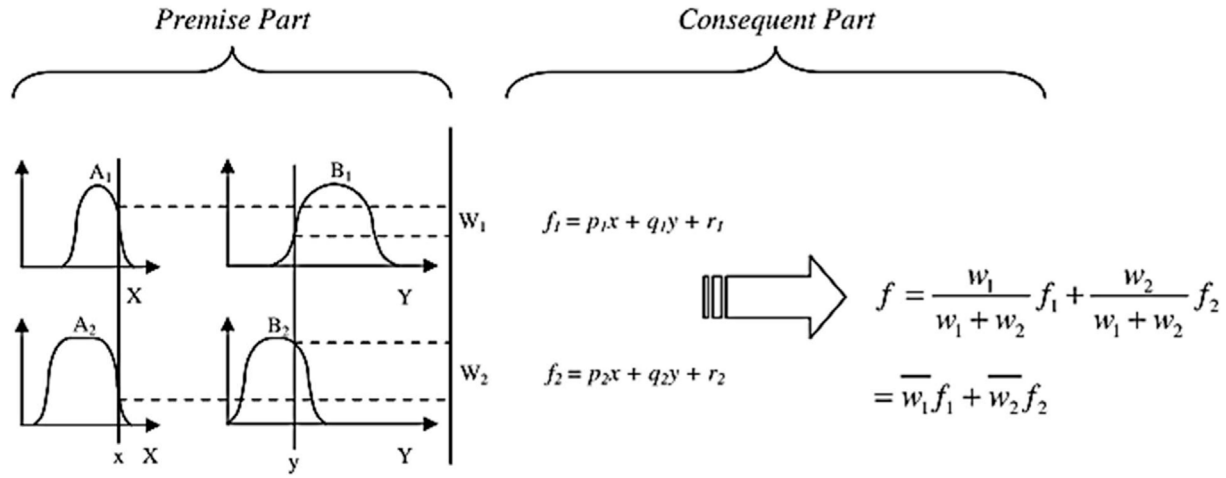

FIGURE 4
Sugeno's Fuzzy if-then rule and fuzzy reasoning mechanism (Noori et al., 2013b).

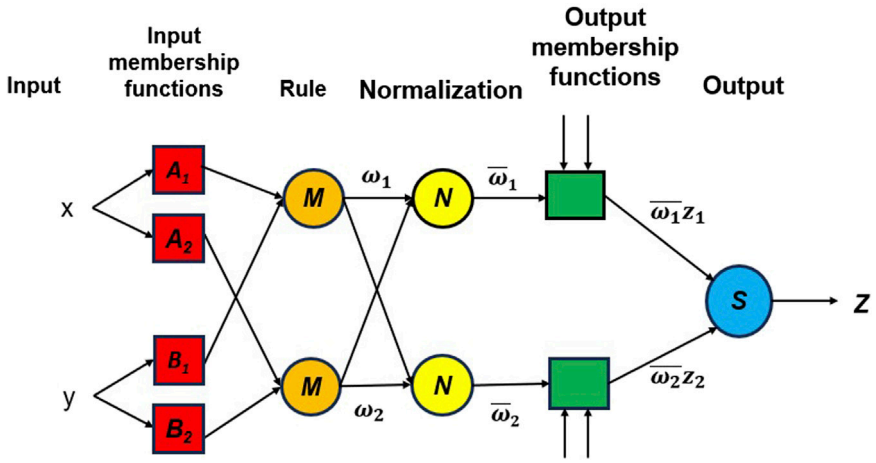

FIGURE 5
Architecture of ANFIS (Lei, 2017).

methods (APHA, 2017; MS682-1:2002, 2002). The pH, COD, total dissolved solids (TDS), total suspended solids (TSS), electrical conductivity (EC), and dissolved oxygen (DO) were all determined. The analyses followed standard methods as prescribed in (APHA, 2017).

Only COD and BOD were determined from samples taken from the Septage lagoon and the effluent-treated wastewater. Samples for the septage lagoon were collected during sludge discharge. To ensure that the samples came from household sources and not from industrial sewage, active attempts were made to consult transporters about the sludge's origin. Each sludge transportation truck produced four 2-L samples: one at the start, two in the middle, and one at the end. These samples were systematically mixed, with double sampling used to ensure quality assurance and homogeneity.

Self-organizing map

The SOM is typically used as a dimensionality reduction approach that can effectively visualize large datasets. This algorithm is based on unsupervised learning and is entirely data-driven. Self-organizing maps are distinguished by their ability to generate internal representations of various aspects of input signals in a spatially organized and effective manner. As a result, the resulting maps closely resemble or mimic topographically structured maps (Kohonen et al., 1996). They operate in a self-study mode, recognizing patterns and grouping them into groups. As this network cannot measure the meaning of the clusters, the users need to interpret the map in a meaningful and useful manner (Rustum, 2009). Self-organizing maps are inspired by neural networks, which are

10.3389/fenve.2024.1373881

TABLE 1 Computed descriptive statistics of KSTP data.

Parameter	Unit	Mean	SD	SE	Max	Min	UB	LB
pH_{inf}	—	7.01	0.46	0.02	8.00	5.40	7.05	6.97
Temp $_{inf}$	^{0}C	24.73	1.83	0.07	29.00	20.40	24.88	24.58
BOD_{5inf}	mg/L	228.47	41.33	2.08	450.00	74.00	232.57	224.38
COD_{inf}	mg/L	358.34	88.49	4.56	552.70	182.00	367.31	349.37
BOD_{inf} SL	mg/L	821.67	542.71	84.76	2329.5	109	992.96	650.36
COD_{inf} SL	mg/L	2615.11	2798.18	437.00	14090.88	826.56	3498.32	1731.89
TDS_{inf}	mg/L	465.15	86.07	3.71	739.00	230.00	472.44	457.87
TSS_{inf}	mg/L	173.28	11.87	0.73	199.00	146.00	174.72	171.85
EC_{inf}	µS/cm	783.83	118.96	4.86	1070.00	441.00	793.38	774.28
$TURB_{inf}$	NTU	9.649	0.581	0.023	11	8	9.695	9.603
DO_{inf}	mg/L	1.12	0.99	0.04	3.21	0.07	1.21	1.03
BOD_{5eff}	mg/L	22.06	7.16	0.36	70.00	5.00	22.76	21.36
COD_{eff}	mg/L	40.41	12.46	0.63	58.20	20.00	41.65	39.17

SD, standard deviations; SE, standard error; UB, Upper Bound of 95%.
Confidence Interval for the mean; LB, Lower bound of 95% Confidence Interval for the mean; BOD, biochemical oxygen demand; COD, chemical oxygen demand; TDS, total dissolved solids; TSS, total suspended solids; EC, electrical conductivity; DO, dissolved oxygen; Temp, Temperature; TURB, turbidity.
Suffixes: inf, influent; eff, effluent; SL, Septage Lagoons

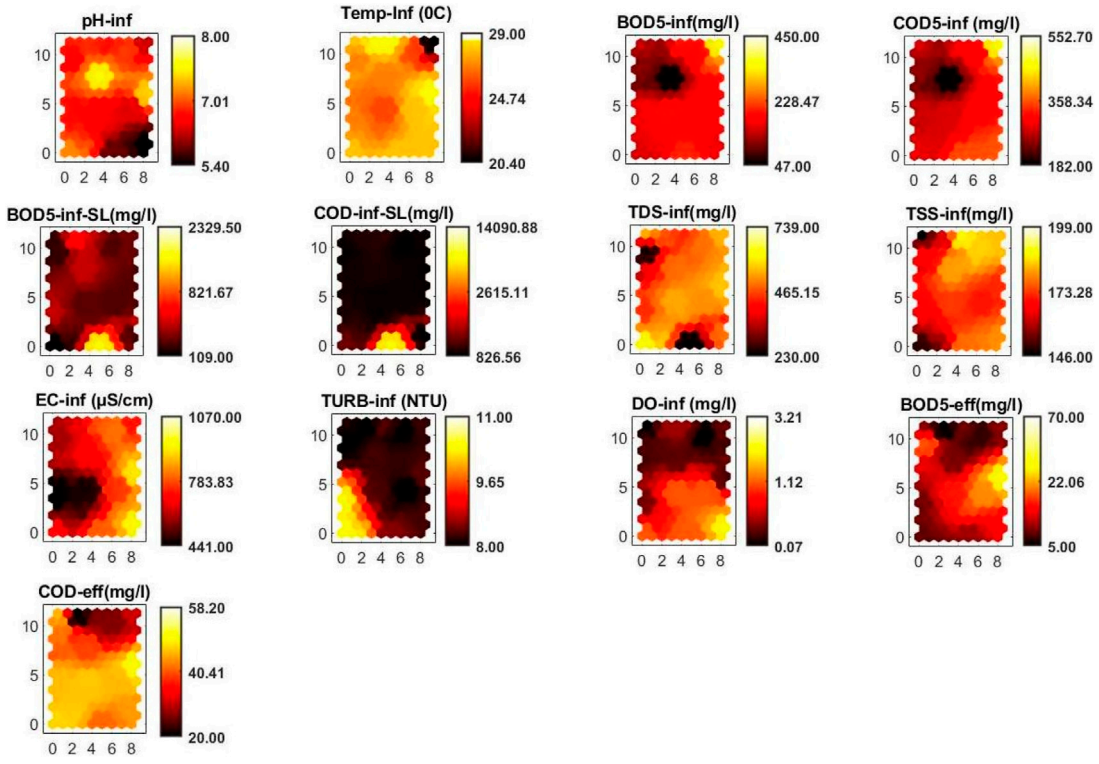

FIGURE 6
SOM component planes.

the foundation of the nervous system. Various philosophies divide the nervous system's signal progression and network constitution into several categories. In one, nearby neurons in a neural network mutually interact and compete with one another, adapting to become specific detectors of various signal prototypes. The learning is unsupervised or self-

TABLE 2 Correlation matrix for variables in code vectors.

	pH_{inf}	T_{inf}	BOD_{5inf}	COD_{inf}	BOD_{inf} SL	COD_{inf} SL	TDS_{inf}	TSS_{inf}	EC_{inf}	$TURB_{inf}$	DO_{inf}	BOD_{5eff}	COD_{eff}
pH_{inf}	1												
T_{inf}	0.161	1											
BOD_{5inf}	−0.461	**−0.606***	1										
COD_{inf}	**−0.615***	**−0.510***	**0.922****	1									
BOD_{inf} SL	−0.251	0.167	0.043	0.061	1								
COD_{inf} SL	−0.307	0.153	0.144	0.215	**0.834****	1							
TDS_{inf}	0.368	−0.125	0.131	0.088	**−0.620***	**−0.599***	1						
TSS_{inf}	−0.199	−0.319	0.339	0.275	0.249	0.035	−0.196	1					
EC_{inf}	−0.135	0.210	0.193	0.411	0.041	0.130	0.086	0.409	1				
$TURB_{inf}$	0.167	0.067	−0.009	−0.048	−0.048	0.125	0.162	−0.386	−0.320	1			
DO_{inf}	**−0.587***	0.204	0.098	0.269	0.110	0.301	0.003	0.024	0.234	0.163	1		
BOD_{5eff}	−0.013	0.154	0.033	0.066	−0.309	−0.157	−0.008	0.003	0.252	−0.237	0.196	1	
COD_{eff}	0.014	0.166	−0.131	−0.052	−0.285	0.050	0.114	−0.441	−0.100	0.380	0.344	**0.625***	1

*Correlation is significant at the 0.05 level (2-tailed).

**Correlation is significant at the 0.01 level (2-tailed).

10.3389/fenve.2024.1373881

TABLE 3 The structure of the ANFIS models developed and tested in the study for predicting effluent BOD values using Gaussian membership functions[a].

Model No	Number of input parameters	Input parameters	Number of membership functions in each input (*Nmf*)	Number of linear parameters $P_1=I\times(N_{input}+1)$	Number of nonlinear parameters $P_2=N_{input}\times N_{mf}\times 2$	Total number of parameters $P=P_1+P_2$	Number of fuzzy rules $I=(N_{mf})^{N^{input}}$
M1	4 (Raw)	T_{inf}, pH_{inf}, DO_{inf}, COD_{eff}	2	48	16	64	16
M2	2 (Raw)	pH_{inf} COD_{eff}	2	12	8	20	4
M3	3 (Raw)	pH_{inf}, EC_{inf}, COD_{eff}	4	320	24	344	64
M4	3 (Raw)	$TURB_{inf}$, EC_{inf}, COD_{eff}	2	24	12	36	8
M5	3 (Raw)	TDS_{inf}, TSS $_{inf}$, COD $_{inf}$	3	108	18	126	27
M6	3 (Raw)	TDS_{inf}, TSS $_{inf}$, COD SL $_{inf}$	3	108	18	126	27
M7	4 (Raw)	T_{inf}, pH_{inf}, DO_{inf}, COD_{eff}	3	324	24	348	81
M8	2 (Raw)	pH_{inf} COD $_{inf}$	2	12	8	20	4
M9	4 (Features)	T_{inf}, pH_{inf}, DO_{inf}, COD_{eff}	2	48	16	64	16
M10	2 (Features)	pH_{inf} CODeff	2	12	8	20	4
M11	3 (Features)	pHinf, EC_{inf}, COD_{eff}	4	320	24	344	64
M12	3 (Features)	$TURB_{inf}$, EC_{inf}, COD_{eff}	2	24	12	36	8
M13	3 (features)	TDS_{inf}, TSS $_{inf}$, COD $_{inf}$	3	108	18	126	27
M14	3 (Features)	TDS_{inf}, TSS $_{inf}$, COD SL $_{inf}$	3	108	18	126	27
M15	4 (Features)	T_{inf}, pH_{inf}, DO_{inf}, COD_{eff}	3	405	24	429	81
M16	2 (Features)	pH_{inf} COD $_{inf}$	2	12	8	20	4

[a]The choice of Gaussian membership functions was because it has just two modified parameters, the center, and width, hence it requires less training data.

organizing in this classification, which serves as the foundation for the development of self-organizing maps.

The main working strategy of such maps is the geometrical transformation of non-linear and complex correlation among high-dimensional data into a relatively simple low-dimensional view. SOM is made up of neurons arranged on standard one or two-dimensional grids, with each neuron, *i*, represented by an *n*-dimensional weight/reference/codebook vector given by,

$$m_i = [m_{i1}, ...m_{in}] \quad (1)$$

where n is the input vector dimension. These weight vectors comprise the codebook, which depicts the characteristics of the data or process. Figure 3 demonstrates that each neuron has two locations: one in the prototype vector, which is the input space, and another in the map grid, which is the output space (Vesanto et al., 2000a; 2000b). Thus, self-organizing maps are a vector projection method that converts high-dimensional input to low-dimensional output. The connection between adjacent n is determined by the neighborhood relationship.

The mapping is performed from the input Euclidean data space $\mathfrak{R}^n$ to a two-dimensional nodule lattice. Every node *i* is connected to a unique reference vector $m_i \in R^n$. When there is input data $x \in \mathfrak{R}^n$, it is compared to all the m_i to find the best match or response. Input is mapped to specific locations during this process. The Euclidean distance $\|x - m_i\|$, as illustrated in Eq. 2 is used to identify the best matching node, m_c, also known as Best Matching Unit as illustrated in Figure 3B (Kangas and Simulation, 2003).

$$\|x - m_c\| = min_i\{\|x - m_i\|\} \quad (2)$$

The basic steps in the development of the map, according to the SOM toolbox developed by the Helsinki University of Technology (Vesanto et al., 2000a), are initialization, training, and validation. Normalization is a process that prevents process variables from having a greater impact than other variables, ensuring that the entire

TABLE 4 The performance of the ANFIS models to predict BOD_5.

Model No	No of Input parameters (N)	CRM			MPE (%)			*R*		
		Training	Testing	Validation	Training	Testing	Validation	Training	Testing	Validation
M1	4 (Raw)	−23.36	21.27	26.76	55.92	48.53	51.24	0.18	0.48	0.39
M2	2 (Raw)	21.89	20.11	26.77	39.76	37.58	48.23	0.66	0.71	0.55
M3	3 (Raw)	−35.91	−24.23	13.44	57.49	52.55	47.44	0.13	0.25	0.58
M4	3 (Raw)	19.16	18.22	−22.11	51.11	46.81	57.32	0.57	0.72	0.67
M5	3 (Raw)	9.45	0.01	5.11	43.23	3.33e-6	2.300e-4	0.71	0.91	0.83
M6	3 (Raw)	−0.02	−0.01	−0.01	0.77	1.54	0.69	0.84	0.79	0.91
M7	4 (Raw)	1.124e-7	3.78e-7	0.03	7.51e-5	8.11e-3	4.66e-4	0.92	0.90	0.81
M8	2 (Raw)	21.03	20.05	−18.58	45.7	38.32	5.88	0.51	0.56	0.71
M9	4 (Features)	1.00e-4	−0.44	0.99	12.24	14.55	22.65	0.89	0.73	0.66
M10	2 (Features)	23.22	−12.62	0.004	46.31	35.22	5.19	0.59	0.71	0.81
M11	3 (Features)	−4.56e-5	−0.234	11.24	5.21	7.33	11.23	0.93	0.86	0.77
M12	3 (Features)	−8.11e-4	−0.025	−0.089	6.01	8.31	17.76	0.85	0.81	0.74
M13	3 (features)	0.03	7.6e-2	−2.29-3	7.22e-4	2.65e-10	5.10e-11	0.85	0.91	0.94
M14	3 (Features)	0.004	0.023	0.072	0.43	4.21	14.23	0.92	0.89	0.79
M15	**4 (Features)**	**3.78e-16**	**1.12e-16**	**−1.02e-15**	**1.56e-14**	**4.13e-10**	**2.30e-14**	**0.99**	**0.87**	**0.94**
M16	2 (Features)	10.68	16.32	8.71	10.78	12.87	9.21	0.82	0.73	0.83

CRM, coefficient of residual mass; MPE, mean percent error; R, correlation coefficient.
The bold values represent the model that had the better performance compared to the rest.

10.3389/fenve.2024.1373881

TABLE 5 Statistics summary of the ANFIS models to predict effluent BOD_5.

Model No	No of Input parameters (N)	Minimum			Maximum			Mean		
		Training	Testing	Validation	Training	Testing	Validation	Training	Testing	Validation
Observed		9	12	7	56	55	40	22.27	21.87	21.64
M1	4 (Raw)	−14.77	−10.90	5.88	46.74	39.34	31.63	22.67	22.01	19.88
M2	2 (Raw)	−17.75	11.22	−29.15	63.53	48.60	36.66	24.46	18.26	20.71
M3	3 (Raw)	−19.99	−14.67	−28.73	109.00	104.00	98.11	23.77	19.72	20.84
M4	3 (Raw)	−18.66	−11.60	−17.74	206.13	199.06	204.68	22.44	21.50	22.89
M5	3 (Raw)	9.11	14.23	8.45	54.75	58.33	43.41	23.81	20.70	23.77
M6	3 (Raw)	9.51	−12.75	8.23	54.22	56.19	39.73	22.11	21.52	21.71
M7	4 (Raw)	9.21	11.92	7.13	55.47	55.14	42.54	22.76	22.19	22.74
M8	2 (Raw)	−8.45	14.23	8.69	54.89	53.99	39.28	22.66	21.59	22.80
M9	4 (Features)	8.79	11.81	6.73	54.32	54.23	41.45	21.90	21.89	21.23
M10	2 (Features)	9.22	13.43	8.91	60.12	57.90	42.90	22.41	21.66	21.17
M11	3 (Features)	10.16	13.89	8.23	58.61	51.70	58.91	22.90	23.71	22.50
M12	3 (Features)	7.90	11.90	8.90	53.80	57.10	39.88	21.98	22.73	21.70
M13	3 (Features)	8.92	13.74	7.89	53.61	51.82	40.71	22.84	22.81	21.72
M14	3 (Features)	9.66	11.27	9.03	53.47	54.71	43.82	22.17	21.57	21.75
M15	**4 (Features)**	**8.86**	**14.12**	**8.19**	**55.62**	**43.29**	**38.56**	**22.31**	**20.74**	**22.08**
M16	2 (Features)	9.41	11.45	8.45	55.39	56.29	41.71	23.80	21.67	22.71

M1, Model No 1.

This is descriptive statistics for the model that had better performance compared to the rest. It has been highlighted to reflect its significance.

10.3389/fenve.2024.1373881

TABLE 6 Comparative studies in utilization of ANFIS for optimization problems.

Reference	Objective	Nature of the data used	Remarks on the model performance
Qiao et al. (2023)	Employed ANFIS to predict removal of pollutants in Wastewater treatment plant	Utilized data that was first screened by utilizing principal Component analysis (PCA) and Orthogonal Experiments	Satisfactory findings with R^2 values greater than 0.950 were notived. However, there was disparities between anticipated and actual results
Cheng et al. (2018)	Predicted influent characteristics using integrated Wavelet packet decomposition with ANFIS	Utilized historical data that was first decomposed by wavelet packet decomposition approach prior to feeding the data into ANFIS	Multi-scale ANFIS methodology that outperformed previous methods for predicting influent characteristics
Obasi et al. (2022)	Applied ANFIS, and a classical multi-linear regression analysis (MLR) to predict the performance of Abuja WWTP	Utilized preprocessed data to predict Conductivity, pH, Iron content, BOD, COD, TSS and TDS	MLR model outperformed ANFIS model

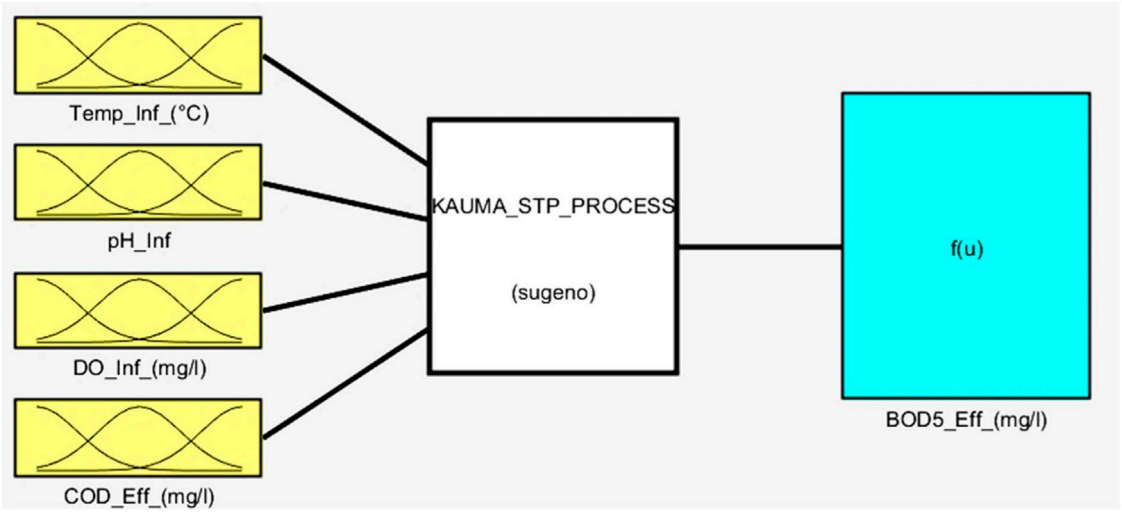

FIGURE 7
The structure of Model number 15.

set of variables has the same significance in the construction of maps. Initialization aids the algorithm's convergence to a good result by assigning weight vector values either randomly or linearly. During this process, each neuron is assigned random weight vectors ranging from zero to one (Vermasvuori et al., 2002). The main goal of training is to find the Best Matching Unit (BMU) or winning node among the map units for each input prototype. This unit is very similar to the input pattern. A distance function is commonly used to measure similarity, with closer distances defining greater similarity as defined by the Euclidean distance function. The best matching unit and its neighboring units are updated to reduce the difference between these units and the input pattern (Hsu, 2006). Two types of algorithms are used for updating: sequential training algorithms and batch training algorithms. Once the best matching unit is identified, its weight vectors are shifted closer to the input vector in the input space, a process known as updating. The best matching unit's topological neighbor units are also treated in the same way. The size of the adjustment of the weight vector is determined by the distance of these neighborhood neurons or units from the winner output array. More information on training the map can be found in Vesanto et al. (2000a), Lopez Garca and Machon Gonzalez (2004), Rustum (2009).

The SOM's quality is determined primarily by two error measurements: quantization error (qe) and topographic error (te) (Jorge et al., 2013). The mean Euclidean distance from the input vector to its best matching unit is used to calculate the quantization error.

This, in turn, provides map resolution and aids in identifying outliers. A high quantization error indicates that those input patterns are most likely outliers. The percentage of input vectors for which the best matching unit and the next best are not grid neighbors is referred to as topologic or topographic error. This error indicates the degree of data topology preservation while the map is fitted into the original dataset.

ANFIS

ANFIS modeling is the method of applying various learning techniques developed in the neural network literature to a fuzzy inference system (FIS) (Brown et al., 1994; Brown et al., 1994). The FIS maps its input space to the output space using a fractional non-linear relationship and a set of fuzzy if-then rules (Noori et al., 2013b. A FIS typically has five components: a fuzzification interface,

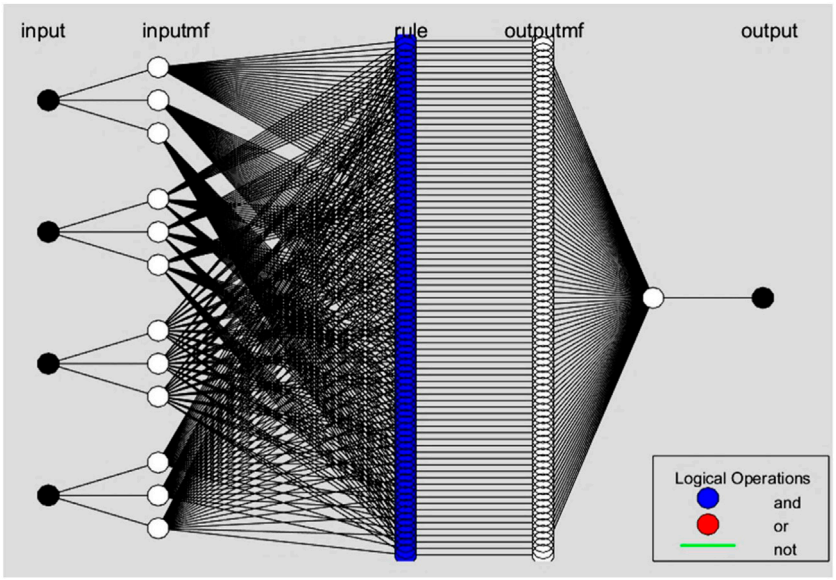

FIGURE 8
Schematic diagram of Model number 15 with 3 membership functions and 81 "IF -THEN" rules.

a rule base, a database, a decision-making unit, and a defuzzification interface. One of the most important steps in ANFIS development is the selection of a FIS type. There are various methods for developing the FIS. The first-order Sugeno FIS with two fuzzy rules (Figure 4) is used in this study as given by Eqs 3, 4:

$$\text{Rule 1: If } x \text{ is } A_1 \text{ and } y \text{ is } B_1; \text{ then } f_1 = p_1x + q_1y + r_1 \quad (3)$$

$$\text{Rule 2: If } x \text{ is } A_2 \text{ and } y \text{ is } B_2; \text{ Then } f_2 = p_2x + q_2y + r_2 \quad (4)$$

where A_1; A_2 and B_1; B_2 are the membership functions (MFs) for inputs x and y; respectively; and p_1;q_1;r_1 and p_2;q_2;r_2 are the parameters of the output function. Also, the output f is the weighted average of the individual rule outputs. To implement these two rules, an equivalent ANFIS structure (Figure 5) should be developed. In Figure 5, the characteristics of each layer are as follows (Jang, 1993; Lei, 2017).

Layer 0: It is called the input layer, and has n nodes where n is the number of inputs to the system

Layer 1: Input membership function—The first layer is used to fuzzificate the inputs, and all the nodes of this layer are adaptive. Its outputs are the membership grade of the inputs as given by Eqs 5, 6

$$o_i^1 = u_{A_i}(x), \quad i = 1, 2. \quad (5)$$

$$o_i^1 = u_{B_{i-2}}(y), \quad i = 3, 4, \quad (6)$$

where $u_{A_i}(x)$ and $u_{B_{i-2}}(y)$ are the fuzzy membership functions. Conventionally, the bell-shaped membership function is used, and it is expressed by Eq. 7

$$u_{A_i}(x) = \frac{1}{1 + \left[\left(\frac{x-c_i}{a_i}\right)^2\right]^{b_i}} \quad i = 1, 2. \quad (7)$$

where a_i, b_i, and c_i are the parameters of the membership functions

Layer 2: Rule—The nodes in this layer are fixed (Not adaptive). These are labeled M to indicate that they play the role of simple multipliers. The outputs of this layer represent the fuzzy strengths ω of each rule and can be expressed as

$$o_1^2 = \omega_i = u_{A_i}(x)u_{B_i}(y), \quad i = 1, 2. \quad (8)$$

Layer 3: Normalization—In this layer, the nodes are also fixed. These nodes are labeled with N, which means that they play a normalization role in the fuzzy strengths from the previous layer. The normalization factor is computed by the sum of the weight functions. The outputs of this layer are called normalized fuzzy strengths and are expressed as shown in Eq. 9

$$o_i^3 = \bar{\omega}i = \frac{\omega_i}{\sum_{i=1}^{2}\omega_i}, i = 1, 2. \quad (9)$$

Layer 4: Output membership function—The nodes of this layer are adaptive ones. Its outputs are represented by Eq. 10

$$o_i^4 = \overline{\omega_i}z_i = \overline{\omega_i}(p_ix + q_iy + r_i), i = 1, 2. \quad (10)$$

where p_i, q_i, r_i are the parameters of the membership functions, respectively.

Layer 5: Output—Only one single fixed node, labeled with S, is in this layer. This node performs the sum of the incoming signals. Thus, the overall output is expressed as shown in Eq. 11.

$$o_i^5 = z = \sum_{i=1}^{2}\overline{\omega_i}z_i = \frac{\sum_{i=1}^{2}\omega_i z_i}{\sum_{i=1}^{2}\omega_i} \quad (11)$$

Model evaluation criteria

After fitting the input data into ANFIS or any other model, it is important to evaluate how well the model performs. MATLAB offers "goodness of fit" which has a set of parameters that describe the model's accuracy. Evaluation can be done graphically using residual plots and

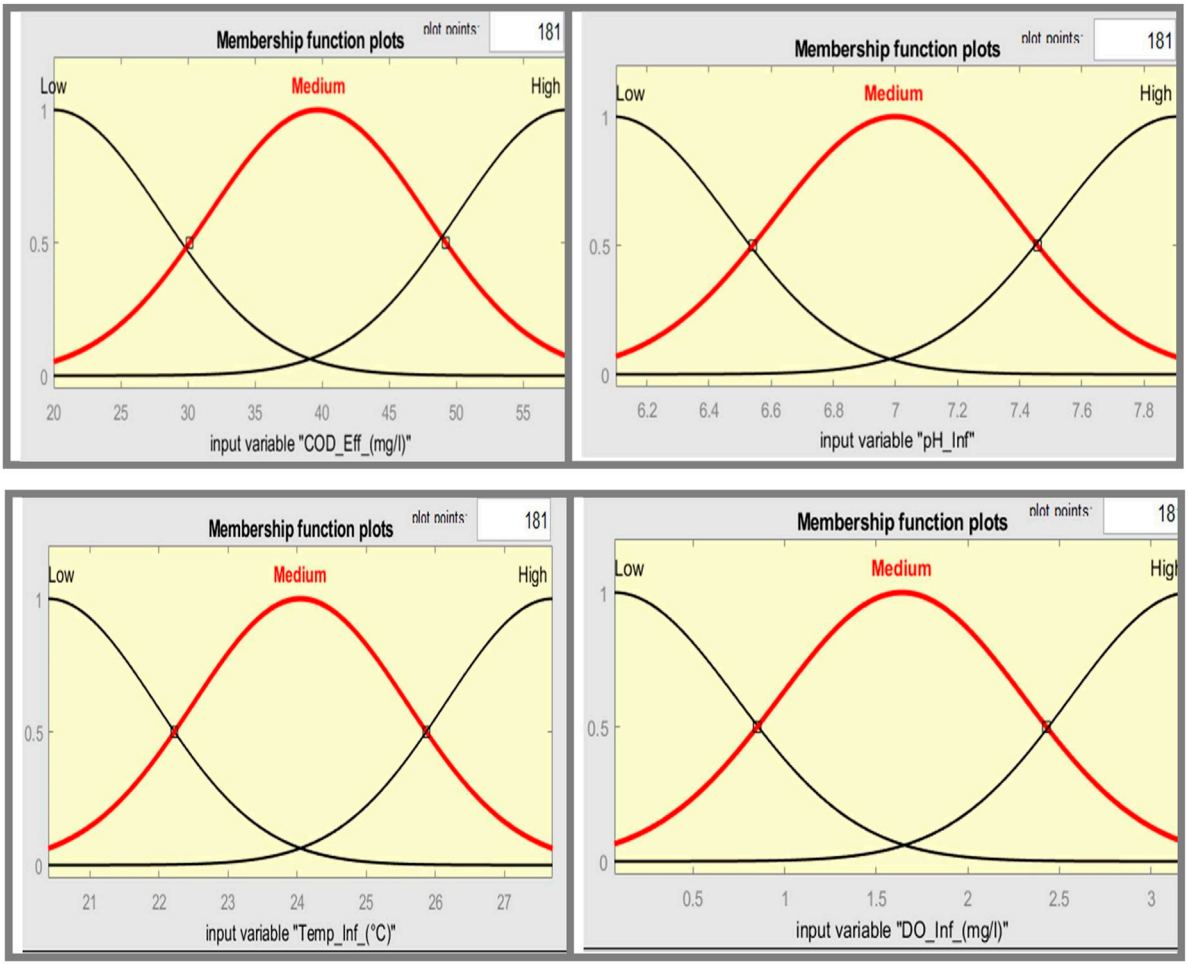

FIGURE 9
Fuzzy membership Functions in the input space.

TABLE 7 The parameters of Gaussian membership functions associated with input variables.

Inputs	Membership function	b (Width)	C (center)
$Temp_{\_Inf}$	Low	1.551	20.4
	Medium	1.549	24.05
	High	1.552	27.7
$pH_{\_inf}$	Low	0.3747	6.09
	Medium	0.3893	6.999
	High	0.389	7.908
$DO_{\_Inf}$	Low	0.6679	0.06926
	Medium	0.6709	1.639
	High	0.6589	3.216
$COD_{\_Eff}$	Low	8.111	20
	Medium	8.11	39.68
	High	8.11	58.2

prediction bounds and numerically using statistical parameters explained below. Graphical measures help the evaluation of the entire dataset at once and can display a wide range of relationships between the model and data (MathWorks, 2020). Numerical evaluation measures include correlation coefficient R, Average Absolute Error (AAE), Mean square error (MSE), and Root Mean Square Error (RMSE). In this study, however, only three indices as given by Eqs 12–14 were used due to their robustness, namely, the correlation coefficient (R) (Wang et al., 2006), the Coefficient of residual mass (CRM) (El-Sadek, 2006), and the Mean percent error (MPE) (Moriasi et al., 2007)

$$R = \frac{N\sum O_i P_i - \sum O_i \sum P_i}{\sqrt{\left[N\sum O_i^2 - \left(\sum O_i\right)^2\right]\left[N\sum P_i^2 - \left(\sum P_i\right)^2\right]}} \quad (12)$$

$$CRM = \frac{\sum_{i=1}^{N} O_i - \sum_{i=1}^{N} P_i}{\sum_{i=1}^{N} O_i} \quad (13)$$

$$MPE = \sum_{i=1}^{N}\left(\frac{|O_i - P_i|}{Oi}\right) \times 100\% \quad (14)$$

where P_i is the predicted value, O_i is the observed value and N is the number of data entries.

10.3389/fenve.2024.1373881

TABLE 8 Optimised fuzzy rules generated using modeling strategy developed in this study for model number 15.

Rule number	Rule antecedent (IF)				THEN	Consequent parameters				
	$Temp_{\_Inf}$	$pH_{\_Inf}$	$DO_{\_Inf}$	$COD_{\_Eff}$		a_1	a_2	a_3	a_4	a_0
1	Low	Low	Low	Low		−0.37	−0.51	−0.23	−0.09	42.17
2	Low	Low	Low	Medium		6.44	−16.84	11.48	−1.66	26.5
3	Low	Low	Low	High		66.22	−35.35	−61.86	−3.48	55.61
4	Low	Low	Medium	Low		−27.29	71.38	88.92	7.02	−112.3
5	Low	Low	Medium	Medium		9.94	26	−45.51	−2.56	40.91
6	Low	Low	Medium	High		−6.99	18.29	38.88	4.8	−28.77
7	Low	Low	High	Low		−222.06	30.32	1.27	−500.78	716.3
8	Low	Low	High	Medium		−23.01	25.19	105.33	10.92	−94.69
9	Low	Low	High	High		95.2	−55.45	−97.03	−5.45	87.23
10	Low	Medium	Low	Low		41.8	−12.55	−21.97	−1.23	19.75
11	Low	Medium	Low	Medium		21.75	−9.81	−0.016	−0.96	15.43
12	Low	Medium	Low	High		15.57	−22.43	−1.24	−2.21	35.28
13	Low	Medium	Medium	Low		46.13	−13.43	−23.49	−1.32	21.12
14	Low	Medium	Medium	Medium		62.95	−26.03	−45.55	−2.56	40.95
15	Low	Medium	Medium	High		58.93	−23.36	−40.88	−7.3	36.75
16	Low	Medium	High	Low		−4.54	11.88	20.79	13.17	−18.69
17	Low	Medium	High	Medium		180.37	−134.38	−235.15	−1.21	211.4
18	Low	Medium	High	High		−13.58	35.53	52.17	3.49	−55.89
19	Low	High	Low	Low		22.7	−43.7	−76.46	54.3	68.74
20	Low	High	Low	Medium		−27.63	72.27	90.47	4.11	−113.7
21	Low	High	Low	High		110.96	−65.28	−114.24	−6.42	102.7
22	Low	High	Medium	Low		36.2	−8.38	−14.66	−0.82	13.18
23	Low	High	Medium	Medium		−3.38	25.84	15.46	0.87	−13.9
24	Low	High	Medium	High		−392.69	833.22	1097.55	101.02	−1,616
25	Low	High	High	Low		175.42	288.84	−605.45	−290.41	454.4
26	Low	High	High	Medium		−3.69	25.65	16.89	0.95	−15.18
27	Low	High	High	High		−6.28	16.42	38.73	1.61	−25.83
28	Medium	Low	Low	Low		55	−23.54	−41.19	−2.31	37.03
29	Medium	Low	Low	Medium		40.66	−12.18	−21.31	−1.2	19.16
30	Medium	Low	Low	High		83.7	−46.29	−81	−4.55	72.82
31	Medium	Low	Medium	Low		31.3	−3.4	−5.96	−0.33	5.355
32	Medium	Low	Medium	Medium		44.51	−14.41	−25.22	−1.42	22.67
33	Medium	Low	Medium	High		−26.27	30.71	120.24	6.76	−108.1
34	Medium	Low	High	Low		66.61	−32.98	−57.72	−3.24	51.89
35	Medium	Low	High	Medium		−7.95	20.81	36.41	9.05	−32.73
36	Medium	Low	High	High		47.25	−18.97	−33.19	−1.87	29.84
37	Medium	Medium	Low	Low		35.79	−9.92	−17.36	−0.98	15.61

(Continued on following page)

TABLE 8 (*Continued*) Optimised fuzzy rules generated using modeling strategy developed in this study for model number 15.

Rule number	Rule antecedent (IF)				THEN	Consequent parameters				
38	Medium	Medium	Low	Medium		55.38	−24.54	−42.95	−2.41	38.61
39	Medium	Medium	Low	High		46.28	−16.43	−28.75	−1.62	25.85
40	Medium	Medium	Medium	Low		40.73	−12.38	−21.67	−1.22	19.48
41	Medium	Medium	Medium	Medium		38.49	−11.75	−20.57	−1.16	18.49
42	Medium	Medium	Medium	High		65.51	−32.73	−57.27	−3.22	51.49
43	Medium	Medium	High	Low		53.96	−23.44	−41.02	−2.31	36.88
44	Medium	Medium	High	Medium		45.13	−16.03	−28.05	−1.58	25.22
45	Medium	Medium	High	High		46.13	−16.04	−28.08	−1.58	25.24
46	Medium	High	Low	Low		29.88	−4.91	−8.6	−0.48	7.732
47	Medium	High	Low	Medium		52.9	−23.44	−41.01	−2.3	36.87
48	Medium	High	Low	High		−57.37	150.08	152.62	14.76	−236.1
49	Medium	High	Medium	Low		84.25	−47.74	−83.55	−4.7	75.11
50	Medium	High	Medium	Medium		−3.83	27.03	17.55	0.99	−15.78
51	Medium	High	Medium	High		129.2	−84.22	−147.39	−8.28	132.5
52	High	High	High	Low		−28.48	74.5	85.37	7.33	−117.2
53	High	High	High	Medium		122.33	−79.33	−138.82	−7.8	124.8
54	High	High	High	High		140.51	−90.26	−157.95	−8.88	142
55	High	Low	Low	Low		50.36	−19.25	−33.68	−1.89	30.28
56	High	Low	Low	Medium		−20.73	56.23	66.91	5.33	−85.32
57	High	Low	Low	High		38.31	−11.28	−19.74	−1.11	17.75
58	High	Low	Medium	Low		32.98	−7.79	−13.64	−0.77	12.26
59	High	Low	Medium	Medium		107.9	−67.76	−118.58	−6.66	106.6
60	High	Low	Medium	High		104.93	−65.22	−114.13	−6.41	102.6
61	High	Low	High	Low		−0.73	24.91	3.34	0.19	−3.002
62	High	Low	High	Medium		86.53	−51.08	−89.38	−5.02	80.35
63	High	Low	High	High		31.99	−5.82	−10.18	−0.57	9.156
64	High	Low	Low	Low		43.22	−13.65	−23.89	−1.34	21.48
65	High	Medium	Low	Medium		42.97	−13.01	−22.77	−1.28	20.47
66	High	Medium	Low	High		−1.95	25.11	8.94	0.5	−8.038
67	High	Medium	Medium	Low		51.25	−21.59	−37.78	−2.12	33.96
68	High	Medium	Medium	Medium		30.94	−5.07	−8.87	−0.5	7.976
69	High	Medium	Medium	High		−2.04	24.33	9.32	0.52	−8.378
70	High	Medium	High	Low		41.02	−13.12	−22.96	−1.29	20.64
71	High	Medium	High	Medium		28.12	−2.94	−5.14	−0.29	4.622
72	High	Medium	High	High		29.61	−4.21	−7.36	−0.41	6.616
73	High	High	Low	Low		42.89	−15.4	−26.94	−1.51	24.22
74	High	High	Low	Medium		42.94	−12.92	−22.6	−1.27	20.32
75	High	High	Low	High		430.33	−319.99	−559.95	−31.47	503.4

(Continued on following page)

TABLE 8 (*Continued*) Optimised fuzzy rules generated using modeling strategy developed in this study for model number 15.

Rule number	Rule antecedent (IF)				THEN	Consequent parameters				
76	High	High	Medium	Low		−6.03	25.77	27.6	1.55	−24.81
77	High	High	Medium	Medium		95.95	−54.8	−95.9	−5.39	86.21
78	High	High	Medium	High		62.88	−28.82	−50.43	−2.83	45.34
79	High	High	High	Low		55.92	−23.33	−40.82	−2.29	36.7
80	High	High	High	Medium		78.63	−43.49	−76.11	−4.28	68.42
81	High	High	High	High		48.13	−18.65	−32.64	−1.83	29.34

inf, Influent; eff, Effluent; Temp, Temperature; DO, dissolved oxygen; COD, chemical oxygen demand.
Fuzzy Inference Diagram for model number 15.

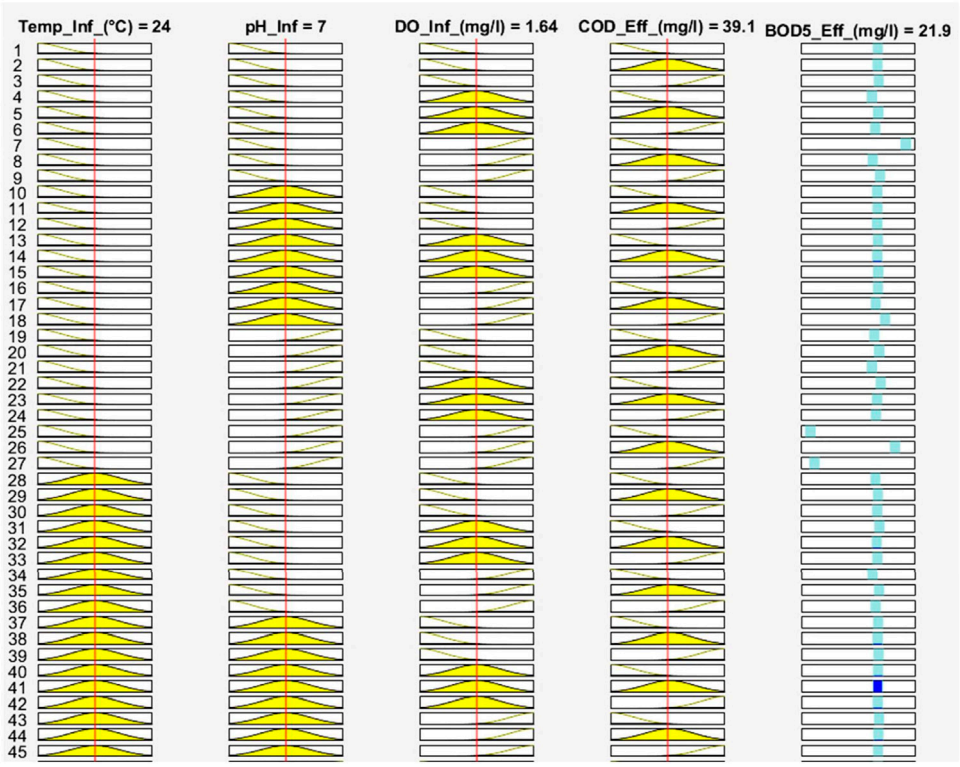

FIGURE 10
(Continued).

The goodness of fit measures the similarity of the shapes of the original and predicted cited time series and ranges between −1 and 1; the absolute value of the correlation coefficient for perfect prediction is unity (Rustum, 2009). The CRM characterizes the tendency to over-estimate CRM < 0 or under-estimate a property (CRM > 0) (Malota et al., 2022) on the other hand, MPE measures the magnitude of errors between the measured and predicted values relative to the measured values. MPE value closer to zero indicates that the predicted values are very close to the measured values (Legates and McCabe, 1999; Malota et al., 2022). To overcome the problem of overfitting, an early stop rule was applied by dividing the KSTP data into three subsets: training (432 data points), validation (92 data sets), and testing (92 data sets).

Ethical consideration

The study sought clearance from the Mzuzu University Research Ethics Committee (MZUNIREC) Ref No: MZUNIREC/DOR/21/62. Permission was also obtained from Lilongwe City Council to engage Laboratory technicians during data collection processes. Informed

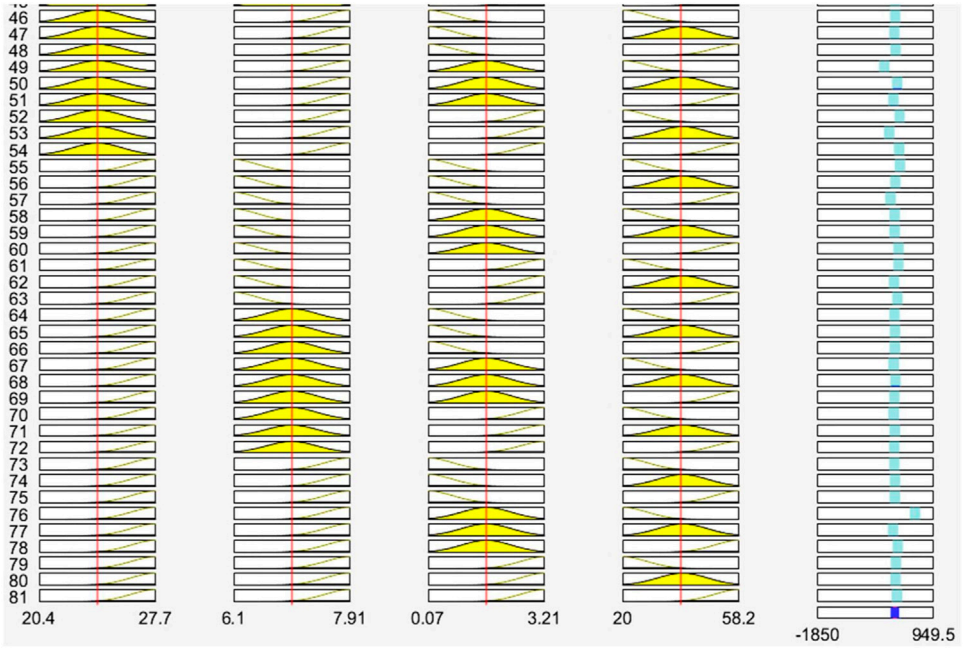

FIGURE 10
(Continued). Fuzzy inference diagram for model number 15 predicting effluent BOD. To obtain the output value as shown in the picture, the user only needs to enter the input values.

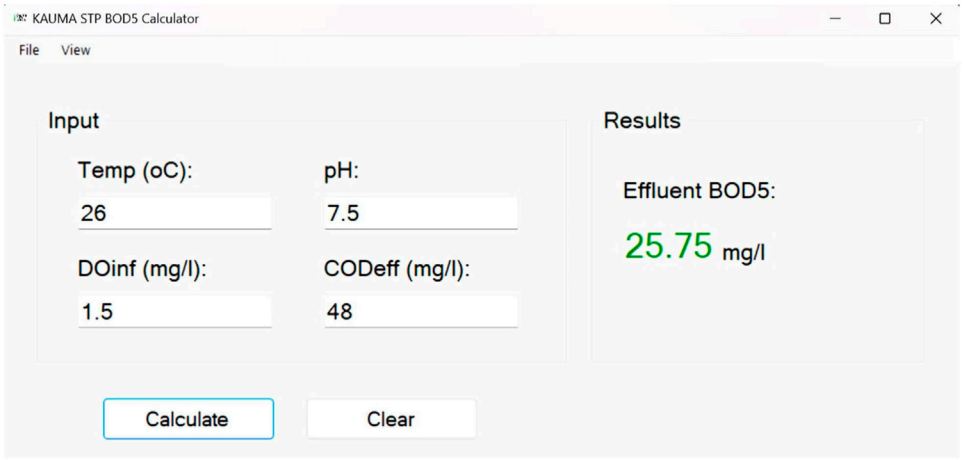

FIGURE 11
Graphical user interface of model number 15. Contrary to Figure 10, To obtain the output value as shown in the picture, the user only needs to enter the input values.

consent was also obtained from the Laboratory technicians and KSTP who participated in the study.

Results and discussions

Descriptive statistics of Kauma sewage treatment plant data

The preprocessed data, with a sample size of 616 data sets per variable, was examined. The estimated descriptive statistics for a number of variables at the KSTP (Table 1) offered an in-depth overview of influent and effluent characteristics. The pH of the influent wastewater averaged 7.01, indicating slightly alkaline conditions, with a standard deviation (SD) of 0.46, indicating steady pH levels. The upper bound (UB) and lower bound (LB) values (7.05 and 6.97, respectively) set the 95% confidence interval for pH readings. In terms of temperature (Temp inf), the mean of 24.73°C demonstrates a moderate thermal condition, with an SD of 1.83 suggesting variability. UB (24.88) and LB (24.58) determined the 95% confidence interval. BOD_5inf and COD_{inf} results, with mean values of 228.47 mg/L and 358.34 mg/L, respectively,

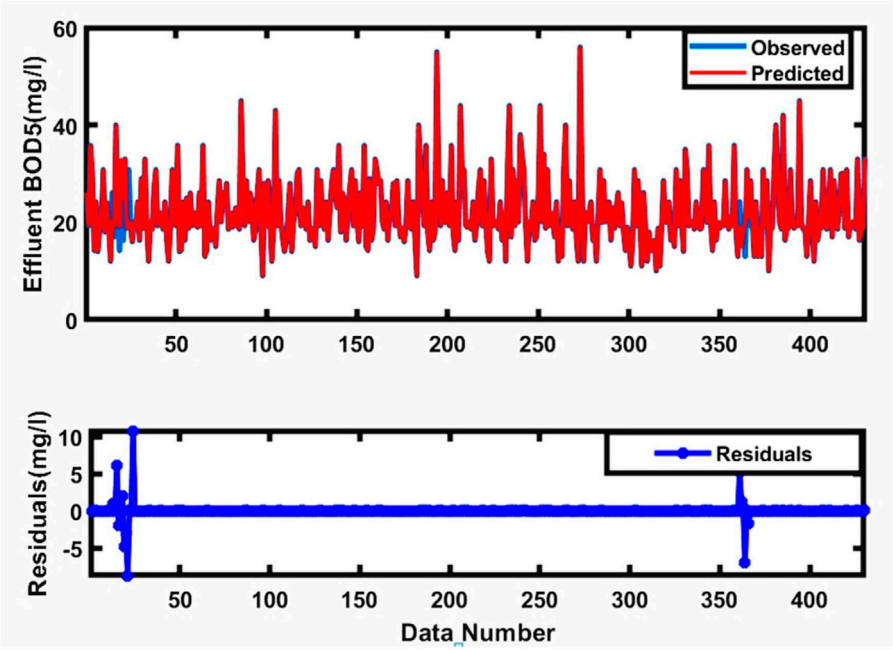

FIGURE 12
Time series plots of observed and predicted BOD during training for model number 15.

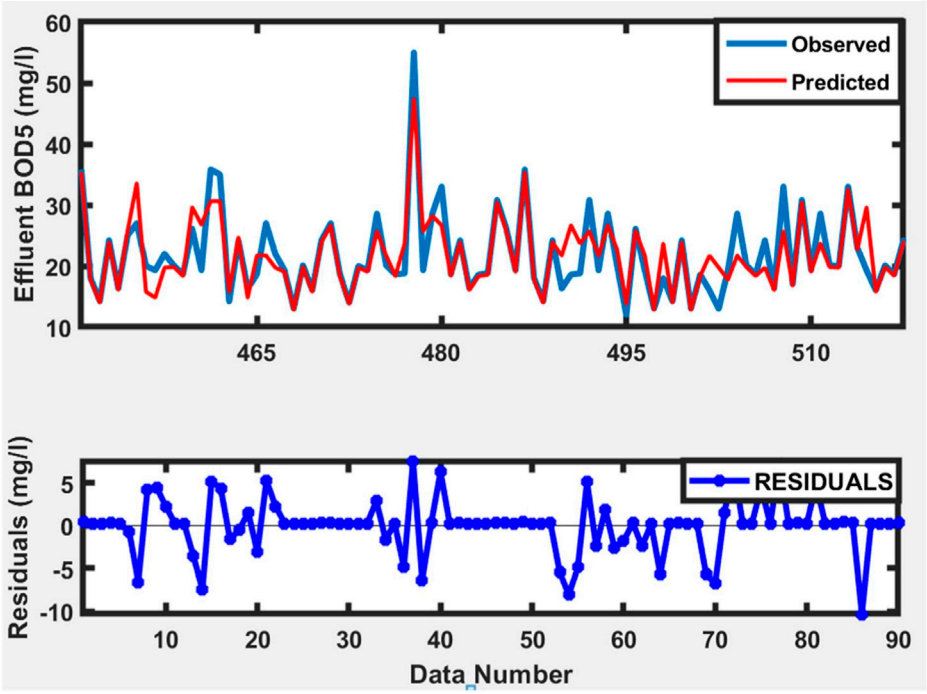

FIGURE 13
Time series plots of observed and predicted BOD during testing for model number 15.

emphasized the organic load in the influent. TDS_{inf} and TSS_{inf} provide information on total dissolved and suspended solids, with values of 465.15 mg/L and 173.28 mg/L, respectively. EC_{inf} (mean: 783.83 S/cm) and $TURB_{inf}$ (mean: 9.649 NTU) measurements provided information about electrical conductivity and turbidity. The mean DO_{inf} of 1.12 mg/L indicated the concentration of dissolved oxygen, which is essential for aerobic living activity. Effluent BOD_{5eff} (mean: 22.06 mg/L) and COD_{eff} (mean:

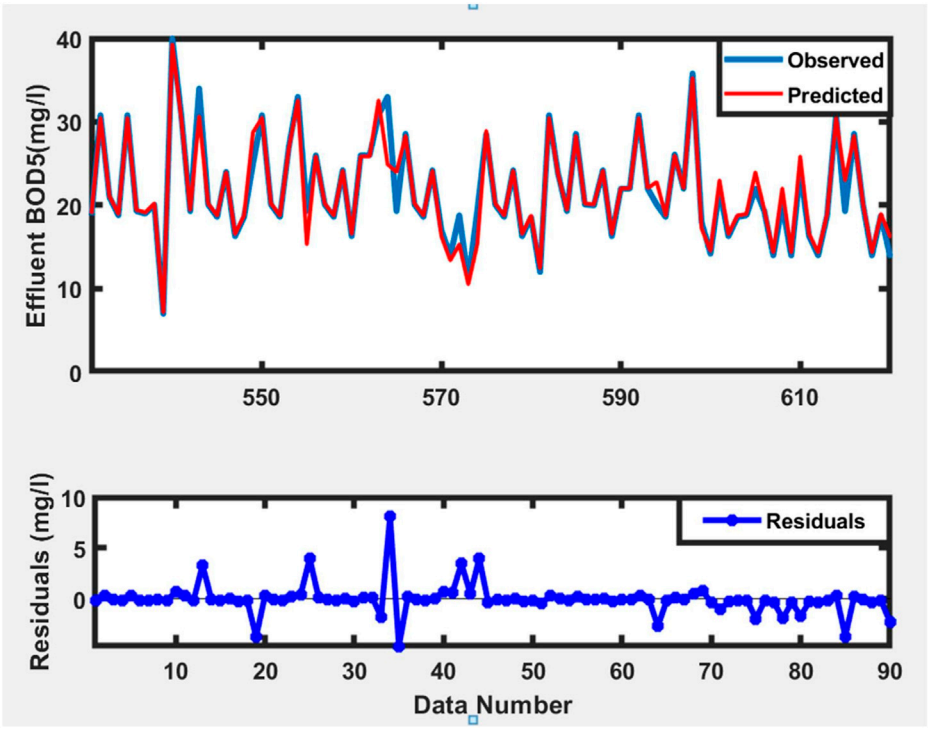

FIGURE 14
Time series plots of observed and predicted BOD during Validation for model number 15.

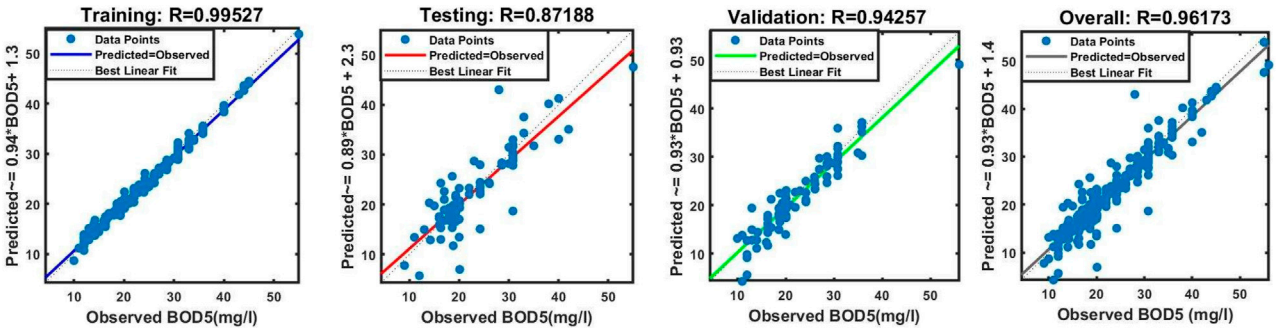

FIGURE 15
The scatter plot of modeled versus observed data during training, testing, and validation for model number 15.

40.41 mg/L) demonstrated a significant reduction in organic and chemical oxygen demand, demonstrating the efficacy of the treatment technology.

The mean COD to BOD_5 ratios were found to be 1.57 and 1.83 for influent and effluent wastewater, respectively. However, samples from septage lagoon had a much higher ratio of 3.18, which is above the average range of 1.25–2.5 for domestic wastewater (Metcalf and Eddy, 2013). This discrepancy stems from various factors as highlighted by Niwagaba et al. (2014). Firstly, wastewater from septic tanks and pit latrines contains more organic and inorganic constituents, such as feces and household chemicals, that can elevate COD levels. In addition, longer retention times in septic tanks and latrines facilitate greater organic decomposition resulting into high COD than BOD_5 levels. Furthermore, anaerobic conditions prevalent in septic tanks produce non-biodegradable compounds that contribute to COD. Lastly there is minimal dilution in septic systems compared to sewered networks, this maintains higher COD concentrations until discharge (Niwagaba et al., 2014).

Before beginning the modeling process, the entire dataset was divided into three sets: the first set of 432 observations was used to train the model, the second set of 92 observations was used to test the model, and the final set of 92 observations was used to validate the model. The study looked at two scenarios: the first consisted of developing an Adaptive Neuro-Fuzzy Inference System (ANFIS) Model from raw data, and the second involved developing a hybrid

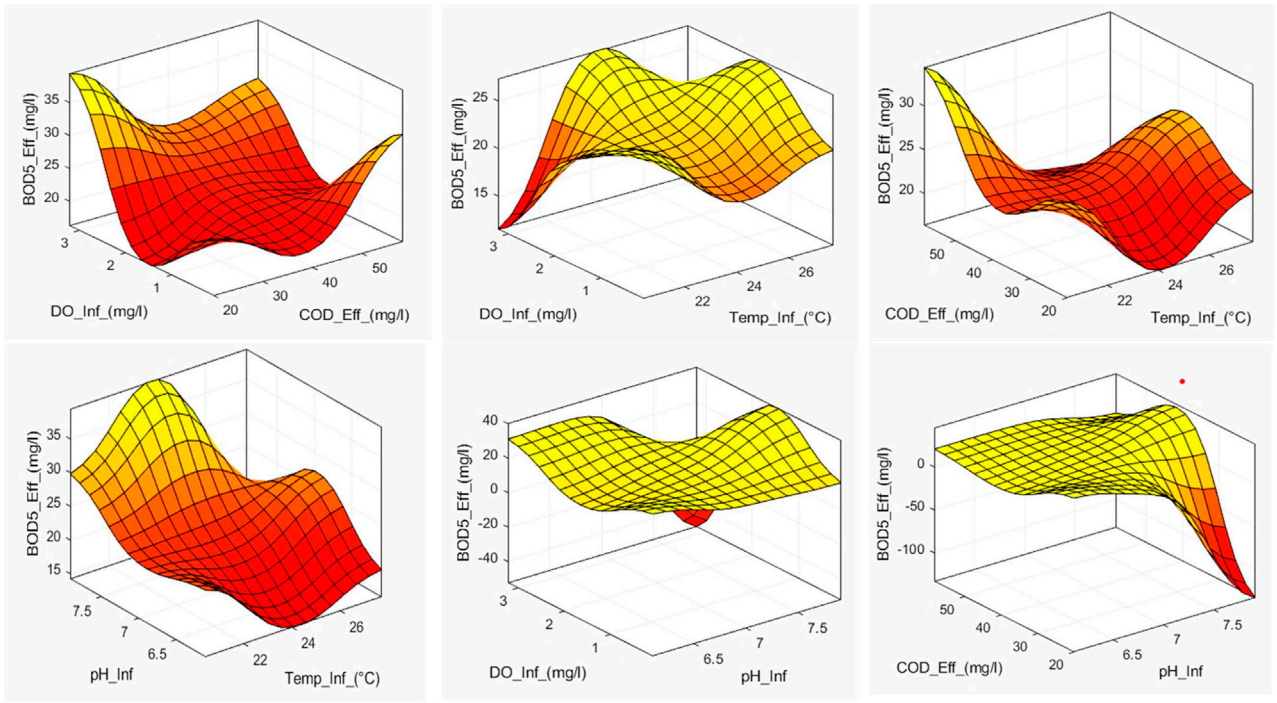

FIGURE 16
3D response graphs for model number 15.

Self-Organizing Map (SOM) and ANFIS model using extracted features.

SOM component planes

The generation of component planes, a key feature of SOMs, is a rigorous procedure that demonstrates relationships between variables in the data. These planes are created during SOM training, which involves mapping the input space onto a two-dimensional grid of neurons. Each neuron corresponds to a weight vector, whose dimensions match those of the input data (Mng'ombe et al., 2023). By iteratively altering these weights, the SOM learns to represent the data's underlying structure. Once trained, component planes are created by assigning colors or intensities to neurons based on the values of specified dimensions in the input data (Kumar et al., 2021a). This visualization technique provides useful insights on the relationships and distributions of distinct elements, making it easier to explore and analyze complex datasets (Nkiaka et al., 2016). These component planes, as shown in Figure 6, represent each variable in the SOM. Each plane is effectively a sliced SOM, with a single vector variable indicating its value in each map unit (Kalteh et al., 2008). To improve readability, the component planes are color-filled or grey-scaled, depicting the feature values of each SOM unit inside the 2-D lattice. Darker hues imply that the associated variable component has a lower relative value. This visual depiction efficiently delineates zones where a variable is high, low, or average, allowing for a simple understanding of the correlation between SOM-simulated values of selected wastewater parameters (Kumar et al., 2021b).

A visual analysis of the component planes indicates that the BOD_{5inf} plane's color (or gray) gradient aligns parallel to the COD_{inf} gradient, demonstrating a correlation where high BOD_{5inf} values are associated with high COD_{inf} values and *vice versa*. Similarly, greater BOD_{5eff} levels correlate with high COD_{eff} levels and *vice versa*. The component planes support a negative association between pH and BOD_5inf, $CODi_{nf}$, and DO_{inf}, with low pH values associated with high BOD_{5inf}, COD_{inf}, and DO_{inf} values. The expected positive association between BOD and COD has been validated, correlating with expectations that COD values are often greater than BOD values, with the ratio fluctuating depending on wastewater characteristics (Rai et al., 2019). The entire correlation matrix containing all 11 variables of the prototype vectors is shown in Table 2. While this table is a simple tool for examining the linear relationships between different variables, its findings are consistent with the cross-correlation indications derived from the much more complex SOM analysis, which resulted in the development of the component planes.

Table 2 presents a thorough perspective of the correlation matrix for the variables within the code vectors, giving insights into the complex relationships between different parameters within the wastewater treatment framework. Among the notable findings was a modest positive correlation between pH and temperature (T_{inf}), indicating a minor tendency for both variables to fluctuate together. Furthermore, a strong negative connection occurred between influent BOD_{5inf} and $CODi_{nf}$, which corresponded to the expected inverse association in wastewater. The component planes revealed the influence of the septage lagoon (BOD_{inf} SL and COD_{inf} SL) on numerous parameters, demonstrating a complicated interaction between the septage lagoon and other wastewater properties. Positive correlations between total dissolved solids (TDS_{inf}) and total suspended solids (TSS_{inf}) in

the influent indicated a simultaneous increase in both metrics. In contrast, electrical conductivity (EC_{inf}) exhibited a negative relationship with turbidity ($TURB_{inf}$), implying that higher electrical conductivity is associated with clearer wastewater. DO_{inf} (dissolved oxygen in influent) had a substantial negative correlation with effluent biochemical oxygen demand (BOD_{5eff}), highlighting the relevance of dissolved oxygen in the treatment process. Furthermore, effluent chemical oxygen demand (COD_{eff}) demonstrated a positive association with TSS_{inf}, indicating a possible relationship between suspended solids concentration and chemical oxygen demand in effluent. In conclusion, our correlation matrix gave a foundational understanding of the interplay of several wastewater metrics, stressing the importance of these correlations in describing wastewater quality, as highlighted by the significant correlations at the 0.05 and 0.01 levels.

ANFIS model structure

Table 3 displays the model architectures of several models developed and evaluated with Gaussian membership functions. Multiple models were developed by experimenting with different combinations of input variables and using various membership functions. The association of these input factors to effluent BOD_5 and the promptness with which each variable could be measured influenced their selection. Given the available database, the inclusion of four input variables was assessed to be the maximum number of combinations possible. For example, when using four inputs, each associated with three membership functions, the total number of adjusted parameters, as calculated by Eq. 15, was 430—well within the 432 data points available for training. The evaluation of five parameters, however, using five parameters could exceed the number of training data sets, limiting the model's degrees of freedom.

$$N_{total} = \left(N_{input} \times N_{mf} \times N_{pp}\right) + \left(l \times N_{cp}\right) \quad (15)$$

$$l = \left(N_{mf}\right)^{N_{input}} \quad (16)$$

$$N_{cp} = N_{input} + 1 \quad (17)$$

where N_{total} is the total number of modified parameters, N_{input} is the number of inputs, N_{mf} is the number of membership functions associated with each input, N_{pp} is the number of modified parameters per membership function, i. e., in the case of the Gaussian membership function; l in Eq. 16 is the number of rules; N_{cp} in Eq. 17 is the number of modified parameters in the sequence part of each rule

Table 4 presents a detailed summary of the performance of produced models in two scenarios: M1–M8, where models were built using raw data, and M9–M16, where models were built using extracted features using SOM. The results show that model M1–M16's performance was unsatisfactory, as shown by higher values of the Coefficient of Residual Mass (CRM) and Mean Percent Errors (MPE). Furthermore, as seen in Table 5, models developed utilizing raw data produced negative results.

Table 4 shows that improving the raw data by pre-processing with the SOM technique considerably improved model performance. Consider models 7 and 15, which both had the same structure—four inputs and three membership functions associated with each input. However, model number 15 outperformed model number 7, with the correlation coefficient in the validation dataset increasing from 0.81 to 0.94. This trend is repeated for the remaining models, demonstrating the effectiveness of raw data pre-processing with the SOM algorithm in enhancing overall model performance.

The ANFIS models' performance, as presented in Tables 4, 5, provides a more comprehensive understanding of the predictive abilities for BOD_5 concentrations. The coefficient of residual mass (CRM), mean percent error (MPE), and correlation coefficient for models with raw and extracted features are presented in Table 4. Model M1, which had four raw input parameters, had negative CRM values during testing and validation, indicating a probable model fitting issue. Similarly, during testing, Model M5 demonstrated an MPE close to zero, indicating a near-perfect match. Models M3 and M11, which used three raw input parameters, had negative CRM values, indicating an overestimation of BOD_5 concentrations. The addition of feature extraction in Models M9–M16 significantly increased performance, with the Model M15 exhibiting excellent results including nearly minimal CRM and MPE values and excellent correlation coefficients.

Table 5 summarizes statistics on predicted effluent BOD_5 concentrations, which offer light on the models' ability to mimic observed values. Models containing raw input parameters, such as M3 and M4, had broader ranges and higher mean values, indicating difficulties in predicting extreme concentrations. Model M5 stood out for its consistency with observed values, having a shorter range and closer mean value alignment. Models M9–M16, on the other hand, demonstrated competitive performance with reduced ranges and mean values by leveraging extracted characteristics. Model M15, in particular, displayed distinct match with observed values. However, negative predictions in raw data, as demonstrated in Models M2 and M8, should be taken into account because they may reflect limits in effectively capturing complex relationships. Overall, the introduction of feature extraction demonstrated potential to enhance the predicted accuracy of ANFIS models for effluent BOD_5 values.

These findings are consistent with previous research, as shown in Table 6, and highlight the need of combining ANFIS algorithms with complementing approaches such as SOM to improve model accuracy. Discrepancies discovered in similar studies highlight the complexities of this methodology and its critical role in improving the reliability and overall performance of ANFIS models.

Given Model 15's higher performance as compared to its competitors, an in-depth scrutiny was conducted solely on this model. Model 15 is distinguished by three membership functions associated with each of its four input variables, namely, T_{inf}, pH_{inf}, DO_{inf}, and COD_{eff}, as illustrated in Figures 7, 8. Figure 9 depicts the membership functions and Gaussian membership functions based on the operational range of the model.

Membership functions play an important role in defining and expressing the fuzzy sets that are essential to a fuzzy inference system. Figures 7–9 exemplify how these functions help to express fuzzy thinking and decision-making based on linguistic considerations. Membership functions, in essence, quantify the degree to which an input value aligns with a given fuzzy set. These functions, which typically span a

specific range of input values, assign a membership degree, ranging from 0 to 1, to each value inside that range. This degree of membership indicates the input value's association with the given fuzzy set, providing a deeper understanding of the input's participation in the larger fuzzy set.

The parameters for the Gaussian membership functions related to input variables are summarized in Table 7, which includes the center (c) and width (b) components. The developed model is distinguished by a thorough set of 81 rules that comprise a total of 429 modified parameters. There are 24 non-linear parameters among these, with the remaining 405 linear parameters forming the model's complicated framework.

Table 8 illustrates the optimized fuzzy rules that govern Model 15. These 81 rules define the complex relationships between input and output variables. Figure 10 illustrates the integration process of these rules, which complements this tabular representation. Table 8 systematically details each rule, with discrete parts dedicated to the "IF and THEN" conditions for each rule. The IF component defines a set of criteria depending on input variables, whereas the THEN component defines the expected consequence or action. For example, rule 1 in Table 8 can be understood as follows:

IF *(TEMP) is Low and (pH) is Low and* (DO_{inf}) *is Low and* (COD_{eff} *is low,* ***THEN*** *(effluent BOD) is 42.17 - (0.37*temp) - (0.51* pH) - (0.23*DO) -(0.09**COD_{eff}*)*

Data that was not used in the training phase was used for testing and validation of the trained model. Figures 11–13 depict time series plots of observed and anticipated effluent BOD_5 alongside their corresponding residuals during the training, testing, and validation processes. Figure 14 depicts the modeled data in comparison to the observed data during the training, testing, and validation phases.

To determine the number of rules, the typical fuzzy inference approach relies on an expert judgment which is well-versed in the simulated system. This expert employs heuristic insights gained from vast experience gained from the simulations. In this study, however, the number of membership functions allocated to each input variable was established empirically by trial and error, eliminating the requirement for an expert judgement. The suggested model accurately determines process conditions by combining values from multiple factors. Furthermore, the suggested model is resistant to missing variables and outliers. In comparison to deterministic models, creating a fuzzy logic model is likewise a relatively simple task.

The interactions between numerous input variables and a single output variable are frequently shown via 3D graphs when using the Fuzzy Toolbox in MATLAB. These graphs support decision-making and aid in understanding fuzzy systems' behavior. To understand a 3D graph produced by the Fuzzy Toolbox, it is necessary to examine its shape, contours, and surface properties. As illustrated in Figure 15 the model input variables ($Temp_{\_Inf}$, $pH_{\_Inf}$, $DO_{\_inf}$, and $COD_{\_eff}$) are represented on the *X* and *Y*-axes of the graphs. These variables frequently match up with linguistic concepts or membership algorithms specified in the fuzzy system. For interpretation, it is crucial to comprehend the range and linguistic significance of these variables. On the 3D graph's Z-axis, the output variable (BOD_{5_eff}) is shown. It displays the system's reaction or output to the supplied inputs. On the graph, the output variable values are typically depicted by color or contour lines.

Conclusion

The current study offers a novel approach for predicting BOD_5 values in wastewater using wastewater data collected from the KSTP in Lilongwe City. To successfully predict effluent BOD_5, the hybrid SOM-ANFIS model was trained, validated, and tested. Initially, a set of measured raw data was used to train and test the ANFIS model. The model did not work well, though, because the raw data was noisy. To tackle this issue, features from the data were extracted using the SOM. These retrieved features were used to train and evaluate a new set of models, thereby improving their performance. The results showed that the SOM-ANFIS model outperformed the ordinary ANFIS model in terms of modeling capabilities and certainty, even when accounting for varying numbers of inputs and fuzzy membership functions. The SOM-ANFIS model was also able to handle blank spaces in the data or missing values without challenges. This implies that SOM assisted models have greater capabilities compared to ordinary ANFIS in predicting BOD_5 for KSTP. Using MATLAB's app designer, an easy-to-use graphical user interface as demonstrated in Figure 16 was developed to improve usability and user-friendliness. The developed GUI was able to facilitate user interaction and understanding the created fuzzy inference system. The developed model is expected to reduce treatment operation and testing costs, allow continuous monitoring, and consequently protect the environment. Future improvement of the developed model will include integrating it with hardware components through the Supervisory Control and Data Acquisition (SCADA) system. The authors recommend for the development of a specialized model, such as a Convolutional Neural Network, intended exclusively for fecal sludge characterization. Considering the fact that faecal sludge characteristics are highly variable with space and time, it is further recommended that data from other sources such as rivers and other wastewater treatment facilities in Malawi and beyond be collected to update the developed models. This will widen the application of developed models to expose them to a wider range of scenarios.

Software availability statement

The SOM Toolbox (Version 2.2) for MATLAB used in this study is freely available for download from GitHub (https://github.com/ilarinieminen/SOM-Toolbox). The study also used the fuzzy logic toolbox available in MATLAB

Data availability statement

The original contributions presented in the study are included in the article/supplementary material, further inquiries can be directed to the corresponding author.

Author contributions

MHM: Conceptualization, Data curation, Formal Analysis, Funding acquisition, Investigation, Methodology, Project administration, Resources, Visualization, Writing–original draft, Writing–review and editing. EM: Conceptualization, Data

curation, Investigation, Methodology, Software, Supervision, Writing–original draft, Writing–review and editing, Formal Analysis, Funding acquisition, Project administration, Resources, Validation, Visualization. BC: Project administration, Supervision, Writing–original draft, Writing–review and editing. RC: Writing–original draft, Writing–review and editing, Methodology.

Funding

The authors declare that financial support was received for the research, authorship, and/or publication of this article. This work received funding from National Commission for Science and Technology (NCST) under NCST Small Grants Scheme. It also received funding from the Malawi Ministry of Education, Science, and Technology under Higher Education Research and Development for Young Researchers (postgraduate) scheme (Ref. No. EDU/HE/21/74).

Acknowledgments

The Authors are grateful to the following people, Dr. Linda Strande (Ph.D.) and the entire team from Eawag (Swiss Federal Institute of Aquatic Science and Technology) for the technical guidance and material support. Lilongwe City Council for the support rendered during data collection, particularly to the following people Eng. Phyllis Mkwezalamba, Mr. Obvious Nyirenda, Mr. John Thyoka, Mr. Chimango Mweso, and Mr. Orymo Nyirenda

Conflict of interest

The authors declare that the research was conducted in the absence of any commercial or financial relationships that could be construed as a potential conflict of interest.

Publisher's note

All claims expressed in this article are solely those of the authors and do not necessarily represent those of their affiliated organizations, or those of the publisher, the editors and the reviewers. Any product that may be evaluated in this article, or claim that may be made by its manufacturer, is not guaranteed or endorsed by the publisher.

References

Abunama, T., Othman, F., Ansari, M., and El-Shafie, A. (2019). Leachate generation rate modeling using artificial intelligence algorithms aided by input optimization method for an MSW landfill. *Environ. Sci. Pollut. Res.* 26 (4), 3368–3381. doi:10.1007/s11356-018-3749-5

Alsulaili, A., and Refaie, A. (2021). Artificial neural network modeling approach for the prediction of five-day biological oxygen demand and wastewater treatment plant performance. *Water Supply* 21 (5), 1861–1877. doi:10.2166/WS.2020.199

APHA (2017). *Standard methods for the examination of water and wastewater*. Washington, D.C., USA: American Public Health Association.

Arlyapov, V. A., Plekhanova, Y. V., Kamanina, O. A., Nakamura, H., and Reshetilov, A. N. (2022). Microbial biosensors for rapid determination of biochemical oxygen demand: approaches, tendencies and development prospects. *Biosensors* 12 (10), 842. doi:10.3390/BIOS12100842

Bekkari, N., and Zeddouri, A. (2019). Using artificial neural network for predicting and controlling the effluent chemical oxygen demand in wastewater treatment plant. *Manag. Environ. Qual. Int. J.* 30 (3), 593–608. doi:10.1108/meq-04-2018-0084

Brown, M., Harris, C. J., and Christopher, J. (1994). *Neurofuzzy adaptive modelling and control*. Hoboken, New Jersey, USA: Prentice Hall.

Cheng, Z., Li, X., Bai, Y., and Li, C. (2018). Multi-scale fuzzy inference system for influent characteristic prediction of wastewater treatment. *Clean. – Soil, Air, Water* 46 (7), 1700343. doi:10.1002/CLEN.201700343

El Alaoui El Fels, A., Mandi, L., Kammoun, A., Ouazzani, N., Monga, O., and Hbid, M. L. (2023). Artificial intelligence and wastewater treatment: a global scientific perspective through text mining. *WaterSwitzerl.* 15 (19), 3487. doi:10.3390/w15193487

El-Sadek, A. (2006). Upscaling field scale hydrology and water quality modelling to catchment scale. *Water Resour. Manag.* 21 (1), 149–169. doi:10.1007/S11269-006-9046-Y

Hassen, E. B., and Asmare, A. M. (2018). Predictive performance modeling of habesha brewery's wastewater treatment plant using artificial neural networks. *J. Environ. Treat. Tech.* 6 (2), 15–25.

Hsu, C.-C. (2006). Generalizing self-organizing map for categorical data. *IEEE Trans. Neural Netw.* 17 (2), 294–304. doi:10.1109/TNN.2005.863415

Jang, J. S. R. (1993). ANFIS: adaptive-network-based fuzzy inference system. *IEEE Trans. Syst. Man Cybern.* 23 (3), 665–685. doi:10.1109/21.256541

Kalteh, A. M., Hjorth, P., and Berndtsson, R. (2008). Review of the self-organizing map (SOM) approach in water resources: analysis, modelling and application. *Environ. Model. Softw.* 23 (7), 835–845. doi:10.1016/J.ENVSOFT.2007.10.001

Kangas, J., and Kohonen, T. (1996). Developments and applications of the self-organizing map and related algorithms. *Math. Comput. Simul.* 41, 3–12. doi:10.1016/0378-4754(96)88223-1

Karami, H., DadrasAjirlou, Y., Jun, C., Bateni, S. M., Band, S. S., Mosavi, A., et al. (2022). A novel approach for estimation of sediment load in dam reservoir with hybrid intelligent algorithms. *Front. Environ. Sci.* 10, 821079. doi:10.3389/fenvs.2022.821079

Karube, I., Matsunaga, T., Mitsuda, S., and Suzuki, S. (1977). Microbial electrode BOD sensors. *Biotechnol. Bioeng.* 19 (10), 1535–1547. doi:10.1002/BIT.260191010

Kohonen, T., Hynninen, J., Kangas, J., and Laaksonen, J. (1996). SOM_PAK: the self-organizing map program package. Available at: http://citeseerx.ist.psu.edu/viewdoc/download?doi=10.1.1.455.8698&rep=rep1&type=pdf.

Kumar, N., Rustum, R., Shankar, V., and Adeloye, A. J. (2021a). Self-organizing map estimator for the crop water stress index. *Comput. Electron. Agric.* 187, 106232. doi:10.1016/J.COMPAG.2021.106232

Kumar, N., Shankar, V., Rustum, R., and Adeloye, A. J. (2021b). Evaluating the performance of self-organizing maps to estimate well-watered canopy temperature for calculating crop water stress index in Indian Mustard (Brassica Juncea). *J. Irrigation Drainage Eng.* 147 (2), 4020040. doi:10.1061/(ASCE)IR.1943-4774.0001526

Legates, D. R., and McCabe, G. J. (1999). Evaluating the use of "goodness-of-fit" Measures in hydrologic and hydroclimatic model validation. *Water Resour. Res.* 35 (1), 233–241. doi:10.1029/1998WR900018

Lei, Y. (2017). Individual intelligent method-based fault diagnosis. *Intelligent Fault Diagnosis Remain. Useful Life Predict. Rotating Mach.*, 67–174. doi:10.1016/B978-0-12-811534-3.00003-2

Lin, W., Hanyue, Y., and Bin, L. (2022). Prediction of wastewater treatment system based on deep learning. *Front. Ecol. Evol.* 10, 1064555. doi:10.3389/fevo.2022.1064555

Liu, Y., Li, J., Wan, N., Fu, T., Wang, L., Li, C., et al. (2020). A current sensing biosensor for BOD rapid measurement. *Archaea* 2020, 1–7. doi:10.1155/2020/8894925

Lopez Garcia, H., and Machon Gonzalez, I. (2004). Self-organizing map and clustering for wastewater treatment monitoring. *Eng. Appl. Artif. Intell.* 17 (3), 215–225. doi:10.1016/J.ENGAPPAI.2004.03.004

Malota, M., Mchenga, J., and Chunga, B. A. (2022). WaSim model for subsurface drainage design using soil hydraulic parameters estimated by pedotransfer functions. *Appl. Water Sci.* 12 (7), 171–211. doi:10.1007/S13201-022-01699-Z

Mathsworks (2020). MATLAB:Getting started Guide (R2020a ed.). Available at: https://www.mathworks.com/products/matlab/getting-started.html.

Metcalf & Eddy (2013). Wastewater engineering: treatment and resource recovery. Available at: https://books.google.com.cu/books?id=6KVKMAEACAAJ.

Mng'ombe, M. H., Chunga, B. A., Mtonga, E. W., Chidya, R. C. G., and Malota, M. (2023). Infilling missing data and outliers for a conventional sewage treatment plant using a self-organizing map: a case study of Kauma Sewage Treatment Plant in Lilongwe, Malawi. *H2Open J.* 6 (2), 280–296. doi:10.2166/H2OJ.2023.013

Mohanty, S., Patra, P. K., Mohanty, A., Harrag, A., and Rezk, H. (2022). Adaptive neuro-fuzzy approach for solar radiation forecasting in cyclone ravaged Indian cities: a review. *Front. Energy Res.* 10, 828097. doi:10.3389/fenrg.2022.828097

Moriasi, D., Arnold, J. G., Van Liew, M. W., Bingner, R. L., Harmel, R. D., and Veith, T. L. (2007). Model evaluation guidelines for systematic quantification of accuracy in watershed simulations. *Trans. ASABE* 50 (3), 885–900. doi:10.13031/2013.23153

MS682-1:2002 (2002). Water quality sampling. Part 1:Guidance on the design, and sampling programs and sampling techniques-. *Malawi Bureau Stand. Vol. Part* 1, 23.

Mtethiwa, A., Munyenyembe, A., Jere, W., and Nyali, E. (2008). Efficiency of oxidation ponds in wastewater treatment. *Int. J. Environ. Res.* 2 (2), 149–152.

Niwagaba, C. B., Mbeguere, M., and Strande, L. (2014). Faecal sludge quantification, characterisation and treatment objectives. *Faecal Sludge Manag.* 35.

Nkiaka, E., Nawaz, N. R., and Lovett, J. C. (2016). Using self-organizing maps to infill missing data in hydro-meteorological time series from the Logone catchment, Lake Chad basin. *Environ. Monit. Assess.* 188 (7), 400–412. doi:10.1007/S10661-016-5385-1

Noori, R., Safavi, S., and Nateghi Shahrokni, S. A. (2013a). A reduced-order adaptive neuro-fuzzy inference system model as a software sensor for rapid estimation of five-day biochemical oxygen demand. *J. Hydrology* 495, 175–185. doi:10.1016/J.JHYDROL.2013.04.052

Noori, R., Safavi, S., and Nateghi Shahrokni, S. A. (2013b). A reduced-order adaptive neuro-fuzzy inference system model as a software sensor for rapid estimation of five-day biochemical oxygen demand. *J. Hydrology* 495, 175–185. doi:10.1016/J.JHYDROL.2013.04.052

Obasi, P. O., Ismail I, A., Abdulazeez, R., Najashi, B. 'u G., Jibril, M., Awaisu Shafiu, I., et al. (2022). Performance analysis and control of wastewater treatment plant using Adaptive Neuro-Fuzzy Inference System (ANFIS) and Multi-Linear Regression (MLR) techniques. *GSC Adv. Eng. Technol.* 4 (2), 001–016. doi:10.30574/GSCAET.2022.4.2.0033

Okeke, O. P., Ismail, I. A., Abdulazeez, R., Bara'u, G. N., M.M, J., Awaisu, S. I., et al. (2022). Performance analysis and control of wastewater treatment plant using Adaptive Neuro-Fuzzy Inference System (ANFIS) and Multi-Linear Regression (MLR) techniques. *GSC Adv. Eng. Technol.* 4 (2), 001–016. doi:10.30574/GSCAET.2022.4.2.0033

Pitman, K., Raud, M., and Kikas, T. (2015). Biochemical oxygen demand sensor arrays. *Agron. Res.* 13 (2), 382–395.

Pourzangbar, A., Jalali, M., and Brocchini, M. (2023). Machine learning application in modelling marine and coastal phenomena: a critical review. *Front. Environ. Eng.* 2, 1235557. doi:10.3389/FENVE.2023.1235557

Qiao, L., Yang, P., Leng, Q., Xu, L., Bi, Y., Xu, J., et al. (2023). Exploring ANFIS application based on actual data from wastewater treatment plant for predicting effluent removal quality of selected major pollutants. *J. Water Process Eng.* 56, 104247. doi:10.1016/J.JWPE.2023.104247

Rai, A., Singh, S., Zia, S., Manikpuri, P., and Alexander, K. (2019). Relation between COD and BOD in Sangam water samples for pre and post bath during Kumbh. Available at: https://www.entomoljournal.com/archives/2019/vol7issue3/PartS/7-3-187-712.pdf.

Ramos, M. J. C., Gonzalez, I. M., Garcia, H. L., Rolle, J. L. C., Leal, E. C., Loff, M., et al. (2013). "Visual supervision of a waste water biological reactor using artificial intelligence algorithms," in 2013 International Conference on New Concepts in Smart Cities: Fostering Public and Private Alliances (SmartMILE), Gijon, Spain, December, 2013.

Ravina, M., Galletta, S., Dagbetin, A., Kamaleldin, O. A. H., Mng'ombe, M., Mnyenyembe, L., et al. (2021). Urban wastewater treatment in african countries: evidence from the hydroaid initiative. *Sustainability* 13 (22), 12828. doi:10.3390/SU132212828

Rustum, R. (2009). Modelling activated sludge wastewater treatment plants using artificial intelligence techniques (fuzzy logic and neural networks). Available at: https://www.ros-test.hw.ac.uk/xmlui/handle/10399/2207.

Rustum, R., and Adeloye, A. (2011a). "Artificial intelligence modeling of wastewater treatment plants: theory, applications and limitations," in *VDM verlag Dr. Muller* (Saarbrücken, Germany: OmniScriptum).

Rustum, R., and Adeloye, A. (2011b). "Artificial intelligence modeling of wastewater treatment plants: theory, applications and limitations," in *VDM verlag Dr. Muller* (Saarbrücken, Germany: OmniScriptum).

Vázquez, R. F., Feyen, L., Feyen, J., and Refsgaard, J. C. (2002). Effect of grid size on effective parameters and model performance of the MIKE-SHE code. *Hydrol. Process.* 16 (2), 355–372. doi:10.1002/HYP.334

Vermasvuori, M., Endén, P., Haavisto, S., and Jämsä-Jounela, S. L. (2002). "The use of Kohonen self-organizing maps in process monitoring," in 1st International IEEE Symposium, Varna, Bulgaria, September, 2002, 2–7.

Vesanto, J., Himberg, J., Alhoniemi, E., and Parhankangas, J. (2000a). SOM toolbox for Matlab 5. Available at: https://citeseerx.ist.psu.edu/viewdoc/download?doi=10.1.1.25.7561&rep=rep1&type=pdf.

Vesanto, J., Himberg, J., Alhoniemi, E., and Parhankangas, J. (2000b). SOM toolbox for matlab 5 libella oy espoo 2000 SOM toolbox for matlab 5. Available at: http://www.cis.hut./projects/somtoolbox/http://www.cis.hut./projects/somtoolbox/.

Wang, X., Mosley, C. T., Frankenberger, J. R., and Kladivko, E. J. (2006). Subsurface drain flow and crop yield predictions for different drain spacings using DRAINMOD. *Agric. Water Manag.* 79 (2), 113–136. doi:10.1016/J.AGWAT.2005.02.002

Ward, B. J., Andriessen, N., Tembo, J. M., Kabika, J., Grau, M., Scheidegger, A., et al. (2021). Predictive models using "cheap and easy" field measurements: can they fill a gap in planning, monitoring, and implementing fecal sludge management solutions? *Water Res.* 196, 116997. doi:10.1016/J.WATRES.2021.116997

Zhu, J., Jiang, Z., and Feng, L. (2022). Improved neural network with least square support vector machine for wastewater treatment process. *Chemosphere* 308, 136116. doi:10.1016/J.CHEMOSPHERE.2022.136116

Frontiers in Environmental Engineering

Advances science and engineering practices to create a safe and sustainable environment

Explores new theories and techniques which provide practical and sustainable solutions to protect the natural ecosystem, address global environmental challenges and improve public health

Discover the latest Research Topics

See more →

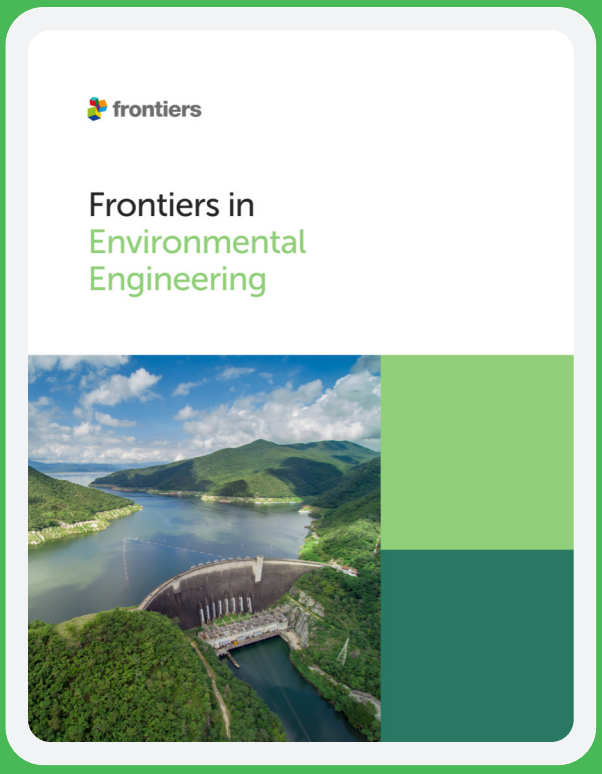

Frontiers

Avenue du Tribunal-Fédéral 34
1005 Lausanne, Switzerland
frontiersin.org

Contact us

+41 (0)21 510 17 00
frontiersin.org/about/contact